Faculteit Wetenschappen
Departement Fysica

Super-resolution estimation of quantitative MRI parameters

Superresolutie schatting van kwantitatieve MRI parameters

Proefschrift voorgelegd tot het behalen van de graad van

Doctor in de Wetenschappen: fysica

aan de Universiteit Antwerpen, te verdedigen door

Gwendolyn VAN STEENKISTE

Promotoren:
Prof. Dr. Jan Sijbers
Dr. Ben Jeurissen
Dr. Dirk H.J. Poot

Antwerpen, 2016

Doctoral committee:

Prof. Dr. Joke Hadermann
Prof. Dr. Jan Sijbers
Prof. Dr. Marleen Verhoye

Prof. Dr. Johan De Mey
Dr. Ben Jeurissen
Dr. Dirk H.J. Poot
Prof. Dr. Colin Studholme

Contact information:

✉ **Gwendolyn Van Steenkiste**
Vision Lab, Dept. of Physics
University of Antwerp (CDE)
Universiteitsplein 1, Building N1.16
B-2610 Wilrijk, Antwerpen, Belgium
☎ +32 3 265 24 58
🖷 +32 3 265 22 45
🖂 gwendolyn.vansteenkiste@uantwerpen.be
🌍 http://visielab.uantwerpen.be/people/gwendolyn-van-steenkiste

Contents

Summary

Magnetic resonance imaging (MRI) is a versatile non-invasive imaging modality. Magnetic resonance (MR) images are created using a combination of a strong magnetic field and radio frequency (RF) pulses. Hence, unlinke other medical imaging techniques, MRI does not use ionizing radiation. The underlying phenomenon of MRI is nuclear magnetic resonance (NMR). Atomic nuclei (e.g. hydrogen protons) placed in an external magnetic field can absorb and emit radio frequency energy. An RF wave is used to excite protons in human tissue. When the RF pulse is switched off, the protons will relax back to its equilibrium state, thereby emitting radiofrequency energy, the MR signal. The relaxation of the protons will depend on the environment of the protons (tissue type and/or pathology). These differences in relaxation generate the anatomical contrast in the MR image. The signal intensities represented by the voxel values in these images, do not only depend on the environment of the proton but also on the sequence parameters, i.e. the settings with which the images are acquired. For example, the signal intensities scale with the spatial resolution of the acquired images and the magnetic field strength. Hence, the anatomical images are qualitative images and interpretation of the images is left to a skilled observer.

MRI can also be used to create quantitative parameter maps. Although these parameter maps have the same appearance as an image, their voxel values represent the tissue parameters instead of a signal intensity on an arbitrary scale. In quantitative MRI, these parameter maps are estimated from a set of acquired MR images using a parameter model, i.e. a set of mathematical equations that describes the MR images in function of the parameter. A precise and accurate high resolution estimation of the parameters is needed in order to detect small changes and/or to visualize small structures.

Acquiring a high resolution data set required for precise and accurate estimation of the parameter maps is a challenging task. The signal intensity of an MR image is proportional to the voxel size, i.e. bigger voxels contain more signal. Hence, increasing the spatial resolution of an MR image decreases the signal intensity. Inherently, each acquired MR image is corrupted by noise. A low signal-to-noise ratio (SNR) does not only lead to a low precision of the estimator, but also might complicate the distinction between the signal of interest and the noise. The SNR of an MR image can be improved either by acquiring the image at a lower spatial resolution or by averaging the signal over multiple acquisitions. However, this leads to an increase in the acquisition time, which in turn decreases patient comfort and increases the chances of motion and motion artifacts, leading to a decrease in image quality. Hence, in each MRI experiment a trade-off has to be made between the spatial resolution, acquisition time and SNR.

To achieve sufficient SNR within a feasible acquisition time, MR images are typically acquired with a low spatial resolution. This low spatial resolution, however, leads to large partial volume effects, i.e. voxels will contain a mixture of different tissue types and thus different signals. Moreover, the low spatial resolution makes it impossible to detect small structures. The goal of this dissertation is to enable high resolution quantitative mapping by improving the trade-off between the spatial resolution, SNR and acquisition time through the development of a super-resolution reconstruction method.

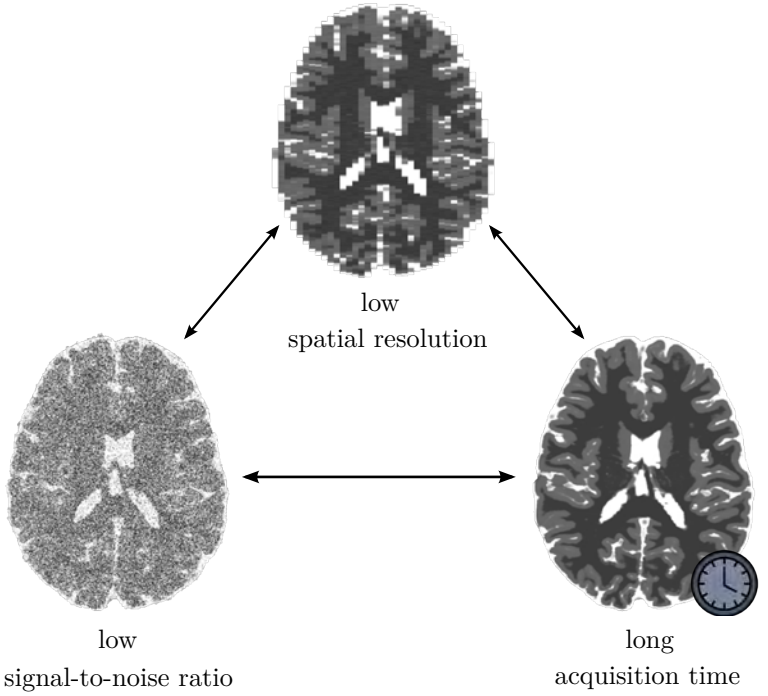

Fig. 1: Trade-off between spatial resolution, acquisition time and SNR.

In part I of this dissertation, the basics of quantitative MRI are covered. Next, part II provides a short introduction to the resolution enhancement technique super-resolution reconstruction. Finally, part III deals with the main contributions of this dissertation.

Quantitative MRI: the basics

Chapter 1 introduces the basic principles of MRI. The signal generation and localization are covered. Furthermore, the relationship between the image quality and acquisition time is discussed. In the following chapters two quantitative MRI techniques T_1 mapping (chapter 2) and diffusion-weighted MRI (chapter 3) are discussed in detail.

The relaxation of the protons after excitation by an RF pulse depends on the tissue properties and can be defined by two relaxation parameters, T_1 and T_2. In quantitative T_1 mapping, the longitudinal or spin-lattice relaxation time T_1 is estimated from a set of T_1-weighted images. In chapter 2 the basics of T_1 relaxation as well as the acquisition of the T_1-weighted images are discussed. The T_1 relaxation time changes according to tissue and pathology, making T_1 mapping useful for a broad range of clinical applications. Although many T_1 acquisition methods have been developed, acquiring T_1-weighted images with the required image quality within clinically feasible scan times remains a challenging task. As a result, T_1 mapping is not yet used in clinical routine. These challenges are discussed in chapter 2 as well.

In diffusion-weighted MRI (dMRI) the image contrast is generated by the molecular diffusion of water molecules, which is correlated with the tissue microstructure. For example, in highly structured tissues, such as white matter, molecules will rather diffuse along the structures than perpendicular to it. The most common way to represent the diffusion is by the diffusion tensor. The challenges hampering high resolution diffustion tensor imaging (DTI) within a clinical feasible scan time are discussed in chapter 3.

Super-resolution reconstruction

In many medical applications, high resolution 3D images are required for visualizing small structures and detecting small structures, allowing an early and accurate diagnosis. However, due to time constraints and hardware limitations, achieving high spatial resolution is not always feasible. A solution is to deal with the time constraints is to use various accelerating techniques such as parallel imaging and simultaneous-multi-slice. An interesting and complementary alternative technique is super-resolution reconstruction (SRR), in which a high resolution image is estimated from a set of acquired low resolution images. These low resolution images each contain different information of the imaged object. Several SR techniques for MRI have already been proposed, a short overview can be found in chapter 4.

Contributions

In chapter 5, SRR is combined with T_1 estimation into one integrated method, by directly estimating a high resolution T_1 map from a set of acquired low resolution T_1-weighted images. Thanks to the acquisition scheme and iterative reconstruction, the high resolution T_1 parameters can be recovered from the low resolution images with an improved accuracy compared to conventional voxel-wise T_1 estimators.

An SR method specifically designed for DTI is presented in chapter 6. Incorporating the DTI model into the SR reconstruction and thereby estimating high resolution DTI parameters directly from a set of low resolution DW images, has several advantages. By allowing a more flexible acquisition set up as well as incorporation of motion correction, SR-DTI outperforms both conventional DT estimators and other existing SR methods in terms of accuracy and precision.

In the final chapter, chapter 7, SR-DTI is applied in two small animal preclinical studies, one on the zebra finch brain and one on the mustached bat brain, in order to visualize small structures, previously undetectable due to the low spatial resolution of the images.

Samenvatting

Magnetische resonantie beeldvorming (MRI) is een krachtige niet-invasieve beeldvormingstechniek die toelaat om de anatomie en fysiologische processen in kaart te brengen. MRI maakt geen gebruik van ioniserende straling maar van een magnetisch veld en radiofrequente elektromagnetische golven. De radiofrequentie elektromagnetische golven worden gebruikt om atoomkernen geëxciteerd. Na excitatie keren de atoomkernen terug naar evenwichtstoestand waarbij energie vrijkomt. De hoeveelheid vrijgekomen energie is afhankelijk van het soort weefsel en wordt gebruikt om een anatomisch contrast te genereren in de beelden. De signaalintensiteiten van deze beelden zijn zowel afhankelijk van de biologische weefselparameters als van de manier waarop de beelden zijn opgenomen (de sequenties parameters). Zo zal de signaalintensiteit onder andere afhangen van de sterkte van het magnetisch veld en de spatiële resolutie van de beelden. De interpretatie van de beelden wordt overgelaten aan geoefende waarnemers.

MRI kan echter ook gebruikt worden om de biologische parameters op kwantitatieve wijze in kaart te brengen. Deze kwantitatieve parameterbeelden zien er uit als kwalitatieve beelden, maar de voxelwaardes hebben een andere betekenis. Waar in een kwalitatief beeld elke voxelwaarde een signaalintensiteit voorstelt op een arbitraire schaal, stelt in kwantitatieve parameterbeelden elke voxelwaarde de numerieke waarde van een biologische weefselparameter voor. In kwantitatieve MRI wordt het signaal van een opgenomen MR beeld beschreven in functie van deze biologische weefselparameters aan de hand van een set van wiskundige vergelijkingen. Wanneer voldoende MR beelden opgenomen worden, kan de biologische weefselparameter geschat worden uit deze opgenomen beelden.

Om kleine veranderingen in de weefselparameters te kunnen detecteren alsook kleine structuren, dienen de parameters geschat te worden op een hoge resolutie met een hoge nauwkeurigheid en precisie. Het opnemen van de MRI-beelden die nodig zijn om precieze, nauwkeurige weefselparameters te schatten op hoge resolutie is echter niet vanzelfsprekend. De signaalintensiteit van een MRI-beeld is evenredig met de grote van de voxels. Hoe groter de voxel, hoe hoger de signaalintensiteit in de voxel. Dus beelden met een hoge spatiële resolutie (kleine voxels) zullen een lagere signaalintensiteit hebben. Elk opgenomen MRI-beeld bevat ruis. Bij een lage signaal-ruisverhouding, kan het voorkomen dat het MRI-signaal niet onderscheidbaar is van de ruis, waardoor kleine structuren vaak niet zichtbaar zijn door de ruis. Daarenboven is ook de precisie van de geschatte parameters evenredig met de signaal-ruisverhouding van de beelden. De signaal-ruisverhouding van een beeld kan verbeterd worden door het beeld meerdere keren op te nemen en dan het gemiddelde van deze beelden te nemen. Dit resulteert echter in een toename van de totale scantijd, die al vrij lang is in kwantitatieve MRI, aangezien meerdere beelden

opgenomen moeten worden om de weefselparameters te kunnen schatten. Lange scantijden zijn niet alleen nadelig is voor het comfort van de patiënt maar hebben ook negatieve gevolgen voor de beeldkwaliteit aangezien de kans dat de patiënt beweegt groter zijn. In elk MRI-experiment moet dus een afweging gemaakt worden tussen de spatiële resolutie, scantijd en signaal-ruisverhouding van de beelden.

Opdat de beelden voldoende SNR zouden bevatten en de scantijd klinisch haalbaar zou zijn, worden de beelden vaak opgenomen met een lage spatiële resolutie. Het verlagen van de spatiële resolutie zorgt niet enkel voor een verhoging van de signaalintensiteit en dus de signaal-ruisverhouding maar ook voor het verkorten van de scantijd, aangezien minder voxels opgenomen moeten worden om de volledige structuur in kaart te brengen. Desalniettemin heeft het opnemen met een lage spatiële resolutie ook zijn nadelen. De grotere voxels bevatten vaak een combinatie van verschillende weefseltypes, waardoor het verkregen signaal een mix is van verschillende signalen afkomstig van verschillende weefseltypes. De weefselparameters geschat uit deze signalen geven vaak geen goed beeld van de werkelijke samenstelling van de voxel. Bovendien zullen kleine structuren niet zichtbaar zijn in de opgenomen beelden, noch in de parameterbeelden. Het doel van deze thesis is om de wisselwerking tussen de spatiële resolutie, scantijd en signaal-ruisverhouding van kwantitatieve MRI-experimenten te verbeteren aan de hand van superresolutie reconstructie, waardoor het mogelijk wordt om precieze en nauwkeurige parameterbeelden te bekomen met een hoge spatiële resolutie, binnen een klinisch haalbare tijd.

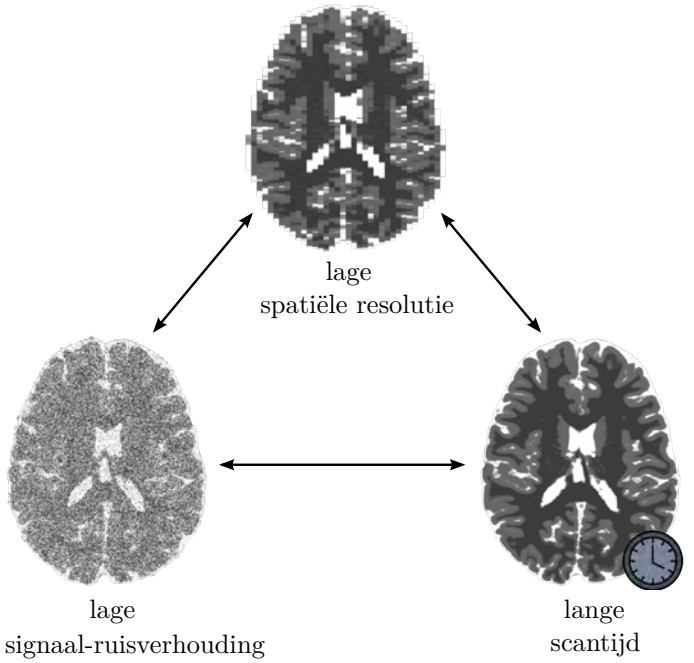

Fig. 2: Wisselwerking tussen de spatiële resolutie, scantijd en signaal-ruisverhouding.

In deel I van deze thesis worden de basisprincipes van kwantitatieve MRI uitgelegd. Een korte introductie tot super-resolutiereconstructie, een techniek waarmee de spatiële resolutie van beelden verhoogd kan worden, wordt gegeven in deel II. In deel III worden de belangrijkste bijdragen van deze thesis weergegeven.

Kwantitatieve MRI: de basis

Hoofdstuk 1 introduceert de basisprincipes van MRI. Er wordt dieper ingegaan op het genereren en lokaliseren van een MRI-signaal. Daarnaast wordt de relatie tussen de beeldkwaliteit (signaal-ruisverhouding en spatiële resolutie) en scantijd uiteengezet. In de volgende hoofdstukken worden twee kwantitatieve MRI-technieken besproken: het in kaart brengen van de longitudinale relaxatietijd T_1 en diffusie-MRI.

De relaxatie van de protonen, na excitatie met een radiofrequente elektromagnetische golf, is afhankelijk van de fysische en biologische parameters van hun omgeving. Deze relaxatie kan beschreven worden aan de hand van twee relaxatietijden: T_1 en T_2. De longitudinale relaxatietijd T_1 wordt in kaart gebracht door deze te schatten uit een reeks T_1-gewogen beelden. De opname van deze T_1-gewogen beelden en het schatten van de T_1-relaxatietijd wordt besproken in hoofdstuk 2. Aangezien de T_1-relaxatietijd afhankelijk is van het weefseltype en pathologie, kan de kennis van de T_1-relaxatietijd bijdragen tot de diagnose van verschillende aandoeningen. Hoewel reeds verschillende opnamemethodes werden ontwikkeld, blijft het opnemen van hoge resolutie T_1 gewogen beelden die geschikt zijn voor een precieze en nauwkeurige schatting van de T_1-relaxatietijd, een uitdagende taak. In hoofdstuk 2 wordt een overzicht gegeven van de verschillende opnamemethodes alsook van de uitdagingen die dienen aangepakt worden om van kwantitatieve T_1-parameterbeelden met een hoge spatiële resolutie een klinische realiteit te maken.

In diffusie-MRI (dMRI) wordt de diffusie van watermoleculen in weefsel gebruikt om de microstructuren van de weefsels in kaart te brengen. Het signaal in een diffusie-gewogen beeld is afhankelijk van de mate en de richting waarin de watermoleculen zich voortbewegen, alsook van de sequentieparameters. De meeste weefsels, zoals de witte materie, bestaan uit geordende microstructuren. De watermoleculen zullen zich eerder beweging langsheen deze structuren dan er loodrecht op. Dus met dMRI kan men informatie bekomen over de onderliggende microstructuren. De meest gebruikte manier om de diffusie voor te stellen is de diffusietensor. Diffusietensor-beeldvorming (DTI), de techniek die bestaat uit het modelleren en schatten van de diffusietensor uit een set van diffusie-gewogen beelden, wordt uitgelegd in hoofdstuk 3. De diffusie-weging van de signalen zorgt voor een daling van het signaal, hierdoor is de signaal-ruisverhouding van diffusie gewogen beelden nog lager dan die van andere MRI beelden. Daarnaast zijn ook meerdere diffusie gewogen beelden, waarin de diffusie telkens gemeten is in een verschillende richting (de diffusiegradiëntrichting), nodig om de diffusietensor te kunnen bepalen, wat leidt tot lange scantijden. Deze en andere uitdagingen die getackeld moeten worden om nauwkeurige, precisie hoge resolutie DTI mogelijk te maken in de klinische praktijk worden besproken op het einde van hoofdstuk 3.

Superresolutie reconstructie

In vele medische toepassingen zijn driedimensionale beelden met een hoge resolutie nodig voor vroege en nauwkeurige diagnose. Het opnemen van deze hoog resolutie beelden is niet altijd haalbaar door een beperkte opnametijd en limitaties opgelegd door de hardware. De meeste technieken leggen de focus op het verminderen van de opnametijd. Een interessant en complementair alternatief is om superresolutie (SR) reconstructie te gebruiken. SR reconstructie bestaat uit het schatten van een beeld met hoge resolutie uit een set van beelden opgenomen met een lage resolutie. Elk van deze opgenomen beelden met bevat verschillende informatie over het gebeeldvormde object. De verschillende methodes die werden ontwikkeld om deze set aan beelden met lage resolutie op te nemen, worden besproken in hoofdstuk 4. Daarnaast wordt in hoofdstuk 4 ook een SR reconstructie techniek voor kwalitatieve MRI geïntroduceerd. De kwantitatieve SR reconstructie technieken die voorgesteld worden in deel III van deze thesis zijn gebaseerd op deze kwalitatieve SR techniek.

Bijdragen

In hoofdstuk 5 wordt SR-T1 voorgesteld, een techniek die SR reconstructie combineert met het schatten van de T_1-relaxatietijd. De T_1-relaxatietijden worden op een grid met hoge resolutie geschat vanuit T_1-gewogen beelden die opgenomen zijn met een lage spatiële resolutie. Hierbij wordt ook in rekening gebracht dat er eventueel beweging heeft plaatsgevonden tussen de opname van de verschillende T_1-gewogen beelden. Aan de hand van eenvoudige numerieke simulaties wordt aangetoond dat het voorgestelde opnameschema en de iteratieve schatting van de T_1-relaxatietijd hoge resolutie informatie kan herstellen. Experimenten waarin het volledige brein wordt gesimuleerd tonen aan dat met SR-T_1 een nauwkeurigere schatting van de T_1-relaxatietijd wordt bekomen dan wanneer conventionele technieken worden gebruikt. In de in vivo experimenten werden T_1 parameterbeelden bekomen met verschillende schattings- en opnamemethodes met elkaar vergeleken. De resultaten tonen aan dat SR-T_1 resulteert in een betere schatting dan de andere methoden.

Een SR methode specifiek ontwikkeld voor DTI, SR-DTI, wordt voorgesteld in hoofdstuk 6. Het integreren van het DTI model in de SR reconstructie, waardoor hoge resolutie DTI parameters rechtstreeks geschat kunnen worden vanuit lage resolutie diffusie-gewogen beelden biedt vele voordelen. In vergelijking met SR-DWI, waar eerst hoge resolutie diffusie gewogen beelden worden geschat uit de lage resolutie diffusie gewogen beelden en de hoge resolutie DTI parameters geschat worden uit de resulterende hoge resolutie diffusie-gewogen beelden, moet voor SR-DTI niet steeds dezelfde set van diffusiegradiëntrichtingen opgenomen worden per snede richting. Hierdoor kunnen de diffusiegradiëntrichtingen zowel geoptimaliseerd worden over de volledige data set als voor elke snederichting afzonderlijk. Dit kan enerzijds gebruikt worden om in totaal meer diffusiegradiëntrichtingen op te nemen of juist om het aantal diffusiegradiëntrichtingen per snederichting onder het minimale vereiste te brengen, waardoor de scantijd vermindert. Bovendien kan hierdoor ook correctie van de bewegingsartefacten en de bijhorende rotatie van de diffusiegadientrichtingen toegevoegd worden aan de schatting van de DTI parameters. De voordelen van SR-DTI werden uitvoerig getest op zowel gesimuleerde als in vivo

data. De experimenten tonen aan dat met SR-DTI preciezere en nauwkeurige hoge resolutie DTI parameters geschat kunnen worden dan met conventionele methodes en SR-DWI.

In het laatste hoofdstuk, hoofdstuk 7, worden enkele toepassingen van SR-DTI methodes besproken. Allereerst worden hoge resolutie DTI parameters geschat met SR-DTI uit beelden opgenomen met een lage resolutie op een standard scanner, visueel vergeleken met hoge resolutie DTI parameters geschat via conventionele methodes uit beelden opgenomen met een hoge resolutie op de human connectome project scanner, die een krachtigere gradiëntenset heeft. Daarnaast werd SR-DTI gebruikt in twee preklinische studies met als doelstelling om de breinconnectiviteit van de zebravink en de vleermuis in kaart te brengen.

Part I

Quantitative MRI: The basics

1

Magnetic resonance imaging

Contents

1.1 Introduction

Magnetic resonance imaging (MRI) is a versatile non-invasive imaging technique that allows in vivo visualization of structure and function. In contrast to many other medical imaging techniques, MRI does not use ionizing radiation, but a strong magnetic field in combination with electromagnetic radio frequency (RF) pulses and time varying gradients. In clinical routine, MRI is used to produce images with a high contrast between the different soft tissues. By using dedicated measurement sequences, MRI can also be used to display several physical phenomena such as brain activation (functional MRI), brain connectivity (diffusion MRI) or blood flow (MR angiography).

The research presented in this thesis is aimed at the development of methods to improve the spatial resolution of MR images. Hence, a basic knowledge of MRI is necessary for good comprehension of the concepts discussed in this thesis. Therefore, in this chapter a summary of the basic principles of MRI is provided. For more elaborate information on MRI we refer to literature [Liang and Lauterbur, 2000, Tofts, 2005, Bernstein et al., 2004].

1.2 Historical overview

MRI is based on nuclear magnetic resonance (NMR), a physical phenomenon in which nuclei in a magnetic field absorb and re-emit radio waves. Isodor Isaac Rabi was the first to describe this phenomenon when he observed that the spin state of atomic nuclei can be changed by exposing them to radio-waves. For this work he was awarded the Nobel Prize in Physics in 1944. Almost a decade later, Felix Bloch and Edward Mills Purcell independently demonstrated that the NMR phenomenon could be used to identify the specific atoms in any solid or liquid placed in a magnetic field [Bloch et al., 1946, Purcell et al., 1946]. They were awarded the Nobel Prize in Physics in 1952 for this work. Since then, NMR has become a powerful tool for chemical and structural analysis of substances.

Twenty years later, Raymon Damadian discovered that the NMR signal of cancerous tissue is different from that of healthy tissue [Damadian, 1971]. This discovery made him realize the potential of NMR in medical imaging, and he filed for a patent a year later. Figure 1.1 shows an illustration of the MRI machine in his patent application. The transition of one-dimensional (1D) NMR signals to two-dimensional (2D) images was made by Paul Lauterbur, who suggested applying magnetic field gradients for encoding [Lauterbur, 1973]. Peter Mansfield developed a method, currently known as echo planar imaging (EPI) to acquire such 2D images in only a few seconds [Mansfield, 1977]. Both scientists received the Noble Prize in Medicine and Physiology in 2003 for their work on non-invasive imaging of the body. A lot of controversy surrounded this Nobel Prize. Although he was the first to acquire a human whole body MR image in 1977 [Damadian et al., 1976], Damadian was not honored by the Nobel Prize committee.

Another breakthrough in MRI that can not be overlooked is the work of Richard Ernst (Nobel Prize in Chemistry in 1991) [Kumar et al., 1975]. He described the application of the Fourier transform to reconstruct 2D images, in combination with switched magnetic field gradients in the time domain for spatial encoding.

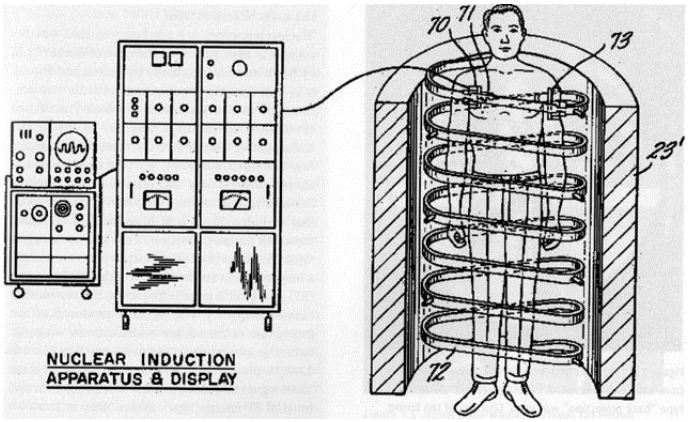

Fig. 1.1: Damadian's "Apparatus and method for detecting cancer in tissue". US patent 3789832 filed 17 March 1972, issued 5 February 1974. Image from the US Patent and Trademark Office.

1.3 Signal generation

1.3.1 Spin physics

All atomic nuclei with an odd number of protons or neutrons possess an intrinsic spin angular momentum $\boldsymbol{J}$:

$$\begin{aligned} \boldsymbol{J} &= \hbar \boldsymbol{I} \\ \|\boldsymbol{J}\| &= \hbar\sqrt{I(I+1)} \end{aligned} \tag{1.1}$$

with $\hbar$ the reduced Planck's constant ($1.05 \times 10^{-34}\,\mathrm{J\,s}$), $\boldsymbol{I}$ the intrinsic spin (dimensionless) and I the intrinsic quantum number. This spin angular momentum can be considered as an outcome of the rotational or spinning motion of the nucleus about its own axis. Therefore, nuclei that have a spin angular momentum are often referred to as nuclear spins. Because the nucleus is a charged particle, this intrinsic angular momentum $\boldsymbol{J}$ is proportionally coupled with a magnetic dipole moment $\boldsymbol{\mu}$:

$$\boldsymbol{\mu} = \gamma \boldsymbol{J}, \tag{1.2}$$

with γ the nucleus-dependent gyromagnetic ratio. When an external magnetic field $\boldsymbol{B}_0$ is applied, the magnetic moment $\boldsymbol{\mu}$ will precess about this magnetic field with an angular frequency known as the Larmor frequency, $\omega_L = \gamma B_0$.

All nuclei for which the spin quantum I is non-zero, exhibit the property of magnetic resonance. ^{1}H, ^{13}C, ^{19}F, ^{23}Na and ^{31}P are some of these nuclei that can be studied with NMR [Shapiro et al., 2002, Yu et al., 2005, Golman et al., 2008]. The most common nucleus considered in clinical MRI exams and the one used in this work, is the hydrogen proton (^{1}H). This proton has a high natural abundance in the body in the form of H_2O water molecules. For ^{1}H, the gyromagnetic ratio is 2.675×10^{8}rad/s/T, and its spin quantum number $I = 1/2$.

When nuclei are placed in an externally applied static magnetic field $\boldsymbol{B}_0$, the orientation of their spin angular momentum, and hence their magnetic moment, will no longer be arbitrary. In a magnetic field, the nuclear magnetic moment can only have $2I + 1$ orientations. Hence, the magnetic moment of a ^{1}H nucleus has two possible states: $+\frac{1}{2}\gamma\hbar$ and $-\frac{1}{2}\gamma\hbar$.

In an external applied static magnetic field $\boldsymbol{B}_0$, the nuclear magnetic dipole moment has a potential energy E. For the hydrogen proton, there are two energy levels:

$$E = -\boldsymbol{\mu} \cdot \boldsymbol{B_0} = \begin{cases} +\frac{1}{2}\gamma\hbar B_0 & \text{spin down,} \\ -\frac{1}{2}\gamma\hbar B_0 & \text{spin up,} \end{cases} \tag{1.3}$$

This splitting of energy levels is called Zeeman-splitting. The higher energy level is referred to as the 'spin down' (anti-parallel with $\boldsymbol{B}_0$) and the lower energy level as 'spin up' (parallel with $\boldsymbol{B}_0$). Transitions between these two energy levels are possible by absorption or emission of a photon with energy $\Delta E = \gamma\hbar B_0$. The energy of these transition photons is proportional to their frequency, $\omega_L = \gamma B_0$, which is called the Larmor frequency.

In practice, matter consists of a large group of similar nuclei. When an ensemble of nuclei is subjected to an external magnetic field $\boldsymbol{B}_0$, the occupation of the energy states (Eq. 1.3), proceeds in accordance with the Boltzmann statics. The spin up state (lower energy) has a higher prevalence than the spin-down state (higher energy):

$$\frac{N_\uparrow}{N_\downarrow} = e^{\frac{\Delta E}{k_B T}} > 1, \tag{1.4}$$

with k_B the Boltzmann constant ($1.380 \times 10^{-23}\,\mathrm{mkg^2/s^2/K}$) and T the absolute temperature and, $N_\uparrow$ and $N_\downarrow$ the number of spins in spin-up and spin-down state respectively. Although the difference in occupation of both states (10^{-5}) is extremely small at body temperature in a magnetic field of clinical strength (3 T), the population difference is significant due to the large number of ^{1}H protons.

1.3.2 Macroscopic magnetization

On a macroscopic scale, the magnetic dipoles can be grouped in spin ensembles, containing a large population of spins within a small volume. In a spin ensemble, the magnetic moments add up to a macroscopic nuclear magnetic momentum $\boldsymbol{M} = [M_x, M_y, M_z]$. In case of hydrogen protons, the macroscopic magnetic moment at equilibrium becomes:

$$\boldsymbol{M}_0 = \chi \boldsymbol{B_0}, \tag{1.5}$$

with χ the magnetic susceptibility which relates the macroscopic magnetization $\boldsymbol{M}$ with the static magnetic field $\boldsymbol{B}_0$. Thus, when $\boldsymbol{B}_0$ is applied along the z-direction, at equilibrium, both transverse components of the macroscopic magnetization ($M_x(0)$ and $M_y(0)$) are zero, while the z-component will be [Abragam, 1989]:

$$M_z(0) = N_s \frac{\gamma^2\hbar^2 B_0}{4k_B T}, \tag{1.6}$$

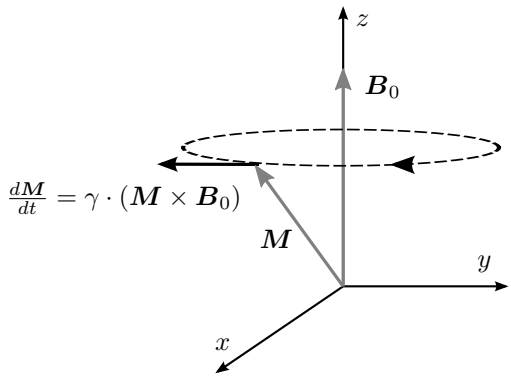

Fig. 1.2: The precession of the spin magnetization vector $\boldsymbol{M}$ around the external magnetic field $\boldsymbol{B}_0$ with an angular frequency ω_L.

with N_s the number of spins in the ensemble.

When this magnetization vector $\boldsymbol{M}$ is placed in an external static magnetic field, it will experience a torque. If the magnetic field $\boldsymbol{B}_0$ is directed along the z-axis, the resulting rate with which $\boldsymbol{M}$ changes in time is given by [Bloch et al., 1946]:

$$\frac{d\boldsymbol{M}}{dt} = \gamma \boldsymbol{M} \times \boldsymbol{B}_0 = [\omega_L M_y, \omega_L M_x, 0], \tag{1.7}$$

with ω_L the Larmor frequency:

$$\omega_L = \gamma B_0. \tag{1.8}$$

From this equation, the solution for the magnetization $\boldsymbol{M}$ is then:

$$\begin{bmatrix} M_x(t) \\ M_y(t) \\ M_z(t) \end{bmatrix} = \begin{bmatrix} cos(\omega_L t) & sin(\omega_L t) & 0 \\ -sin(\omega_L t) & cos(\omega_L t) & 0 \\ 0 & 0 & 1 \end{bmatrix} \begin{bmatrix} M_x(0) \\ M_y(0) \\ M_z(0) \end{bmatrix} \tag{1.9}$$

These equations describe the precession of the magnetization $\boldsymbol{M}$ around the direction of the magnetic field (Fig. 1.2) with angular frequency ω_L.

1.3.3 RF Excitation

When the subject is placed inside an electrically conducting coil, which is perpendicular to the transverse plane, the rotating transverse component of $\boldsymbol{M}$ will induce a voltage in the coil [Bleaney and Bleaney, 1976]. The amplitude of this voltage will be proportional to the magnitude of the transverse component. In order to generate this detectable signal, the system needs to be perturbed from its equilibrium state. This is achieved by applying a second magnetic field $\boldsymbol{B}_1$, which is perpendicular to $\boldsymbol{B}_0$ and oscillating at ω_L. This time varying magnetic field $\boldsymbol{B}_1$, which is an electromagnetic wave generated by a transmitter coil which surrounds the subject, is also called a radio frequency (RF) pulse. Note that $\boldsymbol{B}_1$ is much weaker than $\boldsymbol{B}_0$.

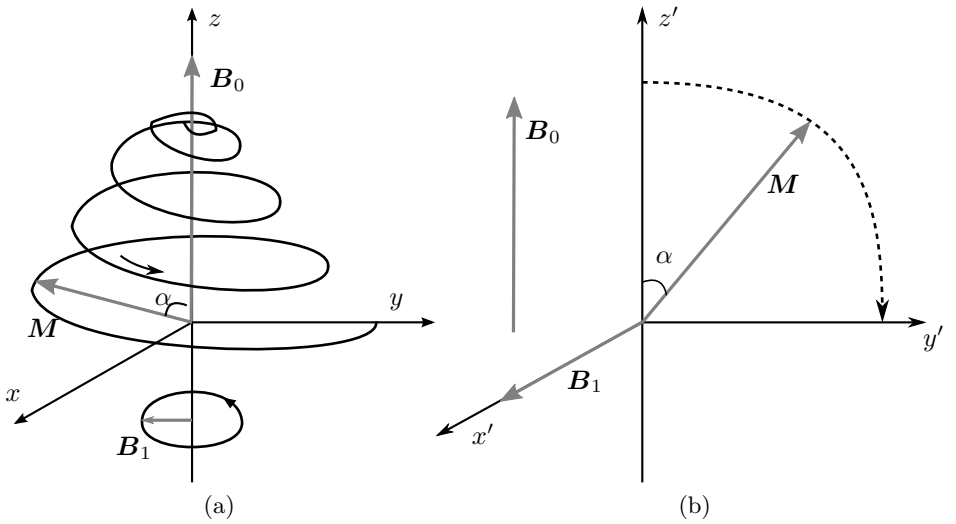

Fig. 1.3: Motion of the magnetization $\boldsymbol{M}$ under the influence of a static magnetic field $\boldsymbol{B}_0$ and a perpendicular time-varying magnetic field $\boldsymbol{B}_1$ in (a) the laboratory reference frame and (b) the rotating reference frame.

Upon applying the RF pulse, the magnetization $\boldsymbol{M}$ will precess simultaneously around both $\boldsymbol{B}_0$ at ω_L and $\boldsymbol{B}_1$ at $\omega_1 = \gamma B_1$. In the laboratory reference frame, which is static with respect to $\boldsymbol{B}_0$, applying $\boldsymbol{B}_1$ causes the magnetization to rotate spirally down on the surface of a sphere (Fig. 1.3a). When a frame rotating about the magnetization $\boldsymbol{B}_0$ and along with $\boldsymbol{B}_1$ at ω_L, is considered, the magnetization is rotated perpendicular to $\boldsymbol{B}_1$ at an angular frequency ω_1 (Fig. 1.3b). Thus, applying an RF-pulse during a time Δt, will flip $\boldsymbol{M}$ to the transverse plane by the angle $\alpha = \gamma B_1 \Delta t$, as illustrated in Fig. 1.3b. Typically, RF pulses are characterized by their flip angle. For example, a 90° RF pulse, will tip the longitudinal magnetization $\boldsymbol{M}$ 90° into the the transverse plane.

1.3.4 Relaxation

Due to the absorption of energy, the system is no longer in equilibrium. Hence, when the RF pulse is switched off, the magnetization will gradually return to its equilibrium state. The absorbed energy is dispersed by a number of processes, known as the relaxation mechanisms. These mechanisms can be grouped into two groups: longitudinal relaxation and a transverse relaxation [Tofts, 2005].

The **longitudinal or spin-lattice relaxation** stems from the redistribution of the spin states in order to reach thermal equilibrium. The energy released during this redistribution, is transferred from the spins to their surrounding environment (the lattice) by molecular vibrations. This results in a growth of M_z, characterized by the longitudinal relaxation time T_1. After a 90° RF pulse, the longitudinal

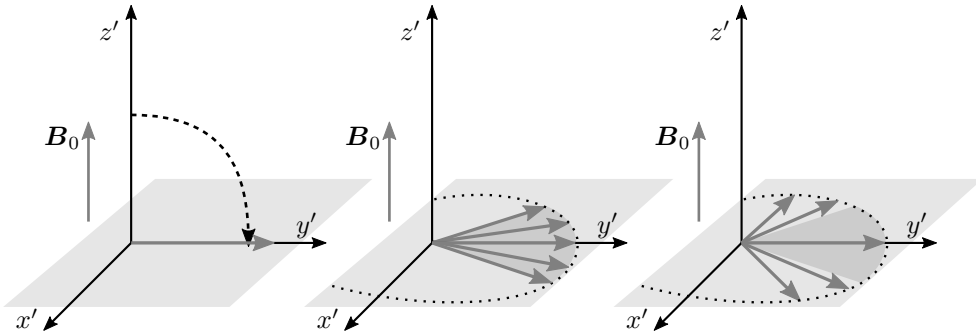

Fig. 1.4: Spin-spin relaxation: The nuclear magnetic dipole moments, which constitute the magnetization $\boldsymbol{M}$, dephase during precession (depicted in a rotating reference frame).

magnetization can be written in function of time:

$$M_z(t) = M_0 \left(1 - \mathrm{e}^{\frac{-t}{T_1}}\right), \tag{1.10}$$

with M_0 the magnetization along $\boldsymbol{B}_0$ at equilibrium. A more detailed discussion on T_1 relaxation can be found in chapter 2.

The **transverse or spin-spin relaxation** is due to the loss in phase coherence of the spins. Random fluctuations of the local magnetic field lead to variations of the Larmor frequency of the different spins. As a result, the inherently coherent spin precession will dephase (Fig. 1.4). Consequently, the net magnetization of the spin ensemble, which is equal to the transversal component of the magnetization vector, will decrease. After a 90° RF pulse, the evolution of M_x and M_y over time can be written as:

$$M_x(t) = M_0 \sin(\omega_L t)\mathrm{e}^{\frac{-t}{T_2}} \tag{1.11}$$

$$M_y(t) = M_0 \cos(\omega_L t)\mathrm{e}^{\frac{-t}{T_2}}. \tag{1.12}$$

The total transversal component, M_{xy}, keeps precessing around the z-axis with a constant angular frequency equal to the original Larmor frequency. In heterogeneous samples, where the differences in magnetic susceptibility cause inhomogeneities in the magnetic field, the decay will be faster than T_2 [Bloembergen et al., 1948]. The transversal relaxation due to these time independent inhomogeneities is called T_2' decay. The total relaxation time is then $\frac{1}{T_2^\star} = \frac{1}{T_2} + \frac{1}{T_2'}$ and the transversal relaxation can be written as:

$$M_{xy} = M_0 \mathrm{e}^{\frac{-t}{T_2\star}}. \tag{1.13}$$

The precessing transverse magnetization can easily be detected. When an electrically conducting coil is placed around the subject in the transverse plane, a voltage will be induced by the rotating magnetization. The amplitude of the voltage will decay exponentially characterized by the transverse relaxation $T_2^\star$. This captured signal is called the free induction decay (FID) signal [Hahn, 1950b, 1953].

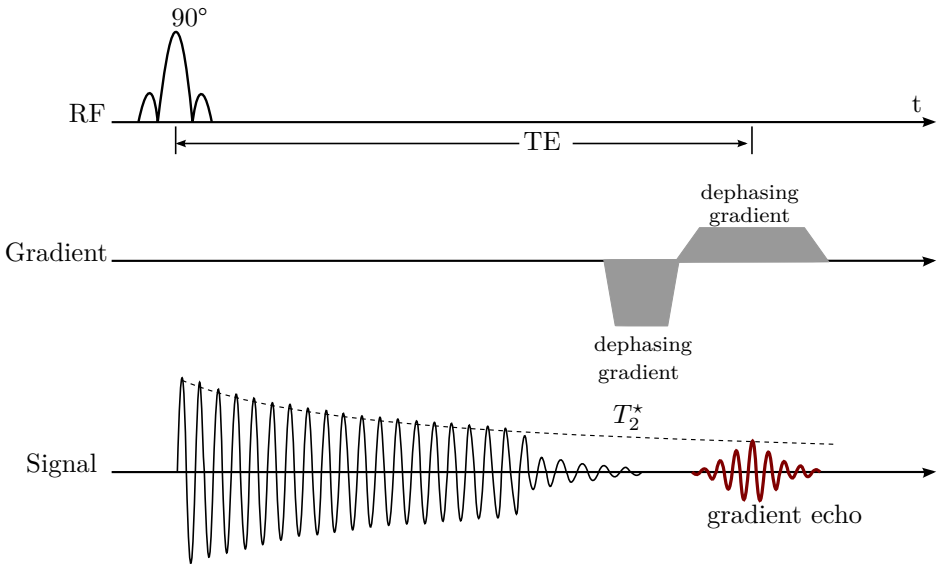

Fig. 1.5: Gradient echo sequence: The FID signal is manipulated by a bi-polar gradient, resulting in a gradient echo at TE.

1.3.5 Image contrast

The image contrast in NMR arises from tissues generating MR signals with different intensities because of their physical properties [Damadian, 1971]. Contrast weighting of the NMR signal is obtained by the design of pulse sequences, which consist of repetitive trains of RF pulses [Perman et al., 1984, Nitz and Reimer, 1999]. In this section the two most basic pulse sequences are described.

In a **gradient echo** (GE) sequence (Fig. 1.5) the FID signal is manipulated by a bi-polar gradient [Frahm et al., 1986, Elster, 1993]. The excitation pulse (α in Fig. 1.5) tilts the magnetization by α degrees. If α is 90°, the longitudinal magnetization is rotated in the transverse plane. The data are sampled during a gradient echo at time TE (TE: echo time) after the excitation pulse. This gradient echo is achieved by dephasing the spins with a negative gradient before they are rephased by an opposite gradient with opposite polarity to generate an echo. The pulse sequence is repeated as many times as the number of phase encoding lines that have to be acquired. The time between two excitation pulses is called the repetition time TR. Changing the TR, TE and flip angles of a GE sequence, influences the contrast weighting. T_2^*-weighted contrast can be achieved by using small flip angles and a long TE and moderate TR. By using large flip angles, a short TR and a short TE, a T_1-weighted signal can be acquired. Using small flip angles in combination with a long TR and a short TE generates proton density contrast.

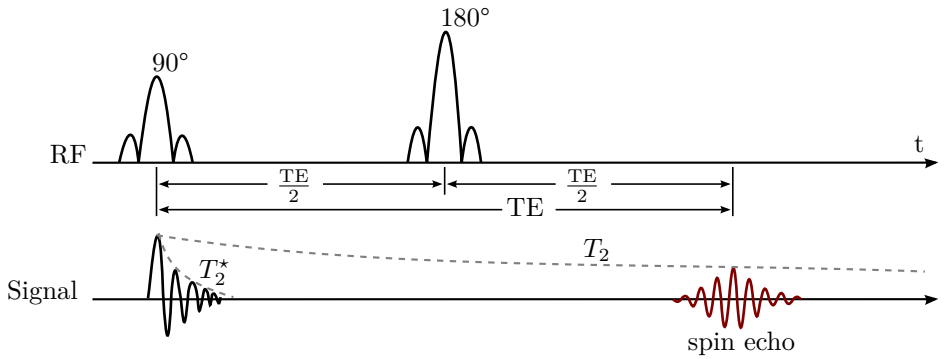

Fig. 1.6: Spin echo sequence: At TE /2 the spins are flipped by applying a 180° pulse. The rephasing spins give rise to a spin echo at time TE.

With a **spin echo** (SE) sequence (Fig. 1.6), pure T_2-weighted contrast can be generated [Hahn, 1950a]. When a 90° pulse rotates the magnetization in the transverse plane, the resulting FID signal quickly decays due to the strong $T_2^\star$-dephasing. If after a time TE /2 a 180° pulse is applied, the spins will be flipped and start to rephase. After another time TE /2, a measurable echo signal is created. Since the spin dephasing due to static magnetic field inhomogeneities is compensated inverting the spins with the 180° refocusing pulse, the decay of the signal at time TE will solely originate from the T_2 relaxation. A SE sequence can also be used to generate proton density or T_1-weighted signals by using a short TE and a long or short TR, respectively [Plewes, 1994].

1.4 Image formation

1.4.1 Spatial encoding

Spatial localization of the NMR signals is essential for the formation of MR images. Hence, the subject is subdivided in voxels (volumetric pixels). The voxel-based encoding of the spatial information is achieved by superimposing spatially dependent magnetic imaging gradients $\boldsymbol{G} = [G_x, G_y, G_z]$ on the main magnetic field $\boldsymbol{B}_0$ [Lauterbur, 1973]. Note that $\boldsymbol{G}$ is small relative to $\boldsymbol{B}_0$. By successive application of the gradients $\boldsymbol{G}$ in three orthogonal directions, the NMR signal gets encoded into a three-dimensional (3D) frequency space, from which then an MRI image can be reconstructed. Although the data can be directly encoded in three dimensions, the classical approach is to encode the image in a number of 2D slices, resulting in a multi-slice image. This multi-slice image is encoded in three consecutive steps:

Slice selection: During the RF pulses a slice-selective magnetic gradient field $\boldsymbol{G}$ is applied. For simplicity we assume that the magnetic gradient field is applied in the z-direction: G_z (Fig. 1.7). However, any slice orientation can be acquired by using a combination of the three orthogonal gradients G_x, G_y and G_z. The linear magnetic gradient causes planes orthogonal to the z-axis to have a different

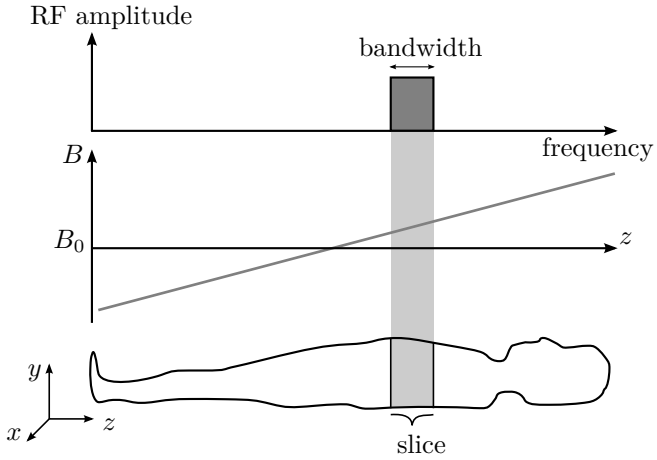

Fig. 1.7: In 2D imaging, an image slice is selectively excited using slice selective gradients.

Larmor-frequency:

$$\omega_L(z) = \gamma(B_0 + G_z z). \tag{1.14}$$

As a result of the spatially varying Larmor-frequency in the z-direction, only the magnetization vectors in a specific slice are in resonance with the RF pulses. Hence, only the magnetization vectors in that specific slice will be excited (Fig. 1.7). The features of this slice can be manipulated by adjusting the gradient or RF properties. The position of the slice can be varied by changing the carrier frequency of the RF pulse, while maintaining the gradient strength. A different region will now fulfill the resonant condition. The slice thickness is controlled by the bandwidth of the RF pulses and the strength of the gradient. Using a stronger gradient or a narrower RF pulse bandwidth will both reduce the slice thickness Δz:

$$\Delta z = \frac{2\pi(\text{RF bandwidth})}{\gamma G_z}. \tag{1.15}$$

In practice, the RF bandwidth is held constant and the slice thickness is varied by adjusting the gradient strenght.

Phase encoding: After the RF pulse, a time-dependent phase encoding gradient G_y is applied in the y-direction for a given time, τ. After time τ, a localized phase difference will be accumulated by the magnetization vectors (Fig. 1.8):

$$\phi(y) = \gamma G_y y \tau. \tag{1.16}$$

Frequency encoding: A frequency encoding gradient G_x is applied in the x-direction during read-out. The application of this gradient results in a variation of the frequency of the spins across the x-direction (Fig. 1.8):

$$\omega(x) = \omega_0 + \gamma G_x x. \tag{1.17}$$

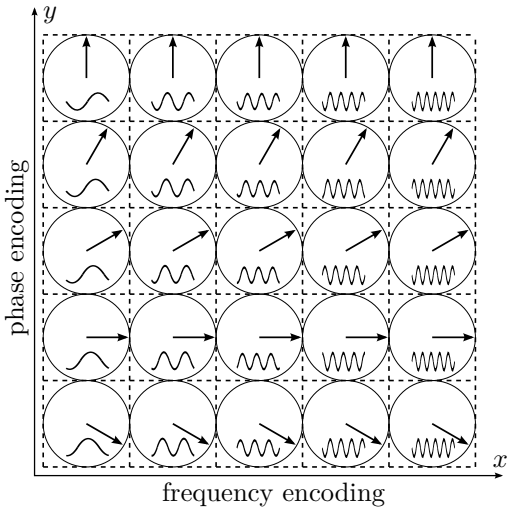

Fig. 1.8: Illustration of phase and frequency distribution after the 2D encoding. The magnetization vectors accumulate a y-position dependent phase by application of a phase encoding gradient. The frequency encoding gradient changes the resonance frequency of the magnetization vectors according to their x-position.

After the recovery time TR, the experiment is repeated with a different phase gradient to obtain 2D information. If the slice selection step is repeated, multiple slices can be collected and 3D information about the object is acquired. To reduce acquisition time, the recovery time of one slice is often used to select other slices (see section 2.6.1.1). For direct 3D image acquisition, the phase encoding is performed along two spatial dimensions.

1.4.2 K-space and image reconstruction

The received signal is the sum of all precessing magnetization vectors. The 2D encoded signal can be written as [Ljunggren, 1983]:

$$S(k_x(t), k_y(t)) = \int\int \rho(x, y, z_0) \mathrm{e}^{-i2\pi(k_x(t)x + k_y(t)y)} dxdy, \tag{1.18}$$

with z_0 the position of the slice selection, $\rho(x, y, z_0)$ the density of the magnetization vectors,

$$k_x(t) = \frac{\gamma}{2\pi} \int_0^t G_x(\tau)\delta\tau \quad \text{and} \quad k_y(t) = \frac{\gamma}{2\pi} \int_0^t G_y(\tau)\delta\tau, \tag{1.19}$$

with t the time between two acquired data points or dwell time. Equation 1.18 is easily extendable to 3D encoding. The signal $S(k_x, k_y)$ spans the so-called k-space [Twieg, 1983, King and Moran, 1984]. Equation 1.18 describes the Fourier relationship between the image data $\rho(x, y, z_0)$ and the measured k-space data $S(k_x, k_y)$. After the k-space is sampled at several frequencies (k_x, k_y), an inverse Fourier transformation $\mathcal{F}^{-1}$ is used to compute the 2D image from the acquired data (Fig. 1.9) [Kumar et al., 1975].

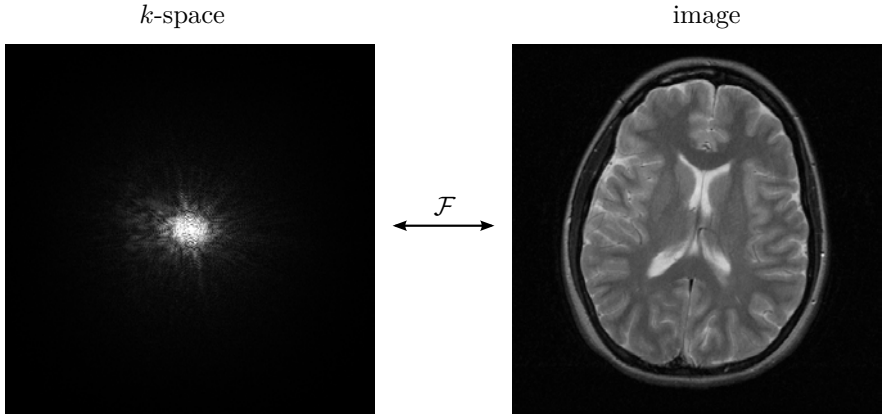

Fig. 1.9: The corresponding image can be reconstructed from the k-space data by using a discrete Fourier transform. Only the magnitude of the complex-valued k-space and image is shown

Many schemes to sample this k-space have been developed, each with their strengths and limitations [Henning, 1999, Lustig et al., 2008]. In this thesis, all data is acquired with a Cartesian sampling scheme. The specific k-space trajectory used to fill the Cartesian grid will depend on the sequence. Sequences are either single or multi-shot. In single shot sequences the complete k-space is obtained after one RF excitation (the 90° pulse in an GE sequence or the $90° - 180°$ pulse combination in a SE sequence). In multi-shot sequences, only a part or even one phase encoding line of k-space is obtained after one RF excitation. Hence, several separate RF excitations are needed to acquire the complete k-space.

In Fig. 1.10a, the k-space trajectory of a spin-echo sequence is showed. Each signal is first slice encoded along the z-axis during the 90° pulse. Starting in the center of k-space, the trajectory is moved to the lower bound of the k-space by shortly switching on a strong negative phase-encoding gradient G_y. A frequency-encoding gradient G_x moves the trajectory to the lower right corner. During the 180° pulse and slice selection gradient the trajectory moves to the upper left corner of the k-space. A positive frequency-encoding gradient G_x moves the trajectory to the right while the MR signal is acquired. In order to fill the k-space completely, this is repeated with increasing phase-encoding gradient strength. The complete data set in k-space is reconstructed to the corresponding image data by using a discrete Fourier transform (Fig. 1.9). In Fig. 1.10b a faster implementation of a Cartesian k-space sampling is given. In single-shot echo planar imaging (ss-EPI) [Mansfield, 1977], after each excitation, the full k-space is traversed using a train of phase encoded gradient echoes (Fig. 1.11). Although this trajectory fills the k-space faster then the spin-echo trajectory, it has some major drawbacks in image quality, which is discusses in section 3.6.1.

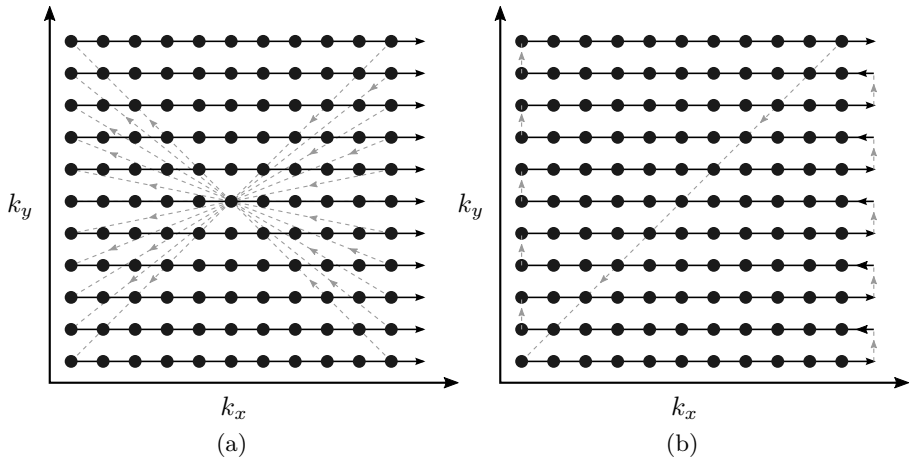

Fig. 1.10: Trajectory in k-space for (a) the spin echo sequence and (b) the echo planar imaging (EPI) sequence. A slice is selected using a gradient along the z-direction G_z, the k-space is traversed using the frequency-encoding G_x and phase-encoding G_y gradients. The gray dashed lines indicate traveling in the k-space without sampling, the black dots indicate the sampled points.

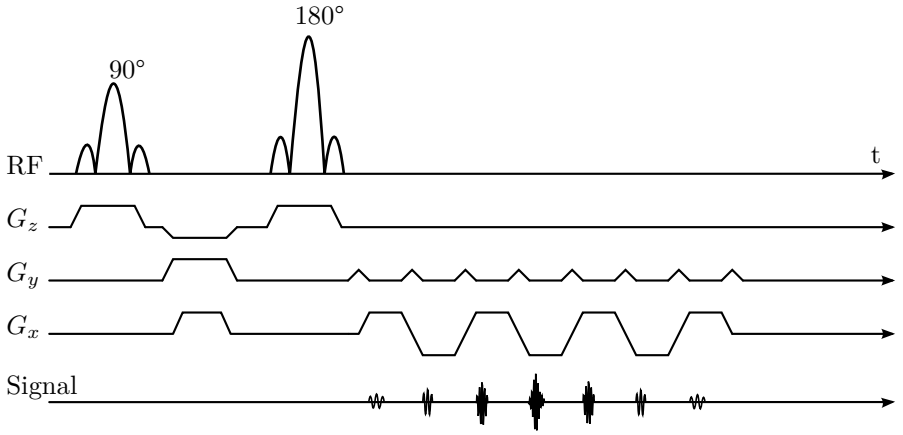

Fig. 1.11: Blipped single shot echo planar imaging (ss-EPI).

1.5 Image quality

In MRI, a compromise has to be made between the acquisition time and the image quality. The acquisition time is dependent on several factors such as the number of signal averages N_{SA}, the repetition time of the sequence TR, the number of phase encoding steps N_{PE} and the number of slices N_s:

$$\text{acquisition time} \propto N_{\mathrm{SA}}\,\mathrm{TR}\,\frac{N_{\mathrm{PE}}}{N_{\mathrm{PE/\,TR}}}\,\frac{N_s}{N_{s/\,\mathrm{TR}}}, \tag{1.20}$$

with $N_{\mathrm{PE/\,TR}}$ the number of phase encoding lines that are acquired within one TR and $N_{s/\,\mathrm{TR}}$ the number of slices that are acquired within one TR.
The quality of an MR image depends on:

- spatial resolution
- image contrast
- signal to noise ratio
- artifacts

So, each MR protocol and its sequence parameters has to be optimized in function of the subject and pathology.

1.5.1 Spatial resolution

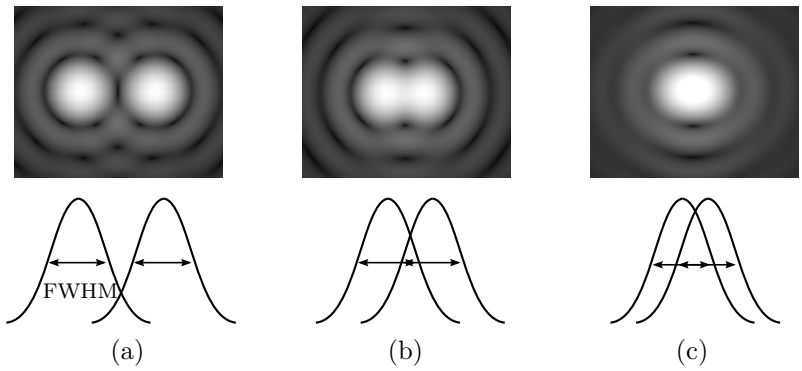

Fig. 1.12: When two points are far apart, they can be resolved because the FWHM of the PSF is smaller than the point sources separations. When the points move closer to each other, the image will look less like two points and will merge together in one single blob.

Consider an object consisting of a single point . The image obtained from it will most likely be a blurred point. Nevertheless, it still can be identified as a point. Another point is added to the object. When the points are far apart, we will see two blurred points (Fig. 1.12a). However, as the two points move closer to each other, the image will look less like two points and will merge together and become a single blob (Fig. 1.12b-c). The threshold of where the two points are still resolved

as two separable points, is called the resolution limit of the imaging system. In other words, the spatial resolution is the smallest distance between two points in an object that can be distinguished as separate details in an image. Thus, the spatial resolution defines how "sharp" the image looks. A low spatial resolution will give fuzzy edges, or a pixelly appearance to the image.

Mathematically, the relationship between an object $O(x, y, z)$ and its image $I(x, y, z)$ can be written as

$$I(x, y, z) = O(x, y, z) * h(x, y, z) \tag{1.21}$$

with $*$ representing the convolution operator and $h(x, y, z)$ the 3D point spread function (PSF). Two point sources can be resolved as long as they are separated by a distance greater than the full width of half maximum (FWHM) of the PSF.

1.5.1.1 Digital resolution

In MRI, the spatial resolution of an image is defined by its voxel size ($[\Delta x, \Delta y, \Delta z]$). The through-plane resolution is defined by the slice thickness Δz. The in-plane resolution is defined by:

$$\begin{cases} \Delta x &= \frac{\mathrm{FOV}_x}{N_{\mathrm{FE}}}, \\ \Delta y &= \frac{\mathrm{FOV}_y}{N_{\mathrm{PE}}} \end{cases} \tag{1.22}$$

with N_{FE} the number of frequency encoding steps, N_{PE} the number of phase encoding steps and FOV the field of view which refers to the distance over which an MR image is acquired or displayed. The matrix size is given as $N_{\mathrm{FE}} \times N_{\mathrm{PE}}$.

The through-plane spatial resolution can be increased by decreasing the slice thickness. This can be done by using a stronger gradient or a narrower RF pulse bandwidth. Thinner slices are less susceptible to partial volume effects, i.e. many voxels will consist of a mixture of signals from different anatomical structures. Thinner slices will also contain less spins and thus will emit less signal. Moreover, decreasing the slice thickness increases the number of slices needed for a full coverage of the subject, which in turn might increase the acquisition time. In practice, the voxel size is limited by the gradient strength, acquisition time and targeted SNR.

1.5.1.2 Spatial resolution and k-space

In Fig. 1.13 the relationship between the k-space and the image resolution and FOV is visualized. To avoid loss of image information, the sampling interval, i.e. the distance between two acquired k-space points (Δk_x and Δk_y) has to satisfy the Nyquist criterion. Furthermore, the k-space sampling is finite: the signal $S(k_x, k_y)$ is not sampled for $|k_x| > k_{\mathrm{max},x}$ and $|k_y| > k_{\mathrm{max},y}$, with $k_{\mathrm{max},x} = (N_{\mathrm{FE}}/2)\Delta k_x$ and $k_{\mathrm{max},y} = (N_{\mathrm{PE}}/2)\Delta k_y$ the maximum frequency sampled in frequency and phase encoding direction, respectively. Therefore, according to the Nyquist criterion, the largest acceptable pixel size of the image is [Mezrich, 1995]:

$$\Delta x = \frac{1}{\mathrm{FOV}_{k,x}} \text{ and } \Delta y = \frac{1}{\mathrm{FOV}_{k,y}}, \tag{1.23}$$

with $\mathrm{FOV}_{k,x} = 2k_{\mathrm{max},x}$ and $\mathrm{FOV}_{k,y} = 2k_{\mathrm{max},y}$. Since $\mathrm{FOV}_x = N_{\mathrm{FE}}\Delta x$ and $\mathrm{FOV}_y = N_{\mathrm{PE}}\Delta y$, the FOV will thus be determined by the sampling interval:

$$\mathrm{FOV}_{x,y} = \frac{1}{\Delta k_{x,y}}. \tag{1.24}$$

In Fig. 1.13c-d the inverse relationship between the spacing of the data samples ($\Delta k_{x,y}$) and the FOV is shown. When the spacing between the acquired data points is increased, the resulting image will have the same voxel size, but the FOV will be smaller. Since the Nyquist criterion is not fulfilled, the edges of the brain which fall outside the smaller FOV will wrap over the sides of the reconstructed images. This phenomenon is called aliasing. In modern clinical MR imaging, aliasing only occurs in the phase-encoding direction. Aliasing in the frequency-encoding direciton is not usually a problem since it is eliminated by signal oversampling or bandpass filtering before reconstruction of the image [Pusey et al., 1986].

Fig. 1.13e-f visualizes the inverse relationship between the voxel size and the range of sampled frequencies in k-space. The sampling rate and spacing (Δk) is kept constant, but the N_{PE} and N_{FE} are reduced, which reduces the maximum acquired frequency k_{max} as well. This manipulation of k-space results in a increase of the voxel size (Δx, Δy). Thus, sampling high frequencies in k-space is required to achieve a high spatial resolution in MRI.

1.5.2 Signal-to-noise ratio

The acquired MRI signal intensity is corrupted by noise. This noise originates from the patient's body (human tissue is electrically conducting) and the receiver circuit of the scanner which cause random fluctuations in the electrical current. In turn, these electrical fluctuations generate fluctuating magnetic fields which induce a noise voltage in the coil [McRobbie et al., 2006].

The signal intensity depends on the specific sequence and sequence parameters, as well as on the spatial resolution or voxel dimensions [Edelstein et al., 1986]:

$$\mathrm{signal} \propto \Delta x \Delta y \Delta z F_{\mathrm{sequence}}, \tag{1.25}$$

with F_{sequence} a sequence dependent factor, which calculates the influence of the relaxation on the signal. Hence, F_{sequence} depends on the sequence parameters such as TR and TE (see section 1.3.5). Furthermore, the signal will also increase with increasing magnetic field strength as the excited magnetization, and thus the observed signal is larger.

The noise, the random differences in voxel values, will be related to the bandwidth (BW) and sequence parameters [Dietrich et al., 2007]:

$$\mathrm{noise} \propto \frac{\sqrt{BW}}{\sqrt{N_{\mathrm{SA}} N_{\mathrm{PE}} N_{\mathrm{FE}}}}, \tag{1.26}$$

with N_{SA} the number of signal averages. The bandwidth corresponds to the range of frequencies captured during the read-out. The speed with which the k-space is traversed is proportional to the bandwidth. Hence, a larger bandwidth means that more information can be collected in a single read-out, speeding up the acquisition.

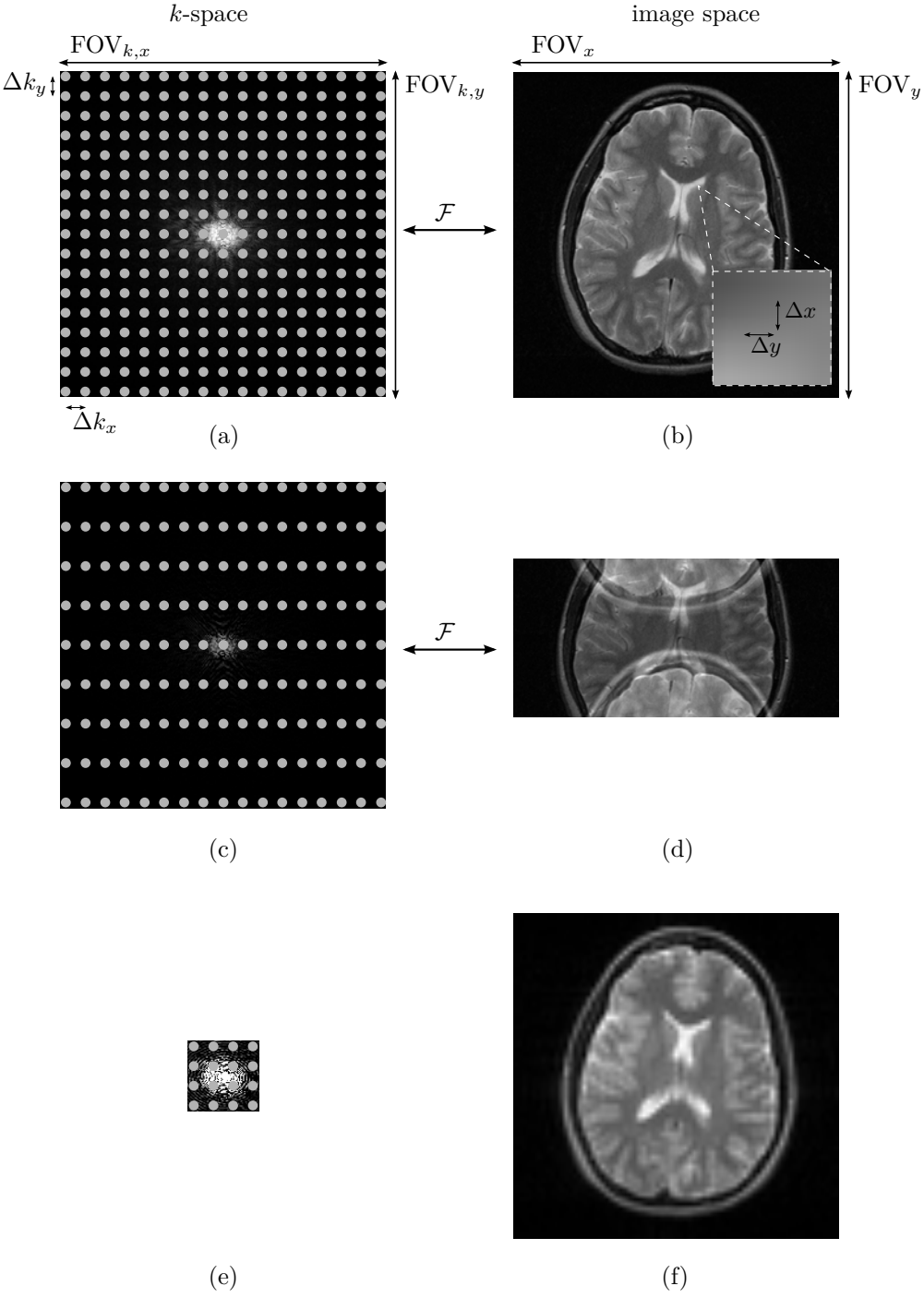

Fig. 1.13: Relationship between k-space sampling and image resolution and FOV. From a fully sampled k-space (a) the corresponding MRI image (b) can be computed. Undersampling the k-space (c) results in aliasing in the image space (d). Decreasing the maximum sampled frequency (e), decreases the spatial resolution of the corresponding image (f).

However, the thermal noise power in the coil is proportional to the bandwidth, which means that increasing the bandwidth leads to increasing the noise level [Redpath, 1998]. On the other hand, a low bandwidth tend to cause chemical shift artefacts [Babcock et al., Dietrich et al.]. The bandwidth can be set on the scanner and will depend on the readout gradient strength and the data sampling rate. The type and quality coils will also have a high impact on the noise level.

Combining these relationships for signal and noise, we get the signal-to-noise ratio (SNR) of an MR image [Ocali and Atalar, 1998]:

$$\mathrm{SNR} \propto \frac{\Delta x \Delta y \Delta z F_{\mathrm{sequence}} \sqrt{N_{\mathrm{SA}} N_{\mathrm{PE}} N_{\mathrm{FE}}}}{\sqrt{BW}} \tag{1.27}$$

Since $\Delta x, \Delta y$ and Δz define the spatial resolution, and $N_{\mathrm{SA}}, N_{\mathrm{PE}}$ and N_{FE} define the acquisition time, one can state that the SNR depends on the spatial resolution and the acquisition time [Macovski, 1996]:

$$\mathrm{SNR} \propto (\text{voxel size}) \sqrt{\text{acquisition time}}. \tag{1.28}$$

Thus in MRI, there is a trade-off between the spatial resolution, SNR and acquisition time of the images. Improving this trade-off is the main goal of the work presented in this thesis.

After the image is acquired, the SNR of the image is typically calculated by taking the ratio of the mean and standard deviation (*std*) of the signal in a homogeneous region [Firbank et al., 1999]:

$$\mathrm{SNR} = \frac{\mathrm{mean}(S)}{\mathrm{std}(S)}. \tag{1.29}$$

If there is no large enough homogeneous region in the image, instead of the standard deviation of the signal, the standard deviation of the noise (the background) is used.

1.5.3 Artifacts

An image artifact is any feature which appears in the image but is not present in the original imaged subject. There is a large variety of possible occurring artifacts [Bellon et al., 1986, Erasmus et al., 2004]. A large group of image artifacts present themselves as 'ghosts', i.e. a faint copy of the anatomy that appears elsewhere along the phase encoding direction in the image. An artifact might also be a distortion in the image, so that straight lines appear curved or a certain area is artificially magnified or reduced. There can be a lack of signal where there should be or vice versa. Based upon their origin, the most common artifacts are typically classified as motion-related, tissue-related and technique-related.

- **Motion** artifacts arise from involuntary movements of the patient or physiological motion such as cardiac pulsation, respiratory movements or swallowing. The motion artifacts lead to blurring and ghosting [Atkinson et al., 1999]. Proper sequence design, fast image acquisition and cardiac gating can compensate these motion artifacts [Noll and Schneider, 1994, Larson et al., 2004, Pipe, 1999]. For example, the EPI sequence is a fast sequence which significantly reduces the risk of motion artifacts.

- An example of a **tissue-related** artifact is image distortions caused by magnetic susceptibility differences between adjacent regions in the subject. At boundaries between regions with different magnetic susceptibility, the magnetic field will be locally distorted and inhomogeneous [Farahani et al., 1990]. These magnetic field inhomogeneities result in variations in precession frequency across the patient and even within individual voxels. These frequency changes produce signal loss from T_2^*-dephasing and interfere with the spatial encoding of the signal, resulting in spatial mismapping of the MR signal. The acquired image will show geometric distortions with a drop-out or piling up of signal in some areas. Susceptibility artefacts might be seen at natural interfaces, e.g. the sinuses and the skull base. However, the most sever susceptibility artifacts are caused by small pieces of metal in the body, such as orthopedic implants [Weiss et al., 1989, Suh et al., 1998].
- Aliasing (Fig. 1.13c-d) and partial volume (section 1.5.1) effects are examples of **technique-related** artifacts.

A more detailed description of image artifacts common to T_1 mapping and diffusion MRI can be found in the corresponding chapters.

1.6 MRI scanner

1.6.1 Hardware

The main component of an MRI scanner is the imaging magnet [McRobbie et al., 2006, Weishaupt et al., 2008]. The large superconducting magnet is used to create a homogeneous static magnetic field $\boldsymbol{B}_0$. The typical field strength of a clinical MRI scanner is 1.5 or 3 T, however some sites also operate a 7 T scanner [van der Kolk et al., 2013]. In pre-clinical imaging, for example small animal imaging, higher magnetic fields are used [Marzola et al., 2003]. Since the magnetic is superconducting, it needs to be at cryogenic temperatures during operation. Therefore, the magnet is cooled by liquid helium [McRobbie et al., 2006]. In order to generate the MR signal, RF pulses are needed. These RF pulses or time varying $\boldsymbol{B}_1$ magnetic fields are created by the RF coil. Usually a body coil is built into the scanner. Other coils, often specifically designed for the imaged body part such as a head coil, knee coil, breast coil, ... can be plugged into the scanner as well. The MR signal emitted by the spins can be detected with the same coil. Since MR signals are very weak, the scan room is shielded with a Faraday cage, to avoid interference with other RF transmitters. The localization of the MR signals is achieved by the imaging gradients, which are produced by three sets of gradient coils, one for each direction.

1.6.2 Safety

Although MRI does not use ionizing radiation to produce images there are still some important safety considerations which one should take into account [Dempsey et al., 2002, De Wilde et al., 2007, Gangarosa et al., 1987]. One of the dangers is associated with ferromagnetic metal objects which are accidentally brought in

the vicinity of the MRI scanner. The magnetic field will pick up and pull (large) ferromagnetic items into the bore of the magnet at high velocity. This does not only damage the scanner and coils, but also puts the patient and anyone in between the object and scanner at risk. Therefore, it is of uttermost importance to not bring ferromagnetic material into the scanner room. Similar forces will work on ferromagnetic metal present in the body. These forces can pull on the ferromagnetic metal, cutting and compressing healthy tissue. Therefore, individuals with old ferromagnetic implants are not imaged. An additional concern is the effect of the static and changing magnetic fields on electronic circuitry, such as pacemakers [Kalin and Stanton, 2005]. When a person with a pacemaker walks through a magnetic field, it can induce currents in the circuit of the pacemaker, causing it to fail, with all consequences. The switching of the magnetic field, i.e. the RF pulses, may induce a current in the pacemaker, causing thermal damage to the device and the cardiac tissue. Moreover the gradient magnetic fields can induce voltages which might cause the pacemaker to malfunction.

The energy deposited by the RF pulses can cause heating of the tissues [Shellock, 2000, Collins et al., 2004]. On clinical MRI scanners, the exposure to RF energy is limited by regulations using the specific absorption rate (SAR) as the limiting measure:

$$\text{SAR} = \text{J of RF/second/kg} = \text{W/kg}. \tag{1.30}$$

The recommended SAR limitations depend on the imaged anatomy. Furthermore, rapid switching of the magnetic gradient, can lead to involuntary nerve stimulation [Schaefer et al., 2000]. This has to be taken into account when a clinical acquisition protocol is designed.

1.7 Quantitative MRI

MRI is accepted as the imaging method of choice for the visualization of internal structures and has become one of the cornerstones in clinical diagnosis. Generally, MRI is used in a qualitative way where the images are interpreted by a skilled observer. The intensities of the qualitative (anatomical) images reflect both the biological parameters of the imaged tissues and the scanner parameters, such as receiver gain, RF pulses and image scaling. This is acceptable for qualitative analysis but prevents proper quantitative analysis of the tissue parameters.

Notwithstanding the value of qualitative imaging, the quantification (or measurement) of tissue parameters with MRI would substantially increase the reproducibility of the research into biological changes in disease, and their response to potential treatments. MRI can evolve from a process of picture taking, where observations are made on the basis of unusually bright, dark, small or large objects, to a measurement process where a whole range of quantities can be tested to see whether they lie in a normal range and whether they have changed from the time of a previous examination. In quantitative MRI (qMRI), qualitative images are replaced by quantitative parameter maps. Although these quantitative parameter maps have the same appearance as an image, they are conceptually different with voxel values having a biological meaning rather than representing signal intensity on an arbitrary scale [Tofts, 2005]. In the following chapters, a more in depth

explanation is given on two quantitative MRI methods: T_1 mapping (Chapter 2) and diffusion MRI (Chapter 3).

1.7.1 Parameter estimation

In qMRI, the acquired MR images are described in terms of the physical parameters by a parametric model, i.e. a set of mathematical equations. These parametric models can be fitted to the data, to obtain estimates of the model parameters. The method to extract the information about the model parameters from the measurements is called an estimator. One of the most common estimators in qMRI is the least squares (LS) estimator. The LS estimator solves the set of equations by minimizing the sum of squared residuals, with a residual the differences between the observed or measured value and the value predicted by the model. LS estimators can be divided into two categories depending on whether or not the residuals are linear in all unknowns: linear least squares (LLS) and non-linear least squares (NLS).

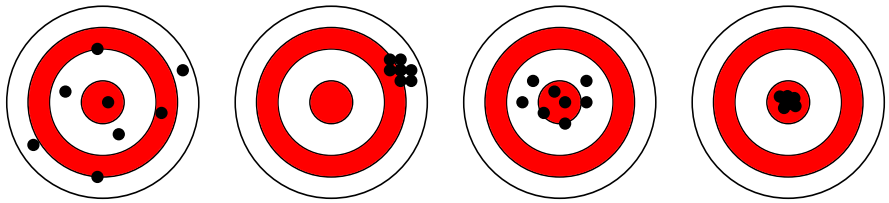

Fig. 1.14: Difference between accuracy and precision when aiming for the center.

1.7.2 Accuracy and precision

Important properties of estimators are the accuracy and precision (Fig. 1.14) [van den Bos, 2007]. Consider an estimator $\hat{\theta}$ of an underlying parameter θ_0 based on N measurements. The accuracy of the estimator measures how close the estimated value is *on average* to the true value. The distance from the average value to the true value, i.e. the systematic estimation error, is called the bias:

$$\text{bias}(\hat{\theta}) = \mathbb{E}[\hat{\theta}] - \theta_0, \tag{1.31}$$

with $\mathbb{E}[\cdot]$ the expectation operator. A good estimator has a high accuracy and thus a low, preferably zero, bias. The estimator is called unbiased if the bias is zero for a finite N.

The precision is a measure of the average spread of the outcomes of the measurements, i.e. how much the value changes when the experiment is repeated. The precision of an estimator is generally quantified by the variance, i.e. the expectation value of the square of the residual of the estimated values:

$$\text{var}(\hat{\theta}) = \mathbb{E}\left[(\hat{\theta} - \mathbb{E}[\hat{\theta}])^2\right]. \tag{1.32}$$

Obviously, a good estimator also should have a high precision and thus a low variance.

The bias and variance are combined in the root mean squared error (RMSE):

$$\begin{aligned} \mathrm{RMSE}(\hat{\theta}) &= \sqrt{\mathrm{bias}(\hat{\theta})^2 + \mathrm{var}(\hat{\theta})} \\ &= \sqrt{\mathbb{E}[||\hat{\theta} - \theta_0||^2]}. \end{aligned} \tag{1.33}$$

Bibliography

A. Abragam. *Principles of Nuclear Magnetism*. Oxford University Press, New York, 1989.

D. Atkinson, D.L. Hill, P.N. Stoyle, P.E. Summers, S. Clare, R. Bowtell, and S.F. Keevil. Automatic compensation of motion artifacts in MRI. *Magnetic Resonance in Medicine*, 41(1):163–170, 1999.

E.E. Babcock, L. Brateman, J.C. Weinreb, S.D. Horner, and R.L. Nunnally.

E.M. Bellon, E.M. Haacke, P.E. Coleman, D.C. Sacco, D.A. Steiger, and R.E. Gangarosa. MRI artifacts: a review. *American Journal of Roentgenology*, 147(6): 1271–1281, 1986.

M.A. Bernstein, K.F. King, and X.J. Zou. *Handbook of MRI pulse sequences*. Elsevier Academic press, Philadelphia, 2004.

B.I. Bleaney and B. Bleaney. *Electricity and magnetism*. Oxford University Press, Oxford, 1976.

F. Bloch, W.W. Hansen, and M. Packard. Nuclear induction. *Physical Review*, 70 (7-8):474–485, 1946.

N. Bloembergen, E.M. Purcell, and R.V. Pound. Relaxation effects in nuclear magnetic resonance absorption. *Physical Review*, 73(7):679, 1948.

C.M. Collins, W. Liu, J. Wang, R. Gruetter, J.T. Vaughan, K. Ugurbil, and M.B. Smith. Temperature and SAR calculations for a human head within volume and surface coils at 64 and 300 MHz. *Journal of Magnetic Resonance Imaging*, 19(5): 650–656, 2004.

R. Damadian. Tumor detection by nuclear magnetic resonance. *Science*, 171(3976): 1151–1153, 1971.

R. Damadian, M. Goldsmith, and L. Minkoff. NMR in cancer: XVI, FONAR image of the live human body. *Physiological chemistry and physics*, 9(1):97–100, 1976.

J.P. De Wilde, D. Grainger, D.L. Price, and C. Renaud. Magnetic resonance imaging safety issues including an analysis of recorded incidents within the UK. *Progress in Nuclear Magnetic Resonance Spectroscopy*, 51(1):37–48, 2007.

M.F. Dempsey, B. Condon, and D.M. Hadley. MRI safety review. *Seminars in Ultrasound, CT and MRI*, 23(5):392–401, 2002.

O. Dietrich, M.F. Reiser, and S.O. Schoenberg.

O. Dietrich, J.G. Raya, S.B. Reeder, M.F. Reiser, and S.O. Schoenberg. Measurement of signal-to-noise ratios in MR images: Influence of multichannel coils, parallel imaging, and reconstruction filters. *Journal of Magnetic Resonance Imaging*, 26(2):375–385, 2007.

W.A. Edelstein, G.H. Glover, C.J. Hardy, and R.W. Redington. The intrinsic signal-to-noise ratio in NMR imaging. *Magnetic Resonance in Medicine*, 3(4): 604–618, 1986.

A.D. Elster. Gradient-echo MR imaging: techniques and acronyms. *Radiology*, 186 (1):1–8, 1993.

L.J. Erasmus, D. Hurter, M. Naude, H.G. Kritzinger, and S. Acho. A short overview of MRI artefacts. *SA Journal of Radiology*, 8(2):13–17, 2004.

K. Farahani, U. Sinha, S. Sinha, L.C.-L. Chiu, and R.B. Lufkin. Effect of field strenght on susceptibility artifacts on magnetic resonance imaging. *Computerized Medical Imaging and Graphics*, 14(6):409–413, 1990.

M.J. Firbank, A. Coulthard, R.M. Harrison, and E.D. Williams. A comparison of two methods for measuring the signal to noise ratio on MR images. *Physics in medicine and biology*, 44(12):N261, 1999.

J. Frahm, A. Haase, and D. Matthaei. Rapid NMR imaging of dynamic processes using the FLASH technique. *Magnetic Resonance in Medicine*, 3(2):321–327, 1986.

R.E. Gangarosa, J.E. Minnis, J. Nobbe, D. Praschan, and R.W. Genberg. Operational safety issues in MRI. *Magnetic Resonance Imaging*, 5(4):287–292, 1987.

K. Golman, J.S. Petersson, P. Magnusson, E. Johansson, P. Akeson, C.M. Chai, G. Hansson, and S. Mansson. Cardiac metabolism measured noninvasively by hyperpolarized 13C MRI. *Magnetic Resonance in Medicine*, 59(9):1005–1013, 2008.

E.L. Hahn. Spin echoes. *Physical Review*, 80(4):580–594, 1950a.

E.L. Hahn. Nuclear induction due to free Larmor precession. *Physical Review*, 77 (2):297, 1950b.

E.L. Hahn. Free nuclear induction. *Physics Today*, 6(11):4–9, 1953.

J. Henning. K-space sampling strategies. *European radiology*, 9(6):1020–1031, 1999.

R. Kalin and M.S. Stanton. Current clinical issues for MRI scanning of pacemaker and defibrillator patients. *Pacing and Clinical Electrophysiology*, 28(4):326–328, 2005.

K.F. King and P.R. Moran. A unified description of NMR imaging, data-collection strategies, and reconstruction. *Medical Physics*, 11(1):1–4, 1984.

A. Kumar, D. Welti, and R.R. Ernst. NMR fourier zeugmatography. *Journal of Magnetic Resonance*, 18(1):69–83, 1975.

A.C. Larson, R.D. White, G. Laub, E.R. McVeigh, D. Li, and O.P. Simonetti. Self-gated cardiac cine MRI. *Magnetic Resonance in Medicine*, 51(1):93–102, 2004.

P.C. Lauterbur. Image formation by induced local interactions: examples employing nuclear magnetic resonance. *Nature*, 242(5394):190–191, 1973.

Z.P. Liang and P.C. Lauterbur. *Principles of Magnetic Resonance Imaging: A Signal Processing Perspective*. The Institute of Electrical and Electronic Engineers Press, New York, 2000.

S. Ljunggren. A simple graphical representation of fourier-based imaging methods. *Journal of Magnetic Resonance*, 54(2):383–43, 1983.

M. Lustig, D.L. Donoho, J.M. Santos, and J.M Pauly. Compressed sensing MRI. *IEEE Signal Processing Magazine*, 25(2):72–82, 2008.

A. Macovski. Noise in MRI. *Magnetic Resonance in Medicine*, 36(3):494–497, 1996.

P. Mansfield. Multi-planar image formation using NMR spin echoes. *Journal of Physics C: Solid State Physics*, 10(3):L55–L58, 1977.

P. Marzola, F. Osculati, and A. Sbarbati. High field MRI in preclinical research. *European journal of radiology*, 48(2):165–170, 2003.

D.W. McRobbie, E.A. Moore, M.J. Graves, and M.R. Prince. *MRI: From picture to proton*. Cambridge University Press, Cambridge, 2006.

R. Mezrich. A perspective on K-space. *Radiology*, 195(2):297–315, 1995.

W.R. Nitz and P. Reimer. Contrast mechanisms in MR imaging. *European Radiology*, 9(6):1032–1046, 1999.

D.C. Noll and W. Schneider. Theory, simulation, and compensation of physiological motion artifacts in functional MRI. In *Proceedings of the IEEE International Conference on Image Processing*, volume 3, pages 40–44, Austin, Texas, USA, 1994.

O. Ocali and E. Atalar. Ultimate intrinsic signal-to-noise ration in MRI. *Magnetic Resonance in Medicine*, 39(3):462–473, 1998.

W.H. Perman, S.K. Hilal, H.E. Simon, and A.A. Maudsley. Contrast manipulation in NMR imaging. *Magnetic Resonance Imaging*, 2(1):23–32, 1984.

J.G. Pipe. Motion correction with PROPELLOR MRI: application to head motion and free-breathing cardiac imaging. *Magnetic Resonance in Medicine*, 42(5): 963–969, 1999.

D.B. Plewes. Contrast mechanisms in spin-echo MR Imaging. *Radiographics*, 14 (6):1389–1404, 1994.

E.M. Purcell, H.C. Torrey, and R.V. Pound. Resonance absorption by nuclear magnetic moment in a solid. *Physical Review*, 69(1-2):37–38, 1946.

E. Pusey, R.B. Lufkin, R.K. Brown, M.A. Solomon, D.D. Stark, R.W. Tarr, and W.N. Hanafee. Magnetic resonance imaging artifacts: mechanism and clinical significance. *RadioGraphics*, 6(5):891–911, 1986.

T.W. Redpath. Signal-to-noise ratio in MRI. *The British Journal of Radiology*, 71 (847):704–707, 1998.

D.J. Schaefer, J.D. Bourland, and J.A. Nyenhuis. Review of Patient Safety in Time-Varying Gradient Fields. *Journal of Magnetic Resonance Imaging*, 12(1): 20–29, 2000.

E.M. Shapiro, A. Borthakur, A. Gougoutas, and R. Reddy. 23Na MRI accurately measures fixed charge density in articular cartilage. *Magnetic Resonance in Medicine*, 47(2):284–291, 2002.

F.G. Shellock. Radiofrequency Energy-Induced Heating During MR Procedures: A Review. *Journal of Magnetic Resonance Imaging*, 12(1):30–36, 2000.

J.S. Suh, E.K. Jeong, K.H. Shin, J.H. Cho, J.B. Na, D.H. Kim, and C.D. Han. Minimizing artifacts caused by metallic implants at MR imaging: experimental and clinical studies. *American Journal of Roentgenology*, 171(5):1207–1213, 1998.

P. Tofts. *Quantitative MRI of the Brain.* John Wiley & Sons, New York, 2005.

D.B. Twieg. The k-trajectory formulation of the NMR imaging process with applications in analysis and synthesis of imaging methods. *Medical Physics*, 10 (5):610–621, 1983.

A. van den Bos. *Parameter Estimation for Scientists and Engineers.* John Wiley & Sons, New York, 2007.

A.G. van der Kolk, J. Hendrikse, J.J. Zwanenburg, F. Visser, and P.R. Luijten. Clinical applications of 7T MRI in the brain. *European journal of radiology*, 82 (5):708–718, 2013.

D. Weishaupt, V.D. Kochli, and B. Marincek. *How does MRI work?: An introduction to the physics and function of magnetic resonance imaging.* Srpinger-Verlag, Heidelberg, 2 edition, 2008.

R.A. Weiss, L.A. Saint-Louis, B.G. Haik, C.D. McCord, and J.L. Taveras. Mascara and eyelining tattoos: MRI aftifacts. *Analysis of Ophthalmology*, 21(4):129–131, 1989.

J.-X. Yu, V.D. Kodibagkar, W. Cui, and R.P. Mason. 19F: A Versatile Reporter for Non-Invasive Physiology and Pharmacology Using Magnetic Resonance. *Current medicinal chemistry*, 12(7):819–848, 2005.

2

Quantitative T1 mapping

Contents

2.1 Introduction

The spin-lattice relaxation time, T_1, is one of the fundamental tissue properties on which clinical magnetic resonance imaging (MRI) contrast is based. Generally, the signal in a T_1-weighted image is inversely related to the T_1 relaxation time in a nonlinear manner. Since T_1 is an intrinsic biophysical property of the tissue, an accurate measurement of T_1 is important. Additionally to tissue characterization, knowledge of the T_1 relaxation time can also be used for contrast agent uptake studies, and the measurements of perfusion or blood volume. However, many factors, such as the proton density and the sequence parameters, influence the signal of a T_1-weighted image. As such, the absolute intensity in a T_1-weighted image has no absolute meaning. The image provides only qualitative information and diagnosis relies on visual interpretation. To allow absolute quantification of T_1, a set of T_1-weighted images with different contrast settings are required. From this set of images, a T_1 map can then be estimated, representing the estimate T_1 value in each voxel. Unlike conventional qualitative T_1-weighted imaging, quantitative T_1 mapping allows objective comparison across subjects, protocols, sites and time [Ashton, 2010]. Note that the T_1 values are dependent on the temperature and magnetic field strength [Bottomley et al., 1986, Korb and Bryant, Rooney et al.].

In this chapter the acquisition of T_1-weighted images and the estimation of a T_1 map are explained. A short overview of the most frequently used T_1 measuring sequences is given as well. Furthermore, we discuss the potential of T_1 mapping as well as the most important limitations and pitfalls of T_1 mapping.

2.2 T_1 relaxation

As explained in chapter 1, applying an radio frequency (RF) pulse to a system of spins will perturb the magnetization from its equilibrium position. After the RF pulse it immediately starts to relax, back to a state of equilibrium. The absorbed energy is dispersed by a number of processes, where energy is transferred away from the spins to the lattice (T_1 or spin-lattice relaxation) or redistributed within the spin system (T_2 or spin-spin relaxation, see section 1.3.5).

The time constant T_1 describes how the longitudinal magnetization M_z recovers. This recovery is influenced by the fluctuating magnetic fields at proton resonance frequency, arising from the motion of neighboring atoms. The random tumbling of the water molecule, described by a rotational correlation time, alters the angle between the protons over time and causes fluctuations in the magnetic field. For example, protons in lipids are affected by adjacent protons. Since the protons are less mobile, there tends to be more energy at the proton resonance frequency, which results in a shorter T_1 for lipids. Therefore, T_1 provides information about the mobility of the molecules (mainly water protons) and their binding to macromolecules.

T_1 is primarily used to assess macromolecular content, water binding, and water content in a variety of pathologies. Beyond intrinsic tissue effects, the T_1 can also be influenced through the introduction of paramagnetic material under the form of contrast agents, such as gadolinium diethylenetriaminepentaacetic acid (Gd-DTPA) [Erlemann et al., 1989]. Gadolinium forms a strong paramagnetic center, disrupting the local magnetic field. Hence, the water molecules which are tumbling and

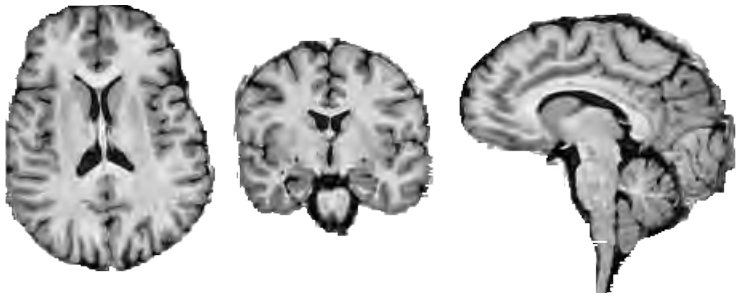

(a) T_1-weighted image

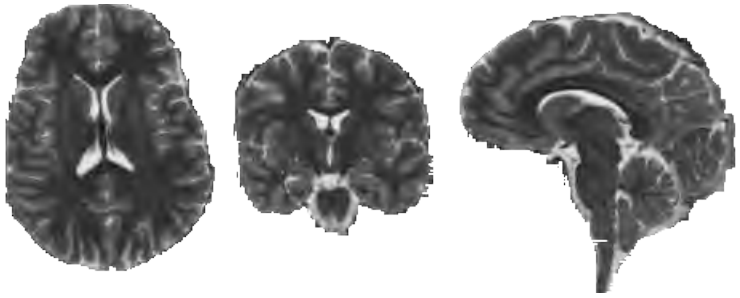

(b) T_1 map

Fig. 2.1: T_1 weighted image (a) and T_1 map of the normal human brain. The longitudinal magnetization of tissue with shorter T_1 (white matter) has recovered more before the read out, resulting in a brighter signal than for tissues with a longer T_1 (gray matter).

diffusing past this molecule experience substantial magnetic fluctuations. This application is particularly useful for quantifying properties of blood flow, such as perfusion [Covarrubias et al., 2004] and blood volume [Bruening et al., 1996].

Since the T_1 value is related to macromolecule concentration, water binding and water content, many biological tissues have distinct T_1 relaxation times. The differences in T_1 values (Fig. 2.1b) are exploited to produce images with T_1-weighted contrast. Because the longitudinal magnetization of the tissue with longer T_1 has recovered less before read out, it will be less bright in the image relative to the shorter T_1 components, whose longitudinal magnetization has experienced a more complete recovery. For example in the brain, the presence of myelin causes white matter to have a shorter T_1 than gray matter. Thus in a T_1-weighted image (Fig. 2.1a), white matter will be brighter than gray matter.

2.3 Acquisition of T_1-weighted image

To measure a T_1-weighted image which reflects the recovery of the magnetization to its equilibrium, the magnetization first needs to be perturbed from its equilibrium position. The golden standard method to measure an image with T_1-weighted contrast is the inversion recovery (IR) sequence, shown in Fig. 2.2 [Drain, 1949, Hahn,

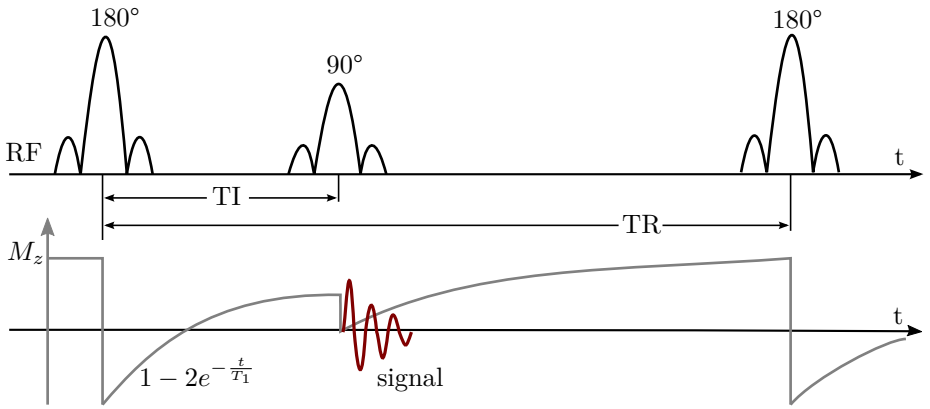

Fig. 2.2: Inversion recovery sequence: The longitudinal magnetization is inverted by a 180° pulse. After inversion time TI, the magnetization is read out by using a 90° pulse.

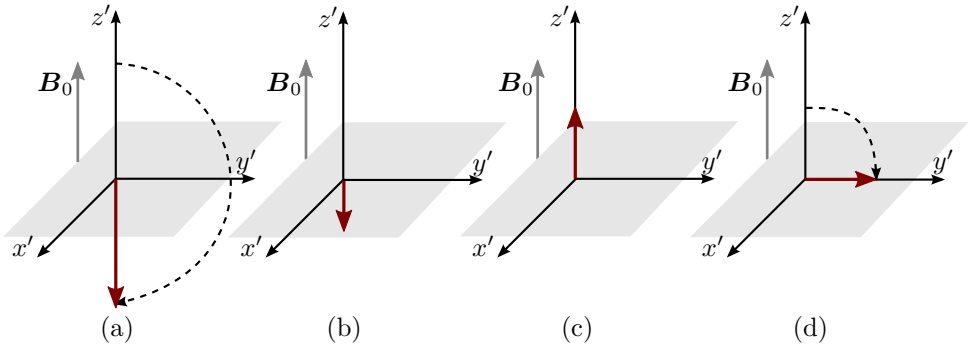

Fig. 2.3: Effect of inversion recovery sequence (Fig. 2.2) on longitudinal magnetization M_z. (a) The 180° flips the longitudinal magnetization M_z, (b)-(c) the longitudinal magnetization relaxes and starts to grow to equilibrium, (d) a 90° pulse tips the magnetization in the transverse plane before readout.

1949, Tofts, 2005, Crawley and Henkelman, 1988]. In this method, an inversion pulse, typically a 180° pulse, flips the longitudinal magnetization (which was at equilibrium) from the $+z$-axis to the -z-axis (Fig. 2.3a). After this inversion pulse, during an inversion time TI the longitudinal magnetization recovers (Fig. 2.3b-c) according to the following Bloch equation:

$$\frac{dM_z}{dt} = \frac{M_0 - M_z}{T_1}. \tag{2.1}$$

After this time TI, an excitation pulse (90° pulse in Fig. 2.2) tips the current longitudinal magnetization in the transverse plane (Fig. 2.3d), where it gives rise to an free induction decay (FID) signal. The amplitude of this FID signal depends on how much the longitudinal magnetization has recovered during the period TI:

$$M_z = M_0(1 - 2e^{-\frac{\mathrm{TI}}{T_1}}). \tag{2.2}$$

To acquire a T_1-weighted image instead of a T_1-weighted signal, the IR sequence is combined with encoding gradients as explained in section 1.4.1. Thus to acquire a T_1-weighted image, the inversion recovery sequence has to be repeated N_{pe} (number of phase encoding lines) times, with each FID being encoded with a different phase-encoding gradient. The time between two repetitions of the sequence, i.e. the time between the inversion pulses, is called the repetition time TR. To avoid signal saturation, this repetition time is preferably long enough (TR $\geq 5T_1$) so that the longitudinal magnetization is fully recovered before perturbing it again.

2.4 Estimation of T_1 map

If several T_1-weighted images, with a well-chosen range of inversion times are acquired, a T_1 map can be estimated by voxel-wise fitting the following signal equation to the acquired data [Bernstein et al., 2004]:

$$S(\mathrm{TI}) = a + be^{-\frac{\mathrm{TI}}{T_1}}, \tag{2.3}$$

with $S(\mathrm{TI})$ the complex signal measured at time TI and a and b complex-valued parameters which depend on the proton density and acquisition parameters such as the RF pulses and timings. When the inversion pulse is 180° and the excitation pulse 90°, this model simplifies to a 2 parameter model:

$$S(\mathrm{TI}) = \rho(1 - 2e^{\frac{\mathrm{TI}}{T_1}} + e^{-\frac{\mathrm{TR}}{T_1}}). \tag{2.4}$$

with ρ a constant depending on the proton density. When the assumptions, exact 180° and 90° pulses and long TR, are valid, the signal-to-noise (SNR) in the fitted values of T_1 increase when the number of parameters is reduced [Crawley and Henkelman, 1988, MacFall et al., 1987, Weiss et al., 1980]. Traditionally, the nonlinear fit is performed using a Levenberg-Marquardt algorithm [Marquardt, 1963, More, 1978].

In Fig. 2.4 the variation of the signal amplitude $S(\mathrm{TI})$ in function of the inversion time TI is shown. At short inversion times, the longitudinal magnetization (Eq. 2.2)

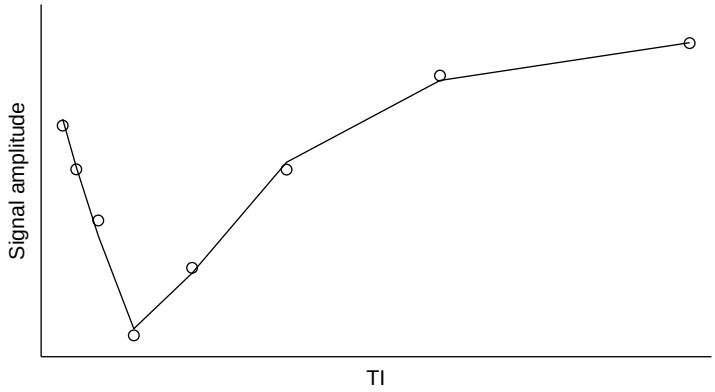

Fig. 2.4: Measured signal amplitude in function of the inversion time TI for the IR sequence.

is negative, and hence the phase of the transverse magnetization created by the readout pulse is inverted. However, the magnitude images are insensitive to the phase of the transverse magnetization and are strictly positive. The most used solution is to fit the acquired magnitude data to the modulus of the modeled signal given in Eq. 2.3. Other techniques try to restore the polarity by finding the position of the null point, i.e. the point where the signal is at minimum [Nekolla et al., 1992, Bakker et al., 1984]. Alternatively the relative phase of the magnitude images can also be used to determine the sign of the transverse magnetization [Gowland and Leach, 1991].

2.5 Applications

The spin-lattice relaxation time T_1 varies according tissue type and pathological state [Damadian, 1971]. Therefore, the use of T_1 as differentiating factor for different diseases [Bottomley et al., 1987, Cheng et al., 2012], such as multiple sclerosis [Larsson et al., 1989, Truyen et al., 1996, Vrenken et al., 2006], epilepsy [Conlon et al., 1988], stroke [DeWitt et al., 1987], dementia [Erkinjuntti et al., 1987], has been studied. Recently, a lot of advancement has been made in T_1 mapping of the heart, allowing to characterize diffuse/infiltrative myocardial diseases [Li et al., 2012, Xue et al., 2013, Kellman et al., 2013, Jellis and Kwon, 2014, Smit et al., 2014, Kellman and Hansen, 2014] . Furthermore, T_1 mapping has also been proven useful for the characterization of tumors [Englund et al., 1986, Kurki and Komu, 1995, Naruse et al., 1986]. Molecules containing paramagnetic materials give rise to much larger local magnetic field, and hence more rapid T_1 relaxation. Since the relaxation rate, $1/T_1$, increases proportionally to the concentration of contrast agent, it is possible to monitor changes in contrast agent concentration by measuring the T_1 [Caravan et al., 1999, 2009]. This can for example be used to measure blood volume in the brain [Schwarzbauer et al., 1993, Cheng, 2007] or the breakdown of the blood-brain barrier [Tahere et al., 2011, van Vliet et al., 2014]. Perfusion of blood into a voxel will introduce unperturbed magnetization into that

voxel, increasing the apparent relaxation rate. Therefore, T_1 mapping is also often used in perfusion studies [Peeters et al., 2004, Kershaw and Buckley, 2006, Detre et al., 1992].

2.6 Overview of T1 measurement sequences

Many sequences have been proposed for the measurement of T_1. Only the three most common T_1 mapping techniques: inversion recovery (IR), Look-Locker (LL) and variable flip angle (VFA) are discussed in this section.

2.6.1 Inversion recovery sequences

An inversion recovery pulse sequence consists of two parts. The first part includes the inversion pulse, an optional spoiler gradient after the pulse, and, if the inversion pulse is slice selective, an associated slice-selection gradient. The second part of the sequence is played out after a time TI. Typically, this part is a self-contained pulse sequence, used to read out the signal. The first part is considered as the IR module and the second part as the imaging sequence. Generally, in a IR pulse sequence, one IR module is played for each imaging sequence (see section 2.6.1.2). There exist several strategies for (multi-slice) 2D as well as 3D IR sequences.

2.6.1.1 Multi-slice IR sequences

In a multi-slice IR sequence, additional slices are excited and acquired while waiting for the spins in the first slice to reach equilibrium. The number of slices that can be acquired within one TR depends on the TR and the multi-slice scheme:

- **Sequential IR acquisition** [Park et al., 1985]: The slices are arranged in IR-module - imaging sequence pairs within one TR, where an odd-even slice ordering is assumed (Fig. 2.5a). Let T_a be the minimum length of the imaging pulse sequence for one slice and one encoding and TI the time between the inversion pulse and the imaging sequence for a given slice, i.e. the inversion time. Then the number of slices that can be acquired, N_{slice} within one TR can be expressed as

$$N_{\text{slice}} = \lfloor \frac{\text{TR}}{\text{TI} + T_a + T_{\text{ir}}} \rfloor. \tag{2.5}$$

  where T_{ir} is the duration of the inversion RF pulse and the slice gradients and the operator $\lfloor \cdot \rfloor$ denotes that N_{slice} is rounded down to the closest natural number. When TI is short, this scheme is efficient and a large number of slices can be acquired within one TR. However, for longer TI, considerable idle time is present, resulting in fewer slices per TR and reduced efficiency.

- **Interleaved IR acquisition** [Park et al., 1985]: The idle time for a given slice location is used to play out IR modules and/or imaging sequences for other slices (Fig. 2.5b). During the first part of a TR, a series of IR modules for N_{slice} slices is played out, whereas the imaging sequences for these slices are executed during a later part of the same TR. As such, the number of slices

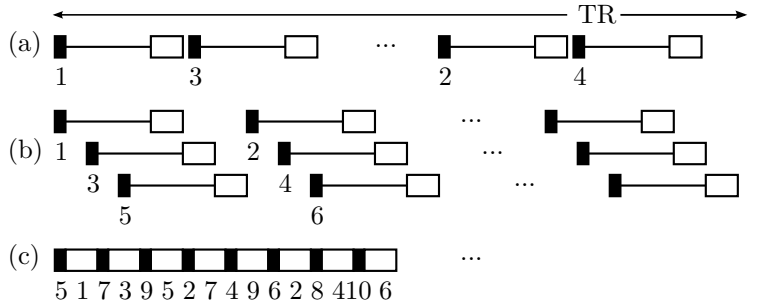

Fig. 2.5: Three acquisition schemes for 2D multislice imaging: (a) sequential IR acquisition, (b) interleaved IR acquisition, (c) distributed IR acquisition. The black box represents the IR module, the white box the imaging sequence, the solid line linking the two boxes denotes the idle time, the number denotes the slice index. Figure based on [Bernstein et al., 2004]

that can be acquired per TR is increased, reducing the number of acquisition needed for the desired slice coverage and thereby the overall scan time:

$$N_{\text{slice}} = \begin{cases} \lfloor \frac{\text{TR} - \text{TI} - T_{\text{ir}}}{T_a} \rfloor \text{ if } 2\,\text{TI} \geq 2\,\text{TR} \\ 1 + \lfloor \frac{\text{TI} - T_{\text{ir}}}{T_a} \rfloor \text{ if } 2\,\text{TI} < \text{TR}\,. \end{cases} \tag{2.6}$$

When $2\,\text{TI} \ll \text{TR}$ even more slices than predicted by Eq. 2.6 can be acquired. The disadvantage of this scheme is that idle time still may exist since each inversion module and its associated imaging sequences for a given slice need to be acquired during the same TR.

- **Distributed IR acquisition** [Oh et al., 1991]: The idle time is used to play out the inversion module or the imaging sequences for slices that may not be covered during the same TR (Fig. 2.5c). For example, the inversion module is played during the fourth TR interval, while the accompanying imaging sequences for this slice is played during the fifth TR interval. A drawback of this approach is that TR, TI and the number of slices are tightly coupled together, compromising the flexibility of independently choosing TR and TI [Listerud et al., 1996].

2.6.1.2 Imaging sequences

Several types of imaging sequences can be used to decode the FID signal, the most common ones are mentioned here.

Inversion recovery gradient echo (IR GE)

In the most basic version of an IR sequence, a gradient echo (GE) sequence (Fig. 1.5) is used to read out the signal. An IR GRE sequence consists of the inversion (180°) pulse and the excitation (90°) pulse. A time TE after the mid-point of the excitation pulse, the data is sampled using a pair of bipolar gradient pulses. The downside of this method is that the acquired images are more frequently troubled

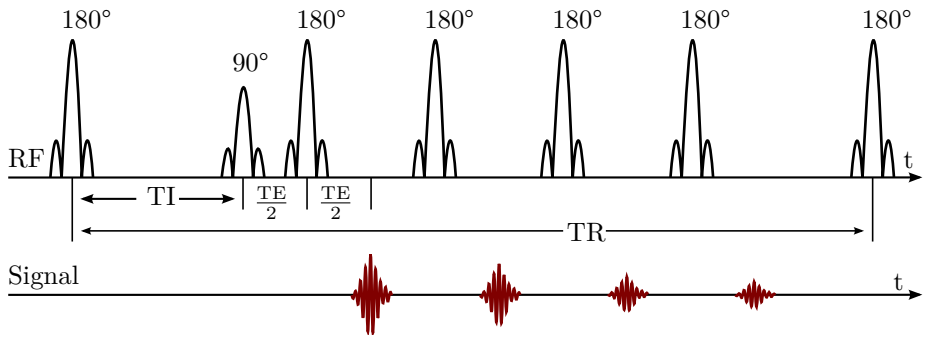

Fig. 2.6: Inversion Recovery Turbo/Fast spin echo (IR TSE/FSE) sequence: an echo train of refocusing pulses acquires multiple phase encoding lines of the image in one TR.

by susceptibility and chemical shift artifacts.

Inversion recovery spin echo (IR SE)
An IR SE sequence [Drain, 1949, Hahn, 1949] is a conventional SE sequence (Fig. 1.6) preceded by a 180° inversion pulse, with TI the time between the inversion pulse and the first (90°) pulse of the SE sequence. If the TR is longer than the time needed for the magnetization to reach steady-state, T_1 can be estimated independent of the flip angles, resulting in precise and accurate estimates. However, the long TR results in an overall long acquisition time. Thus, although IR SE produces an excellent image contrast, it is too time-consuming to use in clinical practice for T_1 mapping.

Inversion recovery turbo/fast spin echo (IR TSE/FSE)
With a fast spin echo (FSE) or turbo spin echo (TSE) sequence (Fig. 2.6) an echo train of evenly spaced refocusing pulses is used to acquire multiple phase encoding lines of the data, i.e. a different phase encoding line is acquired for each echo. The time between the successive echoes is called the Inter Echo Spacing (IES). The IES remains fixed as the RF pulses are all evenly spaced apart in time. The echo train length (ETL) or turbo factor (TF) gives the number of echoes in the spin echo train. Thus increasing the number of echoes in an echo train will decrease the scan time. When combining FSE with an IR-module, the maximum number of slices that can be accommodated within one TR will not only depend on how the multi-slice is acquired but also on the ETL and IES. For sequential IR FSE:

$$N_{\text{slice}} = \frac{\text{TR}}{\text{TI} + (\text{IES} \times \text{ETL})}, \tag{2.7}$$

and for interleaved IR FSE:

$$N_{\text{slices}} = \frac{\text{TI}}{\text{IES} \times \text{ETL}}. \tag{2.8}$$

For very high turbo factors, the number of slices is going to be restricted. A compromise between number of slices and speed of acquisition is required.

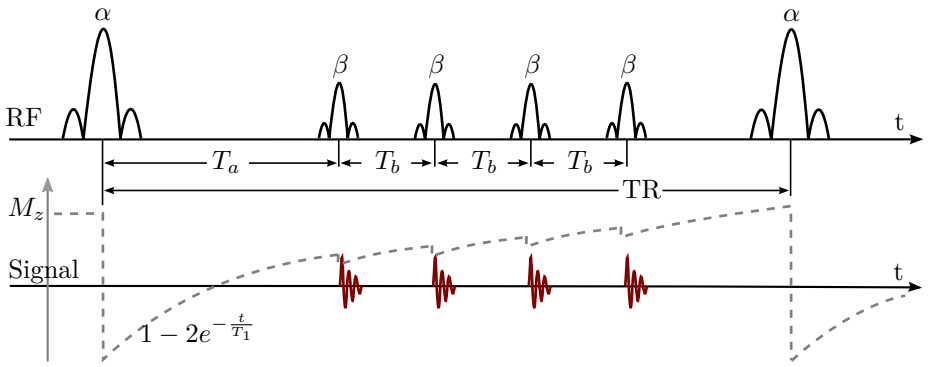

Fig. 2.7: Look-Locker sequence: an inversion pulse α is followed by a train of β pulses which measures the longitudinal magnetization at different inversion times $(T_a + (n-1)T_b)$ during one TR.

In theory, by using long echo trains, IR FSE offers the opportunity to acquire T_1-weighted images at a high spatial resolution within short scan times. However, in reality, this is often not possible, since due to the many large RF pulses used by the IR FSE sequence, specific absorption rate (SAR) limits are easily reached. Moreover, FSE k-space lines are acquired from different echoes, i.e. different k-space lines are acquired at different TE. The echo time that dominates the image contrast is the effective echo time $\mathrm{TE}_{\mathrm{eff}}$. Since the center of k-space dominates the image contrast, the $\mathrm{TE}_{\mathrm{eff}}$ is arranged to coincide with the central parts of k-space. If spatial frequencies which are not part of the center of the k-space are acquired with a longer TE, they will be attenuated by T_2 relaxation and some spatial resolution will be lost [Constable et al., 1992]. Thus an arbitrarily long echo train cannot be used without impairing the spatial resolution.

Inversion recovery echo planar imaging (IR EPI)
The FID can also be encoded using an EPI sequence (Fig. 1.11), as EPI encoding has no effect on the longitudinal magnetization [Ordidge et al., 1990, Clare and Jezzard, 2001]. Although this method allows for fast acquisition it has some major drawbacks in terms of image quality. Due to the limited bandwidth in the phase encoding direction, EPI images are prone to geometrical distortions caused by magnetic inhomogeneities (see section 3.6.1). Furthermore, due to the power requirements for the imaging gradients, the spatial resolution obtainable with EPI is limited by the strength of these imaging gradients [Dickinson et al., 1989].

2.6.2 Look-locker methods

LL sequences [Look and Locker, 1970] are closely related to IR sequence. The magnetization is also prepared by an inversion pulse (α in Fig. 2.7), but instead of measuring only one inversion time per TR, the magnetization is measured at several inversion times by application of a train of small read out pulses (β in Fig. 2.7). The usage of small angle RF pulses only minimally disrupts the longitudinal

magnetization during its T_1 recovery. Therefore, it is not necessary to wait until equilibrium is reached as sampling is performed in a continuous manner. However, the perturbation of the longitudinal relaxation by the train of β pulses hastens the recovery [Look and Locker, 1970, Brix et al., 1990]. Consequently, the signal can no longer be described by the signal model in Eq. 2.3, unless this equation is fit to the data with an "effective T_1" or T_1^* instead of T_1 [Look and Locker, 1970, Brix et al., 1990, Deichmann and Haase, 1992]. A look-up table can then be used to convert T_1^* into T_1. Assuming an equal time T_b between each β pulse, the signal after the n-th read-out pulse is given by [Brix et al., 1990, Nkongchu and Santyr, 2005]:

$$S_n = |\sin\beta M_n e^{-\frac{\mathrm{TE}}{T_2^*}}|, \tag{2.9}$$

with M_N the magnetisation just before the n-th read out pulse [Look and Locker, 1970]:

$$M_n = M_e q[F + (\cos\beta E_b)^{n-1}(Q - F)] \tag{2.10}$$

$$F = \frac{1 - E_b}{1 - \cos\beta E_b} \tag{2.11}$$

$$Q = \frac{F\cos\alpha\cos\beta E_r E_a\left[1 - (\cos\beta E_b)^{N-1}\right]}{1 - \cos\alpha\cos\beta E_r E_a(\cos\beta E_b)^{N-1}} + \frac{\cos\alpha E_a(1 - E_r) - E_a + 1}{1 - \cos\alpha\cos\beta E_r E_a(\cos\beta E_b)^{N-1}} \tag{2.12}$$

where $E_b = \exp(-T_b/T_1)$, $E_a = \exp(-T_a/T_1)$, $E_r = \exp(-T_a/T_1)$, N the number of β pulses, T_1 the time between the inversion pulse α and the first read out pulse β and $t_r = TR - T_a - (N-1)T_b$. The 2D sequence version of the LL sequence is called the TOMROP-sequence (T One by Multiple Read out Pulses) [Brix et al., 1990]. In a TOMROP sequence, gradient echoes are used to record the signal amplitude following the read out pulses. After these gradient echoes, the remaining transverse magnetization is destroyed by spoiler gradients [Gowland and Leach, 1992]. Instead of a GE read-out [Deichmann and Haase, 1992], an EPI read-out [Gowland and Mansfield, 1992, Freeman et al., 1998, Deichmann, 2005, Shin et al., 2009] can be used as well in combination with a LL approach, although these sequences suffer from a low SNR and/or severe image distortions and [Deichmann, 2005].

Since the technique assumes perfect RF pulses of negligible duration, it is sensitive to B_1 field inhomogeneities [Cooper et al., 2012]. Moreover, the use of the readout train reduces the SNR of the acquired images [Constantinides et al., 1997, Clare and Jezzard, 2001]. Another downside of LL sequences is that they are not standardly provided at the scanner. Different variants of the LL sequence have been proposed for cardiac T_1 mapping, such as Modified LL Inversion recovery (MOLLI) [Messroghli et al., 2004] and Shortend MOLLI (ShMOLLI) [Piechnik et al., 2010].

2.6.3 Variable flip angle methods

With VFA (Fig. 2.8), a high resolution 3D T_1 map can be acquired within clinically feasible scan times [Fram et al., 1987, Deoni et al., 2003, 2005, Deoni, 2010, Trzasko

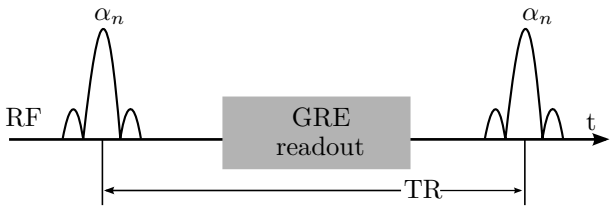

Fig. 2.8: Variable flip angle sequence.

et al., 2013, Dieringer et al., 2014]. The method requires two or more spoiled gradient-echo images, each acquired with a different flip angle. The signal behavior in a spoiled gradient echo (SPGR) sequence is described by [Deoni et al., 2003]

$$S = K\frac{1 - e^{-\frac{\mathrm{TR}}{T_1}}}{1 - \cos\alpha e^{-\frac{TR}{T_1}}}\sin\alpha, \tag{2.13}$$

with α the flip angle which is varied and K a proportionality factor which incorporates the proton density, coil sensitivity and T_2^* relaxation. When a data set with only two different flip angles α is acquired, the T_1 map can either be derived from Eq. 2.13 by using a nonlinear fit or by using a weighted linear least-squares fitting procedure using [Chang et al., 2008]:

$$\frac{S}{\sin\alpha} = \frac{S}{\tan\alpha}e^{-\frac{\mathrm{TR}}{T_1}} + \text{constant}. \tag{2.14}$$

The proposed signal models assume perfect spoiling of the transverse magnetization before each excitation and a perfect knowledge of the flip angles. Due to B1 field inhomogeneities, the actual flip angles will deviate from their set value, leading to a loss of accuracy of the estimated T_1 map [Mintzopoulos and Inati, 2006, Stikov et al., 2015, Liu et al., 2015, Preibisch and Deichmann, 2009]. These B1 field inhomogeneities can be accounted for by acquiring a B1 field map along with the T_1 weighted images [Deoni, 2007, Pohmann and Scheffler, 2013, Liberman et al., 2014].

2.7 Limitations and pitfalls

Quantitative T_1 mapping knows a broad range of applications, however, since the reliability and accuracy of the estimated T_1 values is still low, quantitative T_1 mapping is not used in clinical routine. There are several possible sources of errors in T_1 measurements, the most common ones are discussed in this section.

2.7.1 Motion

A T_1 map is obtained by voxel-wise fitting the signal equation (Eq. 2.3) to the acquired data. Hence, spatial correspondence between the different T_1-weighted images is crucial. However, due to patient movements or physiological motion

such as cardiac and respiratory motion, the acquired T_1-weighted images might be misaligned. The most common way to correct for motion is to spatially register the T_1-weighted images to a target image, typically one of the acquired images prior to estimation of the T_1 map [Vrenken et al., 2006, Deoni et al., 2003]. However, the difference in signal intensities between the different T_1-weighted images makes this realignment a challenging task. Moreover, by performing motion correction as a pre-processing step prior to T_1 estimation, no feedback mechanism exists between the image registration and T_1 estimation, leading to biased estimates [Ramos-Llorden et al., 2015]. To deal with this issue, recently, model-based motion corrections have been introduced, where the signal model is included in the registration step [Ramos-Llorden et al., 2015, Hallack et al., 2014, Xue et al., 2013].

2.7.2 Specific Absorption Rate (SAR)

The specific absorption rate (SAR) corresponds to the amount of radiofrequency energy deposited in the patient, which may result in heating [Bottomley, 2008]. SAR value is proportional to the square of the static magnetic field amplitude (B_0), the square of the flip angle α and the fraction of duration of the sequence during which the RF waves are transmitted (D) [Bottomley et al., 1985, Hennig, 1988, Ibrahim et al., 2001, Bernstein et al., 2004]:

$$\mathrm{SAR} \propto B_0^2 \alpha^2 D. \tag{2.15}$$

In TSE sequences, the echo train of RF pulses deposits a high RF energy, resulting in a high SAR [Oshio and Feinberg, 1991]. Reducing the SAR can be done by decreasing the number of slices acquired within one TR, either by acquiring thicker slices, thus decreasing the spatial resolution, or by increasing the number of excitations N_{ex}, thus increasing the scan time. Another option is to lower the angle of the used RF pulses, however, this results in a decrease of contrast and SNR [Weigel et al., 2007].

2.7.3 Acquisition time

The total acquisition time of a set of T_1-weighted images is proportional to the number of T_1-weighted images. The scan time of one T_1-weighted image acquired with IR TSE is [Bernstein et al., 2004]:

$$T_{\mathrm{scan}} = \frac{\mathrm{TR}\, N_{\mathrm{PE}} N_{\mathrm{ex}}}{\mathrm{ETL}}, \tag{2.16}$$

with N_{PE} the number of phase encoding lines, ETL te echo train length and N_{ex} the number of times the sequence has to be run to have full slice coverage, i.e. the total number of slices divided by the number of slices acquired per TR (N_{slice}). Eq. 2.16 can also be used to calculate the acquisition time of an IR SE or IR GRE image by setting ETL to one. Since the IR sequence requires long TR, the sequence is quite slow. The acquisition can be speeded up by acquiring less T_1-weighted images, however this comes at the expense of a decrease of precision of the T_1 map, while precise T_1 estimation is necessary as the differences and changes in T_1 tend to be within just a few percent. As mentioned above, reducing the scan time by

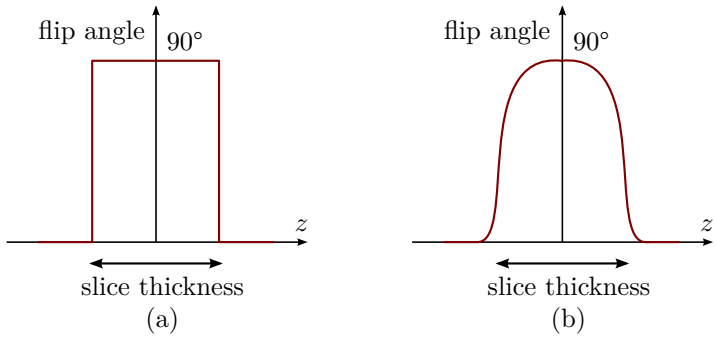

Fig. 2.9: (a) Ideal and (b) Realistic slice profile.

using fast read-out methods comes at the cost of either a significant increase in SAR (TSE) or spatial image distortions (EPI). Thus, the T_1-weighted images are often acquired at a low spatial resolution, reducing the number of phase encoding lines N_{PE} and slices and thereby reducing the total scan time.

2.7.4 Imperfect RF pulses

In section 1.4.1, we assumed that slice selective RF pulses can excite a perfect narrow slab. However in reality, slice selective RF pulses rarely give rise to a square slice profile (Fig. 2.9a), leading to variations in the flip angle across the slice or B_1 field inhomogeneities [Kinglsey et al., 1998, Dowell and Tofts, 2007]. Additionally, the imperfect slice profile (Fig. 2.9b) might also lead to cross-talk between the different slices of a multi-slice image [Bernstein et al., 2004]. There might be loss of signal in one slice due to pre-excitation from an RF pulse meant for another adjacent slice. To counter this, multi-slice images are often acquired with an inter-slice gap [McRobbie et al., 2006]. However, as some parts of the subject are not sampled, inter-slice gaps lead to a loss of information.

Bibliography

E. Ashton. Quantitative MR in multi-center clinical trials. *Journal of Magnetic Resonance Imaging*, 31(2):279–288, 2010.

C.J.G. Bakker, C.N. de Graaf, and P. van Dijk. Restoration of signal polarity in a set of inversion recovery NMR images. *IEEE Transactions on Medical Imaging*, MI-3(4):1972–20, 1984.

M.A. Bernstein, K.F. King, and X.J. Zou. *Handbook of MRI pulse sequences*. Elsevier Academic press, Philadelphia, 2004.

P.A. Bottomley. Turning up the heat on MRI. *Journal of the American College of Radiology*, 5(7):853–855, 2008.

P.A. Bottomley, R.W. Redington, W.A. Edelstein, and J.F. Schenck. Estimating radiofrequency power deposition in body NMR imaging. *Magnetic Resonance in Medicine*, 2(4):336–349, 1985.

P.A. Bottomley, T.H. Foster, R.E. Argersinger, and L.M. Pfeifer. A review of normal tissue hydrogen NMR relaxation times and relaxation mechanisms from 1âĂŞ100 MHz: Dependence on tissue type, NMR frequency, temperature, species, excision, and age. *Medical Physics*, 11(4):425–448, 1986.

P.A. Bottomley, C.J. Hardy, R.E. Argersinger, and G. Allen-Moore. A review of 1H nuclear magnetic resonance relaxation in pathology: are T1 and T2 diagnostic. *Medical Physics*, 14(1):1–37, 1987.

G. Brix, L.R. Schad, M. Deimling, and W.J. Lorenz. Fast and preise T1 imaging using a TOMROP sequence. *Magnetic Resonance Imaging*, 8(4):351–356, 1990.

R. Bruening, K.K. Kwong, M.J. Vevea, F.H. Hochberg, L. Cher, G.T. Harsh, P.T. Niemi, R.M. Weisskoff, and B.R. Rosen. Echo-planar MR determination of relative cerebral blood volume in human brain tumors: T1 versus T2 weighting. *American Journal of Neuroradiology*, 17(5):831–840, 1996.

P. Caravan, J.J. Ellison, T.J. McMurry, and R.B. Lauffer. Gadolinium (III) chelates as MRI contrast agents: structure, dynamics, and applications. *Chemical Reviews*, 99(9):2293–2352, 1999.

P. Caravan, C.T. Farrar, L. Frullano, and R. Uppal. Influence of molecular parameters and increasing magnetic field strength on relaxivity of gadolinium and manganese based T1 contrast agents. *Contrast media & molecular imaging*, 4(2):89–100, 2009.

L.-C. Chang, G.K. Cheng, P.J. Basser, and C. Pierpaoli. Linear least-squares method for unbiased estimation of T1 from SPGR signals. *Magnetic Resonance in Medicine*, 60(2):496–501, 2008.

H.L.M. Cheng. T1 measurement of flowing blood and arterial input function determination for quantitative 3D T1-weighted DCE-MRI. *Journal of Magnetic Resonance Imaging*, 25(5):1073–1078, 2007.

H.L.M. Cheng, N. Stikov, N.R. Ghugre, and G.A. Wright. Practical medical applications of quantitative MR relaxometry. *Journal of Magnetic Resonance Imaging*, 36(4):805–824, 2012.

S. Clare and P. Jezzard. Rapid T1 mapping using multislice echo planar imaging. *Magnetic Resonance in Medicine*, 45(4):630–634, 2001.

P. Conlon, M.R. Trimble, D. Rogers, and C. Callicott. Magnetic resonance imaging in epilepsy: a controlled study. *Epilepsy Research*, 2(1):37–43, 1988.

R.T. Constable, R.C. Smith, and J.c. Gore. Signal-to-noise and contrast in fast spin echo (FSE) and inversion recovery FSE imaging. *Journal of computer assisted tomography*, 16(1):41–7, 1992.

C.D. Constantinides, E. Atalar, and E.R. McVeigh. Signal-to-noise measurements in magnitude images from NMR phased arrays. *Magnetic Resonance in Medicine*, 38(5):852–857, 1997.

M.A. Cooper, T.D. Nguyen, P. Spincemaille, M.R. Prince, J.W. Weinsaft, and Y. Wang. Flip angle profile correction for T1 and T2 quantification with look-locker inversion recovery 2D steady-state free precession imaging. *Magnetic Resonance in Medicine*, 68(5):1579–1585, 2012.

D.J. Covarrubias, B.R. Rosen, and M.H. Lev. Dynamic magnetic resonance perfusion imaging of brain tumors. *The Oncologist*, 9(5):528–537, 2004.

A.P. Crawley and R.M. Henkelman. A comparison of one-shot and recovery methods in T1 imaging. *Magnetic Resonance in Medicine*, 7(1):23–34, 1988.

R. Damadian. Tumor detection by nuclear magnetic resonance. *Science*, 171(3976): 1151–1153, 1971.

R. Deichmann. Fast high-resolution T1 mapping of the human brain. *Magnetic Resonance in Medicine*, 54(1):20–27, 2005.

R. Deichmann and A. Haase. Quantification of T1 values by SNAPSHOT-FLASH NMR imaging. *Journal of Magnetic Resonance*, 96(3):608–612, 1992.

S.C.L. Deoni. High-resolution T1 mapping of the brain at 3T with driven equilibrium single pulse observation of T1 with high-speed incorporation of RF field inhomogeneities (DESPOT1-HIFI). *Journal of Magnetic Resonance Imaging*, 26 (4):1106–1111, 2007.

S.C.L. Deoni. Quantitative relaxometry of the brain. *Topics in Magnetic Resonance Imagingagnetic resonance imaging*, 21(2):101–113, 2010.

S.C.L. Deoni, B.K. Rutt, and T.M. Peters. Rapid combined T1 and T2 mapping using gradient recalled acquisition in the steady state. *Magnetic Resonance in Medicine*, 49(3):515–526, 2003.

S.C.L. Deoni, T.M. Peters, and B.K. Rutt. High-resolution T1 and T2 mapping of the brain in a clinically acceptable time with DESPOT1 and DESPOT2. *Magnetic Resonance in Medicine*, 53(1):237–241, 2005.

J.A. Detre, J.S. Leigh, S. Williams, and A.P. Koretsky. Perfusion imaging. *Magnetic Resonance in Medicine*, 23(1):37–45, 1992.

L.D. DeWitt, J.P. Kistler, D.C. Miller, E.P. Richardson, and F.S. Buonanno. NMR-Neuropathologic correlation in stroke. *Stroke*, 18(2):342–351, 1987.

R. Dickinson, F. Goldie, and D. Firmin. Gradient power requirements for echo-planar imaging. In *Proceedings of the Society for Magnetic Resonance in Medicine*, volume 8, page 828, Amsterdam, The Netherlands, 1989.

M.A. Dieringer, M. Deimling, D. Santoro, J. Wuerfel, V.I. Madai, J. Sobesky, F. von Knobelsdorff-Brenkenhoff, J. Schulz-Menger, and T. Niendorf. Rapid parametric mapping of the longitudinal relaxation time T1 using two-dimensional variable flip angle magnetic resonance imaging at 1.5 Tesla, 3 Tesla and 7 Tesla. *PloS one*, 9(3):e91318, 2014.

N.G. Dowell and P.S. Tofts. Fast, accurate, and precise mapping of the RF field in vivo using the 180 degree signal null. *Magnetic Resonance in Medicine*, 58(3): 622–630, 2007.

L.E. Drain. A Direct Method of Measuring Nuclear Spin-Lattice Relaxation Times. In *Proceedings of the Physical Society. Section A*, volume 62, page 301, 1949.

E. Englund, A. Brun, Z. Gyorffy-wagner, E.-M. Larsson, and B. Persson. Relaxation times in relation to grade of malignancy and tissue necrosis in astrocytic gliomas. *Magnetic Resonance Imaging*, 4(5):425–429, 1986.

T. Erkinjuntti, L. Ketonen, R. Sulkava, M. Vuorialho, and M. Livanainen. Do white matter changes on MRI and CT differentiate vascular dementia from Alzheimer's disease. *Journal of Neurology, Neurosurgery & Psychiatry*, 50(1):37–42, 1987.

R. Erlemann, M.F. Reiser, P.E. Peter, P. Vasallo, B. Nommensen, C.R. Kusnierz-Glaz, J. Ritter, and A. Roessner. Musculoskeletal neoplasms: static and dynamic Gd-DTPA enhanced MR imaging. *Radiology*, 171(3):767–773, 1989.

E.K. Fram, R.J. Herfkens, G.A. Johnsens, G.H. Glover, J.P. Karis, A. Shimakawa, T.G. Perkins, and N.J. Pelc. Rapid calculation of T1 using variable flip angle gradient refocused imaging. *Magnetic Resonance Imaging*, 5(3):201–208, 1987.

A.J. Freeman, P.A. Gowland, and P. Mansfield. Optimization of the ultrafast look-locker echo-planar imaging T1 mapping sequence. *Magnetic Resonance Imaging*, 16(7):765–772, 1998.

P.A. Gowland and M.O. Leach. A simple method for the restoration of signal polarity in multi-image inversion recovery sequences for measuring T1. *Magnetic Resonance in Medicine*, 18(1):224–231, 1991.

P.A. Gowland and M.O. Leach. Fast and accurate measurements of T1 using a multi-readout single inversion-recovery sequence. *Magnetic Resonance in Medicine*, 26 (1):79–88, 1992.

P.A. Gowland and P. Mansfield. Accurate measurement of T1 in vivo in less than 3 seconds using echo-planar imaging. *Magnetic Resonance in Medicine*, 30(3): 351–354, 1992.

E.L. Hahn. An accurate nuclear magnetic resonance method for measuring spin-lattice relaxation times. *Physical Review*, 76(1):145–146, 1949.

A. Hallack, M.A. Chappel, M.J. Gooding, and J.A. Schnabel. A new similarity metric for groupwise registration of variable flip angle sequences for improved T1 estimation in DCE-MRI. In *Proceedings of the International workshop on Biomedical Image Registration (WIBR)*, volume 6, pages 154–163, London, UK, 2014.

J. Hennig. Multiecho imaging sequences with low refocusing flip angles. *Journal of Magnetic Resonance*, 78(3):397–407, 1988.

T.S. Ibrahim, R. Lee, B.A. Baertlein, and P.L. Robitaille. B1 field homogeneity and SAR calculations for the birdcage coil. *Physics in Medicine and biology*, 46 (2):609, 2001.

C.L. Jellis and D.H. Kwon. Myocardial T1 mapping: modalities and clinical applications. *Cardiovascular diagnosis and therapy*, 4(2):126–37, 2014.

P. Kellman and M.S. Hansen. T1-mapping in the heart: accuracy and precision. *Journal of Cardiovascular Magnetic Resonance*, 16(1):2, 2014.

P. Kellman, A.E. Arai, and H. Xue. T1 and extracellular volume mapping in the heart: estimation of error maps and the influence of noise on precision. *Journal of Cardiovascular Magnetic Resonance*, 15(1):56, 2013.

L.E. Kershaw and D.L. Buckley. Precision in measurements of perfusion and microvascular permeability with T1-weighted dynamic contrast-enhanced MRI. *Magnetic Resonance in Medicine*, 56(5):986–992, 2006.

P.B. Kinglsey, R.J. Ogg, W.E. Reddick, and R.G. Steen. Correction of errors caused by imperfect inversion pulses in MR imaging measurement of T1 relaxation times. *Magnetic Resonance Imaging*, 16(9):1049–1055, 1998.

J.-P. Korb and R.G. Bryant.

T. Kurki and M. Komu. Spin-lattice relaxation and magnetization transfer in intracranial tumors in vivo: effects of Gd-DTPA on relaxation parameters. *Magnetic Resonance Imaging*, 13(3):379–385, 1995.

H.B. Larsson, J. Frederiksen, J. Petersen, A. Nordenbo, I. Zeeberg, O. Henriksen, and J. Olesen. Assessment of demyelination, edema, and gliosis by in vivo determination of T1 and T2 in the brain of patients with acute attack of multiple sclerosis. *Magnetic Resonance in Medicine*, 11(3):337–48, 1989.

W. Li, M. Griswold, and X. Yu. Fast cardiac T1 mapping in mice using a model-based compressed sensing method. *Magnetic Resonance in Medicine*, 68(4): 1127–34, 2012.

G. Liberman, Y. Louzoun, and D. Ben Bashat. T1 Mapping using variable flip angle SPGR data with flip angle correction. *Journal of Magnetic Resonance Imaging*, 40(1):171–180, 2014.

J. Listerud, J. Mitchell, L. Bagley, and R. Grossman. OIL FLAIR: Optimized interleaved fluid-attenuated inversion recovery in 2D fast spin echo. *Magnetic Resonance in Medicine*, 36(2):320–325, 1996.

Y. Liu, J.R. Buck, S. Zheng, and V.N. Ikonomidou. Optimizing and comparing the efficiencies of relaxometry sequences in quantitative T1 and T2 imaging. In *Proceedings of the International Society for Magnetic Resonance in Medicine*, volume 23, page 1689, Toronto, Ontario, Canada, 2015.

D.C. Look and D.R. Locker. Time saving in measurement of NMR and EPR relaxation times. *Review of Scientific Instruments*, 41(2):250–251, 1970.

J.R. MacFall, F.W. Wehrli, R.K. Breger, and G.A. Johnson. Methodology for the measurement and analysis of relaxation times in proton imaging. *Magnetic Resonance Imaging*, 5(3):209–220, 1987.

D.W. Marquardt. An Algorithm for Least-Squares Estimation of Nonlinear Parameters. *Journal of the Society for Industrial and Applied Mathematics*, 11(2):431–441, 1963.

D.W. McRobbie, E.A. Moore, M.J. Graves, and M.R. Prince. *MRI: From picture to proton*. Cambridge University Press, Cambridge, 2006.

D.R. Messroghli, A. Radjenovic, S. Kozerke, D.M. Higgins, M.U. Sivananthan, and J.P. Ridgway. Modified look-locker inversion recovery (MOLLI) for high-resolution T1 mapping of the heart. *Magnetic Resonance in Medicine*, 52(1): 141–146, 2004.

D. Mintzopoulos and S. Inati. The effects of magnetic field inhomogeneity on FLASH-based T1 measurements. In *Proceedings of the International Society for Magnetic Resonance in Medicine*, volume 14, page 923, Seattle, Washington, USA, 2006.

J.J. More. The Levenberg-Marquardt algorithm: implementation and theory. In *Numerical Analysis*, pages 105–116. Springer Berlin Heidelberg, 1978.

S. Naruse, Y. Horikawa, C. Tanaka, K. Hirakawa, H. Nishikawa, and K. Yoshizaki. Significance of proton relaxation time measurement in brain edema, cerebral infarction and brain tumors. *Magnetic Resonance Imaging*, 4(4):293–304, 1986.

S. Nekolla, T. Gneiting, J. Syha, R. Deichmann, and A. Haase. T1 maps by k-space reduced snap-shot FLASH MRI. *Journal of computer assisted tomography*, 16 (2):327–332, 1992.

K. Nkongchu and G. Santyr. An improved 3D Look-Lcoker imaging method for T1 parameter estimation. *Magnetic Resonance Imaging*, 32(7):801–807, 2005.

C.H. Oh, S.K. Hilal, I.K. Mun, and Z.H. Cho. An optimized multislice acquisition sequence for the inversion-recovery MR imaging. *Magnetic Resonance Imaging*, 9(6):903–908, 1991.

R.J. Ordidge, P. Gibbs, B. Chapman, M.K. Stehling, and P. Mansfield. High-speed multislice T1 mapping using inversion recovery echo planar imaging. *Magnetic Resonance in Medicine*, 16(2):238–245, 1990.

K. Oshio and D.A. Feinberg. GRASE (Gradient and Spin Echo) imaging: A novel fast MRI technique. *Magnetic Resonance in Medicine*, 20(1):344–349, 1991.

H.W. Park, M.H. Cho, and Z.H. Cho. Time-multiplexed multislice inversion-recovery techniques for NMR imaging. *Magnetic Resonance in Medicine*, 2(6): 534–539, 1985.

F. Peeters, L. Annet, L. Hermoye, and B.E. Van Beers. Inflow Correction of Hepatic Perfusion Measurements Using T 1-Weighted, Fast Gradient-Echo, Contrast-Enhanced MRI. *Magnetic Resonance in Medicine*, 51(4):710–717, 2004.

S.K. Piechnik, V.M. Ferreira, E. Dall'Armellina, L.E. Cochlin, A. Greiser, S. Neubauer, and M.D. Robson. Shortened Modified Look-Locker Inversion recovery (ShMOLLI) for clinical myocardial T1 mapping at 1.5 and 3 T within a 9 heartbeat breathhold. *Journal of Cardiovascular Magnetic Resonance*, 12(1): 69, 2010.

R. Pohmann and K. Scheffler. A theoretical and experimental comparison of different techniques for B1 mapping at very high fields. *NMR in Biomedicine*, 26(3):265–275, 2013.

C. Preibisch and R. Deichmann. Influence of RF spoiling on the stability and accuracy of T1 mapping based on spoiled FLASH with varying flip angles. *Magnetic Resonance in Medicine*, 61(1):125–135, 2009.

G. Ramos-Llorden, A.J. den Dekker, **G. Van Steenkiste**, J. van Audekerke, M. Verhoye, and J. Sijbers. Simultaneous motion correction and T1 estimation in quantitative T1 mapping: an ML restoration approach. In *Proceedings of the IEEE International Conference on Image Processing*, pages 3160–3164, Quebec, Canada, 2015.

W.D. Rooney, G. Johnson, X. Li, E.R. Cohen, S.-G. Kim, K. Ugurbil, and C.S. Jr. Springer.

C. Schwarzbauer, J. Syha, and A. Haase. Quantification of regional blood volumes by rapid T1 mapping. *Magnetic Resonance in Medicine*, 29(5):709–712, 1993.

Wanyong Shin, Hong Gu, and Yihong Yang. Fast high-resolution T1 mapping using inversion - Recovery Look-Locker echo-planar imaging at steady state: Optimization for accuracy and reliability. *Magnetic Resonance in Medicine*, 61 (4):899–906, 2009.

H. Smit, R.P. Guridi, J. Guenoun, D.H.J. Poot, G.N. Doeswijk, M. Milanesi, M.R. Bernsen, G.P. Krestin, S. Klein, and G. Kotek. T1 mapping in the rat myocardium at 7 Tesla using a modified CINE inversion recovery sequence. *Journal of Magnetic Resonance Imaging*, 39(4):901–910, 2014.

N. Stikov, M. Boudreau, I.R. Levesque, C.L. Tardif, J.K. Barral, and G.B. Pike. On the accuracy of T1 mapping: Searching for common ground. *Magnetic Resonance in Medicine*, 73(2):514–522, 2015.

S. Tahere, C. Gasparovic, N.J. Shah, and G.A. Rosenberg. Quantitative measurement of blood-brain barrier permeability in human using dynamic contrast-enhanced MRI with fast T1 mapping. *Magnetic Resonance in Medicine*, 65(4): 1036–42, 2011.

P. Tofts. *Quantitative MRI of the Brain.* John Wiley & Sons, New York, 2005.

L. Truyen, J.H. van Waesberghe, M.A. van Walderveen, B.W. van Oosten, C.H. Polman, O.R. Hommes, H.J. Ader, and F. Barkhof. Accumulation of hypointense lesions ("black holes") on T1 spin-echo MRI correlates with disease progression in multiple sclerosis. *Neurology*, 47(6):1469–76, 1996.

J.D. Trzasko, P.M. Mostardi, S.J. Riederer, and A. Manduca. Estimating T1 from multichannel variable flip angle SPGR sequences. *Magnetic Resonance in Medicine*, 69(6):1787–94, 2013.

E.A. van Vliet, W.M. Otte, J.A. Gorter, R.M. Dijkhuizen, and W.J. Wadman. Longitudinal assessment of blood-brain barrier leakage during epileptogenesis in rats. A quantitative MRI study. *Neurobiology of Disease*, 63:74–84, 2014.

H. Vrenken, J.J.G. Geurts, D.L. Knol, N.L. van Dijk, V. Dattola, B. Jasperse, R.A. van Schijndel, C.H. Polman, J.A. Castelijns, F. Barkhof, and P.J.W. Pouwels. Whole-Brain T1 Mapping in Multiple Sclerosis: Global Changes of Normal-appearing Gray and White Matter. *Radiology*, 240(3):811–820, 2006.

M. Weigel, M. Zaitsev, and J. Hennig. Inversion recovery prepared turbo spin echo sequences with reduced SAR using smooth transitions between pseudo steady states. *Magnetic Resonance in Medicine*, 57(3):631–637, 2007.

G.H. Weiss, R.K. Gupta, J.A. Ferretti, and E.D. Becker. The choice of optimal parameters for measurement of spin lattice relaxation times. *Journal of Magnetic Resonance*, 37(3):369–379, 1980.

H. Xue, A. Greiser, S. Zuehlsdorff, M.P. Jolly, J. Guehring, A.E. Arai, and P. Kellman. Phase-sensitive inversion recovery for myocardial T1 mapping with motion correction and parametric fitting. *Magnetic Resonance in Medicine*, 69(5): 1408–1420, 2013.

3 Diffusion MRI

Contents

3.1 Introduction

Diffusion MRI (dMRI) is an imaging modality within MRI, which allows in vivo investigation and characterization of tissue microstructure. The image contrast in dMRI is generated by the diffusion of water molecules. In this chapter, the basics of diffusion and self-diffusion are covered. Next, we describe how we can measure the diffusion coefficient by sensitizing the NMR signal for diffusion. Last, we explain diffusion tensor imaging, the most popular dMRI technique. This chapter is based on the first chapter of the PhD dissertation by Jeurissen [2012]. For a more in depth overview of dMRI we refer the reader to literature [Tofts, 2005, Johansen-Berg and Behren, 2009, Jones, 2011].

3.2 Self-diffusion

Diffusion refers to the process in which molecules move from a region of higher to a region of lower concentration. The molecules intermingle as result of their kinetic energy. This diffusion process is described by Fick's first law [Fick, 1855]:

$$\boldsymbol{J} = -D\nabla\boldsymbol{C}, \tag{3.1}$$

with $\boldsymbol{J}$ the net particle flux, $\boldsymbol{C}$ the particle concentration and D the diffusion coefficient, which is an intrinsic property of the medium.

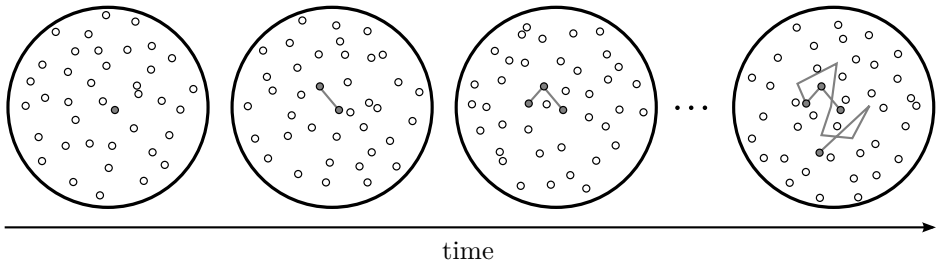

Fig. 3.1: Schematic representation of Brownian motion: molecules are constantly moving around as a result of their thermal energy.

The diffusion phenomenon can be explained by the observations of botanist Robert Brown. When Robert Brown studied pollen grains, which he had suspended in water, he noticed the pollen grains were constantly moving around [Brown, 1828]. After further research, it was realized that it were not the particles themselves moving around, but the water molecules they were suspended in. What Brown had described was the phenomenon of self-diffusion, i.e. molecules in a fluid (e.g. water) are constantly moving around as a result of their thermal energy (Fig. 3.1). If one single molecule could be observed, one would see it tumbling around freely, changing its path each time it collides with another molecule. The trajectory the molecule undertakes can be described by a "random walk", which is also referred to as Brownian motion.

Using a probabilistic framework the behavior of a large group of molecules can be described, relating Brownian motion to macroscopic diffusion. Therefore, Einstein introduced the displacement distribution function, which gives the probability that a single molecule undergoes a displacement within a certain time. When the molecules are free to diffuse, this displacement distribution function or probability density function (PDF), $p(\boldsymbol{r})$ takes the form of a Gaussian distribution, which is centered around zero and whose width is defined by the diffusion coefficient [Einstein, 1905]:

$$p(\boldsymbol{r}) = \frac{1}{\sqrt{(4\pi Dt)^3}} e^{-\frac{\|\boldsymbol{r}\|^2}{4Dt}}, \tag{3.2}$$

with $\boldsymbol{r}$ the displacement vector, t the diffusion time and D the diffusion coefficient, which is the same as the one in Fick's law (Eq. 3.1).

In the simple case of isotropic unrestricted diffusion, the relationship between the mean square displacements of the group of molecules, characterized by Brownian motion, and the diffusion coefficient is described by the well-known Einstein equation for diffusion [Einstein, 1905]:

$$< \|\boldsymbol{r}\|^2 >= 6Dt, \tag{3.3}$$

with $< \|\boldsymbol{r}\|^2 >$ the mean square displacements of the group of molecules and time t, assumed to be long compared to the time between collisions. The isoprobability surface of $p(\boldsymbol{r})$ will be a sphere with radius $\sqrt{6Dt}$ and centered on the origin (Fig. 3.2c). The fact that the isoprobability surface is a sphere shows that in each direction there is an equal probability a molecules displaces itself a given distance from the origin.

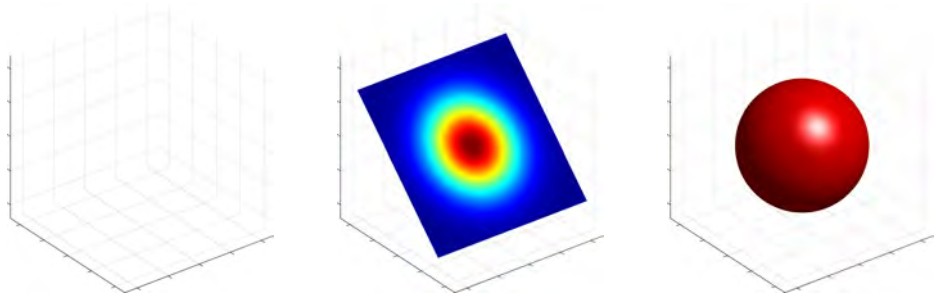

(a) environment (b) PDF (c) Isoprobability surface

Fig. 3.2: Free isotropic (Gaussian) diffusion. Image reproduced with permission from Jeurissen [2012].

3.3 Apparent diffusion

In biological tissue, the diffusing water molecules may encounter hindrances, such as cell membranes or macromolecules, along their random walk. As a result, their mean squared displacement per unit time will be lower than when observed in

'free' water. Thus, when the diffusion coefficient is calculated using Eq. 3.3, the diffusion coefficient will appear to be lower. Therefore, it is convenient to refer to the diffusion coefficient measured in a biological samples as the apparent diffusion coefficient (ADC) [Le Bihan et al., 1986]. Depending on the microstructure of the tissue, the diffusion will be either isotropic or anisotropic.

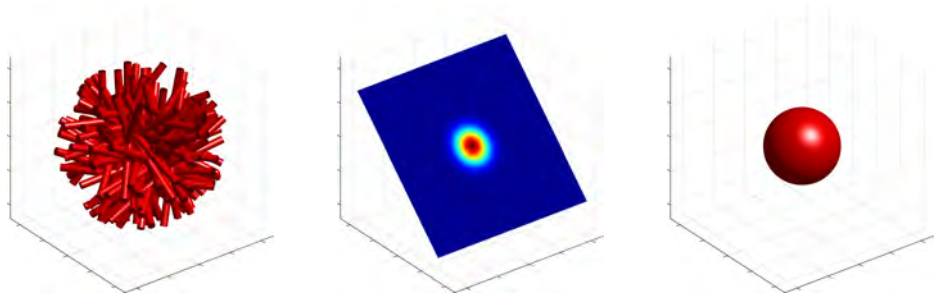

(a) environment (b) PDF (c) Isoprobability surface

Fig. 3.3: Hindered isotropic (Gaussian) diffusion. Image reproduced with permission from Jeurissen [2012].

In unordered tissues, the diffusion will be isotropic, i.e. it has no preferential direction. Hence, the ADC will be independent of the direction it is measured in. Like for free diffusion, the isoprobability surface of p will be a sphere (Fig. 3.3). However, since the molecule displacement is hindered, the radius of this sphere will be smaller.

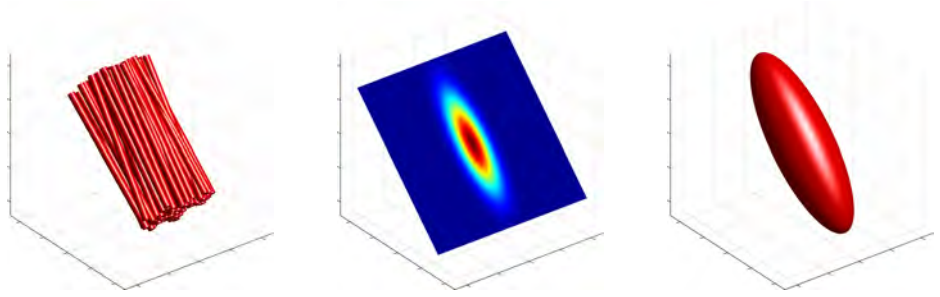

(a) environment (b) PDF (c) Isoprobability surface

Fig. 3.4: Anisotropic (Gaussian) diffusion. Image reproduced with permission from Jeurissen [2012].

Most biological tissues are highly structured. White matter for example consists of parallel axons which are organized into tightly packed nerve bundles. The molecules will rather diffuse parallel to the nerve bundles than perpendicular to them. Hence, the diffusion coefficient will be different along each direction, i.e. the tissue exhibits anisotropic diffusion. As a result, the diffusion can no longer be described by a single scalar diffusion coefficient and a more complex description

of the diffusion is needed. Under the assumption that the diffusion still follows a Gaussian distribution, the diffusion process can be described by a 3×3 tensor (Fig. 3.4):

$$p(\boldsymbol{r}) = \frac{1}{\sqrt{(4\pi t)^3 |\boldsymbol{D}|}} e^{\frac{\boldsymbol{r}^T \boldsymbol{D}^{-1} \boldsymbol{r}}{4r}} \tag{3.4}$$

with $\boldsymbol{D}$ the (apparent) diffusion tensor:

$$\boldsymbol{D} = \begin{bmatrix} D_{xx} & D_{xy} & D_{xz} \\ D_{xy} & D_{yy} & D_{yz} \\ D_{xz} & D_{yz} & D_{zz} \end{bmatrix}, \tag{3.5}$$

which is symmetric and positive definite. Note that since $\boldsymbol{D}$ is symmetric, it is completely defined by its six unique elements. The isoprobability surface of p (Eq. 3.4) takes the form of an ellipsoid (Fig. 3.4). When the diffusion tensor is used to represent isotropic diffusion, $\boldsymbol{D}$ becomes a diagonal matrix, in which the diagonal elements are the same and equal to the diffusion coefficient D.

3.4 Diffusion-weighted MRI

3.4.1 Diffusion-weighted acquisition

Even before the introduction of MR imaging, Stejskal and Tanner [1965] proposed a practical scheme to sensitize the MR signal for diffusion, by adding a pair of pulsed magnetic field gradients of the same polarity on each side of the 180° pulse of a spin echo sequence (Fig. 1.6 in section 1.3.5). In Fig. 3.5 a schematic overview of this Pulsed Gradient Spin-echo (PGSE) sequence is given. The two rectangular diffusion gradient pulses $\boldsymbol{g}(t)$ have an amplitude G ($\|\boldsymbol{g}(t)\| = G$), direction $\hat{\boldsymbol{g}} = \frac{\boldsymbol{g}}{G}$ and a duration δ. The time between the onset of the two gradient pulses is Δ. The first gradient pulse induces a position-dependent phase shift which is proportional to the strength and duration of the gradient:

$$\begin{aligned} \phi_1 &= \gamma \int_0^{\delta} \boldsymbol{g}(t) \cdot \boldsymbol{r}(t) dt \\ &= \gamma \delta G r'_{\boldsymbol{g}}, \end{aligned} \tag{3.6}$$

with $\boldsymbol{r}(t)$ the spin position, which is assumed to be constant during the pulse, and $r'_{\boldsymbol{g}}$ the projection of the spin position on the gradient direction $\hat{\boldsymbol{g}}$. The second gradient induces a similar position-dependent phase shift:

$$\begin{aligned} \phi_2 &= \gamma \int_{\Delta}^{\Delta+\delta} \boldsymbol{g}(t) \cdot \boldsymbol{r}(t) dt \\ &= \gamma \delta G r''_{\boldsymbol{g}}. \end{aligned} \tag{3.7}$$

Applying a 180° pulse between the two gradient pulses inverts the phase change that occurred prior to the 180° pulse. Hence, the resulting phase shift is given by:

$$\phi = \phi_2 - \phi_1 = \gamma \delta G (r''_{\boldsymbol{g}} - r'_{\boldsymbol{g}}). \tag{3.8}$$

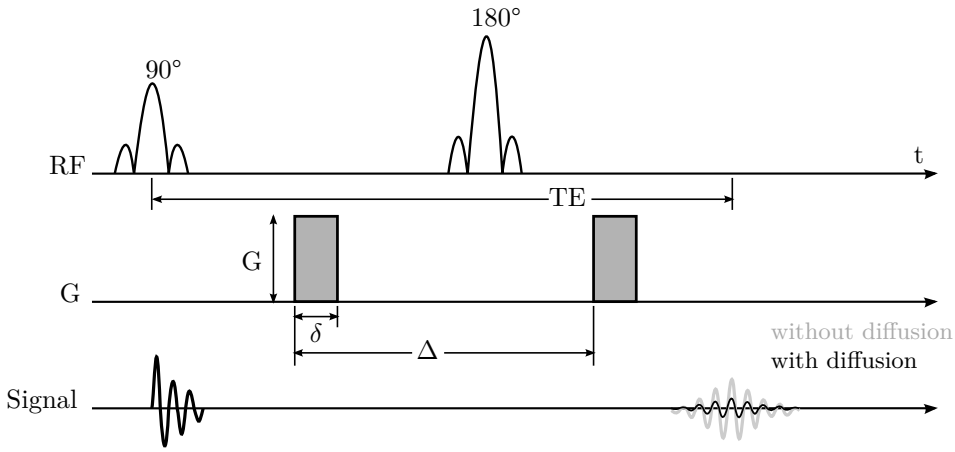

Fig. 3.5: Pulsed Gradient Spin-echo sequence: The gradient pulses induce a position-dependent phase shift. The phase shift of static spins induced by the first gradient is canceled by the second gradient. Each spin that diffuses during time Δ experiences a net phase shift, which is proportional to the distance the individual spin traveled. This net phase shift results in a loss of signal.

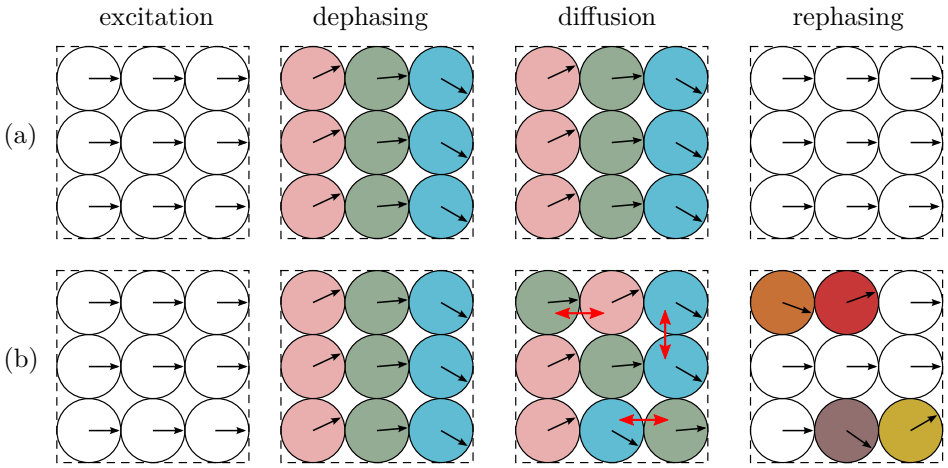

Fig. 3.6: Schematic representation of the diffusion-induced signal attenuation for (a) static spins, (b) moving spins. After excitation the spins dephase due to the diffusion-weighting gradient. Since the diffusion gradient is spatially varying, the spins will have a spatial dependent phase. Spins that diffuse in the orientation of the diffusion gradient will experience a different gradient magnitude during the second, rephasing diffusion gradient. Consequently, the spins will not be in phase, resulting in signal loss. If the spins are static, i.e. they do not diffuse in the direction of the diffusion gradient, they will be fully rephased after the second diffusion gradient.

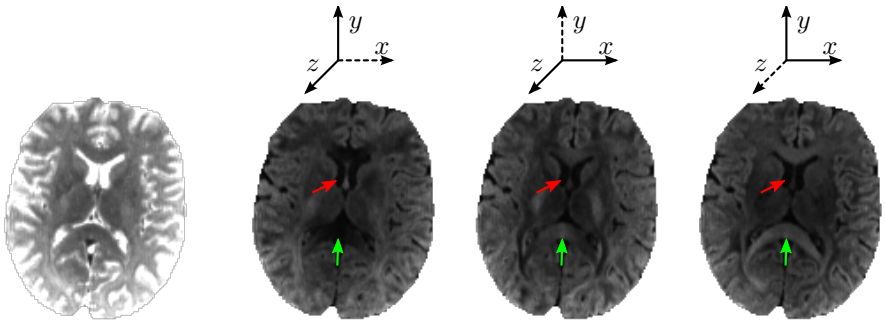

(a) non DW image (b) DW images

Fig. 3.7: Transversal slice of (a) a non DW image and (b) DW images. The diffusion gradient is applied in the x, y and z direction, respectively. In the DW images dark areas correspond with a high diffusivity. The red arrow indicates an area in the cerebrospinal fluid (CSF), which consists mostly (99%) of water. Hence, the diffusion in CSF is isotropic and the signal intensity will be similar independently of the diffusion direction. The green arrow indicates the corpus callosum, which is a white matter structure consisting of fiber bundles which are aligned along x (left-right). The signal loss is large when the diffusion gradient is applied in the x direction, while the area remains bright when the diffusion gradient in the directions perpendicular to the fiber bundles.

If the spins are static, i.e. do not undergo any diffusion along the gradient direction ($r''_{\boldsymbol{g}} = r'_{\boldsymbol{g}}$), the net phase shift ϕ will be zero (Fig. 3.6). The initial induced phase shift of spins that do undergo diffusion along the gradient direction during the time period Δ will not be fully canceled by the second phase shift (Fig. 3.6). Hence diffusing spins experience a net phase shift. The resulting phase incoherence among the spins causes a signal drop compared to the MR signal in absence of diffusion gradients, i.e. the non diffusion-weighted signal $S(0)$ (Fig. 3.7). The amplitude of the attenuated diffusion-weighted (DW) signal S is given by:

$$S = S(0)\langle e^{-i\phi}\rangle \tag{3.9}$$

with $\langle\cdot\rangle$ the ensemble average of the different phase shifts within a voxel.

3.4.2 Q-space

The signal attenuation $A(\boldsymbol{q})$ can be expressed as the 3D Fourier transform $\mathcal{F}$ of the diffusion probability density $p(\boldsymbol{r})$ [Stejskal and Tanner, 1965]:

$$A(\boldsymbol{q}) = \frac{S(\boldsymbol{q})}{S(0)} = \int_{\mathbb{R}^3} p(\boldsymbol{r}) e^{-i\boldsymbol{q}^T\boldsymbol{r}} d\boldsymbol{r} = \mathcal{F}[p(\boldsymbol{r})], \tag{3.10}$$

with $\boldsymbol{q}$ the q-vector:

$$\boldsymbol{q} = \gamma\delta\boldsymbol{g}. \tag{3.11}$$

The space of all possible 3D q-vectors is called the q-space. By sampling the diffusion signal along many q-vectors and performing an inverse 3D Fourier transform $\mathcal{F}^{-1}$, the PDF p can be reconstructed. This technique is also called q-space imaging [Callaghan et al., 1988].

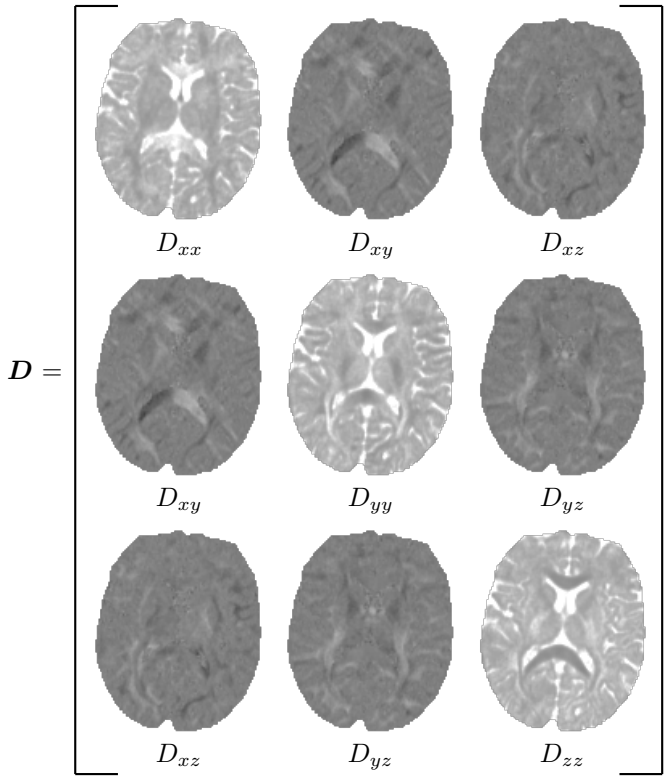

Fig. 3.8: Axial slices of the different diffusion tensor components.

3.5 Diffusion Tensor Imaging (DTI)

3.5.1 DTI model

As explained in section 3.3 the diffusion in an isotropic medium can be described by the diffusion tensor $\boldsymbol{D}$, which reflects the directional dependence of the diffusion properties. In contrast to the diffusion coefficient, the diffusion tensor reflects the underlying diffusion properties of the imaged subject, independently of the orientation of tissue to the gradient direction. The signal amplitude of a DW image can be written in function of the diffusion tensor $\boldsymbol{D}$ by [Basser et al., 1994]:

$$S(\boldsymbol{q}) = S(0)e^{-b\hat{\boldsymbol{g}}^T \boldsymbol{D} \hat{\boldsymbol{g}}}, \tag{3.12}$$

with b the diffusion weighting factor or b-value [Le Bihan et al., 1986]:

$$b = \gamma^2 \delta^2 (\Delta - \frac{1}{3}\delta) G^2, \tag{3.13}$$

and $(\Delta - \frac{1}{3}\delta)$ the diffusion time.

Using Eq. 3.12, which is widely known as the DTI model, the apparent diffusion tensor $\boldsymbol{D}$ can be estimated from a reference image and a set of DW images. In Fig. 3.8 axial slices of the individual components of the diffusion tensor are imaged. The diagonal elements of the diffusion tensor $\boldsymbol{D}$ correspond to the diffusivity along the three orthogonal axes. The off-diagonal elements correspond to the correlation between the displacements along the axes.

3.5.2 Acquisition

To be able to estimate the diffusion tensor, one needs a minimum of six DW images, acquired with the same b-value and different non-collinear diffusion gradients, in combination with a reference image. This reference image is preferably an image acquired without diffusion weighting [Basser et al., 1994]. The choice of diffusion strength and gradient direction influences the precision of the estimated diffusion tensor parameters. Hence, a lot of research has been done on these topics.

When the diffusion tensor is used to model the diffusion, a two-point estimate is preferable in terms of SNR [Jones et al., 1999]. It is suggested to acquire the reference image without diffusion weighting: $b = 0\,\mathrm{s/mm^2}$) and to acquire the DW images with a b-value around $1000\,\mathrm{s/mm^2}$ [Papadakis et al., 1999, Jones et al., 1999]. Although the diffusion tensor can be estimated from six DW images, it is suggested to acquire more of them, i.e. to oversample the q-space [Papadakis et al., 1999]. The most direct way to remove this directional bias is to sample more diffusion gradient directions, typically at least 30 unique, uniformly distributed directions [Jones, 2004]. This uniform distribution is obtained by uniformly distributing the directions over a unit sphere using an algorithm based on minimization of electrostatic repulsion [Jones et al., 1999].

3.5.3 Geometrical interpretation

The diffusion tensor can be decomposed into its real eigenvectors and eigenvalues:

$$\boldsymbol{D} = \boldsymbol{E}\boldsymbol{\Lambda}\boldsymbol{E}^{-1}, \tag{3.14}$$

with $\boldsymbol{E} = [\boldsymbol{e}_1\ \boldsymbol{e}_2\ \boldsymbol{e}_3]$ the three orthonormal eigenvectors, and

$$\boldsymbol{\Lambda} = \begin{bmatrix} \lambda_1 & 0 & 0 \\ 0 & \lambda_2 & 0 \\ 0 & 0 & \lambda_3 \end{bmatrix} \tag{3.15}$$

the positive eigenvalues [Hasan et al., 2001]. The eigenvalues correspond to the diffusivities along the principal axes of the diffusion tensor, which are given by the three eigenvectors. By convention the eigenvalues and eigenvectors are sorted according to a decreasing value of the eigenvalues: ($\lambda_1 \geq \lambda_2 \geq \lambda_3$). Consequently, the first eigenvector $\boldsymbol{e}_1$ describes the dominant diffusion direction. Given this interpretation, the diffusion tensor can be visualized as an ellipsoid (Fig. 3.9). The axes of the ellipsoid are given by the eigenvectors $\boldsymbol{e}_i$ and the ellipsoid's stretch along each axis is described by the eigenvalues λ_i. The ellipsoid corresponds to the isoprobability surface of the Gaussian diffusion model given in Eq. 3.4.

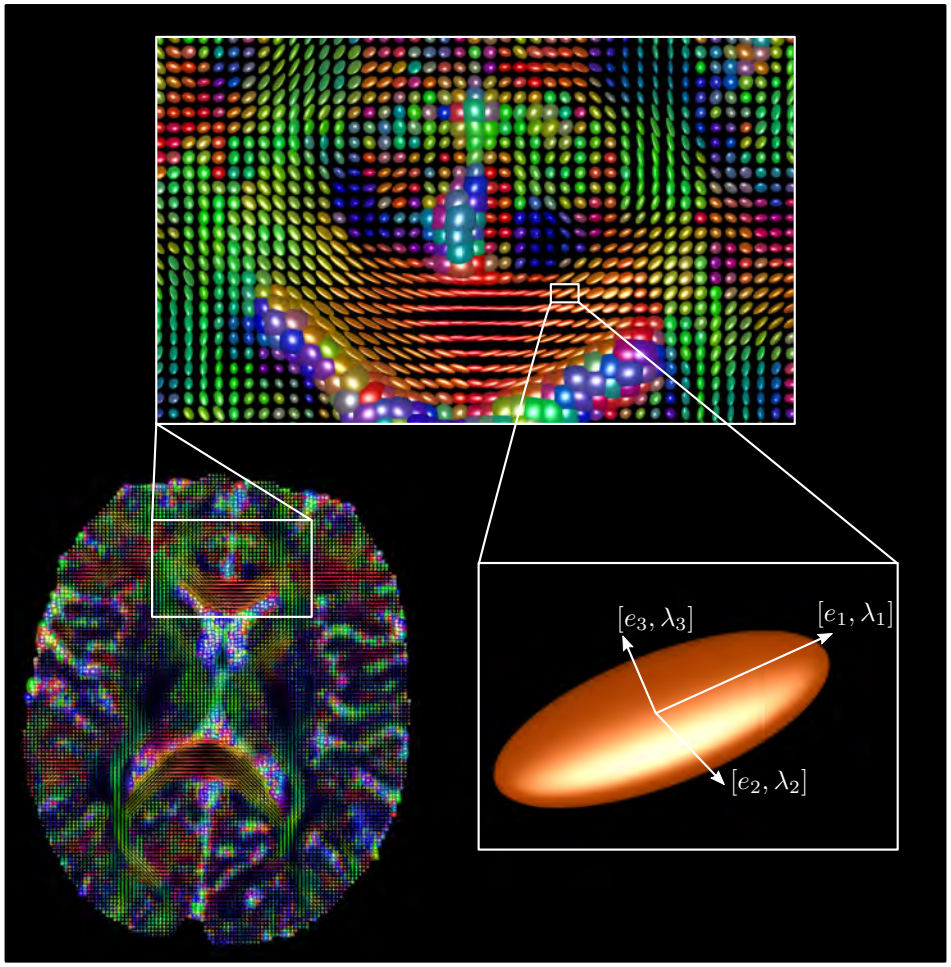

Fig. 3.9: Transversal slice in which the diffusion tensors are represented as ellipsoid. Each ellipsoid is uniquely determined by the eigenvectors and eigenvalues of the diffusion tensor they represent. The ellipsoids are color coded depending on the direction of the first eigenvector: left-right (red), anterior-posterior (green) and superior-posterior (blue).

3.5.4 Scalar invariants

Although the eigenvalues of the diffusion tensor can be compared and analyzed individually, the information is often combined into different rotationally invariant scalar measures that characterize the diffusion profile [Bahn, 1999]. Note that only the measures used in this thesis are mentioned.

- The **Mean diffusivity (MD)** (Fig. 3.10a) is the average diffusion coefficient:

$$\mathrm{MD} = \frac{\lambda_1 + \lambda_2 + \lambda_3}{3}. \tag{3.16}$$

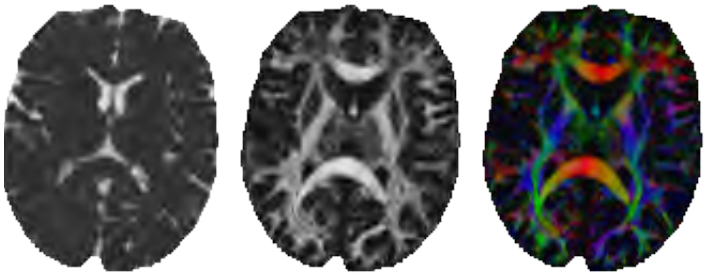

(a) MD (b) FA (c) DEC FA

Fig. 3.10: Overview of some of the scalar invariants derived from the diffusion tensor. The DEC FA map is color encoded for the principal diffusion direction: left-right (red), anterior-posterior (green) and superior-posterior (blue)

The MD can also be calculated by taking the sum of the diagonal tensor elements, i.e. the trace and divide it by three:

$$\mathrm{MD} = \frac{1}{3}\,\mathrm{trace}(\boldsymbol{D}) = \sum_{i=1}^{3} D_{ii}. \tag{3.17}$$

- **Fractional anisotropy (FA)** (Fig. 3.10b) is a measure of the degree of diffusion anisotropy. Since the FA is normalized, it can take values between zero (isotropic diffusion) and one (diffusion constrained along one single axis). The FA can either be calculated by taking the square root of the variance of the eigenvalues divided by the magnitude of the tensor [Basser, 1995]:

$$\mathrm{FA} = \sqrt{\frac{3}{2}\frac{(\lambda_1 - \mathrm{MD})^2 + (\lambda_2 - \mathrm{MD})^2 + (\lambda_3 - \mathrm{MD})^2}{\lambda_1^2 + \lambda_2^2 + \lambda_3^2}}. \tag{3.18}$$

or by [Ozarslan et al., 2005]

$$\mathrm{FA} = \sqrt{\frac{1}{2}\left(3 - \frac{1}{\mathrm{trace}(\boldsymbol{R}^2)}\right)}, \tag{3.19}$$

with R the unitless and normalized diffusion tensor:

$$\boldsymbol{R} = \frac{\boldsymbol{D}}{\mathrm{trace}(\boldsymbol{D})} \tag{3.20}$$

The FA map is often co-displayed with the orientation of the principal eigenvector in a directionally encoded color (DEC) FA map. The orientation of the principal eigenvector is represented by a direction encoding RGB-map, where red stands for left-right, green for anterior-posterior and blue for superior-inferior [Pajevic and Pierpaoli, 1999]. The intensity of the DEC FA map reflects the anisotropy (Fig. 3.10c).

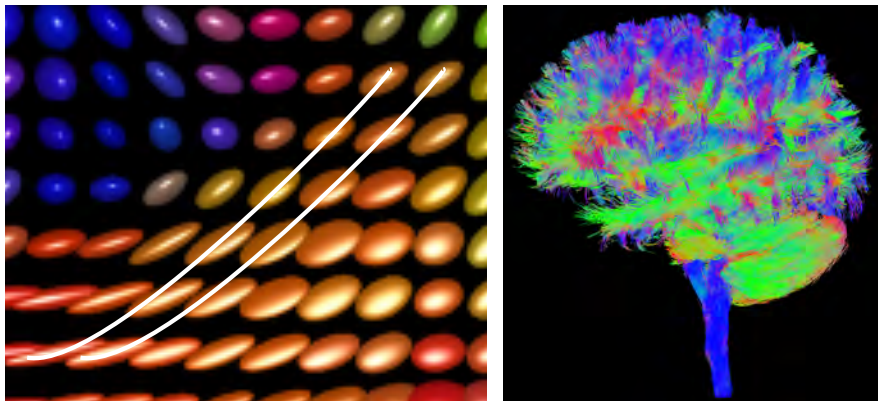

(a) (b)

Fig. 3.11: Example of deterministic tractography: (a) part of transversal slice (full slice in Fig. 3.9), (b) Sagittal view of full brain tractography, color encoded for the principal diffusion direction: left-right (red), anterior-posterior (green) and superior-posterior (blue).

3.5.5 Fiber tractography

Fiber tractography is a method for identifying and visualizing the neural connections, i.e. white matter tracts, in a non invasive way. Using the ability of DTI to reflect the underlying tissue structures, the local fiber orientation is measured in each voxels. These directions can be joined to reconstruct entire pathways and hence brain connections. A variety of fiber-tracking algorithms have been introduced [Mori and Van Zijl, 2002]. The most simple form is streamline or deterministic tractography. This technique consists of starting at a seed location and following the preferred direction $\boldsymbol{e}_1$ until the next voxel. The tracking can be continued in the new direction and is carried on until the entire pathway is traced (Fig. 3.11).

3.5.6 Applications

DTI is a powerful tool to characterize the structural integrity of neural tissue and to noninvasively trace neuronal tracts in the brain and spine. This has lead to many clinical application that have increased the diagnostic potential in neurological disorders [Sundgren et al., 2004, Lerner et al., 2014, Dong et al., 2003]. For example, DTI has been used to study patients with stroke [Werring et al., 2000] and tumors [Mori et al., 2002], neurodegenerative disorders such as epilepsy [Eriksson et al., 2001], alzheimer [Rose et al., 2000] and multiple sclerosis [Filippi et al., 2001], and neuropsychiatric disorders [Lim and Helpern, 2002] such as schizophrenia [Kubicki et al., 2007] and autism [Bernea-Goraly et al., 2004]. Furthermore, DTI and tractography are also used in neurosurgical planning [Nimsky et al., 2005]. In order to use DTI to evaluate pathological states in the brain, one should be familiar with the DTI characteristics of the normal brain. Therefore, DTI has been used extensively to study the brain development [Neil et al., 2002, Bui et al., 2006] and

maturation [Mukherjee et al., 2002]. Apart from brain imaging, DTI has also been applied successfully in cardiac and skeletal muscle [Dou et al., 2002b, Zaraiskaya et al., 2006].

3.6 Challenges and limitations

Although dMRI has a broad range of known applications, reliable diffusion data remains a challenging task [Jones and Cercignani, 2010, Le Bihan et al., 2006]. Only the challenges tackled in the following chapters are discussed here.

3.6.1 EPI distortions

DW images are typically acquired with EPI sequences because it allows to collect a full DW slice in a single shot and, hence, in a very short time. However, due to the very low bandwidth in the phase encoding direction, resonance frequency offsets cause misplacement of intensities by several voxels [Jezzard and Balaban, 1995]. Moreover, the distortions are non-linear, making it possible that the signal intensity from neighboring voxels collapses into a single voxel, resulting in pile-up of signal in one area and drop-outs of signal in the other [Jones and Cercignani, 2010]. The primary source of resonance frequency offsets are local magnetic field inhomogeneities. These inhomogeneities are produced by discontinuities in magnetic susceptibility, such as those occurring at tissue/air interfaces. Therefore, susceptibility or EPI distortions are typically observed near the sinuses.

EPI distortions can be corrected for by unwarping the distorted images using a deformation field or displacement map. This displacement map is computed from a field map (Fig. 3.12), which maps the off-resonance frequencies. Commonly, this field map is calculated from the phase difference between two images acquired with different echo times [Jezzard and Balaban, 1995]. Several other methods to acquire this field map have been proposed as well [Chen and Wyrwicz, 1999, Schmithorts et al., 2001].

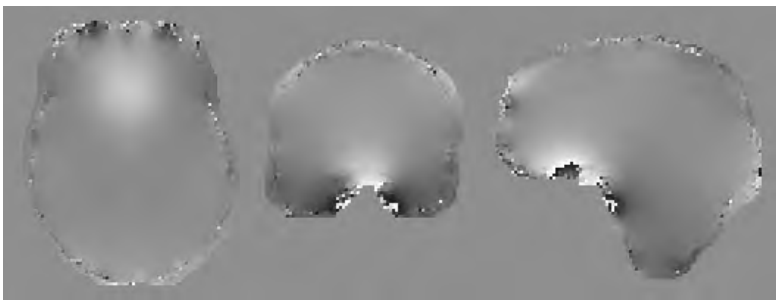

Fig. 3.12: Transversal, coronal, and sagittal slice of an acquired field map.

An alternative approach to correct for EPI distortions consists of acquiring the desired data set a second time, completely identically apart from an opposite phase encoding direction. Since the images have an opposite phase encoding, the distortions will be in opposite direction (Fig. 3.13a-b). These distorted images can

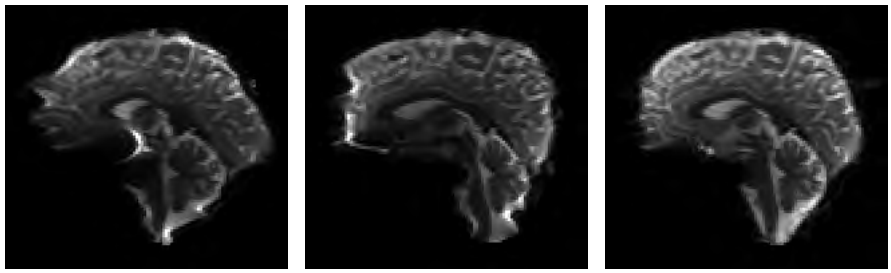

(a) (b) (c)

Fig. 3.13: (a) and (b) Sagittal slices of EPI images, acquired with opposite phase-encoding directions (anterior-posterior). (c) Axial slice of corrected image.

then be combined to a distortion-corrected image (Fig. 3.13c), without the loss of information [Andersson et al., 2003, Holland et al., 2010].

3.6.2 Motion

Motion of the subject while scanning is inevitable. Even when the subject itself would not move, there is still physiological motion, such as cardiac pulsation. While any MRI sequence is more or less prone to motion artifacts, dMRI is exquisitely sensitive to motion. In dMRI, the signal is sensitized to the microscopic motion of the water molecules. In the presence of macroscopic motion, the spins experience large displacements (10 to 100 times larger than those induced by diffusion). This results in large random phase shifts, introducing ghosting, blurring and signal loss, thereby severely degrading the image quality [Skare and Andersson, 2001, Dou et al., 2002a].

To minimize the motion sensitivity, DW images are commonly acquired with fast sequences such as single-shot EPI, which fully samples the k-space at once. Additionally, after acquisition, head motion is often corrected for by realigning the DW images, typically to a non DW image, using a rigid registration algorithm [Netsch and Muiswinkel, 2004]. However, the differences in contrast between the images, the low spatial resolution and low SNR make the alignment a challenging task. Moreover, the DW images also contain orientational information. Thus, each rotation applied to the DW image, also has to be applied to the diffusion gradient direction [Leemans and Jones, 2009].

3.6.3 Eddy currents

When the diffusion gradients are switched on and off, the time-varying magnetic field generates electrical currents (eddy currents) in nearby conducting media. The eddy currents generate local magnetic field gradients that will either add to or subtract from the gradients that are used for spatial encoding. As a result, the actual gradient profiles that the spins in the imaged subject will experience, differs from those programmed to produce and reconstruct the image. This error in the gradients leads to geometric distortions in the final images [Jezzard et al., 1998].

In most acquisition methods, the eddy current effects are self-compensated because the spatial encoding gradients are applied for short periods and the rising and falling edges of the gradients are close together in time. Relatively, diffusion gradients are on during a longer time period, separating the rising and falling parts of the gradient waveform, so that the eddy currents are no longer self-compensated [Jones and Cercignani, 2010].

Generally, eddy currents are minimized at the acquisition stage [Reese et al., 2003], however, residual eddy currents will remain. A common strategy to correct for the effect of eddy currents is by realigning the DW images to a non DW image using affine registration algorithms [Netsch and Muiswinkel, 2004]. Typically, the eddy current correction is combined with the motion correction and one global affine transformation is used to correct for both.

3.6.4 Trade-off between SNR, acquisition time and spatial resolution

Since in dMRI one measures signal attenuation, DW images inherently have a relatively low SNR. In DTI, low SNR in the DW images does not only lead to imprecision in the measured diffusivity but also leads to systematic inaccuracies in the FA [Pierpaoli and Basser, 1996]. Furthermore, multiple DW images are required to model the diffusion, leading to long acquisition times. Thus, to obtain reasonable SNR, DW images are often acquired at a low spatial resolution. In a clinical setting, the typical spatial resolution will be ranging from 2 to 3 mm isotropic [Alexander, 2007]. Given that the diameter of an axon is of the order of $1\,\mu m - 20\,\mu m$, large partial volume effects will occur [Alexander, 2007, Oouchi et al., 2007]. In voxels consisting of a mixture of signals from different anatomical structures, the DTI model is incapable of describing the fiber orientations within that one voxel [Tuch et al., 2002]. Increasing the spatial resolution would reduce partial volume effects and thereby enable resolving finer structures and smaller bundles of axons.

A variety of methods have been developed to improve the trade-off between spatial resolution, acquisition time and SNR in dMRI. In track density imaging (TDI) the spatial resolution is enhanced using post-processing methods based on diffusion MRI fiber-tracking [Calamante et al., 2010]. The high resolution track density maps are created through counting the number of tracts present in each element of a sub-voxel grid. Although this method does enhance the spatial resolution, the resulting high resolution images can only be used qualitatively to visualize smaller structures and not quantitatively [Calamante, 2016]. The acquisition of the DW images can be speeded up by using parallel imaging techniques or simultaneous multi-slice acquisition. Parallel imaging works by acquiring a reduced amount of k-space data with an array of receiver coils [Blaimer et al., 2004, Deshmane et al., 2012]. These undersampled data can be acquired more quickly, but the undersampling leads to aliased images. One of several parallel imaging algorithms can then be used to reconstruct artifact-free images from either the aliased images (SENSE-type reconstruction [Pruessmann et al., 1999]) or from the undersampled data (GRAPPA-type reconstruction [Griswold et al., 2002]). In simultaneous multi-slice [Setsompop et al., 2012] several slices are excited at once.

With standard 2D k-space encoding alone, the images from simultaneously excited slices are not distinguishable. Nonetheless, the use of an RF receive coil array can provide the extra spatial encoding that will allow these images to be separated [Feinberg and Setsompop, 2013].

3.6.5 Beyond DTI

A recent study has shown that, at current resolution, the DTI model is inadequate in the majority of white matter voxels as result of partial volume effects, posing significant problems for DTI fiber tractography and the interpretation of DTI integrity metrics [Jeurissen et al., 2013]. One of the key limitations of DTI is that it can only recover a single fiber orientation in each voxel, since it can only model Gaussian diffusion and the Gaussian function is not equipped to deal with multiple fiber configurations. This limitation is not only a major obstacle for tractography, but also has a large impact on the scalar measures derived from the tensor [Alexander et al., 2001].

To deal with these issues, a numerous amount of more complex models and techniques have been proposed, such as multiple-component DTI [Pasternak et al., 2006, Alexander and Barker, 2005, Chen et al., 2004], High-Angular-Resolution DW Imaging (HARDI) [Frank, 2002], Q-Ball Imaging (QBI) [Tuch, 2004, Perrin et al., 2005, Descoteaux et al., 2007], Diffusion spectrum Imaging [Wedeen et al., 2005, 2008], ... Although these techniques might provide more accurate results, they often come at the cost of long acquisition times or have strong demands on the magnetic field gradient hardware. For a more detailed overview of these methods the interested reader is referred to literature [Jones, 2011, Johansen-Berg and Behren, 2009]

Bibliography

A.L. Alexander, K.M. Hasan, M. Lazar, J.S. Tsuruda, and D.L. Parker. Analysis of partial volume effects in diffusion-tensor MRI. *Magnetic Resonance in Medicine*, 45(5):770–780, 2001.

D.C. Alexander. Axon radius measurements in vivo from diffusion MRI: a feasibility study. In *Proceedings of the IEEE International Conference on Computer Vision*, volume 11, pages 1–8, Rio de Janeiro, Brazil, 2007.

D.C. Alexander and G.J. Barker. Optimal imaging parameters for fibre-orientation estimation in diffusion MRI. *NeuroImage*, 27(2):357–367, 2005.

J.L.R. Andersson, S. Skare, and J. Ashburner. How to correct susceptibility distortions in spin-echo echo-planar images: Application to diffusion tensor imaging. *NeuroImage*, 20(2):870–888, 2003.

M.M. Bahn. Comparison of scalar measures used in magnetic resonance diffusion-tensor imaging. *Journal of Magnetic Resonance*, 139(1):1–7, 1999.

P.J. Basser. Inferring microstructural features and the physiological state of tissues from diffusion-weighted images. *NMR in Biomedicine*, 8(7):333–344, 1995.

P.J. Basser, J. Mattiello, and D. LeBihan. Estimation of the effective self-diffusion tensor from the NMR spin echo. *Journal of Magnetic Resonance Series B*, 103 (3):247, 1994.

N. Bernea-Goraly, H. Kwon, V. Menon, S. Eliez, L. Lotspeich, and A.L. Reiss. White matter structure in autism: preliminary evidence from diffusion tensor imaging. *Biological psychiatry*, 55(3):323–326, 2004.

M. Blaimer, F. Breuer, M. Mueller, R.M. Heidemann, M.A. Griswold, and P.M. Jakob. SMASH, SENSE, PILS, GRAPPA: how to choose the optimal method. *Topics in Magnetic Resonance Imaging*, 15(4):223–236, 2004.

R. Brown. A brief account of microscopical observations made in the month on June, July and August 1827 on the particles contained in the pollen of plants and on the general existence of active molecules in organic and inorganic bodies. *Philosophical Magazine*, 4(21):161–173, 1828.

T. Bui, J.L. Daire, F. Chalard, I. Zaccaria, C. Alberti, M. Elmaleh, C. Garel, D. Luton, N. Blanc, and G. Sebag. Microstructural development of human brain assessed in utero by diffusion tensor imaging. *Pediatric Radiology*, 36(11): 1133–1140, 2006.

F. Calamante. Super-Resolution Track Density Imaging: Anatomic Detail versus Quantification. Technical report, 2016.

F. Calamante, J.D. Tournier, G.D. Jackson, and A. Connelly. Track-density imaging (TDI): super-resolution white matter imaging using whole-brain track-density mapping. *NeuroImage*, 53(4):1233–1243, 2010.

P.T. Callaghan, C.D. Eccles, and Y. Xia. NMR microscopy of dynamic displacements: k-space and q-space imaging. *Journal of Physics E: Scientific Instruments*, 21(8):820, 1988.

N. Chen and A.M. Wyrwicz. Correction for EPI distortions using multiecho gradient-echo imaging. *Magnetic Resonance in Medicine*, 41(6):1206–1213, 1999.

Y. Chen, W. Guo, Q. Zeng, G. He, B.C. Vermure, and W. Liu. Recovery of intra-voxel structure from HARD DWI. In *Proceedings of the IEEE International symposium on Biomedical Imaging*, volume 2, pages 1028–1031, Washington, DC, USA, 2004.

M. Descoteaux, E. Angelino, S. Fitzgibbons, and R. Deriche. Regularized, fast, and robust analytical Q-ball imaging. *Magnetic Resonance in Medicine*, 58(3): 497–510, 2007.

A. Deshmane, V. Gulani, M.A. Griswold, and N. Seiberlich. Parallel MR imaging. *Journal of Magnetic Resonance Imaging*, 36(1):55–72, 2012.

Q. Dong, R.C. Welsh, T.L. Chenevert, R.C. Carlos, P. Maly-Sundgren, D.M. Gomez-Hassan, and S.K. Mukherji. Clinical applications of diffusion tensor imaging. *Journal of Magnetic Resonance Imaging*, 19(1):6–18, 2003.

J. Dou, T.G. Reese, W-.Y.I. Tseng, and V.J. Wedeen. Cardiac diffusion MRI without motion effects. *Magnetic Resonance in Medicine*, 48(1):105–114, 2002a.

J. Dou, T.G. Reese, W.Y.I. Tseng, and V.J. Wedeen. Cardiac diffusion MRI without motion effects. *Magnetic Resonance in Medicine*, 48(1):105–114, 2002b.

A. Einstein. Über die von der molekularkinetischen Theorie der Wärme geforderte Bewegung von in ruhenden Flüssigkeiten suspendierten Teilchen. *Annalen der Physik*, 322(8):549–560, 1905.

S. Eriksson, F.J. Rugg-Gunn, M.R. Symms, G.J. Barker, and J.S. Duncan. Diffusion tensor imaging in patients with epilepsy and malformations of cortical development. *Brain*, 124(3):617–626, 2001.

D.A. Feinberg and K. Setsompop. Ultra-fast MRI of the human brain with simultaneous multi-slice imaging. *Journal of Magnetic Resonance*, 229:90–100, 2013.

A. Fick. On liquid diffusion. *Philosophical Magazine*, 10(63):30–39, 1855.

M. Filippi, M. Cercignani, M. Inglese, and M.A. Horsfield. Diffusion tensor magnetic resonance imaging in multiple sclerosis. *Neurology*, 56(3):304–311, 2001.

L.R. Frank. Characterization of anisotropy in high angular resolution diffusion-weighted MRI. *Magnetic Resonance in Medicine*, 47(6):1083–1099, 2002.

M.A. Griswold, P.M. Jakob, R.M. Heidemann, M. Nittka, V. Jellus, J. Wang, B. Kiefer, and A. Haase. Generalized autocalibrating partially parallel acquisitions (GRAPPA). *Magnetic Resonance in Medicine*, 47(6):1202–1210, 2002.

K.M. Hasan, P.J. Basser, D.L. Parker, and A.L. Alexander. Analytical computation of the eigenvalues and eigenvectors in DT-MRI. *Journal of Magnetic Resonance*, 152(1):41–47, 2001.

D. Holland, J.M. Kuperman, and A.M. Dale. Efficient correction of inhomogeneous static magnetic field-induced distortion in echo planar imaging. *NeuroImage*, 50 (1):1–18, 2010.

B. Jeurissen. *Improved analysis of brain connectivity using high angular resolution diffusion MRI.* PhD thesis, 2012.

B. Jeurissen, A. Leemans, J.D. Tournier, D.K. Jones, and J. Sijbers. Investigating the prevalence of complex fiber configurations in white matter tissue with diffusion magnetic resonance imaging. *Human Brain Mapping*, 34(11):2747–2766, 2013.

P. Jezzard and R.S. Balaban. Correction for geometric distortion in echo planar imaging from B0 field variations. *Magnetic Resonance in Medicine*, 34(1):65–73, 1995.

P. Jezzard, A.S. Barnett, and C. Pierpaoli. Characterization of and correction for eddy current artifacts in echo planar diffusion imaging. *Magnetic Resonance in Medicine*, 39(5):801–812, 1998.

H. Johansen-Berg and T.E.J. Behren. *Diffusion MRI: From Quantitative Measurement to In vivo Neuroanatomy*. Academic Press, Cambridge, 2009.

D.K. Jones. The Effect of Gradient Sampling Schemes on Measures Derived from Diffusion Tensor MRI: A Monte Carlo Study. *Magnetic Resonance in Medicine*, 51(4):807–815, 2004.

D.K. Jones. *Diffusion MRI: Theory, Methods, and Applications*. Oxford University Press, New York, 2011.

D.K. Jones and M. Cercignani. Twenty-five pitfalls in the analysis of diffusion MRI data. *NMR in Biomedicine*, 23(7):803–20, 2010.

D.K. Jones, M.A. Horsfield, and A. Simmons. Optimal strategies for measuring diffusion in anisotropic systems by magnetic resonance imaging. *Magnetic Resonance in Medicine*, 42(3):515–525, 1999.

M. Kubicki, R. McCarley, C.F. Westin, H.J. Park, S. Maier, R. Kikinis, F.A. Jolesz, and M.E. Shenton. A review of diffusion tensor imaging studies in schizophrenia. *Journal of psychiatric research*, 41(1):15–30, 2007.

D. Le Bihan, E. Breton, D. Lallemand, P. Grenier, E. Cabanis, and M. Lavel-Jeantet. MR imaging of intravoxel incoherent motions: application to diffusion and perfusion in neurlogical disorders. *Radiology*, 131(2):401, 1986.

D. Le Bihan, C. Poupon, A. Amadon, and F. Lethimonnier. Artifacts and pitfalls in diffusion MRI. *Journal of Magnetic Resonance Imaging*, 24(3):478–488, 2006.

A. Leemans and D.K. Jones. The B-matrix must be rotated when correcting for subject motion in DTI data. *Magnetic Resonance in Medicine*, 61(6):1336–1349, 2009.

A. Lerner, M.A. Mogensen, P.E. Kim, M.S. Shiroishi, D.H. Hwang, and L. Meng. Clinical Applications of Diffusion Tensor Imaging. *World Neurosurgery*, 82(1-2): 96–109, 2014.

K.O. Lim and J.A. Helpern. Neuropshyciatric applications of DTI - a review. *NMR in Biomedicine*, 15(7-8):587–593, 2002.

S. Mori and P. Van Zijl. Fiber tracking: principles and strategies. *NMR in Biomedicine*, 15(7):468–480, 2002.

S. Mori, K. Frederiksen, P. van Zijl, B. Stieltjes, M.A. Kraut, M. Solaiyappan, and M.G. Pomper. Brain white matter anatomy of tumor patients evaluated with diffusion tensor imaging. *Annals of Neurology*, 51(3):377–380, 2002.

P. Mukherjee, P. Miller, J.S. Shimony, J.V. Philip, D. Nehra, A.Z. Snyder, T.E. Conturo, J.J. Neil, and R.C. McKinstry. Diffusion-tensor MR imaging of gray and white matter development during normal human brain maturation. *American Journal of Neuroradiology*, 23(9):1445–1456, 2002.

J. Neil, J. Miller, P. Mukherjee, and P.S. Huppi. Diffusion tensor imaging of normal and injured developing human brain - a technical review. *NMR in Biomedicine*, 15(7-8):543–552, 2002.

T. Netsch and A. Muiswinkel. Quantitative evaluation of image-based distortion correction in diffusion tensor imaging. *IEEE Transactions on Medical Imaging*, 23(7):789–798, 2004.

C. Nimsky, O. Ganslandt, P. Hastreiter, R. Wang, T. Benner, A.G. Sorensen, and R. Fahlbusch. Preoperative and intraoperative diffusion tensor imaging-based fiber tracking in glioma surgery. *Neurosurgery*, 56(1):130–138, 2005.

H. Oouchi, K. Yamada, K. Sakai, O. Kizu, T. Kubota, H. Ito, and T. Nishimura. Diffusion anisotropy measurement of brain white matter is affected by voxel size: Underestimation occurs in areas with crossing fibers. *American Journal of Neuroradiology*, 28(6):1102–1106, 2007.

E. Ozarslan, B.C. Vemurci, and T.H. Mareci. Generalized scalar measures for diffusion MRI using trace, variance, and entropy. *Magnetic Resonance in Medicine*, 53(4):866–876, 2005.

S. Pajevic and C. Pierpaoli. Color schemes to represent the orientation of anisotropic tissues from diffusion tensor data: Application to white matter fiber tract mapping in the human brain. *Magnetic Resonance in Medicine*, 42(3):526–540, 1999.

N.G. Papadakis, D. Xing, G.C. Houston, J.M. Smith, M.I. Smith, M.F. James, A.A. Parson, C.L.H. Huang, L.D. Hall, and T.A. Carpenter. A study of rotationally invariant and symmetric indices of diffusion anisotropy. *Magnetic Resonance in Medicine*, 17(6):881–892, 1999.

O. Pasternak, N. Sochen, and Y. Assaf. PDE based estimation and regularization of multiple diffusion tensor fields. In *Visualization and image processing of tensor fields*. Springer, Berlin, 2006.

M. Perrin, C. Poupon, B. Rieul, P. Leroux, A. Constantinesco, J.F. Mangin, and D. LeBihan. Validation of q-ball imaging with a diffusion fibre-crossing phantom on a clinical scanner. *Philosophical Transcations of the Royal Society of London B: Biological Sciences*, 360(1457):881–91, 2005.

C. Pierpaoli and P.J. Basser. Towards a quantitative assesment of diffusion anisotropy. *Magnetic Resonance in Medicine*, 36(6):893–906, 1996.

K.P. Pruessmann, M. Weiger, M.B. Scheidegger, and P. Boesiger. SENSE: Sensitivity encoding for fast MRI. *Magnetic Resonance in Medicine*, 42(5):952–962, 1999.

T.G. Reese, O. Heid, R.M. Weisskoff, and V.J. Wedeen. Reduction of eddy-current-induced distortion in diffusion MRI using a twice-refocused spin echo. *Magnetic Resonance in Medicine*, 49(1):177–182, 2003.

S.E. Rose, F. Chen, J.B. Chalk, F.O. Zelaya, W.E. Strugnell, M. Benson, J. Semple, and D.M. Doddrel. Loss of connectivity in Alzheimer's disease: an evaluation of white matter tract integrity with colour coded MR diffusion tensor imagin. *Journal of Neurology, Neurosurgery & Psychiatry*, 69(4):528–530, 2000.

V.J. Schmithorts, B.J. Dardzinski, and S.K. Holland. Simultaneous correction of ghost and geometric distortion artifacts in EPI using multiecho reference scan. *IEEE Transactions on Medical Imaging*, 20(6):535–539, 2001.

K. Setsompop, J. Cohen-Adad, B.A. Gagoski, T. Raij, A. Yendiki, B. Keil, V.J.. Wedeen, and L.L. Wald. Improving diffusion MRI using simultaneous multi-slice echo planar imaging. *NeuroImage*, 63(1):569–580, 2012.

S. Skare and J.L.R. Andersson. On the effects of gating in diffusion imaging of the brain using single shot EPI. *Magnetic Resonance Imaging*, 19(8):1125–1128, 2001.

E.O. Stejskal and J.E. Tanner. Spin diffusion measurements: spin echoes in the presence of a time dependent field gradient. *The journal of chemical physics*, 42 (1):288–292, 1965.

P.C. Sundgren, Q. Dong, D. Gomez-Hassan, S.K. Mukherji, P. Maly, and R. Welsh. Diffusion tensor imaging of the brain: review of clinical applications. *Diagnostic Radiology*, 46(5):339–350, 2004.

P. Tofts. *Quantitative MRI of the Brain*. John Wiley & Sons, New York, 2005.

D.S. Tuch. Q-ball imaging. *Magnetic resonance in Medicine*, 52(6):1358–1372, 2004.

D.S. Tuch, T.G. Reese, M.R. Wiegell, N. Makris, J.W. Belliveau, and J. Van Wedeen. High angular resolution diffusion imaging reveals intravoxel white matter fiber heterogeneity. *Magnetic Resonance in Medicine*, 48(4):577–582, 2002.

V.J. Wedeen, P. Hagmann, W.Y. Tseng, T.G. Reese, and R.M. Weisskoff. Mapping complex tissue architecture with diffusion spectrum magnetic resonance imaging. *Magnetic Resonance in Medicine*, 54(6):1377–1386, 2005.

V.J. Wedeen, R.P. Wang, J.D. Schmahmann, T. Benner, W.Y.I. Tseng, G. Dai, D.N. Pandya, P. Hagmann, H. D'Arceuil, and A.J. Crespigny. Diffusion spectrum magnetic resonance imaging (DSI) tractography in corssing fibers. *NeuroImage*, 41(4):1267–1277, 2008.

D.J. Werring, A.T. Toosy, C.A. Clark, G.J. Parker, G.J. Barker, D.H. Miller, and A.J. Thompson. Diffusion tensor imaging can detect and quantify corticospinal tract degeneration after stroke. *Journal of Neurology, Neurosurgery & Psychiatry*, 69(2):269–272, 2000.

T. Zaraiskaya, D. Kumbhare, and M.D. Noseworthy. Diffusion tensor imaging in evaluation of human skeletal muscle injury. *Journal of Magnetic Resonance Imaging*, 24(2):402–408, 2006.

Part II

Super-Resolution Reconstruction

4

Super-resolution reconstruction

Contents

4.1 Introduction

In many medical applications, high resolution 3D images are required for early and accurate diagnosis. However, due to acquisition time constraints and hardware limitations, achieving this high spatial resolution is not always feasible. Therefore, several image processing techniques to augment the spatial resolution a posteriori have been introduced [Kang and Chaudhuri, 2003, Park et al., 2003, Farsiu et al., 2004, Greenspan, 2009, Van Reeth and Tham, 2012]. On a standard MRI scanner, a basic interpolation (zero-filling) is available to decrease the voxel size of the images. Although this facilitates the visualization, no new information is introduced into the image [Bernstein et al., 2001]. Super-resolution reconstruction (SRR) techniques give the opportunity to efficiently improve the spatial resolution of the acquired images [Plenge et al., 2012]. In SRR, an unaliased high resolution image is estimated from a series of low resolution images. The low resolution images are acquired in such a way that each low resolution image contributes new information to the reconstruction process. It is important to note that there is a difference between SRR and SR restoration. Although the goal of both SR concepts is to recover high-frequency information that is lost or degraded during the image acquisition, the causes of the loss of high-frequency information are different [Kang and Chaudhuri, 2003]. SR restoration, which was introduced in optics, refers to algorithms that mainly operate on a single image and attempt to recover information beyond the diffraction cutoff frequency by extrapolation. While the SR reconstruction method tries to recover the high-frequency components corrupted by aliasing. When talking about SR in this thesis we are referring to SRR based methods.

Several different methodologies are developed in order to recover the high resolution information from the acquired low resolution data. These methodologies can be classified into two different techniques [Shilling, 2009]: frequency domain [Kim and Su, 1993, Kim et al., 1990, Tsai and Huang, 1984] and spatial domain [Van Reeth and Tham, 2012]. The methods developed in this thesis are based in the spatial domain, as such only SR methods working in the spatial domain will be discussed in this chapter. First we will give a short recap of the resolution challenges in MRI and introduce SRR as a possible solution. Next, we explain a specific SRR method for structural MRI, on which the methods developed in this thesis are based.

4.2 Resolution challenges in MRI

As discussed in section 1.5, in each MRI experiment a trade-off has to be made between the spatial resolution, the SNR and the acquisition time. Although a high resolution 3D image is desired, 3D image acquisition is not always effective or possible. Therefore, it is most common to acquire a set of 2D slices, i.e. a multi-slice image. Acquiring this image at high resolution might allow observation of smaller details, but typically reduces the SNR, while a certain level of SNR is required to distinguish the signal of interest from the noise. The SNR could be improved by averaging over multiple acquisition of the signal, however this increases the acquisition time, while this is costly, uncomfortable for the patient and induces motion artifacts in the images. Moreover, the slice thickness is determined by the

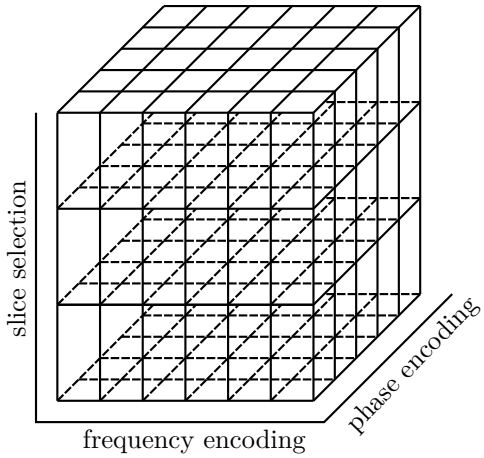

Fig. 4.1: Schematic representation of low resolution image, which has a high isotropic in-plane resolution and a slice thickness larger than this in-plane resolution.

slice selection pulse, which in turn is determined by hardware limitations coupled with pulse sequence timing considerations, making the acquisition of thin slices not always feasible. As a result, multi-slice images are often acquired with a high in-plane resolution and thicker slices (Fig. 4.1). However, these thick slices lead to large partial volume effects (Fig. 4.2), which arise when two different tissues occur within a single voxel.

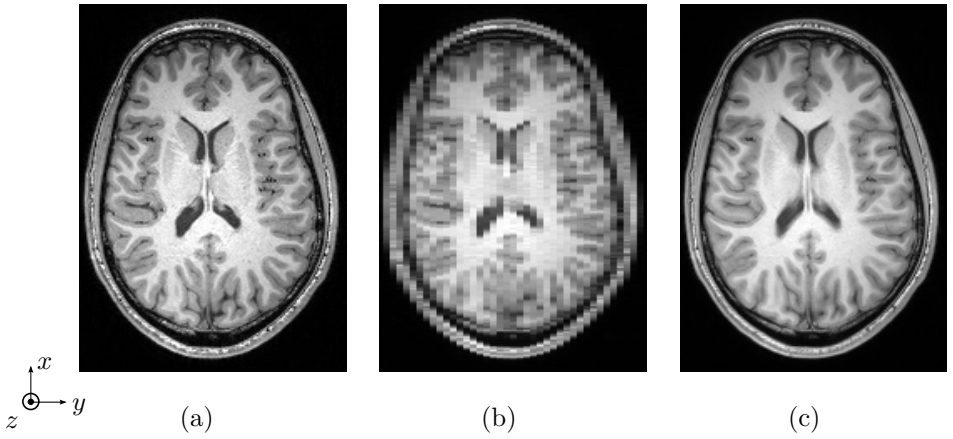

Fig. 4.2: (a) A high resolution and (b) low resolution image acquired with slice selection along y (c) low resolution image acquired with slice selection along z. Due to partial volume effects the borders between different tissues are blurred in the low resolution image.

The trade-off between spatial resolution, acquisition time and SNR can be improved at acquisition level by techniques such as parallel MRI [Pruessmann et al., 1999, Blaimer et al., 2004, Griswold et al., 2002], PROPELLER [Pipe, 1999], compressed sensing [Lustig et al., 2007] and simultaneous multi slice [Setsompop et al., 2012, Feinberg and Setsompop, 2013]. An interesting complementary alternative is to use SRR.

4.3 Super-resolution reconstruction

In SRR several distinct low resolution observations of the same object are combined to reconstruct a high resolution image. The first imaging domain in which SR algorithms were applied was video processing [Tsai and Huang, 1980], where a high resolution frame was created from consecutive frames where the object was moved by a subpixel amount through a simple translation. The first application of SR to MRI was reported in a patent filed in 1997 [Fiat, 1997].

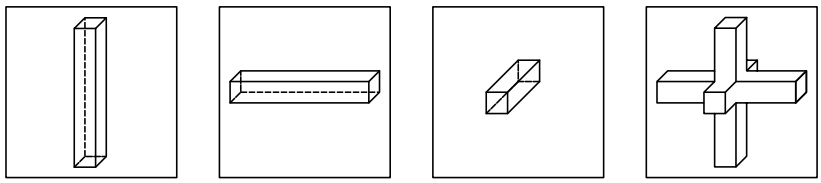

Fig. 4.3: The low resolution k-space boundaries for the SR experiments by Herment et al. [2003]. (a-c) Sampled k-space data from the three 3D MRI acquisitions, (d) effective k-space sampling boundary.

One of the first experiments with SR in MRI was performed by Herment et al. [2003]. Their method combines partial k-space data, which are successively acquired by rotating the acquisition matrix of highly anisotropic 3D magnetic resonance angiography (MRA) volumes (Fig. 4.3a-c). To reconstruct the image, the unknown regions contained in the compound volume of the three k-space data volumes (Fig. 4.3d) was zero-filled. The other parts of k-space were weighted by the number of times the k-space region had been acquired. Next, a Fourier transformation was used to calculate the high resolution image. The results showed an improvement in the spatial resolution, but only in the directions shared by the high-frequency k-space data samples. Making their method useful for imaging tissues with specific direction such as arteries, but not for brain imaging, where isotropic resolution is desired. Since then, several attempts have been made to improve both the in-plane and the through-plane resolution of MR images.

4.3.1 In-plane improvement

The earlier SR methods [Peled and Yeshurun, 2001, Carmi et al., 2006] focussed on the improvement of the in-plane resolution of MR images. To achieve this in-plane resolution improvement, several images with a subpixel shifted FOV in the in-plane directions were acquired (Fig. 4.4). Next, SR methods were used to

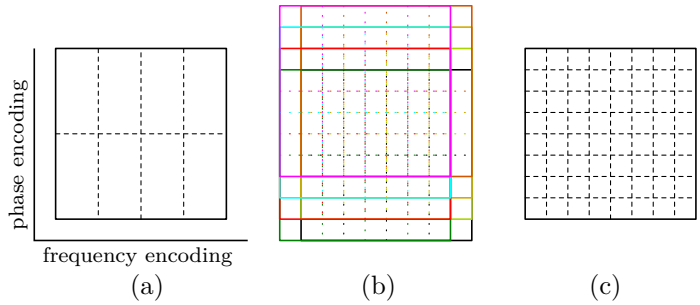

Fig. 4.4: SR experiment by Peled and Yeshurun [2001]. (a) Configuration for one low resolution image, pixel size: 2×4 high resolution pixel units. (b) Eight low resolution images with subpixel spatial shifts (c) High resolution scan. Note that only the frequency and phase encoding direction are shown

produce a high resolution image. However, the validity of these methods was questioned by Scheffler [2002]. MRI images are Fourier-encoded in the frequency domain (k-space) and the FOV in the spatial domain is directly controlled by the choice of $\frac{1}{\Delta k}$ (see section 1.5.1). Consequently, if the resolution and FOV of the low resolution images are identical, then the locations of the frequency samples must be identical. The subpixel shift of the FOV in the in-plane direction corresponds with a linear phase modulation in the k-space. As a result, the shifted images acquire no new frequency content. Since the images contain the same information, except for measurement noise, it is not possible to improve the resolution. Greenspan et al. [2002] showed that similar in-plane resolution improvements as in [Peled and Yeshurun, 2001] can be replicated by using zero-padding interpolation. According to both Scheffler [2002] and Greenspan et al. [2002], the apparent improvement in the in-plane resolution was due to an improvement in the SNR.

4.3.2 Through-plane improvement

As the through-plane resolution of multi-slice images is often lower than the in-plane resolution, most SR methods focus on decreasing the slice thickness and reaching voxel isotropy [Greenspan et al., 2002, Shilling et al., 2009, Poot et al., 2010]. In the slice selection direction, undersampling of the data results in aliasing [Pipe, 1998, Noll et al., 1997]. This aliasing provides the basis for using SR algorithms to enhance the spatial resolution in the slice selection direction. Various acquisition and reconstruction strategies for SR in the slice selection direction have been proposed [Park et al., 2003, Plenge et al., 2012, Van Reeth and Tham, 2012]. They will be discussed in the next section.

4.4 Spatial domain approach

In SRR a specific acquisition scheme is combined with a reconstruction method. To recover the high resolution information from the low resolution images an observation or acquisition model is used. This acquisition model shows how the

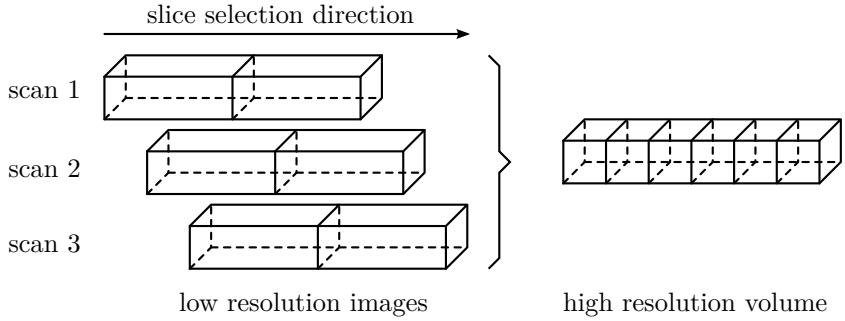

Fig. 4.5: Three parallel low resolution multi-slices scans, shifted in the through-plane direction.

low resolution images are obtained from the imaged subject. The super-resolution reconstruction is then an inverse problem. In this section, different acquisition schemes, the acquisition model and reconstruction methods will be discussed.

4.4.1 Acquisition strategies

In MRI, there is a consensus that resolution enhancement is not achievable in the in-plane directions, since the Fourier encoding scheme excludes aliasing in the frequency and phase encoding directions [Scheffler, 2002]. Therefore, the low resolution images are acquired with an high isotropic in-plane resolution and a slice thickness larger than this in-plane resolution (Fig. 4.1). In multi-slice acquisitions, increasing the slice thickness improves the SNR of the acquired images. Moreover, as less slices need to be acquired to cover the region of interest, in turn the acquisition time might be reduced. Throughout this work, the anisotropy of the voxels is quantified with an anisotropy factor AF, defined as the ratio between the slice thickness and the voxel size in the frequency and phase encoding direction.

In order to recover the high resolution information, the low resolution images need to contain complementary information about the object. Several strategies can be adopted to acquire such a set of low resolution images [Shilling et al., 2008, Van Reeth and Tham, 2012].

- **Parallel stacks acquisition**: Several low resolution images are acquired, shifted in the through-plane dimension by a known subpixel distance [Greenspan et al., 2002, Ben-Ezra et al., 2010]. In Fig. 4.5 the concept is shown for 3 low resolution images. To reach isotropic resolution, a minimum of N low resolution images is needed, whereby N is the ratio between the through-plane and in-plane resolution.

- **Orthogonal acquisition**: Three orthogonal scans, one sagittal, one transversal and one coronal are acquired, as shown in Fig. 4.6 [Souza and Robert, 2008, Gholipour et al., 2010a]. Each acquired low resolution image has only one low-resolution axis, i.e. the slice selection direction, which is compensated for by acquisition of the other volumes.

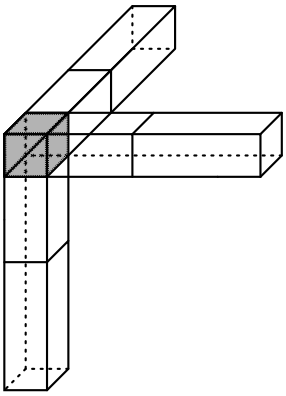

Fig. 4.6: Three orthogonal low resolution multi-slices scans.

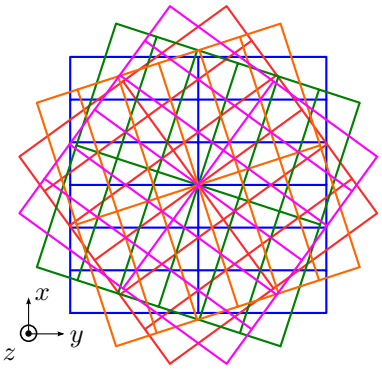

Fig. 4.7: Five rotated low-resolution multi-slice scans.

- **Multi-orientated acquisition**: This is an extended version of the orthogonal acquisition, where the acquisition plane is rotated around one or multiple encoded axis [Shilling et al., 2009, Poot et al., 2010]. In Fig. 4.7 a scheme where low resolution images are rotated about the phase encoding axis (y-axis) is shown. Rotation in image space results in a rotation in frequency domain. As such, acquiring the low resolution images with different slice orientations ensures that each low resolution image covers a different part of k-space. When the rotation is only performed about one fixed axis (frequency or phase encoding direction), the k-space can only be sampled in a cylinder with radius $\frac{1}{a}$, with a the voxel size in phase or frequency encoding direction. To ensure a short acquisition time, the minimal number of slice orientations that maximally covers the k-space by rotating about the center, is chosen. Preferably, the cylinder is completely sampled while the overlap between the different k-spaces is as small as possible. Hence the number of slice orientations, n, needed to fill the k-space of the high resolution imaged object with a minimal overlap is given by [Plenge et al., 2012]

$$n = [\frac{\pi}{2}\,\mathrm{AF}], \tag{4.1}$$

  with the operator $[\cdot]$ denoting that n is rounded to the closest natural number. The n images are then acquired rotated about the chosen axis in incremental steps of $180°/n$.

Both parallel and rotated scan approaches have shown to add information in the slice selection direction. However, acquiring the low resolution images with rotational increments results in a more effective sampling of k-space than by shifting the low resolution images by sub-pixel distances along the slice selection direction [Shilling et al., 2008, Plenge et al., 2012]. The latter approach corresponds to increasing the sampling density of the object after convolving it with the slice excitation profile. If, on the other hand, the slice selection direction is rotated, the narrow slice selection bandlimit of each image is oriented in a different direction of

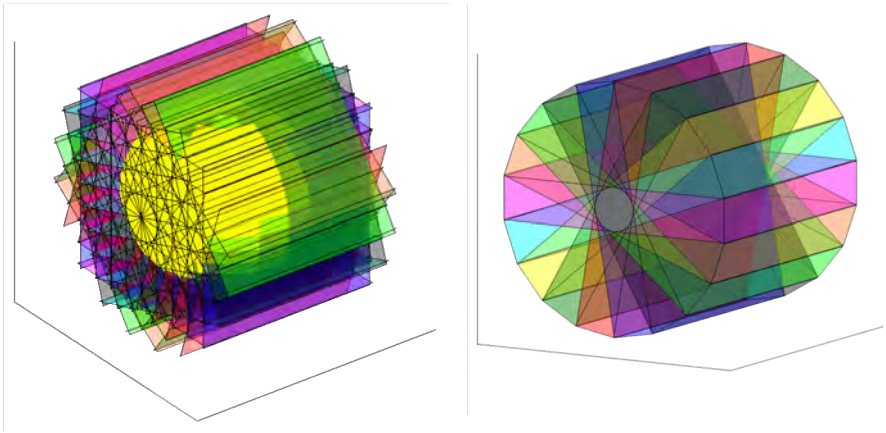

(a) Image space (b) k-space

Fig. 4.8: Set of low resolution multi-slice images in image space (a) and k-space (b) . In (a) each plane depicts a slice of a low resolution multi-slice image, the gap between the planes represents the slice thickness. In (b) the boundary of each colored box represent the maximum frequencies sampled by the low resolution image.

the 3D frequency spectrum of the imaged object. In this case, the low resolution data set will contain high spatial frequencies in all dimensions (Fig. 4.8). It has been discussed by Van Reeth and Tham [2012] and Manivannan et al. [2013] that the orthogonal scan combination has the advantage of minimizing the redundancy between each acquired low resolution image, however we believe that this depends on the AF of the low resolution images. Moreover, some artifacts only occur in the phase encoding direction. Thus by rotating the slice orientation around the phase encoding direction, rather than acquiring three orthogonal acquisition, the artifacts will be the same for each low resolution image, and easier to correct. Hence, further quantitative research is needed to define what the most efficient acquisition strategy is for SR in MRI.

4.4.2 Acquisition model

The acquisition model describes how the low resolution images are obtained from the high resolution scene. The used acquisition model is a trade off between a realistic model and a feasible solution. Generally, the acquisition model can be decomposed in a geometric transform, a linear space-invariant blurring model and a linear downsampling operator (Fig. 4.9) [Elad and Feuer, 2006, Plenge et al., 2012] .

Let $\boldsymbol{r} \in \mathbb{R}^{N_{\boldsymbol{r}} \times 1}$ be a vector representing the $N_{\boldsymbol{r}}$ (unknown) intensities $\boldsymbol{r}(j)$ (with j the voxel index, $j = 1, ..., N_{\boldsymbol{r}}$) of a noiseless, high resolution MR image sampled at the N_r 3D grid points $\boldsymbol{x} \in \mathbb{R}^{3 \times N_r}$. Furthermore, let $\boldsymbol{s}_m \in \mathbb{R}^{N_{\boldsymbol{s}_m} \times 1}$ ($m = 1, ..., M$, with M the number of low resolution images) be a vector of $N_{\boldsymbol{s}_m}$ signal intensities $\boldsymbol{s}_m(l)$ (with l the voxel index, $l = 1, ..., N_{\boldsymbol{s}_m}$) of a noiseless low

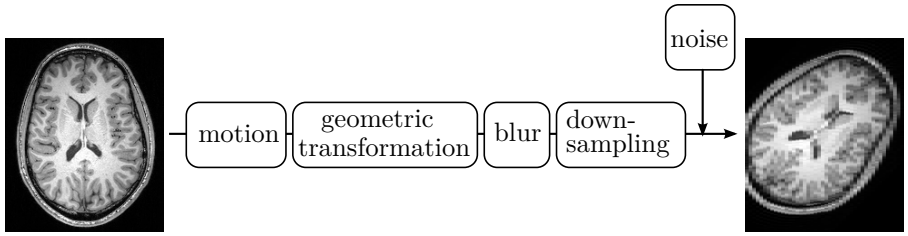

Fig. 4.9: The acquisition model.

resolution multi-slice MR image sampled at the $N_{\boldsymbol{s}_m}$ 3D grid points $\boldsymbol{y} \in \mathbb{R}^{3\times N_{\boldsymbol{s}_m}}$. Finally, let $\boldsymbol{A}_m \in \mathbb{R}^{N_{\boldsymbol{s}_m}\times N_{\boldsymbol{r}}}$ be a linear operator defining the transformation of the high resolution image $\boldsymbol{r}$ to the low resolution image $\boldsymbol{s}_m$. Then, the signal magnitude in voxel l of $\boldsymbol{s}_m$ may be described as:

$$\boldsymbol{s}_m(l) = \sum_{j=1}^{N_{\boldsymbol{r}}} \boldsymbol{A}_m(l,j)\boldsymbol{r}(j). \tag{4.2}$$

The acquired low resolution images $\tilde{\boldsymbol{s}}_m \in \mathbb{R}^{N_{\boldsymbol{s}_m}\times 1}$ are subject to noise:

$$\tilde{\boldsymbol{s}}_m = \boldsymbol{s}_m + \boldsymbol{e}_m, \tag{4.3}$$

with $\boldsymbol{e}_m \in \mathbb{R}^{N_{\boldsymbol{s}_m}\times 1}$ a vector representing the noise. When a single coil MR acquisition of magnitude images is considered, the noisy voxel intensities $\tilde{\boldsymbol{s}}_m(l)$ can be modeled as Rician distributed random variables [Gudbjartsson and Patz, 1995, den Dekker and Sijbers, 2014]. For a multi-coil acquisition, the magnitude data are governed by a non-central chi distribution [Constantinides et al., 1997, den Dekker and Sijbers, 2014]. When the SNR is high enough ($\gg 3$), which is typically the case for the low resolution voxels $\tilde{\boldsymbol{s}}_m(l)$, both distributions are well approximated by a Gaussian distribution [Gudbjartsson and Patz, 1995, Andersen and Krisch, 1996, Constantinides et al., 1997].

Introducing the homogeneous coordinates $\boldsymbol{x}'(:,j) = (\boldsymbol{x}^T(j,:)\ 1)^T$ and $\boldsymbol{y}'(:,l) = (\boldsymbol{y}^T(l,:)\ 1)^T$, the elements of the projection matrix $\boldsymbol{A}_m$ can be described as

$$\boldsymbol{A}_m(l,j) = \omega\left(\boldsymbol{T}_m\left(\boldsymbol{M}_m\boldsymbol{x}'(:,j)\right) - \boldsymbol{y}'(:,l)\right), \tag{4.4}$$

with $\boldsymbol{T}_m \in \mathbb{R}^{4\times 4}$ an (augmented) affine transformation matrix that maps the points in the high resolution space, $(\boldsymbol{x}(j))$, to the points in the low resolution space, $(\boldsymbol{y}(l))$, $\boldsymbol{M}_m \in \mathbb{R}^{4\times 4}$ an (augmented) affine transformation matrix describing motion and eddy current effects., and ω a point spread function (PSF). The PSF ω is defined by the MR image acquisition method. For multi-slice acquisition methods that sample a rectangular part of the k-space, ω can be modeled as the product of three 1D PSFs that are applied in the three orthogonal directions aligned with the MR image coordinate axes. The PSFs in the frequency and phase encoding direction are defined by the rectangular part of the k-space that is regularly sampled and can thus be modeled by Dirichlet, or periodic sinc, functions. The through-plane PSF depends on the slice selection method. Slice selection is often performed by

applying either a (windowed) sinc or a Gaussian shaped RF pulse, so the sampling in the through-plane (i.e., slice) direction can be modeled by a (smoothed) box or a Gaussian function, respectively [Poot et al., 2010].

The sampling of all M multi-slice low resolution images can be concatenated into one single matrix multiplication,

$$\tilde{\boldsymbol{S}} = \boldsymbol{A}\boldsymbol{r} + \boldsymbol{e}, \tag{4.5}$$

with

$$\tilde{\boldsymbol{S}} = \begin{bmatrix} \tilde{\boldsymbol{s}}_1 \\ \tilde{\boldsymbol{s}}_2 \\ \vdots \\ \tilde{\boldsymbol{s}}_M \end{bmatrix}, \quad \boldsymbol{A} = \begin{bmatrix} \boldsymbol{A}_1 \\ \boldsymbol{A}_2 \\ \vdots \\ \boldsymbol{A}_M \end{bmatrix}, \quad \boldsymbol{e} = \begin{bmatrix} \boldsymbol{e}_1 \\ \boldsymbol{e}_2 \\ \vdots \\ \boldsymbol{e}_M \end{bmatrix}. \tag{4.6}$$

4.4.3 Reconstruction

Recovering $\boldsymbol{r}$ given $\boldsymbol{A}$ and $\boldsymbol{S}$, is an inverse problem which can be formulated as a least squares problem

$$\boldsymbol{r} = \arg\min_{\boldsymbol{r}} \sum_{m=1}^{M} \|\tilde{\boldsymbol{s}}_m - \boldsymbol{A}_m \boldsymbol{r}\|_2^2. \tag{4.7}$$

Even though the number of low resolution samples ($\sum_{m=1}^{M} N_{\boldsymbol{s}_m}$) usually exceeds the number of high resolution samples ($N_{\boldsymbol{r}}$), the problem stated in Eq. 4.7 still is ill-conditioned, in the sense that its solution is very sensitive to noise. Inverting the effects of $\boldsymbol{A}$ could possible amplify the effects of noise in the measured data, making the solution of Eq. 4.7 highly sensitive to measurement noise.

To stabilize and constrain the solution, some form of regularization needs to be included. The regularization is interpreted as incorporating prior knowledge about the solution, e.g. a certain smoothness. A standard used regularization is Tikhonov regularization [Engl et al., 2000], which penalizes the amount of high spatial-frequency energy in the estimated high-resolution image. The regularized least squares problem becomes:

$$\boldsymbol{r} = \arg\min_{\boldsymbol{r}} \sum_{m=1}^{M} \|\tilde{\boldsymbol{s}}_m - \boldsymbol{A}_m \boldsymbol{r}\|_2^2 + \lambda \|\boldsymbol{R}(\boldsymbol{r})\|_2^2, \tag{4.8}$$

where $\boldsymbol{R}$ specifies the regularization term and λ a scalar weight defining the strength of the regularization. The regularization weight λ can either be chosen manually using visual inspection or automatically using the L-curve technique. Various types of regularization might be used such as Laplacian prior, total variation, Gaussian and Gibbs priors. In our implementation we used the squared Laplacian as regularization term:

$$\boldsymbol{R}(\boldsymbol{r}) = \left(\frac{\delta^2 \boldsymbol{r}}{\delta x_1^2}\right) + \left(\frac{\delta^2 \boldsymbol{r}}{\delta x_2^2}\right) + \left(\frac{\delta^2 \boldsymbol{r}}{\delta x_3^2}\right), \tag{4.9}$$

with x_i $(i = 1, 2, 3)$ the spatial dimension over which the partial derivative is taken. The discrete second derivative is calculated by

$$\frac{\delta^2 \boldsymbol{r}}{\delta x_i^2}|_{\boldsymbol{x}} = \boldsymbol{r}(\boldsymbol{x} - \boldsymbol{o}_i) - 2\boldsymbol{r}(\boldsymbol{x}) + \boldsymbol{r}(\boldsymbol{x} + \boldsymbol{o}_i), \tag{4.10}$$

with $\boldsymbol{o}_i$ the base vecotrs of the grid of $\boldsymbol{r}$

In general, the solution of Eq. 4.8 is given by:

$$\hat{\boldsymbol{r}} = (\boldsymbol{A}^T\boldsymbol{A} + \lambda \boldsymbol{R}^T\boldsymbol{R})^{-1}\boldsymbol{A}^T\tilde{\boldsymbol{S}}. \tag{4.11}$$

For realistic image dimensions, a direct solution of Eq. 4.11 is generally infeasible, due to the size of the matrix $\boldsymbol{A}$. Therefore, usually iterative methods are applied to approximate the solution. Several iterative methods have been proposed. Plenge et al. [2012] quantitatively and qualitatively compared reconstructions obtained from six different SR methods. No particular method significantly outperformed the others. Each model has its own pros and cons and its performance depends on the nature of the data on which it is applied [Van Reeth and Tham, 2012].

In this thesis a solution of Eq. 4.8 is obtained with the conjugate gradients method [Hestenes and Stiefel, 1952], because of its fast convergence properties. As previously mentioned, the matrix $\boldsymbol{A}$ is large, often even too large to store, even as sparse matrices. If the transformation $\boldsymbol{T}$ is an affine transformation, $\boldsymbol{M}$ and $\boldsymbol{T}$ can be combined into one single affine transformation and the acquisition of the low resolution images can be reformulated as an affine transformation of the object, followed by the filter operations of the sampling function described by ω. The affine transformations are applied using a combination of shear transformations as described by Poot et al. [2010].

4.5 Applications

SR has been successfully applied in anatomical [Poot et al., 2010, Plenge et al., 2012], functional [Peeters et al., 2004] as well as diffusion brain MRI Scherrer et al. [2012], Poot et al. [2013], Fogtmann et al. [2014]. One of the biggest application domains of SR is fetal brain imaging [Rousseau et al., 2006, 2010, Gholipour et al., 2010b, Oubel et al., 2012, Fogtmann et al., 2012]. Typically, fetal brain images have a lower SNR than adult brain images because the signal strength received by the scanner is relatively weak due to the large distance between the fetal brain and the receiver coil. Furthermore, the fetus brain is much smaller than an adult brain. An additional challenge in fetal MRI is the elevated motion of the fetal brain.

Bibliography

A.H. Andersen and J.E. Krisch. Analysis of noise in phase contrast MR imaging. *Medical Physics*, 23(6):857–869, 1996.

A. Ben-Ezra, H. Greenspan, and Y. Rubner. Regularized super-resolution of brian MRI. In *Proceedings of the IEEE International Symposium on Biomedical Imaging*, volume 7, pages 860–863, Rotterdam, The Netherlands, 2010.

M.A. Bernstein, S.B. Fain, and S.J. Riederer. Effect of windowing and zero-filled reconstruction of MRI data on spatial resolution and acquisition strategy. *Journal of Magnetic Resonance Imaging*, 14(3):270–280, 2001.

M. Blaimer, F. Breuer, M. Mueller, R.M. Heidemann, M.A. Griswold, and P.M. Jakob. SMASH, SENSE, PILS, GRAPPA: how to choose the optimal method. *Topics in Magnetic Resonance Imaging*, 15(4):223–236, 2004.

E. Carmi, S. Liu, N. Alon, A. Fiat, and D. Fiat. Resolution enhancement in MRI. *Magnetic Resonance Imaging*, 24(2):133–154, 2006.

C.D. Constantinides, E. Atalar, and E.R. McVeigh. Signal-to-noise measurements in magnitude images from NMR phased arrays. *Magnetic Resonance in Medicine*, 38(5):852–857, 1997.

A.J. den Dekker and J. Sijbers. Data distributions in magnetic resonance images: A review. *Physica Medica*, 30(7):725–741, 2014.

M. Elad and A. Feuer. Restoration of a single superresolution image from several blurred, noisy, and undersampled measured images. *IEEE Transactions on Image Processing*, 15(6):1413–1428, 2006.

H.W. Engl, M. Hanke, and A. Neubauer. *Regularization of inverse problems*. Kluwer Academic Publishers, Berlin, 2000.

S. Farsiu, D. Robinson, M. Elad, and P. Milanfar. Advances and challenges in super-resolution. *International Journal of Imaging Systems and Technology*, 14 (2):47–57, 2004.

D.A. Feinberg and K. Setsompop. Ultra-fast MRI of the human brain with simultaneous multi-slice imaging. *Journal of Magnetic Resonance*, 229:90–100, 2013.

D. Fiat. Method of enhancing an MRI signal, 1997.

M. Fogtmann, S. Seshamani, K. Kim, T. Chapman, and C. Studholme. A unified approach for motion estimation and super resolution reconstruction from structural Magnetic Resonance imaging on moving subjects. In *Proceedings of the MICCAI Workshop on Perinatal and Paediatric Imaging*, pages 9–26, Nice, France, 2012.

M. Fogtmann, S. Seshamani, C. Kroenke, X. Cheng, T. Chapman, J. Wilm, F. Rousseau, and C. Studholme. A unified approach to diffusion direction sensitive slice registration and 3-D DTI reconstruction from moving fetal brain anatomy. *IEEE Transactions on Medical Imaging*, 33(2):272–289, 2014.

A. Gholipour, J.A. Estroff, M. Sahin, S.P. Prabhu, and S.K. Warfield. Maximum a posteriori estimation of isotropic high-resolution volumetric MRI form orthogonal thickslice scans. In *Proceedings of the Medical Image Computing and Computer-Assisted Intervention, MICCAI*, pages 109–116, Beijing, China, 2010a.

A. Gholipour, J.A. Estroff, and S.K. Warfield. Robust super-resolution volume reconstruction from slice acquisitions: Application to fetal brain MRI. *IEEE Transactions on Medical Imaging*, 29(10):1739–1758, 2010b.

H. Greenspan. Super-resolution in medical imaging. *The Computer Journal*, 52(1): 43–63, 2009.

H. Greenspan, G. Oz, N. Kiryati, and S. Peled. MRI inter-slice reconstruction using super-resolution. *Magnetic Resonance in Medicine*, 20(5):437–446, 2002.

M.A. Griswold, P.M. Jakob, R.M. Heidemann, M. Nittka, V. Jellus, J. Wang, B. Kiefer, and A. Haase. Generalized autocalibrating partially parallel acquisitions (GRAPPA). *Magnetic Resonance in Medicine*, 47(6):1202–1210, 2002.

H. Gudbjartsson and S. Patz. The Rician Distribution of Noisy MRI Data. *Magnetic Resonance in Medicine*, 34(6):910–914, 1995.

A. Herment, E. Roullot, I. BLoch, O. Jolivet, A.D. Cesare, F. Frouin, J. Bittoun, and E. Mousseaux. Local Reconstruction of Stenosed Sections Artery Using Multiple MRA Acquisitions. *Magnetic Resonance in Medicine*, 49(4):721–742, 2003.

M.R. Hestenes and E. Stiefel. Method of conjugate gradients for solving linear systems. *Journal of Research of the National Bureau of Standards*, 49(6):409–436, 1952.

M.G. Kang and S. Chaudhuri. Super-resolution image reconstruction. *IEEE Signal Processing Magazine*, 20(3):19–20, 2003.

S. Kim and W.-Y. Su. Recursive high-resolution reconstruction of blurred multiframe images. *IEEE Transactions on Image Processing*, 2(4):234–539, 1993.

S.P. Kim, N.K. Bose, and H.M. Valenzuela. Recursive reconstruction of high resolution image from noisy undersampled multiframes. *IEEE Transactions on Acoustics, Speech, and Signal Processing*, 38(6):1013–1027, 1990.

M. Lustig, D. Donoho, and J.M. Pauly. Sparse MRI: Application of compressed sensing for rapid MR imaging. *Magnetic Resonance in Medicine*, 58(6):1182–1195, 2007.

N. Manivannan, B.D. Clymer, A. Bratasz, and K.A. Powell. Streaking artifact reduction in orthogonal super resolution reconstruction of MRI data sets. In *Proceedings of the International Society for Magnetic Resonance in Medicine*, volume 21, page 3726, Salt Lake City, Utah, USA, 2013.

D.C. Noll, F.E. Boada, and W.F. Eddy. A spectral approach to analyzing slice selection in planar imaging: Optimization for through-plane interpolation. *Magnetic Resonance in Medicine*, 38(1):151–160, 1997.

E. Oubel, M. Koob, C. Studholme, J.L. Dietemann, and F. Rousseau. Reconstruction of scattered data in fetal diffusion MRI. *Medical Image Analysis*, 16(1): 28–37, 2012.

S.C. Park, M.K. Park, and M.G. Kang. Super-resolution image reconstruction: a technical overview. *IEEE Signal Processing Magazine*, 20(3):21–36, 2003.

F. Peeters, L. Annet, L. Hermoye, and B.E. Van Beers. Inflow Correction of Hepatic Perfusion Measurements Using T 1-Weighted, Fast Gradient-Echo, Contrast-Enhanced MRI. *Magnetic Resonance in Medicine*, 51(4):710–717, 2004.

S. Peled and Y. Yeshurun. Superresolution in MRI: application to human white fiber tract vizualization by diffusion tensor imaging. *Magnetic Resonance in Medicine*, 45(1):29–35, 2001.

J.G. Pipe. Asymmetric sampling along k_sliceselect in two-dimensional multislice MRI. *Magnetic Resonance in Medicine*, 39(4):625–634, 1998.

J.G. Pipe. Motion correction with PROPELLER MRI: Application to head motion and free-breating cardiac imaging. *Magnetic Resonance in Medicine*, 42(5): 963–969, 1999.

E. Plenge, D.H.J. Poot, M. Bernsen, G. Kotek, G. Houston, P. Wielopolski, L. Van Der Weerd, W.J. Niessen, and E. Meijering. Super-resolution methods in MRI: Can they improve the trade-off between resolution, signal-to-noise ratio, and acquisition time? *Magnetic Resonance in Medicine*, 68(6):1983–1993, 2012.

D.H.J. Poot, V. Van Meir, and J. Sijbers. General and efficient super-resolution method for multi-slice MRI. In *Proceedings of the Medical Image Computing and Computer-Assisted Intervention, MICCAI*, pages 615–622, Beijing, China, 2010.

D.H.J. Poot, B. Jeurissen, Y. Bastiaensen, J. Veraart, W. Van Hecke, P.M. Parizel, and J. Sijbers. Super-resolution for multislice diffusion tensor imaging. *Magnetic Resonance in Medicine*, 69(1):103–113, 2013.

K.P. Pruessmann, M. Weiger, M.B. Scheidegger, and P. Boesiger. SENSE: Sensitivity encoding for fast MRI. *Magnetic Resonance in Medicine*, 42(5):952–962, 1999.

F. Rousseau, O.A. Glenn, B. Iordanova, C. Rodriguez-Carranza, D.B. Vigneron, J.A. Barkovich, and C. Studholme. Registration-Based Approach for Reconstruction of High-Resolution In Utero Fetal MR Brain Images. *Academic Radiology*, 13(9): 1072–1081, 2006.

F. Rousseau, K. Kim, C. Studholme, M. Koob, and J.L. Dietemann. On super-resolution for fetal brain MRI. In *Proceedings of the Medical Image Computing and Computer-Assisted Intervention, MICCAI*, pages 355–362, Beijing, China, 2010.

K. Scheffler. Superresolution in MRI? *Magnetic Resonance in Medicine*, 47(2): 392–397, 2002.

B. Scherrer, A. Gholipour, and S.K. Warfield. Super-resolution reconstruction to increase the spatial resolution of diffusion weighted images from orthogonal anisotropic acquisitions. *Medical Image Analysis*, 16(7):1465–1476, 2012.

K. Setsompop, J. Cohen-Adad, B.A. Gagoski, T. Raij, A. Yendiki, B. Keil, V.J.. Wedeen, and L.L. Wald. Improving diffusion MRI using simultaneous multi-slice echo planar imaging. *NeuroImage*, 63(1):569–580, 2012.

R.Z. Shilling. *A multi-stack framework in magnetic resonance imaging.* PhD thesis, 2009.

R.Z. Shilling, S. Ramamurthy, and Brummer. M.E. Sampling strategies for super-resolution in multi-slice MRI. In *Proceedings of the International Conference on Image Processing (ICIP)*, pages 2240–2243, San Diego, CA, USA, 2008.

R.Z. Shilling, T.Q. Robbie, T. Bailloeul, K. Mewes, R.M. Mersereau, and Brummer. M.E. A super-resolution framework for 3D imaging using 2D multislice MRI. *IEEE Transactions on Medical Imaging*, 28(5):633–644, 2009.

A. Souza and S. Robert. Model-based super-resolution for MRI. In *Proceedings of the IEEE engineering in Medicine an Biology Society*, volume 30, pages 430–434, Vancouver, Canada, 2008.

R. Tsai and T. Huang. Moving image restoration and registration. In *Conference proceedings of the IEEE International conference on Acoustics, Speech, and Signal Processing*, volume 5, pages 418–421, Denver, Colorado, USA, 1980.

R. Tsai and T.S. Huang. Multiframe image restoration and registration. In T.S. Huang, editor, *Advances in Computer Vision and Image Processing.* JAI Press, Inc., Gulf Breeze, 1984.

E. Van Reeth and I. Tham. Super-resolution in magnetic resonance imaging: A review. *Concepts in Magnetic Resonance A*, 40(6):306–325, 2012.

Part III

Contributions

5

Super-resolution T1 mapping

Contents

The work in this chapter has been published in:

- **G. Van Steenkiste**, D.H.J. Poot, B. Jeurissen, A.J. den Dekker, F. Vanhevel, P.M. Parizel, and J. Sijbers. Super-resolution T1 estimation: quantitative high resolution T1 mapping from a set of low resolution T1 weighted images with different slice orientations. *Magnetic Resonance in Medicine*, in press, 2016b
- **G. Van Steenkiste**, D.H.J. Poot, B. Jeurissen, A.J. den Dekker, and J. Sijbers. Super-resolution T1 mapping: a simulation study. In *Proceedings of the International Society for Magnetic Resonance in Medicine*, volume 23, page 1679, Toronto, Ontario, Canada, 2015a
- **G. Van Steenkiste**, D.H.J. Poot, B. Jeurissen, A.J. den Dekker, and J. Sijbers. High resolution T1 estimation from multiple low resolution magnetic resonance images. In *Proceedings of the IEEE International Symposium on Biomedical Imaging*, volume 12, pages 1036–1039, New York, NY, USA, 2015b

5.1 Introduction

The spin-lattice relaxation time, T_1, is one of the fundamental tissue properties on which clinical MRI contrast is based. Since, at a fixed field strength, T_1 is an intrinsic biophysical property of tissues [Bottomley et al., 1987, Oros-Peusquens et al., 2008], it is an important differentiating factor for diseases such as multiple sclerosis [Truyen et al., 1996], epilepsy [Conlon et al., 1988] and dementia [Erkinjuntti et al., 1987], and for the characterization of tumours [Englund et al., 1986, Kurki and Komu, 1995, Naruse et al., 1986]. Furthermore, T_1 is also used for contrast agent uptake studies, as well as for the measurement of perfusion [Peeters et al., 2004, Kershaw and Buckley, 2006] and blood volume [Cheng, 2007]. In a single clinical T_1-weighted image, the signal strength is not only characterized by the tissue but also by the specific pulse sequence parameters such as the inversion time or the flip angle. As such, the intensity in a T_1-weighted image is not quantitative. The image provides only qualitative information and diagnosis relies on visual interpretation. To allow absolute quantification of T_1, a set of T_1-weighted images with different contrast settings (i.e., sequence parameters) is required. From this set of images, a T_1 value can be estimated for each voxel. Unlike conventional qualitative T_1-weighted imaging, quantitative T_1 mapping allows objective comparison across subjects, protocols, sites and time [Ashton, 2010].

The gold standard T_1 sequence is the inversion recovery spin echo (IR SE) sequence [Drain, 1949, Hahn, 1949, Tofts, 2005, Crawley and Henkelman, 1988]. In this sequence, the longitudinal magnetization is inverted, after which the magnetization is allowed to recover back to its equilibrium state during an inversion time TI. The recovery rate is characterized by the tissue-specific relaxation constant T_1. A set of images, with a well-chosen range of inversion times, can be used to quantitatively estimate a T_1 map. Unfortunately, the acquisition time of the set of T_1-weighted images needed for an accurate and precise T_1 map is not clinically feasible [Tofts, 2005].

Most developments in T_1 quantification sequences focus on reducing the acquisition time of the T_1-weighted images either by improving the read-out method of the recovering magnetization [Look and Locker, 1970, Messroghli et al., 2010b,a, Clare and Jezzard, 2001, Mulkern et al., 1990, Zhu and Penn, 2005] or by using variable flip angles (VFA) [Deoni et al., 2005, Deoni, 2007, 2010, Liberman et al., 2014, Trzasko et al., 2013] to generate T_1 contrast. In faster read-out methods, such as fast/turbo spin echo (FSE/TSE) [Mansfield, 1977, Mulkern et al., 1990, Zhu and Penn, 2005] or echo planar imaging (EPI) [Mansfield, 1984, Clare and Jezzard, 2001], multiple k-space lines are acquired after inversion of the longitudinal magnetization. Unfortunately, the radio frequency (RF) pulses used in TSE deposit a high energy, which limits the spatial resolution of the images as specific absorption rate (SAR) limits are easily exceeded [Zhu and Penn, 2005]. Furthermore, EPI images generally suffer from spatial distortions due to off resonance effects.

Alternative T_1 quantification schemes are the Look-Locker (LL) method [Look and Locker, 1970] and its variants [Messroghli et al., 2010b,a], which reduce the acquisition time by measuring multiple readouts after each inversion pulse. After inversion, the magnetization is progressively tipped into the transverse plane using a series of small flip angles. Unfortunately, the use of these small flip angles results in

a lower signal-to-noise ratio (SNR) of the acquired images [Crawley and Henkelman, 1988, Clare and Jezzard, 2001]. Moreover, repeatedly sampling the recovering magnetization hastens its recovery [Kay and Henkelman, 1991]. Consequently, the measured longitudinal relaxation time will be shorter than T_1. As the measured relaxation time depends on the flip angles, an accurate knowledge of these flip angles is needed for an accurate T_1 estimation. This makes LL type sequences vulnerable to B1 field inhomogeneities [Kaptein et al., 1976, Stikov et al., 2015].

A T_1 map can also be estimated from spoiled gradient-echo images acquired at two different flip angles [Deoni et al., 2005, Deoni, 2007, 2010, Liberman et al., 2014, Trzasko et al., 2013]. These VFA methods are known for their ability to acquire high resolution T_1 maps in a short acquisition time. However, to achieve sufficient accuracy and precision, VFA measurements require a careful selection of pulse sequence parameters as well as the knowledge of the flip angles [Preibisch and Deichmann, 2009]. The actual flip angles might differ from their set values due to B1 field inhomogeneities, making the T_1 estimation prone to errors leading to a loss of accuracy of the estimated T_1 map [Mintzopoulos and Inati, 2006, Liu et al., 2015, Stikov et al., 2015]. In general, the choice of T_1 quantification sequence is about finding the right balance between precision, accuracy and speed.

The acquisition time of IR SE and IR TSE can be shortened by acquiring fewer T_1-weighted images. However, this comes at the expense of decreasing the precision of the T_1 map, while precise T_1 estimation is necessary as the clinically observed differences in T_1 values are typically only within a few percent. Alternatively, the acquisition time can also be shortened by acquiring the T_1-weighted images at a lower spatial resolution. As a bonus, increasing the slice thickness increases the SNR of the T_1-weighted images as the signal strength scales linearly with the imaged volume. However, thicker slices suffer from increased partial volume effects, making it harder to distinguish small anatomical structures.

It has been shown that spatial super-resolution (SR) reconstruction provides a better trade-off between acquisition time, spatial resolution and SNR in structural and diffusion MRI by reconstructing a high resolution image from a set of anisotropic multi-slice images [Greenspan et al., 2002, Greenspan, 2009, Robinson et al., 2010, Poot et al., 2010, Plenge et al., 2012, Van Reeth and Tham, 2012, Scherrer et al., 2012, Fogtmann et al., 2012, Poot et al., 2013, Fogtmann et al., 2014, **G. Van Steenkiste** et al., 2016a]. The reconstructed high resolution image benefits from the high SNR of the low resolution images, which are acquired with a high in-plane resolution and a low through-plane resolution, i.e. thick slices. The resolution is enhanced by acquiring different, complementary resolution information about the object with each low resolution image. This is ensured by acquiring the low resolution images with a shift in the slice direction [Greenspan et al., 2002], at three orthogonal slice orientations [Fogtmann et al., 2012, Scherrer et al., 2012, Fogtmann et al., 2014] or at rotated slice orientations [Poot et al., 2010, 2013, **G. Van Steenkiste** et al., 2016a]. In quantitative MRI, SR reconstruction benefits from combining the parameter model with the SR model. This has been shown in diffusion MRI, where the diffusion model was combined with the SR model **G. Van Steenkiste** et al. [2016a], Fogtmann et al. [2014], allowing the direct estimation of the desired high resolution quantitative MRI parameters from the low resolution images.

In this chapter, we propose a new SR method, called super-resolution T_1 (SR-T_1), which combines T_1 estimation with super-resolution to reduce the acquisition time of the T_1-weighted images while providing a precise and accurate high resolution T_1 map. In our approach, a high resolution T_1 map is directly estimated from a set of anisotropic low resolution multi-slice IR TSE images. Additionally, the proposed method incorporates a model-based motion correction scheme. By means of experiments performed on synthetic and clinical data, we show that a precise and accurate high resolution T_1 map can be estimated out of a set of low resolution T_1-weighted images, of which the acquisition time is shorter than that of a direct high resolution acquisition.

5.2 Method

In this section, the proposed SR-T_1 estimation method and its acquisition protocol as well as the experiments are described. The SR-T_1 model is based on a combination of a T_1-weighting model and an SR model. To derive this model, we assume that the low resolution T_1-weighted images are acquired with a multi-slice IR SE sequence as this is the gold standard quantitative T_1 sequence and the least vulnerable to B1 inhomogeneities [Bernstein et al., 2004].

5.2.1 T_1 model

Let $\boldsymbol{r}_m \in \mathbb{R}^{N_{\boldsymbol{r}} \times 1}$ ($m = 1, ..., M$, with M the number of images) be a vector representing the $N_{\boldsymbol{r}}$ (unknown) intensities $r_m(j)$ (with j the voxel index, $j = 1, ..., N_{\boldsymbol{r}}$) of a noiseless, high resolution T_1-weighted MR image with inversion time TI_m and sampled at the N_r 3D grid points $\boldsymbol{x} \in \mathbb{R}^{3 \times N_r}$. If the repetition time $\text{TR} \gg T_1$, the (unknown) intensities of $\boldsymbol{r}_m$ can be written in function of the spin-lattice relaxation time $T_1(j)$, with $\boldsymbol{T}_1 \in \mathbb{R}^{N_{\boldsymbol{r}} \times 1}$, and a quantity $\rho(j)$, with $\boldsymbol{\rho} \in \mathbb{R}^{N_{\boldsymbol{r}} \times 1}$, which is proportional to the proton density [Bernstein et al., 2004]:

$$r_m(j) = \rho(j) \left(1 - 2e^{-\frac{\text{TI}_m}{T_1(j)}}\right), \tag{5.1}$$

with TI_m the inversion time at which r_m is acquired and where we assume a perfect 180° inversion pulse.

5.2.2 Super-resolution T_1 model

Let $\boldsymbol{s}_m \in \mathbb{R}^{N_{\boldsymbol{s}} \times 1}$ be a vector of $N_{\boldsymbol{s}}$ signal intensities $s_m(l)$ (with l the voxel index, $l = 1, ..., N_{\boldsymbol{s}}$) of a noiseless low resolution T_1-weighted MR image acquired at the same inversion time TI_m as $\boldsymbol{r}_m$, and sampled at the N_s 3D grid points $\boldsymbol{y} \in \mathbb{R}^{3 \times N_s}$. According to Eq. 4.2, the signal magnitude in voxel l of $\boldsymbol{s}_m$ can be related to the voxel intensities of $\boldsymbol{r}_m$ by

$$s_m(l) = \left| \sum_{j=1}^{N_r} a_m(l, j) r_m(j) \right|, \tag{5.2}$$

with $\boldsymbol{A}_m = (a_m(l,j)) \in \mathbb{R}^{N_s \times N_r}$ a linear operator defining the transformation of the high resolution image $\boldsymbol{r}_m$ to the low resolution image $\boldsymbol{s}_m$ as described in Eq. 4.4.

By combining Eq. 5.1 and Eq. 5.2, the magnitude of the low resolution T_1-weighted image, $\boldsymbol{s}_m$, can be described in terms of a high resolution T_1 and ρ map:

$$s_m(l; \boldsymbol{T}_1, \boldsymbol{\rho}) = \left| \sum_{j=1}^{N_r} a_m(l,j)\rho(j) \left(1 - 2e^{-\frac{\mathrm{TI}_m}{T_1(j)}}\right) \right|. \tag{5.3}$$

The acquired low resolution images $\tilde{\boldsymbol{s}}_m \in \mathbb{R}^{N_s \times 1}$ are subject to noise. When a single coil MR acquisition system is considered, the noisy voxel intensities $\tilde{\boldsymbol{s}}_m(l)$ can be modeled as Rician distributed random variables [Gudbjartsson and Patz, 1995, den Dekker and Sijbers, 2014]. For a multi-coil acquisition, the data are governed by a non-central chi distribution [Constantinides et al., 1997, den Dekker and Sijbers, 2014]. When the SNR is high enough ($\gg 3$), which is typically the case for the low resolution voxels $\tilde{\boldsymbol{s}}_m(l)$, both distributions are well approximated by a Gaussian distribution [Gudbjartsson and Patz, 1995, Andersen and Krisch, 1996, Constantinides et al., 1997]. Therefore, we adopt the assumption of Gaussian distributed noise.

5.2.3 Super-resolution T_1 estimation

By combining all low resolution images, a high resolution ρ and T_1 map can be estimated by minimizing the squared difference between the acquired low resolution T_1-weighted images $\tilde{\boldsymbol{s}}_m$ and the low resolution T_1-weighted images generated by the model (Eq. 5.3):

$$\hat{\boldsymbol{T}}_{\boldsymbol{1}}, \hat{\boldsymbol{\rho}} = \arg\min_{\boldsymbol{T}_{\boldsymbol{1}}, \boldsymbol{\rho}} \left\{ \sum_{m=1}^{M} \sum_{l=1}^{N_s} \|\tilde{s}_m(l) - s_m(l; \boldsymbol{T}_1, \boldsymbol{\rho})\|_2^2 \right\}, \tag{5.4}$$

where the choice of the least squares criterion is motivated by the Gaussian noise assumption. However, this non-linear least squares (NLS) problem is typically ill-conditioned in the sense that its solution is very sensitive to noise. To make the solution more stable and less noisy, regularization terms that penalize large variations in the estimated ρ and T_1 map are included, leading to the following regularized NLS estimator:

$$\hat{\boldsymbol{T}}_{\boldsymbol{1}}, \hat{\boldsymbol{\rho}} = \arg\min_{\boldsymbol{T}_{\boldsymbol{1}}, \boldsymbol{\rho}} \left\{ \sum_{m=1}^{M} \sum_{l=1}^{N_s} \|\tilde{s}_m(l) - s_m(l; \boldsymbol{T}_1, \boldsymbol{\rho})\|_2^2 + \lambda_1 \|\Delta \boldsymbol{T}_{\boldsymbol{1}}\|_2^2 + \lambda_2 \|\Delta \boldsymbol{\rho}\|_2^2 \right\}, \tag{5.5}$$

with Δ the 3D discrete Laplace operator, and λ_1 and λ_2 the corresponding weighting factors [Poot et al., 2013, **G. Van Steenkiste** et al., 2016a].

5.2.4 Implementation

In the in vivo experiments described in the Experiments section, the transformation $\boldsymbol{T}_m$ (Eq. 4.4) was formed by combining the transformation matrix provided by

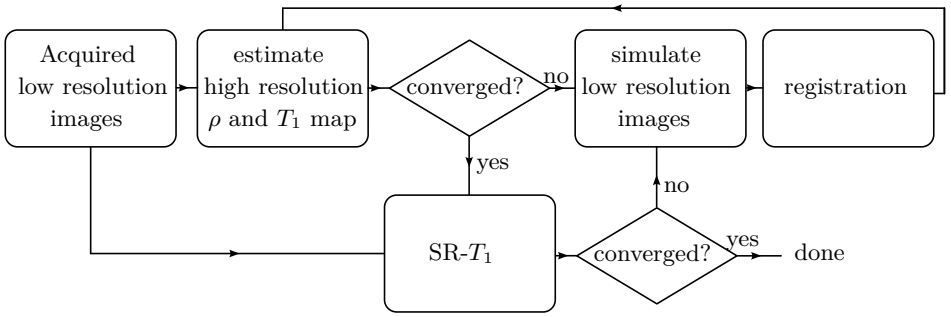

Fig. 5.1: Overview of the SR-T_1 pipeline.

the DICOM header information retrieved from the scanner and a world to voxel transformation. The transformation $\boldsymbol{T}_m$ was combined with the transformation $\boldsymbol{M}_m$ into a single affine transformation, which was applied efficiently using a combination of shear transformations as described by Poot et al. [2010]. The parameters constituting the motion operator $\boldsymbol{M}_m$ were estimated by an iterative model-based motion correction scheme [Bai and Alexander, 2008, Ramos-Llorden et al., 2015]. During the first step of this iterative scheme, $\boldsymbol{M}_m$ was the identity matrix. First, each acquired low resolution image was upsampled to the high resolution grid with the adjoint operator $\boldsymbol{A}'_m$. Next, a T_1 and ρ map were estimated from these upsampled images by NLS fitting the modulus of the model in Eq. 5.1 to the data with the Levenberg-Marquardt algorithm. From these maps, low resolution images were simulated using Eq. 5.3. Finally, these simulated images were rigidly aligned to the acquired images based on mean squared differences minimization, which in turn updates $\boldsymbol{M}_m$. All steps were repeated until the relative decrease in the cost function was smaller than 10^{-6}. The motion operator $\boldsymbol{M}_m$ as well as the T_1 and ρ map that resulted from this procedure were then used to initialize the SR-T_1 estimation (Eq. 5.5). An overview of this motion estimation and SR-T_1 pipeline is given in Fig. 5.1.

For both the in vivo and simulation experiments, the regularization parameter λ_2 was chosen aiming at equal contributions of $\lambda_1\|\Delta\boldsymbol{T_1}\|_2^2$ and $\lambda_2\|\Delta\boldsymbol{\rho}\|_2^2$ to the penalty. To do so, $\|\Delta\boldsymbol{T_1}\|_2^2$ and $\|\Delta\boldsymbol{\rho}\|_2^2$ were calculated from the initial estimates of the T_1 and ρ map. The ratio between those two values is then the ratio between λ_2 and λ_1. As such, only one regularization weight, λ_1, remains, which was chosen by experimenting with a range of values and qualitatively (i.e., visually) determining the best result. The values of λ_1 and λ_2 were then kept constant during the reconstruction. The cost function was minimized with a trust-region Newton method [Coleman and Li, 1996].

The algorithm was implemented using Matlab (MATLAB2014a, The Mathworks Inc.m, Natick, USA) on a PC with a hexa-core CPU @ 3.20 GHz with 64 GB of RAM. The in vivo experiment described in the Experiments section required around 19 GB RAM and the running time was 4.58 hours.

5.2.5 Acquisition protocol

The low resolution T_1-weighted images are acquired with an isotropic in-plane resolution and a slice thickness larger than this in-plane resolution. While the proposed reconstruction method does not imply restrictions on the acquisition setup and the slice orientations, we chose to rotate the slice orientations around the phase encoding axis over sub-pixel shifts in the slice encoding direction. By rotating the slice orientation around the phase encoding axis, each low resolution image has the same phase encoding direction. This assures that image artifacts, that might occur in the phase encoding direction, such as blurring due to a higher T_2-weighing of the signal, will be the same for each low resolution image, and thus will not introduce misalignment between the low resolution images. The number of slice orientations, n, was chosen according to Eq. 4.1 and the images were rotated in incremental steps of $180°/n$ [Plenge et al., 2012, **G. Van Steenkiste** et al., 2016a].

5.3 Experiments

The quality of the high resolution T_1 and ρ maps estimated with the proposed SR-T_1 method was evaluated with both synthetic and in vivo data sets. To improve the numerical performance of the fitting algorithms, the signal intensities of the simulated and in vivo data sets were scaled so that the range of the estimated ρ map equals that of the T_1 map [Gill et al., 1981].

5.3.1 Numerical simulations

The proposed SR-T_1 estimator was first evaluated on a simple numerical phantom (Fig. 5.2a). The $12 \times 12 \times 12$ phantom consisted of distinct regions that are characterized by one out of two T_1 values, corresponding to the T_1 of grey matter (1.607 s) and white matter (0.838 s) [Wright et al., 2008]. From this phantom, which served as ground truth, two noiseless low resolution data sets, with size $12 \times 12 \times 3$ were simulated. The first data set consisted of fourteen T_1-weighted images, each simulated with a unique inversion time, $\text{TI} \in [0.1, \ldots, 3\,\text{s}]$ and all TI equidistant in log space. An overview of the inversion times can be found in Table 5.1. The second data set consisted of seven subsets, each simulated with a different slice orientation and each containing two T_1-weighted images. Each of the in total fourteen T_1-weighted images had a unique inversion time, which were equal to the ones used in the first data set. From the first data set, a low resolution T_1 map with size $12 \times 12 \times 3$, was estimated using a voxel-wise T_1 estimation. From the second data set, a high resolution T_1 map with size $12 \times 12 \times 12$, was estimated twice using SR-T_1: once without regularization ($\lambda_1 = \lambda_2 = 0$ in Eq. 5.5) to show that the parameters are identifiable and once with regularization, $\lambda_1 = 1.0 \cdot 10^{-3}$ and $\lambda_2 = 1.9 \cdot 10^{-4}$ to assess the smoothing caused by the regularization.

5.3.2 Whole brain simulations

5.3.2.1 Generation of ground truth data

Noiseless $434 \times 362 \times 362$ T_1 and ρ maps were generated by combining an anatomical model of a normal human brain [Cocosco et al., 1997] with T_1 and ρ values measured in human brain tissue at 3T [Wright et al., 2008, Gold et al., 2004]. For the three main tissues the used T_1 values were: 0.838 s for white matter, 1.607 s for grey matter and 4.3 s for cerebrospinal fluid (CSF). The ρ map was normalized with the maximum value of ρ such that $\rho_j \in [0, \ldots, 1]$. From these maps, 50 T_1-weighted images, with size $120 \times 120 \times 120$, were simulated each with a different TI, where the TIs were selected in the interval $[0.1, \ldots, 15]$s, equidistantly spaced in the log space. Next, from these T_1-weighted images a $120 \times 120 \times 120$ T_1 and ρ map were estimated by voxel-wise NLS fitting using the model in Eq. 5.1. These maps served as the ground truth maps.

5.3.2.2 Simulation of T_1-weighted data

From the ground truth ρ and T_1 maps, two low resolution T_1-weighted data sets, with noise standard deviation 0.02 and size $120 \times 120 \times 30$, were simulated using Eq. 5.3. The SNR, defined as the ratio of the spatial mean to the standard deviation of the signal, was calculated in a small homogeneous white matter region in a T_1-weighted image simulated with TI = 100 ms and found to be equal to 115. Both data sets were composed of 14 T_1-weighted images, each simulated with a unique inversion time, equidistant in the log space. An overview of the inversion times can be found in Table 5.1. In the first data set, LR1, all low resolution T_1-weighted images were simulated with the same slice orientation. As such, this data set corresponds to a conventional T_1-weighted data set with a low, anisotropic resolution. The second data set, LR2, was simulated according to the proposed SR acquisition setup. This data set consisted of seven sub data sets, each containing two T_1-weighted images. Each subset was simulated with a different slice orientation by rotating about the phase encoding axis in incremental steps of 25.7°. Both data sets were simulated 50 times, each time with a different noise realization.

5.3.2.3 T_1 estimation

From each LR1 data set, a $120 \times 120 \times 120$ T_1 map was estimated by transforming the low resolution T_1-weighted images to the $120 \times 120 \times 120$ high resolution grid with the adjoint operator $\boldsymbol{A}'$ prior to applying the conventional voxel-wise T_1 estimation method. From each LR2 data set, a $120 \times 120 \times 120$ T_1 map was estimated using the proposed SR-T_1 estimation method with $\lambda_1 = 50$ and $\lambda_2 = 1.32$.

5.3.2.4 Quantification of T_1 estimation

To quantitatively evaluate the quality of the T_1 estimation methods, the root mean squared error (RMSE) between the estimated T_1/ρ and the ground truth T_1/ρ was calculated in each voxel of the high resolution grid. Moreover, the bias and standard deviation were also calculated in each voxel. In order to have a quantitative measure, the RMSE, absolute value of the bias and standard deviation

Orientation	TI_m (ms)
S	100
	624
S>T 25.7°	370
	2310
T>S −38.6°	220
	1370
T>S −12.9°	130
	811
T>S 13.0°	480
	3000
T>S 38.6°	284
	1780
S>T −25.7°	169
	1050

Table 5.1: Overview of the slice orientations and corresponding inversion times TI_m. T = transversal and S = sagittal.

were averaged over the white matter (WM) voxels as well as over the grey matter (GM) voxels.

5.3.3 In vivo data

5.3.3.1 Acquisition

To evaluate the proposed SR-T_1 method with human in vivo data, several T_1-weighted data sets of a healthy 28-year old male volunteer were acquired with a Prismafit (3T; Siemens AG, Siemens Medical Solution, Erlangen, Germany) using a 32-channel head coil. To limit the scan time per session, the data sets were acquired during three different scan sessions. One data set was acquired with VFA, the other data sets were acquired with an interleaved multi-slice IR TSE, with turbo factor 10, without slice gap and with 100% sampling. Each IR TSE data set was acquired at fourteen different inversion times, which were the same as those used in the simulation experiments (Table 5.1). The slice thickness of the anisotropic low resolution data set was chosen in order to have whole brain coverage without exceeding SAR limits. A detailed overview of the acquisition parameters of these data sets can be found in Table 5.2. During the first scan session the following data sets were acquired:

- **LR1**: 1 mm × 1 mm × 4 mm IR TSE data set. All fourteen T_1-weighted images were acquired with the same slice orientation.
- **LR2**: 1 mm × 1 mm × 4 mm IR TSE data set consisting of seven subsets, each including two T_1-weighted images. Each subset had a different slice orientation, which was rotated around the phase encoding direction in incremental steps of 25.7°. The slice orientations are given in Table 5.1. Each of the in

Data set :	**LR1**	**LR2**	**LR2a LR2b**	**VFA**	**HR**
In-plane resolution (mm^2)	1×1	1×1	1×1	1×1	1×1
Slice thickness (mm)	4	4	4	1	1
Acquisition matrix	256×256	256×256	256×256	256×256	256×256
Slices	40	40	40	144	40
Brain coverage (%)	100	100	100	100	28
n	1	7	7	1	1
M	14	14	14	-	14
TR (ms)	5000	5000	5000	10	6000
TE (ms)	8.8	8.8	8.8	2.0	11.0
Scan time (min)	28	28	28	7	30

Table 5.2: Overview of the relevant acquisition parameters of the clinical data sets. n is the number of slice orientations and M the number of inversion times.

total fourteen low resolution T_1-weighted images was acquired at a different inversion time (Table 5.1).

- **VFA**: 1 mm × 1 mm × 1 mm VFA data set consisting of two T_1-weighted images acquired with the flip angle set to 4° and 21°.

During the second scan session the following data sets were acquired:

- **LR2a** and **LR2b**: Two data sets were acquired with the same acquisition setup as the one used for the **LR2** data set from the first scan session

During the third scan session the following data set was acquired:

- **HR**: 1 mm × 1 mm × 1 mm IR TSE T_1-weighted data set. To limit acquisition time and SAR deposit, only 40 slices were acquired in the sagittal direction.

5.3.3.2 T_1 estimation

From the LR1 data set, a T_1 and ρ map were estimated with the following conventional T_1 estimation procedure. First, the acquired images were corrected for motion by rigid registration using mutual information. Next, the corrected images were upsampled to a 1 mm × 1 mm × 1 mm grid with the adjoint operator $\boldsymbol{A}'$. Finally, a 1 mm × 1 mm × 1 mm T_1 and ρ map were estimated using a voxel-wise

NLS fit optimized with the Levenberg-Marquardt algorithm. The same procedure, without the upsampling, was used to estimate a $1\,\text{mm} \times 1\,\text{mm} \times 1\,\text{mm}$ T_1 and ρ map from the HR data set. The proposed SR-T_1 method ($\lambda_1 = 1.0 \cdot 10^{-3}, \lambda_2 = 0.6 \cdot 10^{-3}$) was used to estimate $1\,\text{mm} \times 1\,\text{mm} \times 1\,\text{mm}$ T_1 and ρ maps from the data sets LR2, LR2a and LR2b. From the VFA data set, a $1\,\text{mm} \times 1\,\text{mm} \times 1\,\text{mm}$ T_1 map was calculated using a voxel-wise LS fit [Deoni et al., 2005].

5.3.3.3 Quantification of T_1 estimation

The T_1 and ρ maps estimated from the different data sets were compared qualitatively by visual inspection. Furthermore, the spatial resolution of the different T_1 maps was assessed by measuring the average width over 25 edge profiles. The edge width, defined as the width (in high resolution voxels) from 10% to 90% of the edge height, was measured by least squares fitting of the sigmoid function [Greenspan et al., 2002]:

$$f(q) = a_1 + \frac{a_2}{1 + \exp(-a_3(q - a_4))}, \tag{5.6}$$

where it is easy to show that the edge width is given by $4.4/a_3$. The SNR of the T_1-weighted data sets was computed in a uniform region in the corpus callosum of the T_1-weighted image acquired with $\text{TI} = 100\,\text{ms}$. For the data set VFA, the SNR was computed in the image acquired with flip angle set to 21°. Additionally, to assess the precision of the T_1 estimation, the standard deviation of the estimated T_1 maps was computed in a uniform region in the corpus callosum.

5.4 Results

5.4.1 Numerical simulations

Figure 5.2 shows the ground truth phantom, three orthogonal views of the ground truth T_1 and ρ map (Fig. 5.2a) and the T_1 and ρ map for the different estimation methods. In the low resolution T_1 and ρ map (Fig. 5.2b) the partial volume effects are so large that in the middle slice the structure of the phantom is not visible. In the initial estimated T_1 map (Fig. 5.2c), the structure of the phantom is visible in the middle slices. However, the edges between the different tissues are blurred. In the corresponding ρ map, the structures are not visible. Using SR-T_1 clearly enhances the spatial resolution of the estimated T_1 and ρ map (Fig. 5.2d-e): they both approximate the ground truth very well. In the reconstruction without regularization (Fig. 5.2d), the edges between the two different tissues are sharp. Although the use of regularization (Fig. 5.2e) does result in a minor smoothness of the edges between the tissues, it is clear that SR-T_1 still outperforms the initial estimation and the low resolution estimation.

5.4.2 Synthetic whole brain simulations

In Fig. 5.3 and Fig. 5.4 a transversal slice of the T_1 (Fig. 5.3) and ρ (Fig. 5.4) map estimated from the GT data, the LR1 data and the LR2 data are shown. The respective RMSE maps are shown in the second row. In Table 5.3 the RMSE,

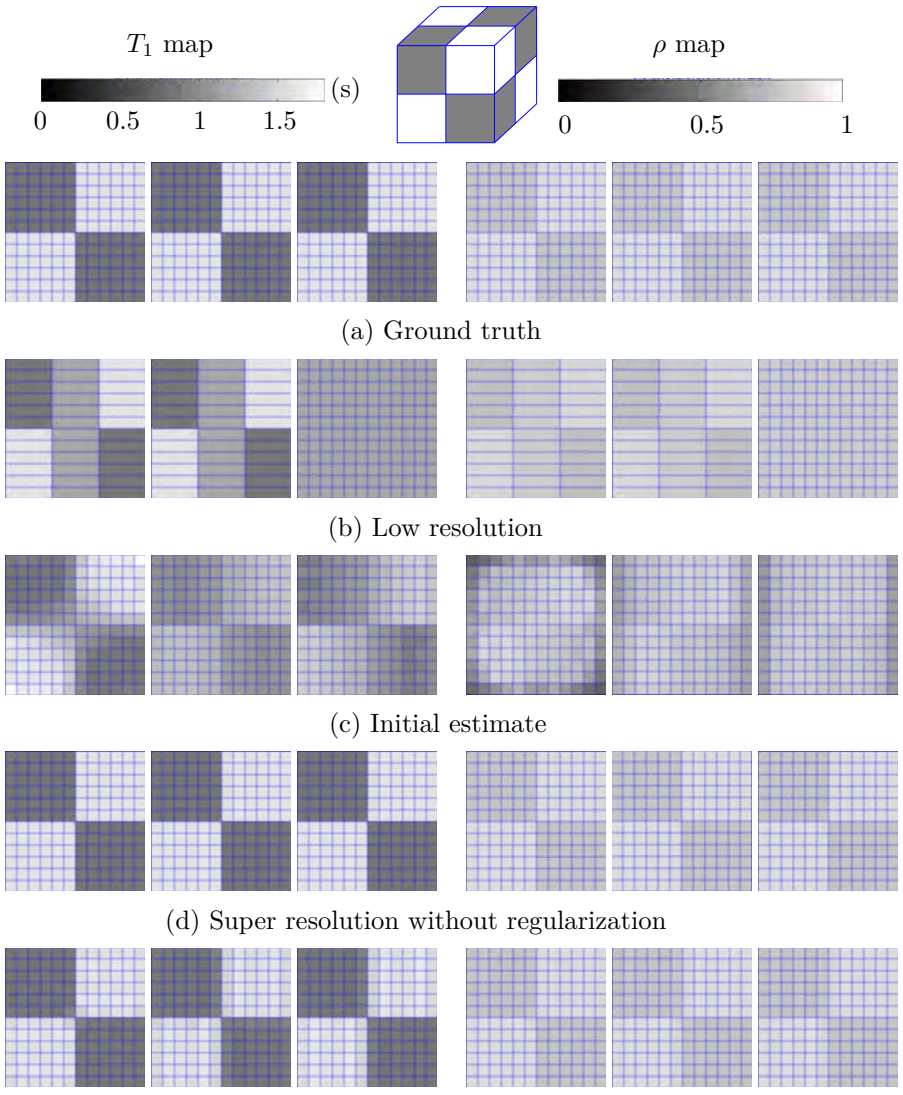

(a) Ground truth

(b) Low resolution

(c) Initial estimate

(d) Super resolution without regularization

(e) Super resolution with regularization

Fig. 5.2: 3D view of the numerical phantom and three orthogonal views of the (a) ground truth (b) low resolution, (c) initial estimate, (d) SR ($\lambda_1 = \lambda_2 = 0$), (e) SR ($\lambda_1 = 1.0 \cdot 10^{-3}$ and $\lambda_2 = 1.9 \cdot 10^{-4}$) T_1 map (left) and ρ map (right). The blue lines depict the borders of the voxels.

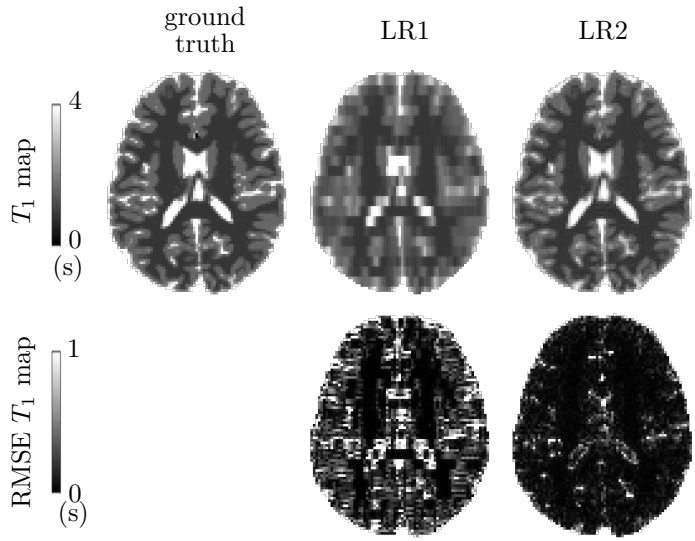

Fig. 5.3: Transversal slice of the T_1 and RMSE T_1 maps from the conventional T_1 estimation on LR1 and the SR-T_1 estimation on LR2.

	WM LR1	WM LR2	GM LR1	GM LR2
RMSE $\hat{\boldsymbol{T}}_1$ (s)	0.119	0.040	0.203	0.097
Bias $\hat{\boldsymbol{T}}_1$ (s)	0.119	0.036	0.203	0.092
Std $\hat{\boldsymbol{T}}_1$ (s)	0.003	0.015	0.002	0.021
RMSE $\hat{\boldsymbol{\rho}}$	0.010	0.008	0.029	0.014
Bias $\hat{\boldsymbol{\rho}}$	0.009	0.005	0.028	0.012
Std $\hat{\boldsymbol{\rho}}$	0.002	0.005	0.002	0.005

Table 5.3: RMSE, bias and standard deviation (std) of the T_1 and ρ estimator averaged over the white matter (WM) and grey matter (GM) voxels.

absolute bias and standard deviation averaged over the white matter voxels (WM) and the grey matter voxels (GM) are given. The voxel-wise estimated T_1 and ρ maps (LR1 in Fig. 5.3 and in Fig. 5.4) suffer from high partial volume effects due to the low spatial resolution of the T_1-weighted images. The SR-T_1 estimation enhances the resolution of the T_1-weighted images from data set LR2. In the resulting T_1 and ρ map, fine structures are clearly visible, while in the voxel-wise estimated T_1 and ρ map the fine structures are blurred. This is supported by the RMSE: overall the RMSE is smaller for the T_1 and ρ map estimated with SR-T_1 than for the voxel-wise estimated T_1 and ρ map. Although the standard deviation is higher for the SR-T_1 estimation than for the voxel-wise estimation, the bias is much lower.

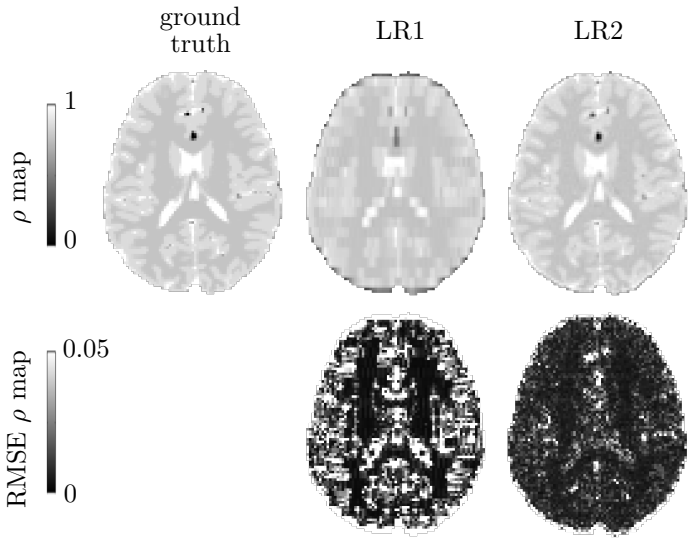

Fig. 5.4: Transversal slice of the ρ and RMSE ρ maps from the conventional T_1 estimation on LR1 and the SR-T_1 estimation on LR2.

5.4.3 In vivo data

In Table 5.4 the SNR of the acquired data sets is given. As the low resolution data sets (LR1, LR2, LR2a and LR2b) are acquired with the same spatial resolution, their SNR should be the same. Additionally, Table 5.4 also reports the spatial mean, standard deviation and SNR (defined as the ratio of the spatial mean to the standard deviation) calculated in a uniform region of the corresponding estimated T_1 map. There is a small loss in precision for the SR-T_1 estimation method compared to the conventional voxel-wise NLS estimation from T_1-weighted images with a low spatial resolution. Note, however, that since the low resolution data had a different acquisition time than the high resolution data, no direct comparison can be made between the standard deviations and SNR of the different T_1 maps. However, taking into account that the standard deviation is inversely proportional to the square root of the scan time, and that only 28% of the brain was covered within 30 min of scan time, it is clear that the standard deviation of the estimated HR T_1 map would be almost four times as low as the one given in Table 5.4 when the whole brain would have been acquired within 30 minutes.

5.4.3.1 SR-T_1 versus low resolution acquisition

Figures 5.5 and 5.6 shows a transversal and coronal slice of the T_1 and ρ map estimated from the data set LR1 and from the data set LR2. Due to the low spatial resolution of the T_1-weighted images, many partial volume effects occur in the conventional voxel-wise estimated T_1 (Fig. 5.5a) and ρ (Fig. 5.6a) map from data set LR1, blurring fine structures. Estimating the T_1 (Fig. 5.5b) and ρ (Fig. 5.5b) map with SR-T_1 enhances the spatial resolution of the T_1 and ρ map, reducing the partial volume effects. As a result, the interfaces between the different tissue

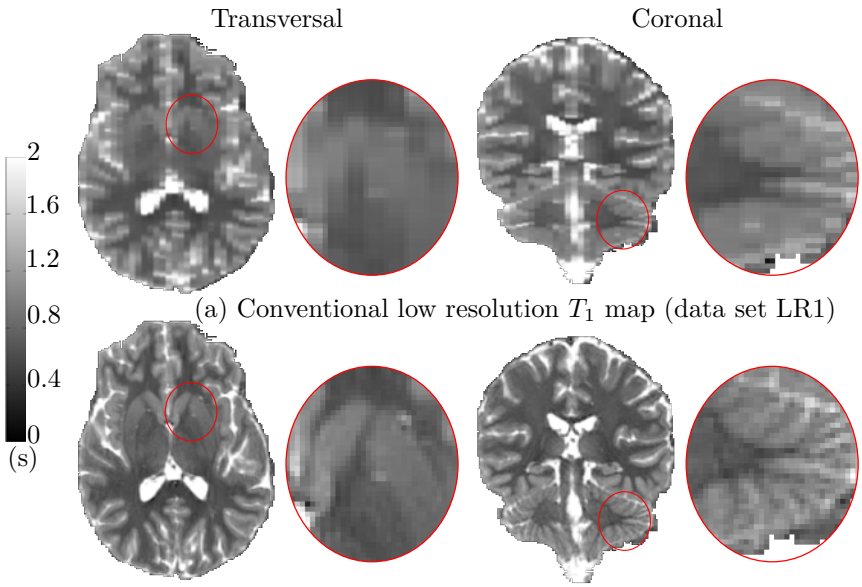

(a) Conventional low resolution T_1 map (data set LR1)

(b) Super-resolution T_1 map (data set LR2)

Fig. 5.5: Transversal and coronal slice and zoom in of the T_1 maps estimated from (a) data set LR1 and (b) data set LR2.

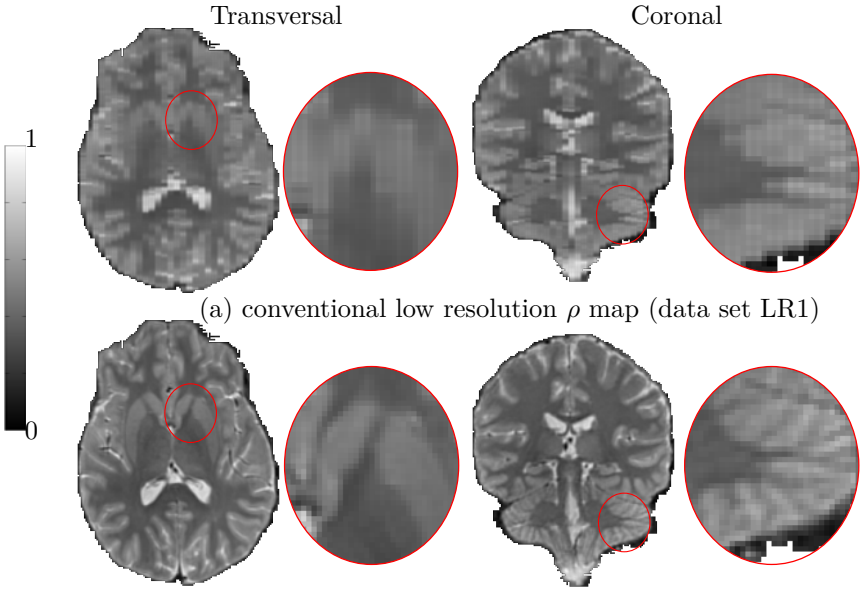

(a) conventional low resolution ρ map (data set LR1)

(b) Super-resolution ρ map (data set LR2)

Fig. 5.6: Transversal and coronal slice and zoom in of the ρ maps estimated from (a) data set LR1 and (b) data set LR2.

Data set	SNR acquired data	estimation method	average T_1 (ms)	std T_1 (ms)	SNR T_1
LR1	15.75	voxel-wise NLS	476	23.86	19.95
LR2	15.75	SR-T_1	475	32.10	14.80
LR2a	14.91	SR-T_1	483	33.00	14.64
LR2b	15.01	SR-T_1	477	34.33	13.90
VFA	24.98	voxel-wise NLS	1040	94.22	11.04
HR	5.30	voxel-wise NLS	487	35.94	13.55

Table 5.4: For each data set (column 1), the SNR of the acquired T_1-weighted data (column 2), the applied estimation method (column 3), the spatial average (column 4), standard deviation (column 5) and SNR (column 6) of T_1 in a uniform region of the corpus callosum in the corresponding estimated T_1 maps, are given. As the acquisition times of the VFA and HR data set are different from the low resolution data sets ('LR'), the standard deviations of these T_1 maps can not be compared directly.

types are more clear. This can be appreciated even more from the zooms shown in Fig. 5.5 and Fig. 5.6. A transversal zoom on the caudate nucleus-head, the putamen and the globus pallidus is shown. In the zoom on the T_1 and ρ map estimated from the data set LR1, the three different structures are hard to distinguish from each other. In the T_1 and ρ map estimated with SR-T_1 from the data set LR2, the interface between the different tissue types is more clear, making it easier to outline the different structures. The same can be seen in the coronal zoom on the cerebellum. The interface between white and grey matter is better defined for the SR T_1 map than for the LR1 T_1 map. This is confirmed by the edge width measurement. The average edge width for the data set LR1 is 5.3 voxels and for data set LR2 2.1 voxels.

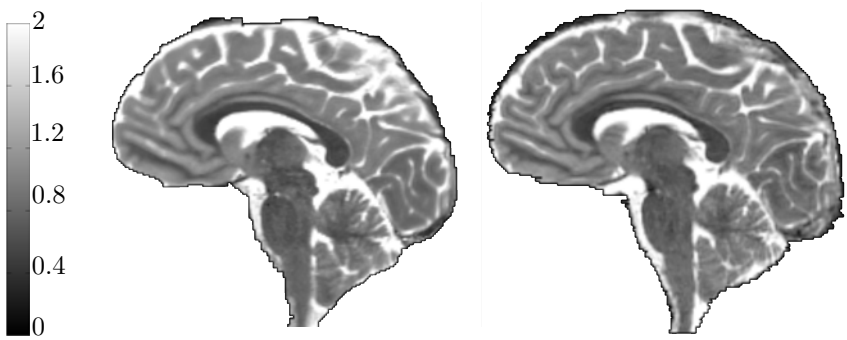

(a) HR T_1 map (b) SR T_1 map

Fig. 5.7: Sagittal slice of (a) the HR T_1 map and (b) the SR-T_1 T_1 map estimated from data set LR2b.

5.4.3.2 SR-T_1 versus high resolution acquisition

In Fig. 5.7, a sagittal slice from the T_1 map estimated with SR-T_1 from the data set LR2a (Fig. 5.7b) is compared with one from the T_1 map which was voxel-wise estimated from the data set HR (Fig. 5.7a). In both slices, the same level of fine structures can be observed. This is supported by the edge width which is 2.1 voxels for the data set HR. Moreover, visually, both T_1 maps show a similar range of T_1 values. This is supported by the average T_1 value in a homogeneous region in the corpus callosum which is given in Table 5.4.

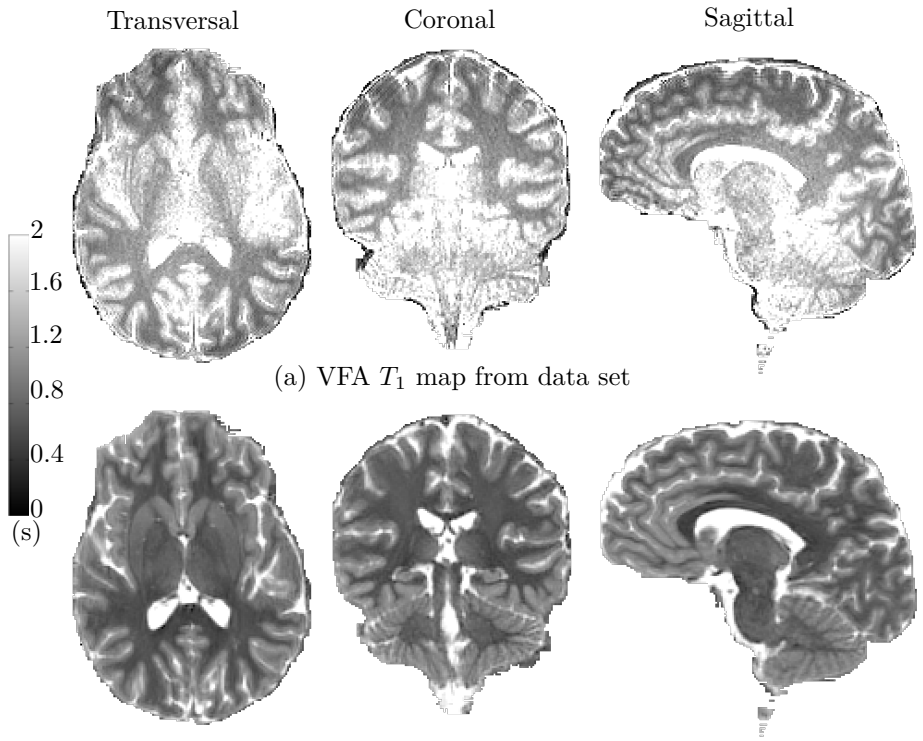

(a) VFA T_1 map from data set

(b) Super-resolution T_1 map from data set LR2

Fig. 5.8: Transversal, coronal and sagittal slice of (a) the T_1 map estimated from data set VFA and (b) the SR-T_1 T_1 map estimated from data set LR2.

5.4.3.3 SR-T_1 versus VFA acquisition

Figure 5.8 shows three orthogonal slices of the T_1 map estimated from the VFA data set and of the T_1 map estimated with SR-T_1 from the LR2 data set. Although the VFA data set is acquired at an isotropic $1\,\text{mm} \times 1\,\text{mm} \times 1\,\text{mm}$ resolution, small structures cannot be distinguished properly due to the noise and image artefacts.

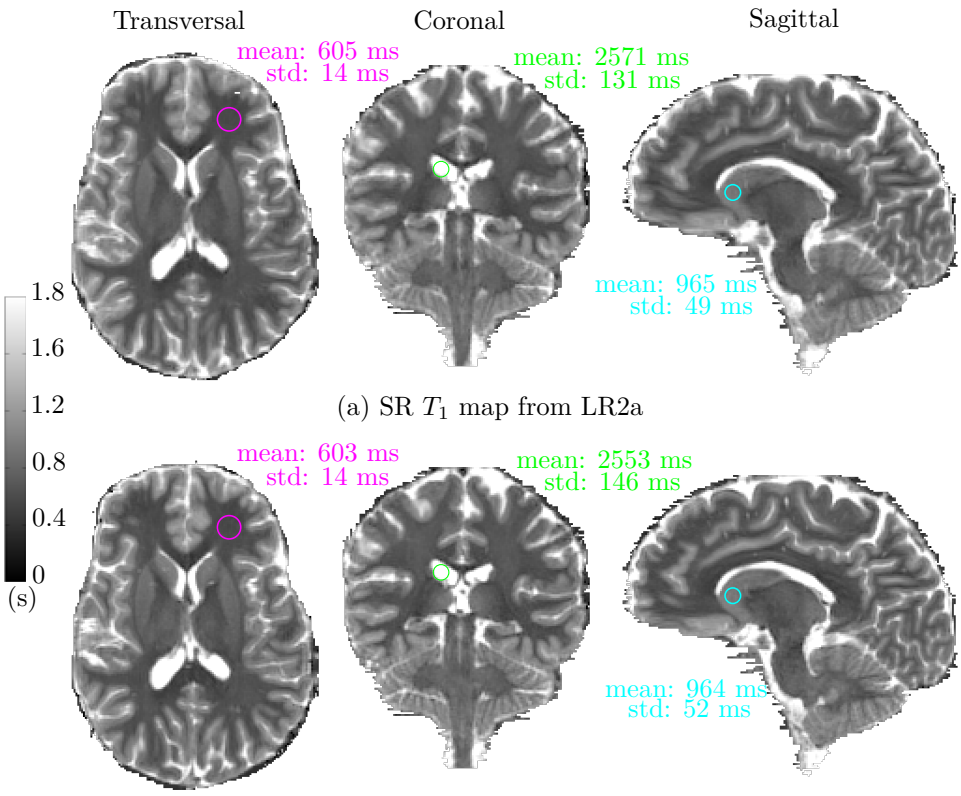

(a) SR T_1 map from LR2a

(b) SR T1 map from LR2b

Fig. 5.9: Transversal, coronal and sagittal slice of the SR-T_1 T_1 map estimated from (a) data set LR2a and (b) data set LR2b. Mean and standard deviation values of T_1 are calculated in the areas marked by the differently colored circles. The pink circle lies in the white matter, the green circle in the CSF and the blue circle in de caudate nucleus.

5.4.3.4 Reproducibility of SR-T_1

Figure 5.9 shows three orthogonal views of the T_1 maps estimated using SR-T_1 from the data set LR2a (Fig. 5.9a) and the data set LR2b (Fig. 5.9b). Visually, both T_1 maps exhibit the same level of details. In Fig. 5.9, the average and standard deviation of the T_1 values within three homogeneous regions (one in each tissue type), is reported. It is clear that both T_1 maps show a similar range of T_1 values in the different tissues.

5.5 Discussion

Increasing the spatial resolution in quantitative T_1 mapping is challenging because of the trade-off between the spatial resolution, the acquisition time, and the SNR. To improve this trade-off, we proposed a new SR acquisition and reconstruction method

specific for quantitative T_1 mapping, SR-T_1. The reconstruction method combines SR reconstruction and T_1 estimation into one integrated approach, enabling the direct estimation of an isotropic high resolution T_1 map from a set of anisotropic low resolution T_1-weighted images. A direct acquisition of a set of high resolution T_1-weighted images needed for whole brain T_1 mapping is infeasible due to the SAR limitations. By increasing the slice thickness and thus decreasing the number of slices needed for whole brain coverage, the energy deposited by the pulses decreases. As such, by acquiring anisotropic low resolution T_1-weighted images, the SAR limit is not exceeded.

5.5.1 Improving spatial resolution with SR-T_1

Using simple numerical simulations we have shown that the specific acquisition scheme and iterative reconstruction can recover high resolution information. These results are confirmed by the whole brain simulation, where the T_1 maps estimated from two low resolution data sets are compared to the ground truth T_1 map. Both low resolution data sets have the same acquisition time as they have the same resolution and number of inversion time. They differ only in the acquisition geometry as one of the data sets is simulated with different slice orientations. The results show that the SR-T_1 method enhances the resolution and improves the RMSE of the T_1 and ρ estimator, compared to a conventional voxel-wise T_1 estimation. The simulation experiment also shows an increase in the standard deviation when SR-T_1 mapping is used over conventional voxel-wise T_1 estimation. By increasing the regularization strength (λ_1, λ_2) the standard deviation will decrease (increase of precision), however, this comes at the cost of an increased bias and blurring of the fine structures. This same trend is observed in the in vivo experiment. Both visual comparison with a conventional low and high resolution data set as well as the computation of the average edge width, show that SR-T_1 improves the spatial resolution of the acquired low resolution T_1-weighted images. The in vivo experiments also show that multiple experiments with the same setup, result in similar T_1 maps, showing that the proposed SR-T_1 method provides reproducible results.

5.5.2 Reducing the acquisition time with SR-T_1

In this chapter, we demonstrated that SR-T_1 can improve the resolution while maintaining the same acquisition time and SNR of the acquired images. Alternatively, the proposed SR-T_1 technique can also be used to shorten the acquisition time or to improve the SNR of the estimated T_1 maps. Improving the acquisition time would enable quantitative T_1 mapping in clinical routine. As the anisotropic T_1-weighted images are acquired with less slices, their acquisition time will be shorter. If the same number of inversion times is used as for the isotropic T_1-weighted images, the overall acquisition time decreases. The isotropic resolution information is then recovered by the iterative reconstruction. By improving the SNR of the acquired images, the precision of the T_1 estimator increases. Because of their thick slices, the anisotropic low resolution T_1-weighted images have a higher SNR than isotropic high resolution T_1-weighted images. Furthermore, as the acquisition time of the

low resolution T_1-weighted images is shorter, more inversion times can be acquired within the same overall acquisition time than when high resolution T_1-weighted images are used.

5.5.3 Underestimation of T_1

For both the conventional NLS estimator and the proposed SR-T_1 estimator, the T_1 values estimated from the data acquired with the IR TSE sequence are lower than those estimated from the VFA data and those found in literature [Badve et al., 2015, Wansapura et al., 1999, Wright et al., 2008]. Note, however, that the T_1 values reported in literature are quite diverse and depend on the acquisition settings such as echo train length and the number of acquired slices [Wright et al., 2008, Eldeniz et al., 2015]. Possible reasons for the underestimation of T_1 are magnetization transfer effects, inter-slice cross-talk, inversion profile effects, short TR, perfusion effects [Zhu and Penn, 2005, Eldeniz et al., 2015, Stikov et al., 2015, van Gelderen et al., 2016]. However, the factors leading to the different in vivo T_1 relaxation times still have to be thoroughly investigated. Our simulations show that the SR-T_1 estimator is accurate and precise. Moreover, comparing a T_1 map estimated with SR-T_1 with a T_1 map estimated with a conventional technique (upsampling followed by voxelwise fitting), shows that comparable T_1 values are found. Thus the bias is not caused by the proposed SR-T_1 estimator but by the incapability of the signal model to describe the signal accurately. As suggested by Zhu and Penn [2005], this bias can be significantly reduced by a correction scheme based on linear regression which calculates the *true* T_1 from the underestimated T_1, which, however, is outside the scope of this work.

5.5.4 Other T_1 models

In the in vivo experiments, we chose to combine the proposed SR-T_1 with the widely available IR TSE sequence. However, the proposed method can also be combined with faster T_1 sequences, such as IR TSE with time-efficient slice ordering [Zhu and Penn, 2005] or simultaneous multi-slice techniques [Gagoski et al., 2015], which would shorten the acquisition time.

5.6 Conclusion

In this paper, we proposed SR-T_1, a new T_1 estimation method which combines SR reconstruction with T_1 parameter estimation into one integrated estimation method and produces a high resolution T_1 map directly from a set of low resolution T_1-weighted images. Furthermore, a specific acquisition scheme for these low resolution T_1-weighted images, using a stock sequence, was provided. The proposed technique enables high resolution $1\,\text{mm} \times 1\,\text{mm} \times 1\,\text{mm}$ whole-brain IR T_1 mapping, previously infeasible with IR due to SAR limitations. As the technique is complementary with other acquisition schemes, faster T_1 sequences could be combined with SR-T_1, which would enable the use of quantitative high resolution T_1 mapping through SR-T_1 in clinical routine.

Bibliography

A.H. Andersen and J.E. Krisch. Analysis of noise in phase contrast MR imaging. *Medical Physics*, 23(6):857–869, 1996.

E. Ashton. Quantitative MR in multi-center clinical trials. *Journal of Magnetic Resonance Imaging*, 31(2):279–288, 2010.

C. Badve, A. Yu, M. Rogers, D. Ma, Y. Liu, M. Schluchter, J. Sunshine, M. Griswold, and V. Gulani. Simultaneous T1 and T2 Brain Relaxometry in Asymptomatic Volunteers using Magnetic Resonance Fingerprinting. *Tomography*, 1(2):136–144, 2015.

Y. Bai and D.C. Alexander. Model-based registration to correct for motion between acquisitions in diffusion MR imaging. In *Proceedings of the IEEE International symposium on Biomedical Imaging*, volume 5, pages 947–950, Paris, France, 2008.

M.A. Bernstein, K.F. King, and X.J. Zou. *Handbook of MRI pulse sequences*. Elsevier Academic press, Philadelphia, 2004.

P.A. Bottomley, C.J. Hardy, R.E. Argersinger, and G. Allen-Moore. A review of 1H nuclear magnetic resonance relaxation in pathology: are T1 and T2 diagnostic. *Medical Physics*, 14(1):1–37, 1987.

H.L.M. Cheng. T1 measurement of flowing blood and arterial input function determination for quantitative 3D T1-weighted DCE-MRI. *Journal of Magnetic Resonance Imaging*, 25(5):1073–1078, 2007.

S. Clare and P. Jezzard. Rapid T1 mapping using multislice echo planar imaging. *Magnetic Resonance in Medicine*, 45(4):630–634, 2001.

C.A. Cocosco, V. Kollokian, R.K.-S. Kwan, and A.C. Evans. BrainWeb: Online Interface to a 3D MRI SImulated Brain Database. *NeuroImage*, 5(4):S425, 1997.

T.F. Coleman and Y. Li. An interior trust region approach for nonlinear minimzation subject to bounds. *SIAM Journal on optimization*, 6(2):418–445, 1996.

P. Conlon, M.R. Trimble, D. Rogers, and C. Callicott. Magnetic resonance imaging in epilepsy: a controlled study. *Epilepsy Research*, 2(1):37–43, 1988.

C.D. Constantinides, E. Atalar, and E.R. McVeigh. Signal-to-noise measurements in magnitude images from NMR phased arrays. *Magnetic Resonance in Medicine*, 38(5):852–857, 1997.

A.P. Crawley and R.M. Henkelman. A comparison of one-shot and recovery methods in T1 imaging. *Magnetic Resonance in Medicine*, 7(1):23–34, 1988.

A.J. den Dekker and J. Sijbers. Data distributions in magnetic resonance images: A review. *Physica Medica*, 30(7):725–741, 2014.

S.C.L. Deoni. High-resolution T1 mapping of the brain at 3T with driven equilibrium single pulse observation of T1 with high-speed incorporation of RF field inhomogeneities (DESPOT1-HIFI). *Journal of Magnetic Resonance Imaging*, 26 (4):1106–1111, 2007.

S.C.L. Deoni. Quantitative relaxometry of the brain. *Topics in Magnetic Resonance Imagingagnetic resonance imaging*, 21(2):101–113, 2010.

S.C.L. Deoni, T.M. Peters, and B.K. Rutt. High-resolution T1 and T2 mapping of the brain in a clinically acceptable time with DESPOT1 and DESPOT2. *Magnetic Resonance in Medicine*, 53(1):237–241, 2005.

L.E. Drain. A Direct Method of Measuring Nuclear Spin-Lattice Relaxation Times. In *Proceedings of the Physical Society. Section A*, volume 62, page 301, 1949.

C. Eldeniz, J. Finsterbusch, W. Lin, and H. An. TOWERS: T-One with Enhanced Robustness and Speed. *Magnetic Resonance in Medicine*, page DOI: 10.1002/mrm.25864, 2015.

E. Englund, A. Brun, Z. Gyorffy-wagner, E.-M. Larsson, and B. Persson. Relaxation times in relation to grade of malignancy and tissue necrosis in astrocytic gliomas. *Magnetic Resonance Imaging*, 4(5):425–429, 1986.

T. Erkinjuntti, L. Ketonen, R. Sulkava, M. Vuorialho, and M. Livanainen. Do white matter changes on MRI and CT differentiate vascular dementia from Alzheimer‘s disease. *Journal of Neurology, Neurosurgery & Psychiatry*, 50(1):37–42, 1987.

M. Fogtmann, S. Seshamani, K. Kim, T. Chapman, and C. Studholme. A unified approach for motion estimation and super resolution reconstruction from structural Magnetic Resonance imaging on moving subjects. In *Proceedings of the MICCAI Workshop on Perinatal and Paediatric Imaging*, pages 9–26, Nice, France, 2012.

M. Fogtmann, S. Seshamani, C. Kroenke, X. Cheng, T. Chapman, J. Wilm, F. Rousseau, and C. Studholme. A unified approach to diffusion direction sensitive slice registration and 3-D DTI reconstruction from moving fetal brain anatomy. *IEEE Transactions on Medical Imaging*, 33(2):272–289, 2014.

B.A. Gagoski, B. Bilgic, C. Eichner, H. Bhat, P.E. Grant, L.L. Wald, and K. Setsompop. Rare/turbo spin echo imaging with simultaneous multislice wave-caipi. *Magnetic Resonance in Medicine*, 73(3):929–938, 2015.

P.E. Gill, W. Murray, and M.H. Wright. *Practical optimization*. Academic Press, London, 1981.

G.E. Gold, B. Suh, A. Sawyer-Glover, and C. Beaulieu. Musculoskeletal MRI at 3.0T: Initial Clinical Experience. *American Journal of Roentgenology*, 183(5): 343–351, 2004.

H. Greenspan. Super-resolution in medical imaging. *The Computer Journal*, 52(1): 43–63, 2009.

H. Greenspan, G. Oz, N. Kiryati, and S. Peled. MRI inter-slice reconstruction using super-resolution. *Magnetic Resonance in Medicine*, 20(5):437–446, 2002.

H. Gudbjartsson and S. Patz. The Rician Distribution of Noisy MRI Data. *Magnetic Resonance in Medicine*, 34(6):910–914, 1995.

E.L. Hahn. An accurate nuclear magnetic resonance method for measuring spin-lattice relaxation times. *Physical Review*, 76(1):145–146, 1949.

R. Kaptein, K. Dijkstra, and C.E Tarr. A single-scan fourier transform method for measuring spin-lattice relaxation times. *Journal of Magnetic Resonance*, 24(2): 295–300, 1976.

I. Kay and R.M. Henkelman. Practical implementation and optimization of one-shot T1 imaging. *Magnetic Resonance in Medicine*, 22(2):414–424, 1991.

L.E. Kershaw and D.L. Buckley. Precision in measurements of perfusion and microvascular permeability with T1-weighted dynamic contrast-enhanced MRI. *Magnetic Resonance in Medicine*, 56(5):986–992, 2006.

T. Kurki and M. Komu. Spin-lattice relaxation and magnetization transfer in intracranial tumors in vivo: effects of Gd-DTPA on relaxation parameters. *Magnetic Resonance Imaging*, 13(3):379–385, 1995.

G. Liberman, Y. Louzoun, and D. Ben Bashat. T1 Mapping using variable flip angle SPGR data with flip angle correction. *Journal of Magnetic Resonance Imaging*, 40(1):171–180, 2014.

Y. Liu, J.R. Buck, S. Zheng, and V.N. Ikonomidou. Optimizing and comparing the efficiencies of relaxometry sequences in quantitative T1 and T2 imaging. In *Proceedings of the International Society for Magnetic Resonance in Medicine*, volume 23, page 1689, Toronto, Ontario, Canada, 2015.

D.C. Look and D.R. Locker. Time saving in measurement of NMR and EPR relaxation times. *Review of Scientific Instruments*, 41(2):250–251, 1970.

P. Mansfield. Multi-planar image formation using NMR spin echoes. *Journal of Physics C: Solid State Physics*, 10(3):L55–L58, 1977.

P. Mansfield. Real-time echo-planar imaging by NMR. *British medical bulletin*, 40 (2):187–190, 1984.

D.R Messroghli, M. Buehrer, S. Kozerke, S. Nordmeyer, T. Dietrich, K. Atrott, T. Hucko, I. Paetsch, F. Berger, and E. Fleck. Simultaneous T1 mapping, cine imaging, and IR-prepared imaging of the rat heart using Small Animal Look-Locker Inversion recovery (SALLI). In *Proceedings of the International Society for Magnetic Resonance in Medicine*, volume 18, pages 2–3, Stockholm, Sweden, 2010a.

D.R. Messroghli, A. Rudolph, H. Abdel-Aty, R. Wassmuth, T. Kühne, R. Dietz, and J. Schulz-Menger. An open-source software tool for the generation of relaxation time maps in magnetic resonance imaging. *BMC Medical Imaging*, 10(16):1–8, 2010b.

D. Mintzopoulos and S. Inati. The effects of magnetic field inhomogeneity on FLASH-based T1 measurements. In *Proceedings of the International Society for Magnetic Resonance in Medicine*, volume 14, page 923, Seattle, Washington, USA, 2006.

R.V. Mulkern, S.T. Wong, C. Winalski, and F.A. Jolesz. Contrast manipulation and artifact assessment of 2D and 3D RARE sequences. *Magnetic Resonance Imaging*, 8(5):557–566, 1990.

G. Van Steenkiste, D.H.J. Poot, B. Jeurissen, A.J. den Dekker, and J. Sijbers. Super-resolution T1 mapping: a simulation study. In *Proceedings of the International Society for Magnetic Resonance in Medicine*, volume 23, page 1679, Toronto, Ontario, Canada, 2015a.

G. Van Steenkiste, D.H.J. Poot, B. Jeurissen, A.J. den Dekker, and J. Sijbers. High resolution T1 estimation from multiple low resolution magnetic resonance images. In *Proceedings of the IEEE International Symposium on Biomedical Imaging*, volume 12, pages 1036–1039, New York, NY, USA, 2015b.

G. Van Steenkiste, B. Jeurissen, J. Veraart, A.J. den Dekker, P.M. Parizel, D.H.J. Poot, and J. Sijbers. Super-resolution reconstruction of diffusion parameters from diffusion-weighted images with different slice orientations. *Magnetic Resonance in Medicine*, 75(1):181–195, 2016a.

G. Van Steenkiste, D.H.J. Poot, B. Jeurissen, A.J. den Dekker, F. Vanhevel, P.M. Parizel, and J. Sijbers. Super-resolution T1 estimation: quantitative high resolution T1 mapping from a set of low resolution T1 weighted images with different slice orientations. *Magnetic Resonance in Medicine*, in press, 2016b.

S. Naruse, Y. Horikawa, C. Tanaka, K. Hirakawa, H. Nishikawa, and K. Yoshizaki. Significance of proton relaxation time measurement in brain edema, cerebral infarction and brain tumors. *Magnetic Resonance Imaging*, 4(4):293–304, 1986.

A.M. Oros-Peusquens, M. Laurila, and N.J. Shah. Magnetic field dependence of the distribution of NMR relaxation times in the living human brain. *Magnetic Resonance Materials in Physics, Biology and Medicine*, 21(1-2):131–147, 2008.

F. Peeters, L. Annet, L. Hermoye, and B.E. Van Beers. Inflow Correction of Hepatic Perfusion Measurements Using T 1-Weighted, Fast Gradient-Echo, Contrast-Enhanced MRI. *Magnetic Resonance in Medicine*, 51(4):710–717, 2004.

E. Plenge, D.H.J. Poot, M. Bernsen, G. Kotek, G. Houston, P. Wielopolski, L. Van Der Weerd, W.J. Niessen, and E. Meijering. Super-resolution methods in MRI: Can they improve the trade-off between resolution, signal-to-noise ratio, and acquisition time? *Magnetic Resonance in Medicine*, 68(6):1983–1993, 2012.

D.H.J. Poot, V. Van Meir, and J. Sijbers. General and efficient super-resolution method for multi-slice MRI. In *Proceedings of the Medical Image Computing and Computer-Assisted Intervention, MICCAI*, pages 615–622, Beijing, China, 2010.

D.H.J. Poot, B. Jeurissen, Y. Bastiaensen, J. Veraart, W. Van Hecke, P.M. Parizel, and J. Sijbers. Super-resolution for multislice diffusion tensor imaging. *Magnetic Resonance in Medicine*, 69(1):103–113, 2013.

C. Preibisch and R. Deichmann. Influence of RF spoiling on the stability and accuracy of T1 mapping based on spoiled FLASH with varying flip angles. *Magnetic Resonance in Medicine*, 61(1):125–135, 2009.

G. Ramos-Llorden, A.J. den Dekker, **G. Van Steenkiste**, J. van Audekerke, M. Verhoye, and J. Sijbers. Simultaneous motion correction and T1 estimation in quantitative T1 mapping: an ML restoration approach. In *Proceedings of the IEEE International Conference on Image Processing*, pages 3160–3164, Quebec, Canada, 2015.

M.D. Robinson, S.J. Chiu, C.A. Toth, J.A. Izatt, and J.Y. Lo. Novel Applications of Super-Resolution in Medical Imaging. In Peyman Milanfar, editor, *Super-Resolution Imaging*, pages 383–412. CRC Press, Boca Raton, 2010.

B. Scherrer, A. Gholipour, and S.K. Warfield. Super-resolution reconstruction to increase the spatial resolution of diffusion weighted images from orthogonal anisotropic acquisitions. *Medical Image Analysis*, 16(7):1465–1476, 2012.

N. Stikov, M. Boudreau, I.R. Levesque, C.L. Tardif, J.K. Barral, and G.B. Pike. On the accuracy of T1 mapping: Searching for common ground. *Magnetic Resonance in Medicine*, 73(2):514–522, 2015.

P. Tofts. *Quantitative MRI of the Brain*. John Wiley & Sons, New York, 2005.

L. Truyen, J.H. van Waesberghe, M.A. van Walderveen, B.W. van Oosten, C.H. Polman, O.R. Hommes, H.J. Ader, and F. Barkhof. Accumulation of hypointense lesions ("black holes") on T1 spin-echo MRI correlates with disease progression in multiple sclerosis. *Neurology*, 47(6):1469–76, 1996.

J.D. Trzasko, P.M. Mostardi, S.J. Riederer, and A. Manduca. Estimating T1 from multichannel variable flip angle SPGR sequences. *Magnetic Resonance in Medicine*, 69(6):1787–94, 2013.

P. van Gelderen, X. Jian, and J.H. Duyn. Effects of magnetization transfer on T1 contrast in human brain white matter. *NeuroImage*, 128:85–95, 2016.

E. Van Reeth and I. Tham. Super-resolution in magnetic resonance imaging: A review. *Concepts in Magnetic Resonance A*, 40(6):306–325, 2012.

J.P. Wansapura, S.K. Holland, R.S. Dunn, and W.S. jr. Ball. NMR relaxation times in the human brain at 3.0 tesla. *Journal of Magnetic Resonance Imaging*, 9(4):531–8, 1999.

P.J. Wright, O.E. Mougin, J.J. Totman, A.M. Peters, M.J. Brookes, R. Coxon, P.E. Morris, M. Clemence, S.T. Francis, R.W. Bowtell, and P.A. Gowland. Water proton T1 measurements in brain tissue at 7, 3, and 1.5 T using IR-EPI, IR-TSE, and MPRAGE: results and optimization. *Magnetic Resonance Materials in Physics, Biology and Medicine*, 21(1-2):121–130, 2008.

D.C. Zhu and R.D. Penn. Full-brain T1 mapping through inversion recovery fast spin echo imaging with time-efficient slice ordering. *Magnetic Resonance in Medicine*, 54(3):725–731, 2005.

6

Super-resolution Diffusion MRI

Contents

The work in this chapter has been published in:

- **G. Van Steenkiste**, B. Jeurissen, J. Veraart, A.J. den Dekker, P.M. Parizel, D.H.J. Poot, and J. Sijbers. Super-resolution reconstruction of diffusion parameters from diffusion-weighted images with different slice orientations. *Magnetic Resonance in Medicine*, 75(1):181–195, 2016

- **G. Van Steenkiste**, B. Jeurissen, J. Sijbers, and D.H.J. Poot. Super resolution reconstruction from differently oriented diffusion tensor data sets. In *Proceedings of the ISMRM Benelux*, volume 5, Rotterdam, The Netherlands, 2013a

- **G. Van Steenkiste**, B. Jeurissen, J. Sijbers, and D.H.J. Poot. Super resolution reconstruction from differently oriented diffusion tensor data sets. In *Proceedings of the International Society for Magnetic Resonance in Medicine*, volume 21, page 3186, Salt Lake City, Utah, USA, 2013b

- **G. Van Steenkiste**, B. Jeurrisen, D.H.J. Poot, and J. Sijbers. Super-resolution reconstruction of diffusion tensor parameters from multi-oriented diffusion weighted images. In *Proceedings of the workshop "Imaging the brain at different scales: How to integrate multi-scale structural information?"*, Antwerp, Belgium, 2013c

- **G. Van Steenkiste**, B. Jeurissen, D.H.J. Poot, P.M. Parizel, and J. Sijbers. Super-resolution reconstruction of diffusion parameters from multi-oriented diffusion weighted images. In *Proceedings of the ISMRM Benelux*, volume 6, page 39, Maastricht, The Netherlands, 2014a

- **G. Van Steenkiste**, B. Jeurissen, D.H.J. Poot, and J. Sijbers. Super-resolution reconstruction of diffusion parameters from multi-oriented diffusion weighted images. In *Proceedings of the International Society for Magnetic Resonance in Medicine*, volume 22, page 2572, Milan, Italy, 2014b

6.1 Introduction

Diffusion MRI (dMRI) is a noninvasive imaging modality that allows in vivo investigation and characterization of tissue microstructure [Bammer, 2003, Basser et al., 1994]. The presence of diffusion of water molecules will attenuate the signal in the diffusion weighted (DW) images [Stejskal and Tanner, 1965]. Consequently, the signal-to-noise ratio (SNR) of DW images is relatively low. Also, modeling the 3D diffusion requires many DW images, resulting in long scan times and high risk for subject motion. To obtain DW images with a reasonable SNR within a clinically feasible scan time, it is common to acquire DW images with low spatial resolution compared to structural MRI images. In a clinical setting, DW images are typically acquired at a resolution ranging from 2 to 3 mm isotropic [Alexander, 2007]. Given that the diameter of an axon is of the order of $1\,\mu m - 20\,\mu m$, large partial volume effects will occur [Alexander, 2007, Oouchi et al., 2007]. In fact, a recent study has shown that, at the current resolution, the diffusion tensor model (DTI model) is inadequate in the majority of white matter voxels as a result of partial volume effects, posing significant problems for DTI fiber tractography and the interpretation of DTI integrity metrics [Jeurissen et al., 2013]. Even though one is mostly interested in the imaging of bundles of axons, the low spatial resolution limits the use of dMRI to the investigation and characterization of large fiber bundles [Tuch et al., 2002]. Increasing the spatial resolution of dMRI would reduce partial volume effects and thereby enable resolving finer structures and smaller bundles of axons.

Improvement of the spatial resolution in an MR image requires sampling of higher frequencies in k-space. However, sampling a large k-space within a reasonable time frame is a challenging task. DW images are preferably acquired with multi-slice single-shot spin-echo echo planar imaging (ss-EPI) [Mansfield, 1984] or single shot fast spin echo (ss-FSE) sequences [Mansfield, 1977, Turner et al., 1990], which image a whole slice in a single excitation. These sequences provide a fast acquisition and are robust to motion and phase shifts caused by micro motion [Bammer et al., 2005, Skare and Bammer, 2011]. The time required to encode the k-space in a single shot is not negligible, so sampling a larger k-space leads to a larger echo time. Since increasing the echo time exponentially decreases the DW signal [Qin et al., 2009], encoding a larger k-space results in a drop of SNR. Clinical time constraints prohibit the use of extensive averaging to increase the SNR. Hence, there is an inherent trade-off between spatial resolution, SNR, and acquisition time.

Recent work has shown that super-resolution (SR) reconstruction methods (see chapter 4) can provide images with an improved trade-off of spatial resolution, SNR and acquisition time [Gholipour et al., 2010, Greenspan et al., 2002, Kuklisova-Murgasova et al., 2012, Oubel et al., 2012, Plenge et al., 2012, Poot et al., 2010, Ropele et al., 2010, Rousseau et al., 2006, Shilling et al., 2009, Greenspan, 2009, Van Reeth and Tham, 2012]. SR methods combine multiple low resolution images to obtain a high resolution image, where each low resolution image samples the high resolution scene in a different way. In dMRI, several SR methods have been proposed. In Fogtmann et al. [2014], Poot et al. [2013], Scherrer et al. [2012], SR methods developed for structural MRI were successfully applied to improve the through-plane resolution of DW images. In Fogtmann et al. [2014], Scherrer et al.

[2012], the low resolution DW images are acquired with three orthogonal slice orientations, while in Poot et al. [2013] arbitrary slice orientations are allowed. In addition to this type of SR methods, several alternative methods to achieve a high spatial resolution in dMRI have been proposed [Coupé et al., 2013, Nedjati-Gilani et al., 2008]. In Nedjati-Gilani et al. [2008], fiber configurations are recovered on a sub-voxel scale by posing the tractography as an inverse problem with regularization and in Coupé et al. [2013] resolution enhancement is obtained with single image SR techniques exploiting self-similarity across the orthogonal directions that differ in resolution.

The work presented in this chapter belongs to the class of SR methods that require a set of low resolution DW images with multiple slice orientations [Poot et al., 2013, Scherrer et al., 2012]. Those methods generate a set of high resolution DW images where each high resolution DW image is reconstructed from a set of low resolution DW images with the same diffusion weighting and gradient direction. Subsequently, high resolution diffusion parameters are computed from the reconstructed high resolution DW images. Consequently, the relationship between the low resolution DW images from different diffusion gradient directions, that is, the diffusion model, is ignored in the SR reconstruction, which may prevent its preservation in the reconstructed high resolution DW images. Recently, two SR methods that do include a diffusion model were proposed. One method uses the ball-and-stick model in combination with an SR model [Tobisch et al., 2014]. Although this method shows promising results on simulated data, no clinical data experiments have been reported. Moreover, this method does not provide a solution for EPI distortions nor for motion and eddy current distortions. The other method reconstructs 3D DTI parameters iteratively from motion scattered multi-slice DWI sequences acquired from a moving fetal brain [Fogtmann et al., 2014]. However, the acquisition of both methods is restricted to orthogonal DWI stacks, limiting the resolution gain, as will be explained in the methods section. Additionally, all currently available SR methods acquire the same set of q-space points for each slice orientation, which, as we will show, does not optimally samples the q-space. To solve these limitations, we propose an SR method with an integrated diffusion model that directly estimates the diffusion parameters from the low resolution DW images. Additionally, we propose an optimal k- and q-space sampling scheme for the set of low resolution DW images. The main advantage of our approach is that the reconstruction algorithm can deal with and even benefit from arbitrary diffusion gradient and slice orientations as low resolution input.

6.2 Super-resolution diffusion weighted imaging

One way to implement super-resolution in diffusion MRI is by reconstructing a high resolution DW image for each diffusion gradient direction [Poot et al., 2013, Scherrer et al., 2012]. The high resolution DW images are reconstructed using the SR method explained in sections sections 4.4.2 and 4.4.3. From these high resolution DW images, high resolution DT parameters can then be estimated using the DTI model (Eq. 3.12). In this chapter we will call this method the SR-DWI method.

6.3 Super-resolution diffusion tensor imaging

Any diffusion model can be combined with our SR model. Nevertheless, for the sake of simplicity, the methodology and experiments will be explained using the DTI model (Eq. 3.12) as it is one of the simplest and widely used diffusion models.

6.3.1 Log DTI model

Let $\boldsymbol{r}_m \in \mathbb{R}^{N_{\boldsymbol{r}} \times 1}$ ($m = 1, ..., M$, with M the number of images) denote a vector representing the $N_{\boldsymbol{r}}$ (unknown) intensities $r_m(j)$ (with j the voxel index, $j = 1, ..., N_{\boldsymbol{r}}$) of a noiseless, high resolution DW image sampled at the N_r 3D grid points $\boldsymbol{x} \in \mathbb{R}^{3 \times N_r}$. Then, the noise free signal intensity in voxel j of $\boldsymbol{r}_m$ may be described as:

$$\boldsymbol{r}_m(j) = \boldsymbol{r}_0(j) e^{-b_m \boldsymbol{g}_m^T \boldsymbol{D}(j) \boldsymbol{g}_m}, \tag{6.1}$$

with $\boldsymbol{g}_m$, b_m the diffusion gradient direction and diffusion weighted strength with which $\boldsymbol{r}_m$ is acquired, $\boldsymbol{D}(j)$ the diffusion tensor in voxel j and $\boldsymbol{r}_0$ the non-DW signal.

To ensure that the result of the SR-DTI is a positive-definite tensor and to simplify the regularization, we re-parametrize the diffusion tensor $\boldsymbol{D}(j)$ in Eq. 6.1 by its matrix logarithm [Arsigny et al., 2006]

$$\tilde{\boldsymbol{D}}(j) = \log \boldsymbol{D}(j). \tag{6.2}$$

6.3.2 SR-DTI model

Assume that $\boldsymbol{r}_m$ is a vector of intensities representing the high resolution DW image, which serves as the ground truth (GT) image from which an low resolution image $\boldsymbol{s}_m$ is acquired. Let $\boldsymbol{s}_m \in \mathbb{R}^{N_{\boldsymbol{s}} \times 1}$ be a vector representing the $N_{\boldsymbol{s}}$ signal intensities $s_m(l)$ (with l the voxel index, $l = 1, ..., N_{\boldsymbol{s}}$) of a noiseless low resolution DW image sampled at the N_s 3D grid points $\boldsymbol{y} \in \mathbb{R}^{3 \times N_s}$. Assume that $\boldsymbol{s}_m$ is acquired with the same diffusion gradient direction $\boldsymbol{g}_m$ and diffusion weighted strength b_m. According to Eq. 4.2, the signal magnitude in voxel l of $\boldsymbol{s}_m$ can be related to the voxel intensities of $\boldsymbol{r}_m$ by

$$s_m(l) = \left| \sum_{j=1}^{N_r} a_m(l, j) r_m(j) \right|, \tag{6.3}$$

with $\boldsymbol{A}_m = (a_m(l, j)) \in \mathbb{R}^{N_{\boldsymbol{s}} \times N_{\boldsymbol{r}}}$ a linear operator defining the transformation of the high resolution DW image $\boldsymbol{r}_m$ to the low resolution DW image $\boldsymbol{s}_m$ as described in Eq. 4.4.

The acquired image $\boldsymbol{S}_m$ can be modeled as $\boldsymbol{S}_m(l) = \boldsymbol{s}_m(l) + \boldsymbol{e}_m(l)$, with $\boldsymbol{e}_m(l)$ the measurement noise in voxel l. Note that the image is Rician distributed but that for high SNR (SNR >5), the noise can be assumed to be Gaussian distributed [den Dekker and Sijbers, 2014].

By substituting Eq. 6.1 and Eq. 6.2 into Eq. 6.3, the low resolution DW images $\boldsymbol{s}_m$ are predicted from the high resolution non-DW image intensity $\boldsymbol{r}_0$ and the

matrix logarithm of the high resolution diffusion tensor $\tilde{\boldsymbol{D}}$:

$$\boldsymbol{s}_m(l) = \sum_{j=1}^{N_{\boldsymbol{r}}} a_m(l,j)\boldsymbol{r}_0(j)e^{-b_m \boldsymbol{g}_m^T \exp(\tilde{\boldsymbol{D}}(j))\boldsymbol{g}_m}. \tag{6.4}$$

6.3.3 SR-DTI estimation

The high DTI parameters can be estimated by

$$\hat{\tilde{\boldsymbol{D}}}, \hat{\boldsymbol{r}_0} = \arg\min_{\tilde{\boldsymbol{D}}, \boldsymbol{r}_0} \sum_{m=1}^{M} \sum_{l=1}^{N_{\boldsymbol{s}}} \|s_m(l) - S_m(l)\|_2^2 + \boldsymbol{\lambda} R(\tilde{\boldsymbol{D}}, \boldsymbol{r}_0), \tag{6.5}$$

where $\boldsymbol{s}_m$ is a function of $\tilde{\boldsymbol{D}}$ and $\boldsymbol{r}_0$ as given by Eq. 6.4, $R(\tilde{\boldsymbol{D}}, \boldsymbol{r}_0)$ is a regularization function and λ its corresponding weighting factor. The regularization term $R(\tilde{\boldsymbol{D}}, \boldsymbol{r}_0)$ is required since the HR grid generally contains spatial frequencies that are not sampled by any of the LR DW images. Since the log diffusion tensor is estimated, the regularization is performed in the log-Euclidian domain [Arsigny et al., 2006]. As such, the same regularization as in [Poot et al., 2013] can be used. In this regularization term, the high frequencies are minimized by computing the squared Laplacian of the reconstructed log diffusion tensor $\tilde{\boldsymbol{D}}$ and the logarithm of the non-DW image intensity $\boldsymbol{r}_0$.

6.3.4 SR-DTI implementation

In the in vivo experiments described in 6.4.2 the motion operator $\boldsymbol{M}_m$ (Eq. 4.4) that models the motion in between the different low resolution DW images and the eddy current effects, is obtained by affinely registering the low resolution DW images to each other, for example using Elastix [Klein et al., 2010]. By incorporating the motion and eddy current distortions in the acquisition model, the original acquired low resolution DW images can be used as input for the SR-DTI method. So, in contrast with [Scherrer et al., 2012], the high resolution DTI parameters are estimated from the acquired low resolution DW images and not from interpolated low resolution DW images, resulting in a more accurate model. From the affine transformation, $\boldsymbol{M}_m$, the corresponding rotation matrix is derived, which in turn is used to rotate the diffusion gradient directions [Leemans et al., 2009]. As the proposed SR-DTI method can deal with arbitrary diffusion gradient directions, compared to [Oubel et al., 2012] and [Scherrer et al., 2012], no interpolation in q-space is needed. $\boldsymbol{M}_m$ and $\boldsymbol{T}_m$ are both affine transformations and are combined into one affine transformation. The multiplication with $\boldsymbol{A}$, which is specified by this combined transformation, is applied efficiently using shear transformations as described in [Poot et al., 2010].

The nonlinear least squares problem stated in Eq. 6.5 is solved using a trust-region Newton method [Coleman and Li, 1996]. The problem is very 'large-scale' due to the large number of parameters and the coupling between the parameters. The combination of the low resolution data, the reconstructed high resolution DTI parameters and the gradients and Hessians needed in the optimization method, requires a large amount of memory. To reduce memory consumption and the

number of iterations required by the optimization, the region of interest (ROI), e.g. the brain in human brain scans, is split in several blocks, where the high resolution DTI parameters are reconstructed in each block separately.In the experiments, the blocks were $30 \times 30 \times 30$ voxels and had an overlap of 5 voxels in each dimension to avoid block edge artifacts.

To initialize $\tilde{\boldsymbol{D}}$ and $\boldsymbol{r}_0$, first all low resolution DW images were transformed to the high resolution grid with the adjoint transformation $\boldsymbol{A}'_m$. Next, the logarithm of the diffusion tensor was estimated from these images by a non-linear Log-Euclidean framework [Arsigny et al., 2006]. Finally, the logarithm of the high resolution diffusion tensor (Eq. 6.2) and the non-DW signal $\boldsymbol{r}_0$ served as the initialization for the reconstruction.

6.3.5 SR-DTI acquisition set-up

As explained in section 4.3, only the resolution in the slice direction can be improved, therefore the low resolution DW images are acquired with an isotropic in-plane resolution and a slice thickness larger than the in-plane resolution.

In practice, DW images are often acquired with an ss-EPI sequence because of its short measuring times and robustness to phase shifts. Unfortunately, ss-EPI images generally suffer from geometric distortions along the phase encoding direction. Hence, if the low resolution DW images would be acquired with different phase encoding directions, the distortions would, for each low resolution DW image, show up in a different direction, which would result in blurring of the high resolution image. To avoid phase encoding direction dependent distortions, the low resolution DW images are acquired with identical phase encoding directions and thus rotate the frequency and slice encoding axis around the phase encoding axis. The number of slice orientations is chosen following Eq. 4.1.

6.3.5.1 Q-space sampling

In dMRI, not only the spatial resolution is important, but also the angular resolution in q-space [Basser, 2002]. Note that for our method, in contrast to [Poot et al., 2013] and [Scherrer et al., 2012], it is not necessary to use the same set of diffusion gradient directions for each slice orientation. Indeed, the integration of the DTI model into the reconstruction allows low resolution DW images to be acquired with an arbitrary mix of diffusion gradient directions and slice orientations. As such, each low resolution DW image can be acquired with a different gradient direction (sample a different point in q-space), resulting in a denser sampling of the q-space. This denser sampling leads to increased angular resolution and rotation invariant diffusion parameter estimation [Landman et al., 2007]. To obtain uniform q-space sampling, not only the q-space of all the acquired low resolution DW images combined, but also of each group of low resolution DW images with the same slice orientation needs to be sampled uniformly as each group also samples a different part of k-space. The uniform sampling at both levels is achieved with the method of electrostatic repulsion in multiple shells [Caruyer et al., 2013]. Fig. 6.1 shows the classic q-space sampling as used in SR-DWI (Fig. 6.1a) and our proposed q-space sampling (Fig. 6.1b).

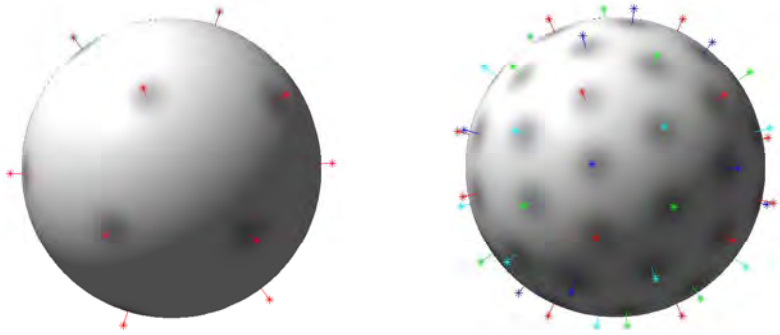

(a) (b)

Fig. 6.1: Sampling strategy for q-space for SR experiment with seven low resolution images with AF = 4: (a) classic q-space sampling and (b) proposed q-space sampling. Each slice orientation is differently colour coded, so the diffusion gradient directions with the same colour belong to the same slice orientation. Note that each diffusion gradient direction in the classical sampled q-space (a) is sampled 4 times.

6.4 Experiments

The SR-DTI method and proposed q-space sampling is validated using a series of experiments that were performed on simulated (section 6.4.1) as well as in vivo data (section 6.4.2). SR-DTI was compared to both SR-DWI (section 6.2) and direct high and low resolution acquisitions.

6.4.1 Simulations

6.4.1.1 Generation of synthetic data

The Numerical Fiber Generator [Close et al., 2009] was used to simulate a noiseless $48 \times 48 \times 48$ DW data set with 1 non-DW image ($b = 0\,\mathrm{s/mm^2}$) and 64 DW images ($b = 1000\,\mathrm{s/mm^2}$). From this DW data set, DTI parameters were calculated, which served as ground truth data set. Based on Eq. 6.4, Rician distributed data sets with anisotropic voxel size and a noise level of $\sigma = 0.2$ were simulated from this ground truth data set. Table 6.1 shows the detailed settings of the simulated images. For each data set, the total number of slices ($M \cdot n_s$, n_s being the number of slices per image) and the in-plane resolution are equal. So, given that the acquisition time of one slice, T_s, is independent of the slice thickness, the total acquisition time, $T_{acq} = M n_s T_s$, is equal for all data sets. The number of slice orientations, n, was chosen according to Eq. 4.1, with the exception of the data set with AF = 6, where $n = 12$ was chosen to obtain a more similar acquisition time. Table 6.1 also defines the naming scheme of the simulated data sets and the corresponding DT estimates. The first part of the name refers to the type of DW data set, where GT refers to the ground truth data set, HR to a high resolution data set, and LR to a low resolution data set. The second part refers to the AF. A 'c' at the end means the classic q-space sampling is used, a 'p' means the proposed q-space sampling is

data	AF	n_S	n	N_{DW}	M	SNR	q-sampling	method	SR result
GT	1	48	1	64	65	∞	classic	DTI	GTDT
HR	1	48	1	14	15	5	classic	DTI	HRDT
LR2	2	24	1	31	32	10	classic	DTI	LRDT2
LR2c	2	24	4	7	32	10	classic	SR-DWI	SRDW2c
								SR-DTI	SRDT2c
LR2p	2	24	4	7	32	10	proposed	SR-DTI	SRDT2p
LR4	4	12	1	62	63	20	classic	DTI	LRDT4
LR4c	4	12	7	8	63	20	classic	SR DWI	SRDW4c
								SR-DTI	SRDT4c
LR4p	4	12	7	8	63	20	proposed	SR-DTI	SRDT4p
LR6	6	8	1	95	96	30	classic	DTI	LRDT6
LR6c	6	8	12	7	96	30	classic	SR-DWI	SRDW6c
								SR-DTI	SRDT6c
LR6p	6	8	12	7	96	30	proposed	SR-DTI	SRDT6p

Table 6.1: Overview of the simulated HR and LR DW data sets. n_S is the number of slices per image, n the number of slice orientations, N_{DW} the number of DW images per slice orientation, M the total number of LR images. The SNR is calculated in the non-DW image.

used. The names of the reconstructed data sets are built in the same way, where the first part indicates the used SR method. When no SR method is used, the first part of the name is kept the same as for the simulated data set.

6.4.1.2 Impact of proposed q-space sampling

Using the classic q-space sampling, at least six non-collinear diffusion gradient directions need to be acquired per slice orientation to avoid that the DTI parameter estimation problem becomes under-determined. This is not the case for the proposed q-space sampling as for each slice orientation a different set of diffusion gradient directions can be used. As such, the total number of non-collinear diffusion gradient directions can still exceed six when less than six diffusion gradient directions per slice orientation are used. To highlight the impact of the proposed q-space sampling, low resolution DW data sets with AF $= 2$ and a different number of diffusion gradient directions per slice orientation, N_{DW}, ranging from 2 to 20, were simulated from the ground truth data set. As these low resolution DW data sets have a different number of low resolution DW images, their acquisition time will not be the same.

6.4.1.3 DTI estimation

From each low resolution DW data set, DTI parameters were reconstructed on a high resolution grid of $48 \times 48 \times 48$ using the SR-DTI method. Additionally, from the low resolution DW data sets with classic q-space sampling, N_{DW} $48 \times 48 \times 48$ high resolution DW images were reconstructed with the SR-DWI method. From

these high resolution DW images, high resolution DTI parameters were estimated with the Log-Euclidian framework. The regularization factor λ was chosen so that the total root-mean-square error (RMSE) on the DTI parameters was minimal. High resolution DTI parameters were estimated from the high resolution data set with the log-Euclidian framework.

6.4.1.4 Quantification of reconstruction

To quantify the reconstruction results, each data set was simulated with 50 noise realizations. Using the ground truth data set, for each of the 50 reconstructions, the RMSE of the fractional anisotropy (RMSE FA), the RMSE of the mean diffusivity (RMSE MD) and the median angular error of the first eigenvector (MAE FE) were calculated. These errors incorporate both the variance and the bias of the reconstruction and are often used to quantify the uncertainty of DTI parameter estimation [Coupé et al., 2013, Poot et al., 2013].

6.4.2 In vivo data

6.4.2.1 Acquisition

For the evaluation of the proposed SR-DTI method with human in vivo data, six data sets of a single healthy 27-year old volunteer were acquired with a Trio Scanner (3T; Siemens AG, Siemens Medical Solution, Erlangen, Germany) with a 32-channel head coil. The acquisition parameters were chosen such that the acquisition time was similar for all DW data sets. The in-plane resolution of all DW data sets, except the isotropic low resolution data set LRi DTI, was 1.5 mm × 1.5 mm and the slice thickness was AF ·1.5 mm. All the DW data sets were acquired with a multi-slice ss-EPI sequence without a slice gap and no averaging. As many acquisition parameters as possible were kept the same in each data set: the field of view 237 mm × 237 mm × 192 mm, acquisition matrix 158 × 158 with 119 phase encoding steps, 100% sampling and the pixel bandwidth 1666 Hz. The non-DW images were acquired with $b = 0\,\mathrm{s/mm^2}$, the DW images with $b = 1000\,\mathrm{s/mm^2}$. Data sets ending with c were acquired with the classic q-space sampling, those ending with p with the proposed q-space sampling. The subsets were acquired with a different slice orientation rotated around the phase encoding axis.

- **LR2p and LR2c**: DW data sets with voxel dimensions 1.5 mm × 1.5 mm × 3 mm (AF = 2) consisting of 4 subsets of DW images. Each subset included 1 non-DW image and 7 DW images and each DW image had a $T_R = 9700$ ms, $T_E = 97$ ms and 64 slices. The total scanning time was 5.17 min.

- **LR4p and LR4c**: DW data sets with voxel dimensions 1.5 mm × 1.5 mm × 6 mm (AF = 4) consisting of 7 subsets of DW images. Each subset included 1 non-DW image and 8 DW images and each DW image had a $T_R = 4900$ ms, $T_E = 97$ ms and 32 slices. The total scanning time was 5.14 min.

- **HRi**: DW data set with voxel dimensions 1.5 mm × 1.5 mm × 1.5 mm, consisting of 1 non-DW image and 14 DW images. Each DW image had a

$T_R = 19\,426$ ms, $T_E = 97.4$ ms and 128 slices. The total scanning time was 4.85 min.

- **LRi**: DW data set with voxel dimensions 2.5 mm × 2.5 mm × 2.5 mm and acquisition matrix 104 × 104, consisting of 1 non-DW image, and 15 DW images.Each DW image had a $T_R = 16\,900$ ms, $T_E = 98$ ms and 69 slices. The total scanning time was 4.51 min.

The lowest TR = 4900 ms is still substantially larger than the T_1 of gray and white matter in the brain (0.9 s-1.4 s, Wright et al. [2008]). Hence, no significant influence of incomplete T_1 relaxation is expected.

To highlight the impact of the proposed q-space sampling, data sets with less than six diffusion gradient directions per slice orientation were created from the LR2p and LR4p data sets. For each acquisition orientation the appropriate number of diffusion gradient directions were selected from the existing 7 or 8 diffusion gradient directions. It is important to notice that in this way, the data sets will have a suboptimal q-space sampling. Moreover, these low resolution DW data sets will have a reduced acquisition time as they contain less DW images.

- **LR2p D5**: LR2p data set with for each of the 4 subsets 1 non-DW image and 5 DW images. The total scanning time would be 3.88 min.

- **LR4p D5**: LR4p data set with for each of the 7 subsets 1 non-DW image and 5 DW images. The total scanning time would be 3.43 min.

- **LR4p D4**: LR4p data set with for each of the 7 subsets 1 non-DW image and 4 DW images. The total scanning time would be 2.86 min.

6.4.2.2 DT estimation and tractography

Each of the anisotropic low resolution DW data sets was used to construct high resolution DTI parameters, with voxel dimensions 1.5 mm × 1.5 mm × 1.5 mm. For the two data sets with classic q-space sampling, LR2c and LR4c the SR-DWI method was used, resulting in the SRDW2 and SRDW4 estimates respectively. The data sets, LR2p (D5) and LR4p (D4 and D5), acquired with the proposed q-space sampling, were reconstructed with the SR-DTI method, resulting in the SRDT2p (D4) and SRDT4p (D4 and D5) estimates, respectively. DTI parameters were directly estimated from the data sets HRi and LRi using the log-Euclidian framework. For each reconstruction, the FA and directionally encoded (DEC) FA map were calculated. Furthermore, whole brain deterministic DTI tractography was performed using MRtrix3 [Tournier et al., 2012]. For each data set, a streamline was launched from fixed equidistant seed points throughout the brain. The minimum fiber length was set to 10 mm, the FA threshold to 0.1 and the step size to 0.15 mm. The SNR of the non-DW image of each of the acquired DW data sets was computed by calculating the ratio of the mean and standard deviation of a uniform region in the corpus callosum.

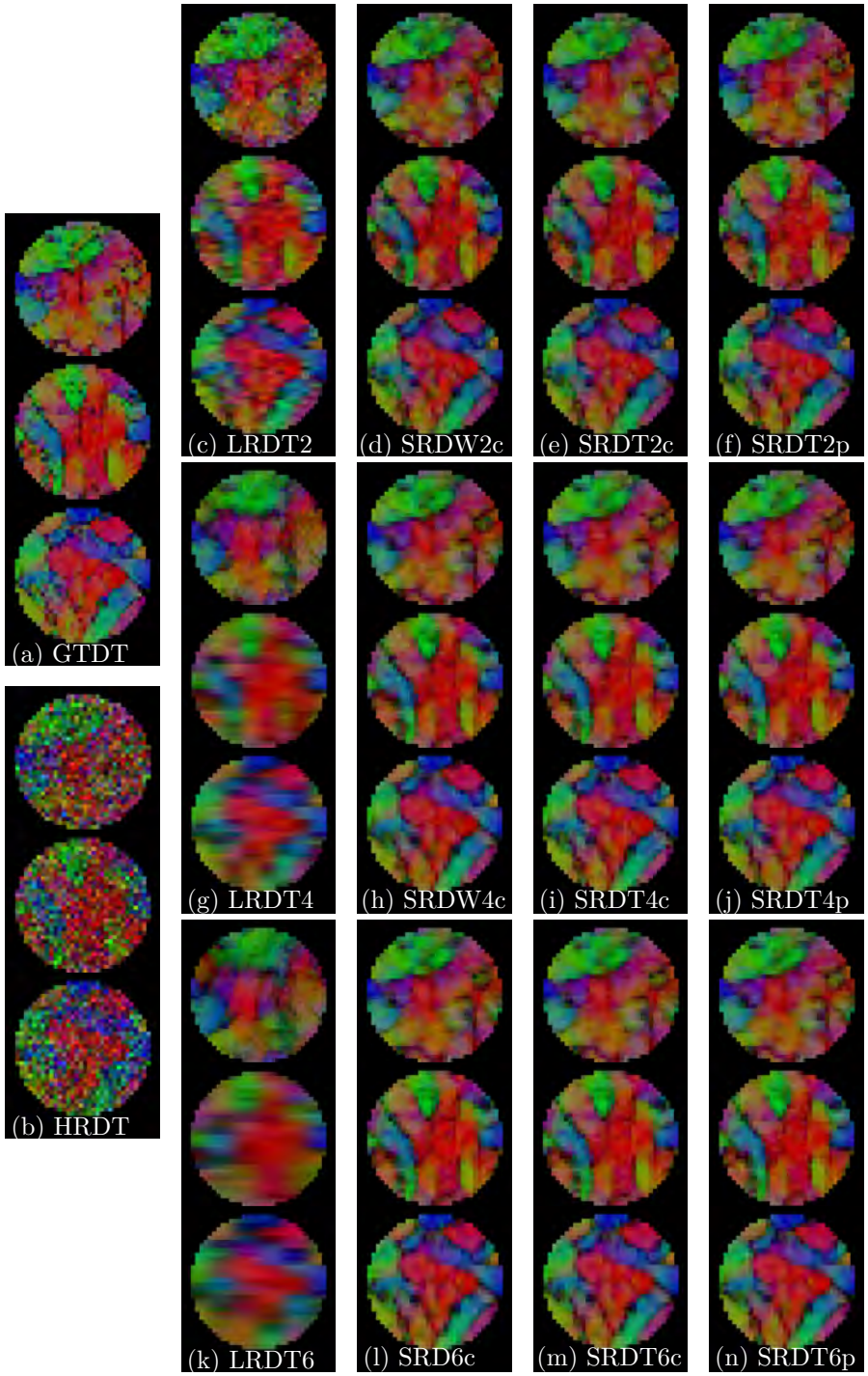

Fig. 6.2: Three orthogonal views of the DEC FA map of the simulated phantom, with directions left - right (red), up - down (blue) and back - front (green) for different data sets which all have the same acquisition time.

6.4.2.3 Quantification of estimation

To quantify the resolution of the (reconstructed) volunteer data sets, the FA along a line segment was plotted for several line segments crossing a border between structures with different FA. The FA on the line segments is obtained by cubic spline interpolation on the FA image. As resolution proxy the apparent width of the anatomically step wise transition in FA is used. This width is defined as the distance between 10% and 90% of the step in FA value. Additionally, to quantify the noise in the FA images, the standard deviation of the high resolution FA maps was computed in a uniform region in the corpus callosum.

6.5 Results

6.5.1 Simulations

Figure 6.2 shows the DEC FA maps constructed from the different simulated data sets. Compared to the data set HRDT (Fig. 6.2b), the anisotropic low resolution data sets (Fig. 6.2c, g and k) have a higher SNR. However, due to the lower through-plane resolution, partial volume effects appear and fine details are lost. These partial volume effects increase with increasing AF. From Fig. 6.2d-f, h-j and l-n it is clear that all the SR data sets show an improvement in details compared to the low resolution DW data sets they stem from. Furthermore, compared with the data set HRDT, smaller details are no longer concealed by the noise. The images closely resemble the ground truth data (Fig. 6.2a). This is confirmed by the quantitative evaluations given in Fig. 6.3, where the error bars represent the 95% confidence interval based on 50 noise realisations. The RMSE FA, MAE FE and RMSE MD are significantly higher for the data set HRDT than for the SR data sets.

6.5.1.1 SR-DTI versus SR-DWI

When the SRDW2c map (Fig. 6.2d) is compared with the SRDT2c and SRDT2p maps (Fig. 6.2e-f), small differences can be observed. Figure 6.3 shows that the RMSE FA and MAE FE are significantly smaller for SR-DTI than for SR-DWI for all AFs. The RMSE MD is not significantly different when low resolution DW images with AF 4 or 6 are used, combined with SR-DTI or SR-DWI. The quantitative measures indicate that using data sets with a higher AF results in a better reconstruction, as all the quantitative measures decrease with increasing AF.

6.5.1.2 Q-space sampling

The differences in the SR-DTI maps with classic (Fig. 6.2e, i, m) and proposed q-space sampling (Fig. 6.2f, j, n) are small and hard to observe. The differences in the quantitative measures (Fig. 6.3) are more clear: the RMSE FA and MAE FE are significant smaller for the SR-DTI reconstructions with the proposed q-space sampling. In the RMSE MD no significantly differences can be observed between the proposed and classic q-space sampling. With increasing AF, the differences in RMSE FA and MAE FE between the classic and proposed q-space sampling decrease.

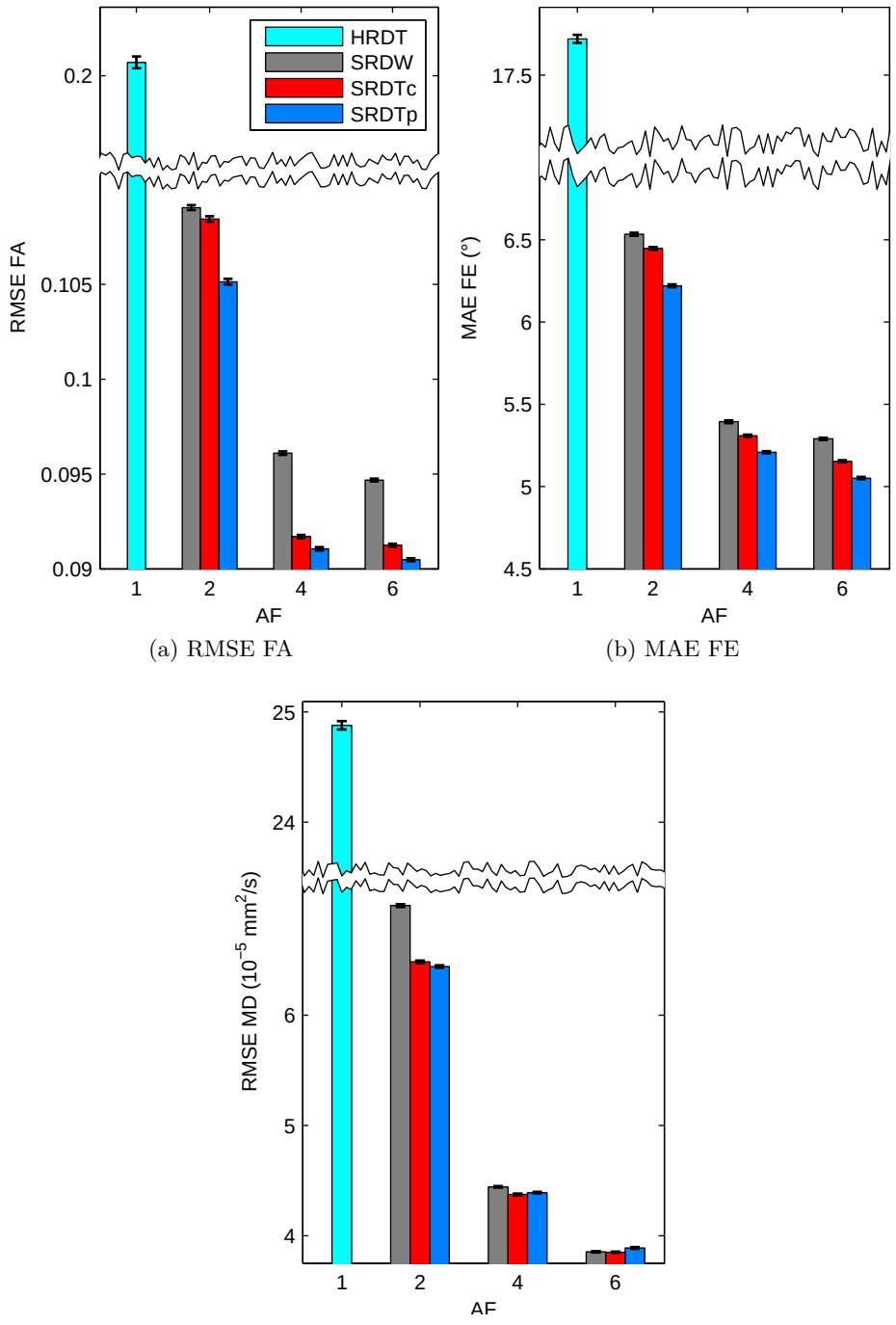

(a) RMSE FA

(b) MAE FE

(c) RMSE MD

Fig. 6.3: Quantitative evaluation of the simulation results. (a) RMSE FA (b) MAE FE and (c) RMSE MD for each of the SR data sets. All the data sets have the same acquisition time. The error bars correspond with the 95% confidence intervals.

6.5.1.3 Influence of number of low resolution DW

In Fig. 6.4, the RMSE FA, MAE FE and RMSE MD are shown as a function of the number of diffusion gradient directions per slice orientation, N_{DW}. It is clear that the reconstruction improves when more low resolution DW images are used, which increases acquisition time. Each of the 4 slice orientations of the LR2p data set has a different set of diffusion gradient directions. As such, when N_{DW} is larger or equal to 2, the total number of diffusion gradient directions in the LR2p data set exceeds the required 6. Therefore, using SR-DTI, high resolution diffusion tensor parameters can be estimated from the LR2p data sets with a N_{DW} lower than 6. The graphs show that with lower N_{DW} and thus in a shorter acquisition time, the SR-DTI with the proposed q-space sampling reconstructs high resolution diffusion tensor parameters with a RMSE FA, MAE FE and RMSE MD comparable to the ones of the SR-DWI and SR-DTI from data with classic q-space sampling and a longer acquisition time. The experiment also shows that with increasing N_{DW}, the differences between the SR-DTI reconstruction from the proposed and from the classical q-space sampling decrease. Even with longer acquisition times and an increased N_{DW}, the SR-DTI method performs better than the SR-DWI method in terms of RMSE FA and RMSE MD.

6.5.2 In vivo data

The SNR values of the non-DW images are $\mathrm{SNR}_{\mathrm{HRi}} = 4.7$, $\mathrm{SNR}_{\mathrm{LR2}} = 8.4$ and $\mathrm{SNR}_{\mathrm{LR4}} = 15.2$. These values demonstrate that, as expected on theoretical grounds, the SNR in actual acquisitions is proportional to the slice thickness.

6.5.2.1 Visual evaluation

Figure 6.5 shows orthogonal slices of the DEC FA map for the high resolution acquisition (HRDT, Fig. 6.5a), low resolution acquisition (LRDT, Fig. 6.5b) and the SR acquisition (SRDT4p, Fig. 6.5c). The DEC FA map of the isotropic HRDT data (Fig. 6.5a) shows fine structures but clearly suffers from a low SNR. As a result, some of the fine details are lost in the noise. Although acquiring the data with a lower isotropic resolution (Fig. 6.5b) does improve the SNR, smaller structures are harder to distinguish due to partial volume effects. Figure 6.5c demonstrates that the SR-DTI method successfully recovers high resolution information while preserving the high SNR of the anisotropic low resolution data set they stem from. This can be even more appreciated from Fig. 6.6, which zooms in on the FA map for the different acquisitions and reconstructions. Figure 6.6 shows the differences between the SR-DWI and SR-DTI reconstruction results. Although the SR-DWI method (Fig. 6.6c and d) recovers most high resolution information, some structures are more clear in the SR-DTI FA maps (Fig. 6.6e and f).

6.5.2.2 Standard deviation on FA

The standard deviations on FA are given in Fig. 6.6. The HRDT FA map (Fig. 6.6a) has the highest standard deviation due to the presence of noise. The standard deviation of the FA maps of both SR methods are lower than the one of the HRDT

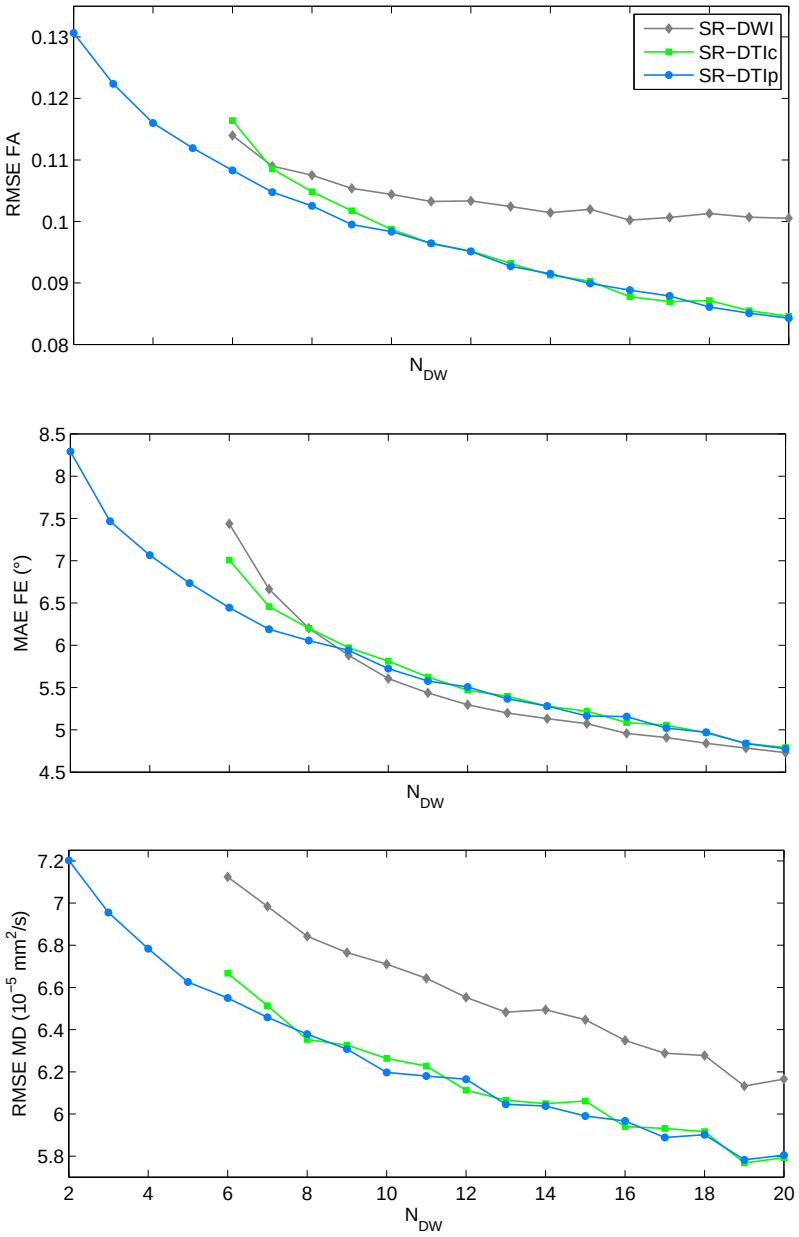

Fig. 6.4: RMSE FA, MAE FE and RMSE MD in function of the number of diffusion gradient directions per slice orientation (N_{DW}) for the different SRR methods if AF = 2. The acquisition time scales linearly with N_{DW}.

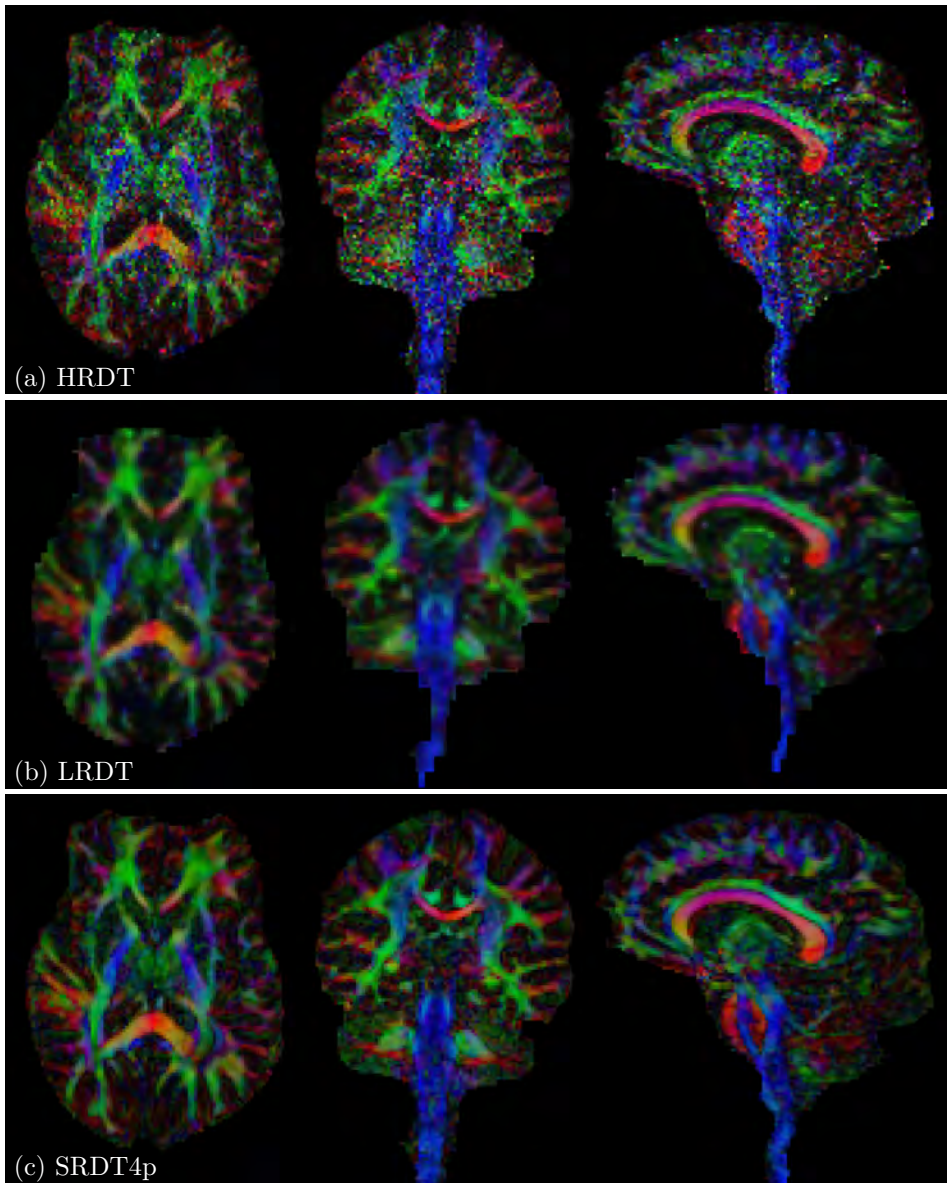

Fig. 6.5: Axial, sagittal and coronal slice of DEC FA maps (red: left - right, green: anterior-posterior, blue: superior - inferior) for different reconstructions. All displayed DEC FA maps have an isotropic voxel size of $1.5\,\mathrm{mm}^3$, the LRDT map is upsampled from $2.5\,\mathrm{mm}^3$ to $1.5\,\mathrm{mm}^3$ voxels using nearest-neighbor interpolation.

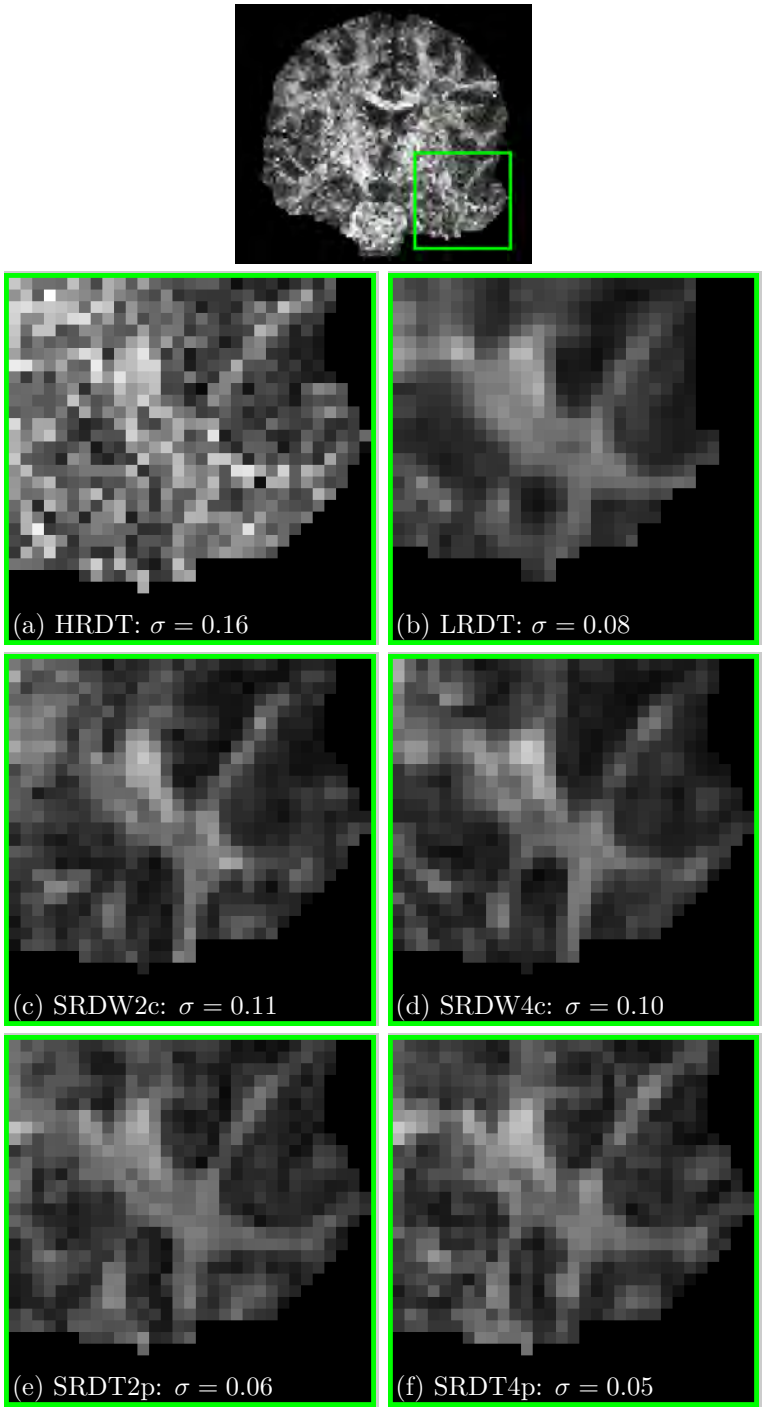

Fig. 6.6: Zoom in on the FA map (isotropic voxels: 1.5 mm) for the different DT data sets and estimations. σ denotes the standard deviation of FA calculated in a uniform region in the corpus callosum.

FA map and of the LRDT FA map (Fig. 6.6b). The SR-DTI FA maps (Fig. 6.6e and f) have a lower standard deviations than the SR-DWI FA maps (Fig. 6.6c and d). As the SNR increases with increasing AF, the standard deviation decreases with increasing AF.

6.5.2.3 Quantitative evaluation of the spatial resolution

Figure 6.8 shows the FA along a line segment for several line segments crossing a border between structures with different FA. The HRDT FA increases fast over a short distance, which is underpinned by the small width of the FA transition, but fluctuates due to the low SNR. The LRDT FA shows less fluctuations, but has a slower increase and the width of the FA transition is larger. Both the SR-DWI FA and the SR-DTI FA increase faster than the LRDT FA and show less fluctuations than the HRDT FA. The width of the FA transition is also smaller for SR-DWI and SR-DTI than for LRDT. Comparing the reconstructions derived from data sets with the same AF, the width of the FA transition is smaller for SR-DTI than for SR-DWI. Between different AFs, overall, the width of the FA transition is smaller for data sets with a higher AF.

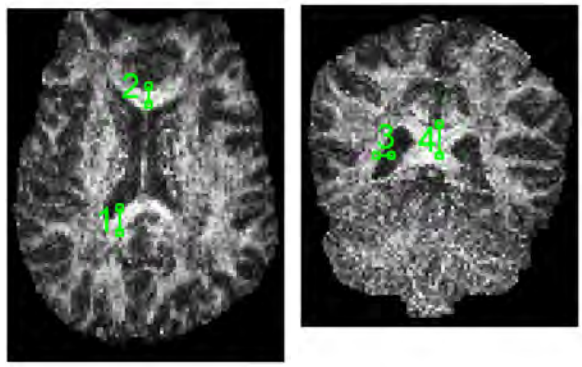

Fig. 6.7: FA images. The green lines depict the line segments used to calculated the width of FA transition given in table 6.2.

6.5.2.4 Evaluation of q-space sampling

In Fig. 6.9 orthogonal slices of the DEC FA maps for the SR-DTI reconstruction on the data sets with less than 6 diffusion gradient directions per slice orientation are shown. It is important to notice that the data sets from which these DEC FA maps are reconstructed, have a sub-optimal q-space sampling. As these data sets are a subset from the LR2p and LR4p data sets, their acquisition time is shorter than the one of the DEC FA maps shown in Fig. 6.5. Although these data sets have shorter acquisition time than the LRDT data set, their DEC FA maps show more details than the LRDT DEC FA map (Fig. 6.5b) and the width of the FA

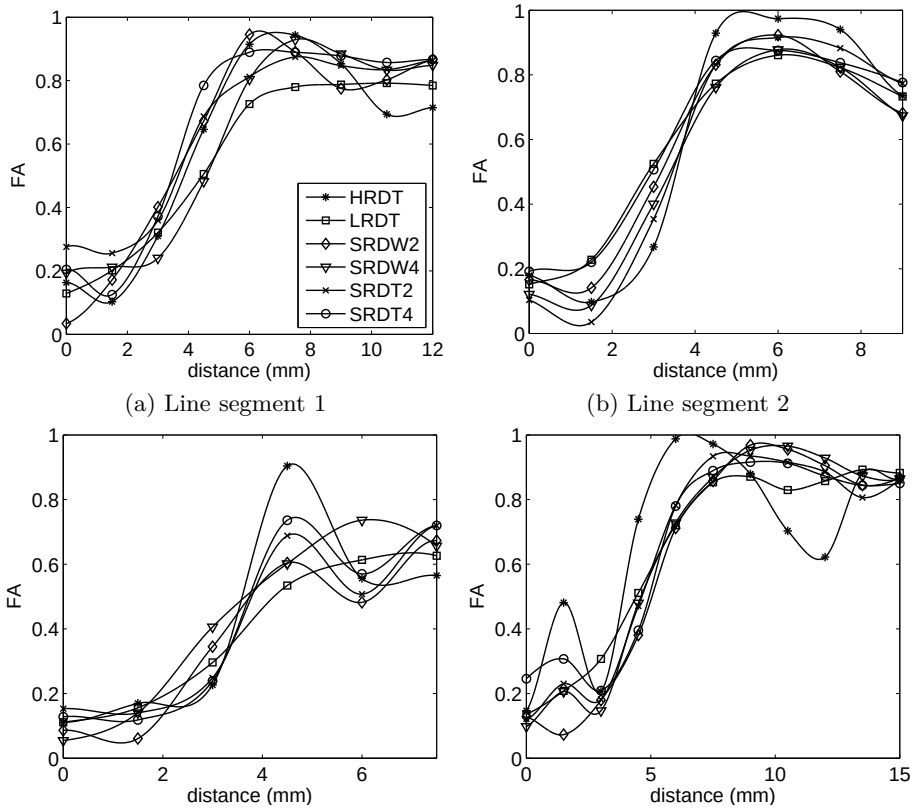

(a) Line segment 1

(b) Line segment 2

(c) Line segment 3

(d) Line segment 4

Fig. 6.8: FA line segments for the different acquisitions and reconstructions. The line segments are drawn on a high resolution FA map in Fig. 6.7

Line segment:	1	2	3	4
HRDT	3.32	1.71	0.72	1.66
LRDT	4.53	3.12	3.40	5.32
SRDW2	3.66	2.61	1.69	3.68
SRDW4	2.50	2.78	3.70	4.21
SRDT2	2.79	2.41	1.60	3.14
SRDT4	2.39	2.46	1.35	2.36
SRDT2 D5	3.14	2.19	1.57	2.39
SRDT4 D5	2.09	2.59	2.45	3.14
SRDT4 D4	3.50	2.57	1.90	2.84

Table 6.2: Width of FA transition across borders (mm). The line segments are plotted in Fig. 6.8 and drawn on a high resolution FA map in Fig. 6.7.

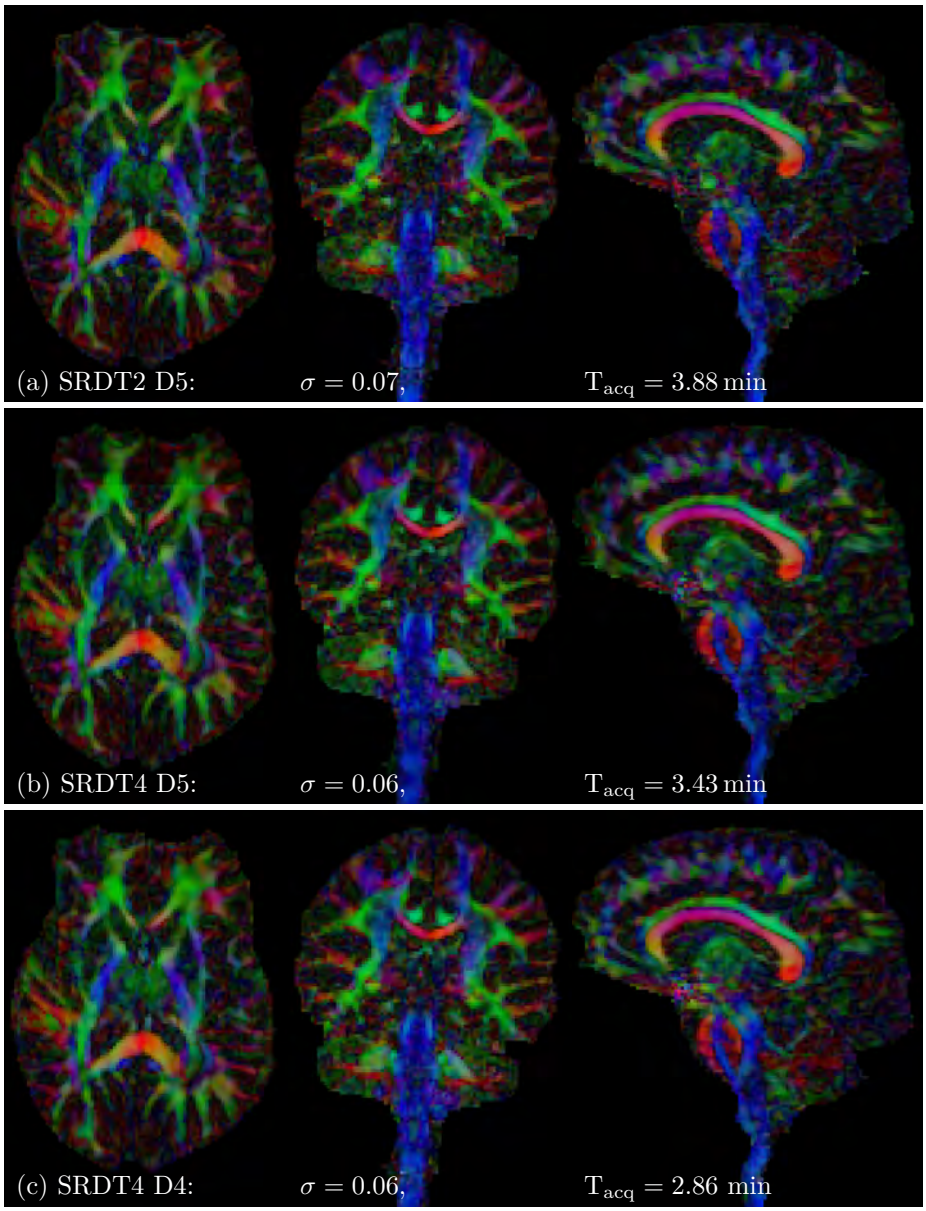

Fig. 6.9: Axial, sagittal and coronal slice of DEC FA maps with isotropic voxels (1.5 mm) (red: left - right, green: anterior-posterior, blue: superior - inferior) for different reconstructions from data sets with a limited number of diffusion gradient directions per slice orientation. σ denotes the standard deviation of FA calculated in a uniform region in the corpus callosum and T_{acq} denotes the acquisition time of the data set the DEC FA map stems from.

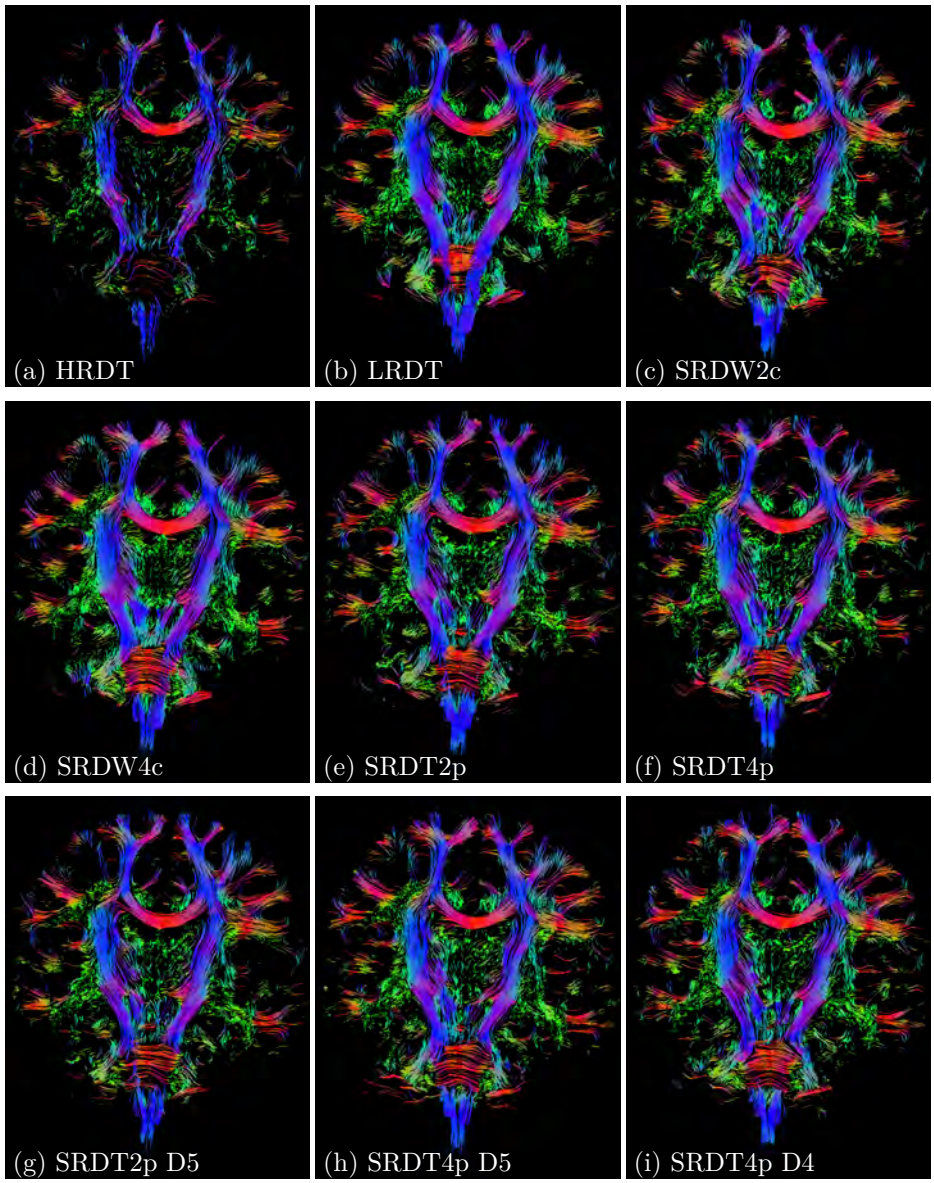

Fig. 6.10: Coronal slab visualization (thickness: 3 mm) through the corticospinal tracts of the whole brain tractography for different reconstructions. The two top rows have the same acquisition time, the acquisition time of the bottom row is shorter.

transition across the borders of two structures is smaller than for the LRDT data set (Fig. 6.8b). The standard deviation on FA is lower than the standard deviation on the HRDT FA.

6.5.2.5 Tractography

Figure 6.10 shows a slab visualization of the whole brain tractography results. The HRDT data set (Fig. 6.10a) provides a poor result with many short tracts due to the low SNR. The track density of the isotropic LRDT data set (Fig. 6.10b) and the SR data sets (Fig. 6.10c-i) is higher, due to their high SNR. The tracks are also longer for these data sets.

6.6 Discussion

Increasing the spatial resolution in DTI is a challenging task because of the trade-off between spatial resolution, SNR and acquisition time. To improve this trade-off, we have proposed an SR-DTI method that reconstructs high resolution diffusion tensor fields from multiple anisotropic low resolution DW images acquired with different slice orientations and diffusion gradient directions. By extending the SR method with the DTI model it is ensured that the solution of the reconstruction satisfies the DTI model. Moreover, the reconstruction of the high resolution DTI parameters is now performed in one step instead of two. Therefore errors will not propagate through the different steps of the reconstruction. Another advantage of the SR-DTI method is that the diffusion gradient directions and slice orientations can be arbitrarily selected. Opposed to the methods by Poot et al. [2013] and Scherrer et al. [2012], it is not required to acquire the same set of diffusion gradient directions for each slice orientation. The possibility to use a different diffusion gradient direction for each low resolution DW image results in a more extended sampling of the q-space. The experiments demonstrate an improved RMSE of the SR DTI parameters compared to those obtained from a high resolution DW acquisition with the same acquisition time. They also show an improvement compared to previously published reconstruction methods.

6.6.1 Motion correction

A correct spatial alignment of the low resolution DW images is crucial for SR. Incorrect registration of the images leads to blurring in the reconstruction and affects the estimated diffusion tensors. Therefore, motion correction with the corresponding b-matrix rotation is included in the SR-DTI method. Currently, the low resolution DW images are first affinely registered and the resulting transformation parameters are then used in the acquisition simulation of the low resolution DW images, to simulate the motion and eddy current effects. By doing so, the SR-DTI method starts from the original acquired low resolution DW images rather than from resampled low resolution DW images as in Scherrer et al. [2012]. The eddy current distortion correction is modeled together with the motion as an affine transformation. Assuming that the eddy currents induce affine deformations is common [Leemans

et al., 2009, Jenkinson et al., 2012, Pierpaoli et al., 2010], even though it is known that the deformations depend on slice position [Jones and Cercignani, 2010]

6.6.2 K-space sampling

In contrast to [Scherrer et al., 2012, Tobisch et al., 2014, Fogtmann et al., 2014], the low resolution DW images are not acquired with three orthogonal slice orientations. In this work, the slice orientations are rotated around the phase encoding axis to prevent blurring due to EPI distortions. This acquisition set up leads to a non-uniform sampling of the k-space, with a higher density in the center of k-space. This oversampling of the center of k-space, which leads to a high SNR of the low frequency range, is often used in MRI as it reduces sensitivity to motion artifacts [Pipe, 1999]. Due to the lower density in the higher frequency range, some high frequencies might not be sampled by any of the low resolution DW images. Therefore, regularization is used to force the amplitude of these under sampled high frequencies towards zero. Furthermore, due to this sampling scheme super-resolution is not possible along the phase encoding direction. Note, however, that this acquisition strategy is only used to avoid inconsistencies due to EPI distortions and is not an inherent limitation of the proposed SR method. The rotation of the slice orientations enables the reconstruction of a high resolution DTI map from low resolution DW images with arbitrary slice thicknesses. The simulation and clinical data experiments compared the reconstruction results of low resolution data sets with AFs. Increasing the AF leads to an increased partial volume effect, as the voxels are larger. However, data with a higher AF has a shorter acquisition time and thus more low resolution DW images can be acquired in the same acquisition time. Moreover, the increase in AF also leads to an increased SNR of the measured data, which, in turn, leads to a more precise estimation of the high resolution DTI parameters. The increased AF and large partial volume effects may complicate accurate motion correction. Moreover, constraints in the hard and software of the MRI scanner limit the choice of the AF in clinical practice.

6.6.3 Q-space sampling

A major advantage of the proposed SR-DTI method over the SR-DWI method, is its flexibility in acquisition set up. In contrast to Poot et al. [2013] and Scherrer et al. [2012], it is no longer required to acquire the same set of diffusion gradient directions per slice orientation and as such a minimum of six diffusion gradient directions per slice orientation. Acquiring a different set of diffusion gradient directions for each slice orientation results in a denser q-space sampling. The experiments show that the SR-DTI method benefits from this denser q-space sampling. With the SR-DTI method and proposed q-space sampling, high resolution DTI parameters can be estimated with the same quality, in terms of RMSE FA, MD and MAE FE, within a shorter scan time compared to the SR-DWI method or direct high resolution acquisition. The impact of the proposed q-space sampling reduces when more low resolution DW images are used. This is expected as an increase in low resolution DW images results in a denser q-space sampling.

6.6.4 EPI distortions

In the proposed method, distortions of the EPI images due to off-resonance effects are not corrected. To prevent problems due to these distortions, the low resolution DW images are acquired with the same phase encoding directions. Due to this choice, the EPI-distortions will not affect the registration of the images and thus will not cause inconsistencies between the diffusion model and acquired data. However, since the distortions are not corrected, the resulting DTI parameter maps will show the EPI-distortions in the phase encoding direction. The use of a field map [Jezzard and Balaban, 1995] or reversed phase encoding [Andersson et al., 2003, Holland et al., 2010] on the low resolution DW images could reduce these problems [Scherrer et al., 2012]. Those correction methods are fully compatible with the proposed reconstruction method, but application of them is beyond the scope of this work.

6.6.5 Other diffusion models

Although in this work the DTI model was used, we would like to point out that the proposed SR framework is generic as other diffusion models can be incorporated analogously. We foresee that models relying on high angular resolution diffusion data would benefit even more from the proposed q-space sampling.

Bibliography

D.C. Alexander. Axon radius measurements in vivo from diffusion MRI: a feasibility study. In *Proceedings of the IEEE International Conference on Computer Vision*, volume 11, pages 1–8, Rio de Janeiro, Brazil, 2007.

J.L.R. Andersson, S. Skare, and J. Ashburner. How to correct susceptibility distortions in spin-echo echo-planar images: Application to diffusion tensor imaging. *NeuroImage*, 20(2):870–888, 2003.

V. Arsigny, P. Fillard, X. Pennec, and N. Ayache. Log-Euclidean metrics for fast and simple calculus on diffusion tensors. *Magnetic Resonance in Medicine*, 56 (2):411–421, 2006.

R. Bammer. Basic principles of diffusion-weighted imaging. *European journal of radiology*, 45(3):169–84, 2003.

R. Bammer, S. Skare, R. Newbould, C. Liu, V. Thijs, S. Ropele, D.B. Clayton, G. Krueger, M.E. Moseley, and G.H. Glover. Foundations of advanced magnetic resonance imaging. *NeuroRx*, 2(2):167–196, 2005.

P.J. Basser. Relationships between diffusion tensor and q-space MRI. *Magnetic Resonance in Medicine*, 47(2):392–397, 2002.

P.J. Basser, J. Mattiello, and D. LeBihan. MR diffusion tensor spectroscopy and imaging. *Biophysical journal*, 66(1):259–267, 1994.

E. Caruyer, C. Lenglet, G. Sapiro, and R. Deriche. Design of multishell sampling schemes with uniform coverage in diffusion MRI. *Magnetic Resonance in Medicine*, 69(6):1534–40, 2013.

T.G. Close, J.D. Tournier, F. Calamante, L.A. Johnston, I. Mareels, and A. Connelly. A software tool to generate simulated white matter structures for the assessment of fibre-tracking algorithms. *NeuroImage*, 47(4):1288–1300, 2009.

T.F. Coleman and Y. Li. An interior trust region approach for nonlinear minimzation subject to bounds. *SIAM Journal on optimization*, 6(2):418–445, 1996.

P. Coupé, J.V. Manjón, M. Chamberland, M. Descoteaux, and B. Hiba. Collaborative patch-based super-resolution for diffusion-weighted images. *NeuroImage*, 83: 245–261, 2013.

A.J. den Dekker and J. Sijbers. Data distributions in magnetic resonance images: A review. *Physica Medica*, 30(7):725–741, 2014.

M. Fogtmann, S. Seshamani, C. Kroenke, X. Cheng, T. Chapman, J. Wilm, F. Rousseau, and C. Studholme. A unified approach to diffusion direction sensitive slice registration and 3-D DTI reconstruction from moving fetal brain anatomy. *IEEE Transactions on Medical Imaging*, 33(2):272–289, 2014.

A. Gholipour, J.A. Estroff, and S.K. Warfield. Robust super-resolution volume reconstruction from slice acquisitions: Application to fetal brain MRI. *IEEE Transactions on Medical Imaging*, 29(10):1739–1758, 2010.

H. Greenspan. Super-resolution in medical imaging. *The Computer Journal*, 52(1): 43–63, 2009.

H. Greenspan, G. Oz, N. Kiryati, and S. Peled. MRI inter-slice reconstruction using super-resolution. *Magnetic Resonance in Medicine*, 20(5):437–446, 2002.

D. Holland, J.M. Kuperman, and A.M. Dale. Efficient correction of inhomogeneous static magnetic field-induced distortion in echo planar imaging. *NeuroImage*, 50 (1):1–18, 2010.

M. Jenkinson, C.F. Beckmann, T.E.J. Behrens, M.W. Woolrich, and S.M. Smith. Fsl. *NeuroImage*, 62(2):782–790, 2012.

B. Jeurissen, A. Leemans, J.D. Tournier, D.K. Jones, and J. Sijbers. Investigating the prevalence of complex fiber configurations in white matter tissue with diffusion magnetic resonance imaging. *Human Brain Mapping*, 34(11):2747–2766, 2013.

P. Jezzard and R.S. Balaban. Correction for geometric distortion in echo planar imaging from B0 field variations. *Magnetic Resonance in Medicine*, 34(1):65–73, 1995.

D.K. Jones and M. Cercignani. Twenty-five pitfalls in the analysis of diffusion MRI data. *NMR in Biomedicine*, 23(7):803–20, 2010.

S. Klein, M. Staring, K. Murphy, M.A. Viergever, and J. Pluim. Elastix: A Toolbox for Intensity-Based Medical Image Registration. *IEEE Transactions on Medical Imaging*, 29(1):196–205, 2010.

M. Kuklisova-Murgasova, G. Quaghebeur, M.A. Rutherford, J.V. Hajnal, and J.A. Schnabel. Reconstruction of fetal brain MRI with intensity matching and complete outlier removal. *Medical Image Analysis*, 16(8):1550–1564, 2012.

B.A. Landman, J.A.D. Farrell, C.K. Jones, S.A. Smith, J.L. Prince, and S. Mori. Effects of diffusion weighting schemes on the reproducibility of DTI-derived fractional anisotropy, mean diffusivity, and principal eigenvector measurements at 1.5T. *NeuroImage*, 36(4):1123–1138, 2007.

A.. Leemans, B. Jeurissen, J. Sijbers, and D.K. Jones. ExploreDTI: a graphical toolbox for processing, analyzing, and visualizing diffusion MR data. In *Proceedings of the International Society for Magnetic Resonance in Medicine*, volume 17, page 3537, Honlulu, Hawaii, USA, 2009.

P. Mansfield. Multi-planar image formation using NMR spin echoes. *Journal of Physics C: Solid State Physics*, 10(3):L55–L58, 1977.

P. Mansfield. Real-time echo-planar imaging by NMR. *British medical bulletin*, 40 (2):187–190, 1984.

G. Van Steenkiste, B. Jeurissen, J. Sijbers, and D.H.J. Poot. Super resolution reconstruction from differently oriented diffusion tensor data sets. In *Proceedings of the ISMRM Benelux*, volume 5, Rotterdam, The Netherlands, 2013a.

G. Van Steenkiste, B. Jeurissen, J. Sijbers, and D.H.J. Poot. Super resolution reconstruction from differently oriented diffusion tensor data sets. In *Proceedings of the International Society for Magnetic Resonance in Medicine*, volume 21, page 3186, Salt Lake City, Utah, USA, 2013b.

G. Van Steenkiste, B. Jeurrisen, D.H.J. Poot, and J. Sijbers. Super-resolution reconstruction of diffusion tensor parameters from multi-oriented diffusion weighted images. In *Proceedings of the workshop "Imaging the brain at different scales: How to integrate multi-scale structural information?"*, Antwerp, Belgium, 2013c.

G. Van Steenkiste, B. Jeurissen, D.H.J. Poot, P.M. Parizel, and J. Sijbers. Super-resolution reconstruction of diffusion parameters from multi-oriented diffusion weighted images. In *Proceedings of the ISMRM Benelux*, volume 6, page 39, Maastricht, The Netherlands, 2014a.

G. Van Steenkiste, B. Jeurissen, D.H.J. Poot, and J. Sijbers. Super-resolution reconstruction of diffusion parameters from multi-oriented diffusion weighted images. In *Proceedings of the International Society for Magnetic Resonance in Medicine*, volume 22, page 2572, Milan, Italy, 2014b.

G. Van Steenkiste, B. Jeurissen, J. Veraart, A.J. den Dekker, P.M. Parizel, D.H.J. Poot, and J. Sijbers. Super-resolution reconstruction of diffusion parameters from diffusion-weighted images with different slice orientations. *Magnetic Resonance in Medicine*, 75(1):181–195, 2016.

S. Nedjati-Gilani, D.C. Alexander, and G.J.M. Parker. Regularized super-resolution for diffusion MRI. In *Proceedings of the IEEE International symposium on Biomedical Imaging*, volume 5, pages 875–878, Paris, France, 2008.

H. Oouchi, K. Yamada, K. Sakai, O. Kizu, T. Kubota, H. Ito, and T. Nishimura. Diffusion anisotropy measurement of brain white matter is affected by voxel size: Underestimation occurs in areas with crossing fibers. *American Journal of Neuroradiology*, 28(6):1102–1106, 2007.

E. Oubel, M. Koob, C. Studholme, J.L. Dietemann, and F. Rousseau. Reconstruction of scattered data in fetal diffusion MRI. *Medical Image Analysis*, 16(1): 28–37, 2012.

C. Pierpaoli, L Walker, M.O. Irfanoglu, A. Barnett, P. Basser, L-C. Chang, C. Koay, S. Pajevic, G. Rohde, J. Sarlls, and M. Wu. TORTOISE: an integrated software package for processing of diffusion MRI data. In *Proceedings of the International Society for Magnetic Resonance in Medicine*, volume 18, page 1597, Stockholm, Sweden, 2010.

J.G. Pipe. Motion correction with PROPELLER MRI: Application to head motion and free-breating cardiac imaging. *Magnetic Resonance in Medicine*, 42(5): 963–969, 1999.

E. Plenge, D.H.J. Poot, M. Bernsen, G. Kotek, G. Houston, P. Wielopolski, L. Van Der Weerd, W.J. Niessen, and E. Meijering. Super-resolution methods in MRI: Can they improve the trade-off between resolution, signal-to-noise ratio, and acquisition time? *Magnetic Resonance in Medicine*, 68(6):1983–1993, 2012.

D.H.J. Poot, V. Van Meir, and J. Sijbers. General and efficient super-resolution method for multi-slice MRI. In *Proceedings of the Medical Image Computing and Computer-Assisted Intervention, MICCAI*, pages 615–622, Beijing, China, 2010.

D.H.J. Poot, B. Jeurissen, Y. Bastiaensen, J. Veraart, W. Van Hecke, P.M. Parizel, and J. Sijbers. Super-resolution for multislice diffusion tensor imaging. *Magnetic Resonance in Medicine*, 69(1):103–113, 2013.

W. Qin, C.S. Yu, F. Zhang, X.Y. Du, H. Jiang, Y.X. Yan, and K.C. Li. Effects of echo time on diffusion quantification of brain white matter at 1.5T and 3.0T. *Magnetic Resonance in Medicine*, 61(4):755–760, 2009.

S. Ropele, F. Ebner, F. Fazekas, and G. Reishofer. Super-resolution MRI using microscopic spatial modulation of magnetization. *Magnetic Resonance in Medicine*, 64(6):1671–1675, 2010.

F. Rousseau, O.A. Glenn, B. Iordanova, C. Rodriguez-Carranza, D.B. Vigneron, J.A. Barkovich, and C. Studholme. Registration-Based Approach for Reconstruction of High-Resolution In Utero Fetal MR Brain Images. *Academic Radiology*, 13(9): 1072–1081, 2006.

B. Scherrer, A. Gholipour, and S.K. Warfield. Super-resolution reconstruction to increase the spatial resolution of diffusion weighted images from orthogonal anisotropic acquisitions. *Medical Image Analysis*, 16(7):1465–1476, 2012.

R.Z. Shilling, T.Q. Robbie, T. Bailloeul, K. Mewes, R.M. Mersereau, and Brummer. M.E. A super-resolution framework for 3D imaging using 2D multislice MRI. *IEEE Transactions on Medical Imaging*, 28(5):633–644, 2009.

S.T. Skare and R. Bammer. EPI-based pulse sequences for diffusion tensor MRI. In *Diffusion MRI*, pages 182–202. Oxford University Press, New York, 2011.

E.O. Stejskal and J.E. Tanner. Spin diffusion measurements: spin echoes in the presence of a time dependent field gradient. *The journal of chemical physics*, 42 (1):288–292, 1965.

A. Tobisch, P.F. Neher, M.C. Rowe, K.H. Maier-Hein, and H. Zhang. Model-based super-resolution of diffusion MRI. In *Proceedings of the MICCAI Workshop: Computational Diffusion MRI and Brain Connectivity*, pages 25–34, Boston, USA, 2014.

J.D. Tournier, F. Calamante, and A. Connelly. MRtrix: Diffusion tractography in crossing fiber regions. *International Journal of Imaging Systems and Technology*, 22(1):53–66, 2012.

D.S. Tuch, T.G. Reese, M.R. Wiegell, N. Makris, J.W. Belliveau, and J. Van Wedeen. High angular resolution diffusion imaging reveals intravoxel white matter fiber heterogeneity. *Magnetic Resonance in Medicine*, 48(4):577–582, 2002.

R. Turner, D. Le Bihan, J. Maier, R. Vavrek, L.K. Hedges, and J. Pekar. Echo-planar imaging of intravoxel incoherent motion. *Radiology*, 177(2):407–414, 1990.

E. Van Reeth and I. Tham. Super-resolution in magnetic resonance imaging: A review. *Concepts in Magnetic Resonance A*, 40(6):306–325, 2012.

P.J. Wright, O.E. Mougin, J.J. Totman, A.M. Peters, M.J. Brookes, R. Coxon, P.E. Morris, M. Clemence, S.T. Francis, R.W. Bowtell, and P.A. Gowland. Water proton T1 measurements in brain tissue at 7, 3, and 1.5 T using IR-EPI, IR-TSE, and MPRAGE: results and optimization. *Magnetic Resonance Materials in Physics, Biology and Medicine*, 21(1-2):121–130, 2008.

7 Applications

Contents

The work in this chapter has been published in:

- **G. Van Steenkiste**, J. Hamaide, B. Jeurissen, D.H.J. Poot, J. Van Audekerke, J. Sijbers, and M. Verhoye. Super-resolution structural connectivity and anatomy of the zebra finch brain. In *Proceedings of the ISMRM Benelux*, volume 7, page O029, Ghent, Belgium, 2015a
- **G. Van Steenkiste**, J. Hamaide, B. Jeurissen, D.H.J. Poot, J. Van Audekerke, J. Sijbers, and M. Verhoye. Combination of super-resolution reconstruction diffusion tensor imaging and track density imaging reveals song control system connectivity in zebra finches. In *Proceedings of the International Society for Magnetic Resonance in Medicine*, volume 23, page 2861, Toronto, Ontario, Canada, 2015b
- **G. Van Steenkiste**, B. Jeurissen, S. Baete, A.J. den Dekker, D.H.J. Poot, F. Boada, and J. Sijbers. High resolution diffusion tensor imaging in a clinically feasible scan time. In *Proceedings of the second Belgian Neuroinformatics Congress*, Leuven, Belgium, 2015c
- **G. Van Steenkiste**, B. Jeurissen, S. Baete, A.J. den Dekker, D.H.J. Poot, F. Boada, and J. Sijbers. In vivo high resolution diffusion tensor imaging in a clinically acceptable scan time by combining super resolution reconstruction with simultaneous multi-slice acquisition. In *Proceedings of the ISMRM Benelux*, volume 8, pages P–036, Eindhoven, The Netherlands, 2016a
- S.D. Washington, S. Radtke-Schuller, J. Hamaide, **G. Van Steenkiste**, J. Sijbers, S. Deleye, J.S. Kanwal, J.J. Wenstrup, G. de Groof, S. Liang, J. Van Audekerke, M. Verhoye, and A. Van der Linden. Magnetic resonance imaging and histology based brain atlases of the mustached bat, Pteronotus parnellii. In *Proceedings of the ISMRM Benelux*, volume 8, pages P–055, Eindhoven, The Netherlands, 2016
- **G. Van Steenkiste**, B. Jeurissen, S. Baete, A.J. den Dekker, D.H.J. Poot, F. Boada, and J. Sijbers. High resolution diffusion tensor reconstruction from simultaneous multi-slice acquisitions in a clinically feasible scan time. In *Proceedings of the International Society for Magnetic Resonance in Medicine*, volume 24, page 0002, Singapore, 2016b

Acknowledgements:

- Data were provided [in part] by the Human Connectome Project, WU-Minn Consortium (Principal Investigators: David Van Essen and Kamil Ugurbil; 1U54MH091657) funded by the 16 NIH Institutes and Centers that support the NIH Blueprint for Neuroscience Research; and by the McDonnell Center for Systems Neuroscience at Washington University.

7.1 SR-DTI versus Human Connectome Project Scanner

High resolution in vivo diffusion tensor imaging (DTI) within clinically feasible scan times is a challenging task. Multiple diffusion weighted (DW) images are needed to estimate the diffusion parameters and inherently, DW images have a low signal-to-noise ratio (SNR). Improving the SNR of the DW images by increasing the number of averages would require an infeasible long acquisition time. As a result, to ensure sufficient SNR, DW images are often acquired with a low spatial resolution leading to large partial volume effects. One way to improve the trade-off between the spatial resolution, acquisition time and SNR is acquiring the data with an MRI scanner with stronger gradients (Human Connectome Project (HCP) scanner [Ugurbil et al., 2013] which allows a shorter TE and consequently a higher SNR. Complementary, recent developments in acquisition techniques, such as simultaneous multi-slice (SMS) [Setsompop et al., 2012], provide a significant reduction of the acquisition time. With the introduction of super-resolution reconstruction techniques for DTI (SR-DTI) [**G. Van Steenkiste** et al., 2016c] (see chapter 6), high resolution DTI has become more feasible on MRI scanners with a regular gradient set. In this work, we propose to combine SR-DTI with SMS acquisitions (SMS-SR-DTI). This enables high resolution in vivo DTI within a clinically feasible scan time on a common MRI scanner.

7.1.1 Method

The quality of a high resolution DTI map obtained with SR-DTI was qualitatively compared with the quality of a low resolution DTI map and a high resolution HCP DTI map.

- **SMS-SR-DTI data**: Four DW data sets with voxel size 1.25 mm×1.25 mm× 2.5 mm were acquired on a 3 T clinical scanner with a common gradient set (80 mT/m, Prisma, Siemens, Erlangen Germany), using SMS echo-planar imaging (EPI) and an SMS factor of 3. Each data set was acquired with a different slice orientation, which was rotated around the phase encoding axis with incremental steps of 45°. Each of the four data sets consisted of 12 DW images (b=1000 s/mm^2) and two non-DW images (b=0 s/mm^2). One of the non-DW images was collected with reversed phase encoding blips. The diffusion gradient directions were sampled differently for each subset, leading to a total of 48 unique diffusion gradient directions. The overall scan time was 7min24. The acquired DW images were first corrected for EPI distortions by using reversed phase encoding correction [Andersson et al., 2003, Smith et al., 2004]. From the corrected DW images, high resolution DTI parameters were estimated on a grid with voxel size 1.25 mm × 1.25 mm × 1.25 mm using SR-DTI [**G. Van Steenkiste** et al., 2016c]. The motion was modeled within the SR-DTI model (Eq. 6.4) by an affine transformation, which was estimated using an iterative model based registration method [Bai and Alexander, 2008].
- **Low resolution data**: Two non-DWI (b=0 s/mm^2), one with reversed phase encoding, and 31 DW (b=1000 s/mm^2) images with voxel size 2 mm × 2 mm ×

2 mm were acquired on the same scanner as the SMS-SR-DTI data. The acquisition time was 7min31. Prior to estimating the DTI parameters using weighted linear least squares, the images were corrected for EPI distortions by using reversed phase encoding direction and upsampled to a grid with voxel size 1.25 mm × 1.25 mm × 1.25 mm.

- **HCP data**: From a pre-processed HCP data set (300 mT/m) with voxel size 1.25 mm × 1.25 mm × 1.25 mm, one non-DW (b=0 s/mm^2) and 40 DW (b=1000 s/mm^2) images were selected. The total acquisition time was 7min36.

From each DTI parameter set, a directionally encoded color fractional anisotropy (DEC FA) map was calculated.

7.1.2 Results

Figure 7.1 illustrates a transversal, coronal and sagittal slice of the DEC FA map for the low resolution data (Fig. 7.1), the HCP data (7.1b) and the SMS-SR-DTI data (7.1c). Note that as each data set is acquired at a different scanner and from a different healthy volunteer, no direct quantitative comparison can be made between the different data sets. The SMS-SR-DTI map shows finer structures compared to the low resolution map. The SMS-SR-DTI map and the HCP map show a similar level of detail. In Fig. 7.2 a coronal zoom on the posterior region of the corona radiate (pcr, left column) and a transversal zoom on the cerebellum (right column) are shown. In both the SMS-SR-DTI and HCP maps, the pcr, tapetum and superior longitudinal fasciculus (slf) can be delineated while in the low resolution map, the tapetum is not discernible from the pcr and slf due to large partial volume effects.

7.1.3 Conclusion

SR-DTI was combined with an SMS acquisition to estimate DTI parameters with a high resolution from DW images acquired in a clinically feasible scan time. For a fixed acquisition time and with data acquired on an MRI scanner with weaker gradients, SMS-SR-DTI accomplishes a resolution visually similar to the HCP data. The use of SMS-SR-DTI opens up exciting possibilities for diffusion MRI in research and clinical routine.

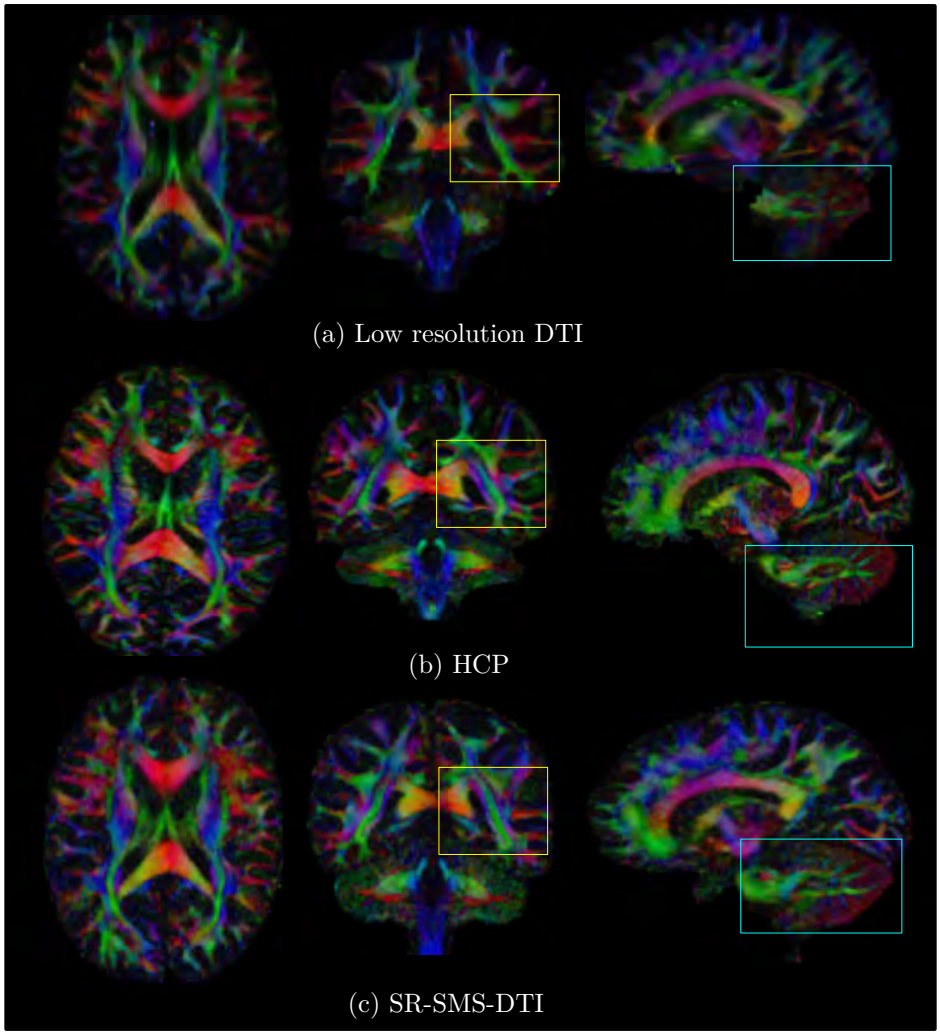

Fig. 7.1: Transversal, coronal and sagittal slice of the DEC FA maps for the different data sets. Colored boxes depict the areas in which the zoom in Fig. 7.2 are taken.

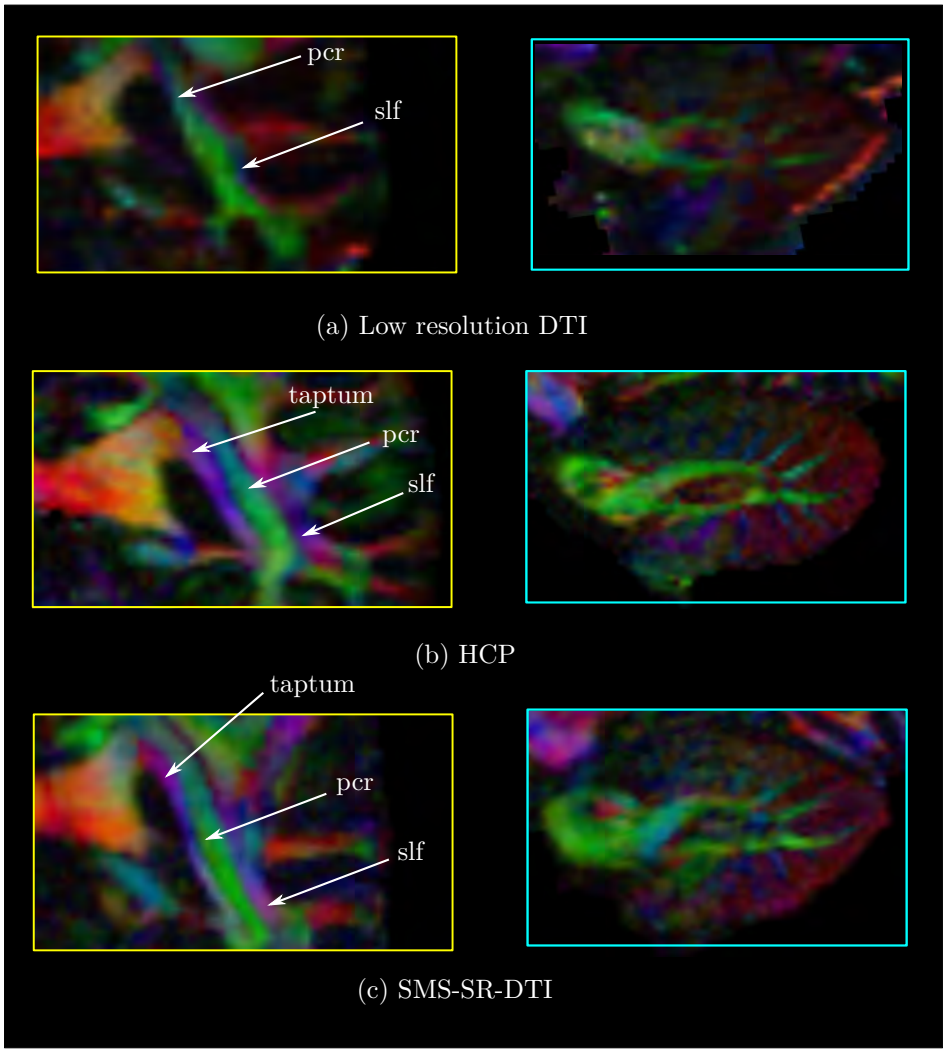

Fig. 7.2: Left: coronal zoom on the posterior region of corona radiate, Right: transversal zoom on the cerebellum.

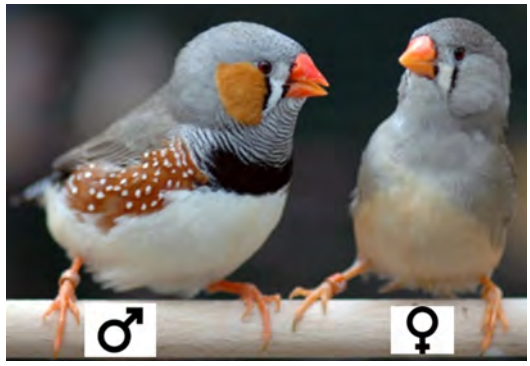

Fig. 7.3: Male and female zebra finch.

7.2 Combination of SR-DTI and TDI applied on the zebra finch brain

So far, structural investigation of the zebra finch (*Taeniopygia guttata*, Fig. 7.3) brain was mainly performed by invasive methods such as histology [Nottebohm and Arnold, 1976]. This methodology, however, does not allow quantitative investigation of whole-brain structural connectivity. A recent proof-of-principle study using in vivo DTI in adult zebra finches confirmed sexual dimorphism in the song control system [Hamaide et al., 2014]. However, the DW data acquired in that study, had a low spatial resolution of 0.19 mm × 0.19 mm × 0.24 mm. In order to better understand of the anatomical substrate underlying the observed differences, DTI data with a higher and preferably isotropic spatial resolution is required. Acquiring DW data at such a high isotropic spatial resolution covering the entire brain is, however, not feasible in a reasonable acquisition time using a conventional spin echo DW (SE-DW) or SE-EPI sequence. Therefore, a SR ex vivo DTI protocol and reconstruction, that improves the trade-off between acquisition time, spatial resolution and SNR of DTI parameters, was implemented. The SR-DTI method was combined with track density imaging (TDI) [Calamante et al., 2010], as it has been shown in other small animal studies that TDI facilitates delineation of a large number of brain regions and small white matter bundles [Richards et al., 2014, Ullman et al., 2013]. Here, the data set of an adult male zebra finch, obtained by the combination of SR-DTI and TDI is presented.

7.2.1 Method

7.2.1.1 Sample preparation

One adult male zebra finch kept in normal, non-breeding housing conditions was euthanized by an intramuscular injection of pentobarbital (60 mg/kg) and transcardially perfused first with ice-cold saline and second with an ice-cold 4 % paraformaldehyde (PFA) in 0.1 M Phosphate Buffered Saline (PBS; pH 7.4) solution supplemented with gadolinium (1 % Dotarem, 0.05 mmol/ml gadoteric acid). Next, the brains were post-fixed overnight with 4 % PFA in 0.1 M PBS enriched with 1 %

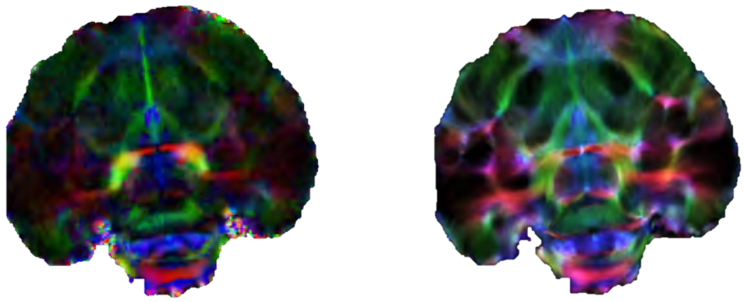

(a) SR-DTI DEC FA (b) SR-TDI

Fig. 7.4: (a) Directionally encoded color FA map of SR-DTI parameters on a 0.078 mm × 0.078 mm × 0.078 mm grid and (b) Directionally encoded color SR-TDI map on a 0.04 mm × 0.04 mm × 0.04 mm grid.

Dotarem after which the tissue was transferred to 0.1 M PBS with 1 % Dotarem and kept at 4 °C.

7.2.1.2 Acquisition

Eight hours prior to ex vivo imaging the brains were removed from the refrigerator in order to acclimatize to the ambient bore temperature. The zebra finch head was imaged with a spin echo sequence on a 9.4 T MRI scanner (Bruker, Biospin, Germany) with a circular polarized transmit resonator, quadrature receive surface coil and a 600 mT/m gradient insert. Fifteen sets of low resolution images were acquired, each with a different slice orientation, which was rotated around the phase encoding axis at incremental steps of 12°. Each of these sets consisted of one non DW image ($b = 0\,\mathrm{s/mm^2}$) and six DW images ($b = 2500\,\mathrm{s/mm^2}$) with following acquisition parameters: FOV (15 mm × 15 mm), TE 26 ms, TR 10 000 ms, acquisition matrix (192 × 137) zero-filled to (192 × 192), in-plane resolution of 0.078 mm × 0.078 mm, 37 slices, slice thickness 0.32 mm, δ 6 ms, Δ 14 ms, 1 repetition. Per slice orientation, the scanning time was 2h 40min. As the diffusion gradient directions were different for each slice orientations, a total of 90 unique diffusion gradient directions was acquired. The brains were kept in the skull during the entire procedure as to prevent mechanical damage throughout the different tissue processing and imaging steps. All experimental procedures were approved by the local Ethics Committee for Animal Experiments.

7.2.1.3 Super-resolution reconstruction

From the acquired low resolution DW images, high resolution diffusion tensor parameters were estimated on a 0.078 mm × 0.078 mm × 0.078 mm grid, using SR-DTI. The motion parameters used in SR-DTI were estimated using an iterative model-based motion correction scheme [Bai and Alexander, 2008], which included the corresponding correction of the gradient directions [Leemans and Jones, 2009].

7.2.1.4 Track density imaging

In order to obtain fiber orientation distribution functions (fODFs) suitable for probabilistic fiber tracking, the following steps were performed. First, a dense set of high resolution DW images were simulated from the high resolution DTI parameters. Next, the white matter fiber response function was extracted from the high resolution DW data using the recursive calibration method described in [Tax et al., 2014]. Finally, fODFs were obtained by performing constrained spherical deconvolution [Tournier et al., 2007], using the high resolution DW images and the single fiber response function created above, adopting the quadratic programming approach outlined in [Jeurissen et al., 2014]. The spherical harmonic series describing the fODFs was truncated at order 8. Probabilistic whole brain tractography was then performed using second order integration over the fODFs [Tournier et al., 2010]. 108 Streamlines were generated using the following parameters: fODF amplitude threshold of 0.1, step size of 0.08 mm, and a maximum angle between steps of 9Âř. From the resulting tractogram, track density maps were calculated at a resolution of $0.04\,\text{mm} \times 0.04\,\text{mm} \times 0.04\,\text{mm}$ [Calamante et al., 2010]. All steps were performed using MRtrix version 3 [Tournier et al., 2012].

7.2.2 Results

The directionally encoded color SR-TDI maps provide clear anatomical contrast of several components of the song control (e.g. Area X, LMAN, RA; Fig. 7.5), auditory (e.g. FieldL, MLd;Fig. 7.5) and visual system (e.g. Entopallium; Fig. 7.5). Structural connectivity such as tracts connecting distinct brain areas (e.g. tractus OM) and laminae subdividing the zebra finch brain in separate parts (e.g. LFS, LaM etc. Fig. 7.5), are most clearly visualized on the individual and color-coded SR-TDI maps Fig. 7.5). The obtained TDI maps (Fig. 7.6a) show great similarities with online available myelin stained histological slices (Karten-Mitra atlas, Fig. 7.6b) and with previously published high-resolution starling DTI data [De Groof et al., 2006].

7.2.3 Discussion

The current data set enables 3D whole-brain qualitative assessment of structural connectivity of several areas of the zebra finch brain. The obtained resolution of the acquired dataset and clear anatomical contrast allows delineation of brain regions of interest. This ex vivo experiment illustrates that the combination of SR-DTI and TDI can provide clear delineation of the anatomy of the song control system, without proportionally extending the acquisition time. The possibility to perform targeted or even whole-brain fiber tractography on the obtained high-resolution dataset might lead to a further insight into zebra finch brain connectivity both in health, e.g. throughout the critical period of vocal learning, and along the course of pathology.

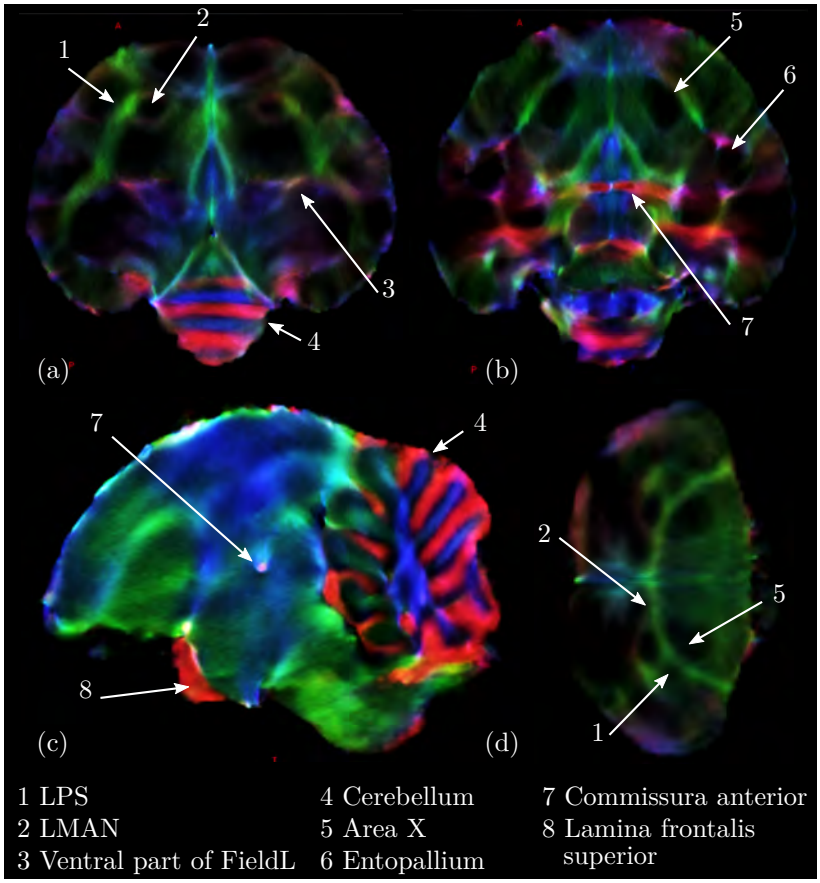

Fig. 7.5: (a) axial section through LMAN, (b) axial section through commissura anterior, (c) midsagittal section and (d) coronal section through LMAN of the SR-TDI maps of the zebra finch brain.

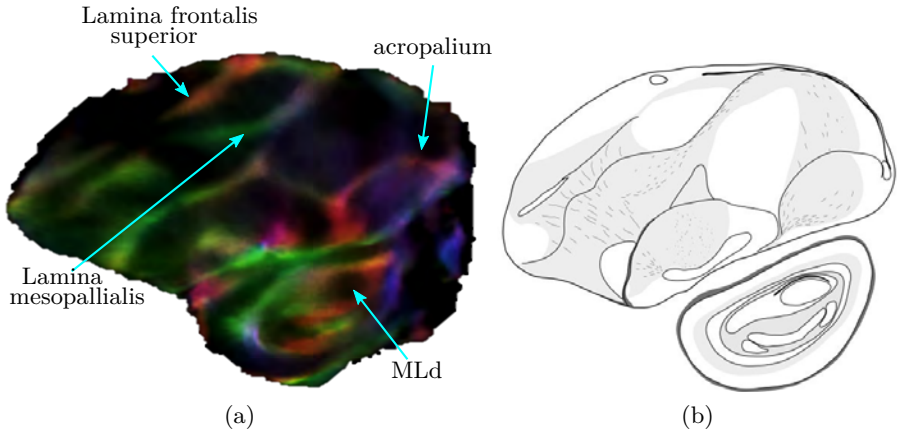

Fig. 7.6: Correspondence between (a) sagittal section of SR-TDI map and (b) Karten-Mitra atlas.

7.2.4 Conclusion

In conclusion, the combination of SR-DTI and TDI has been successfully applied in pre-clinical small animal research, paving the way for exciting future studies aimed at the establishment of structural connectivity in early development or assessing (early) defects in structural connectivity attributed to neurodegenerative disorders.

7.3 SR-DTI of the Mustached Bat

Fig. 7.7: Mustach bat. By Alex Borisenko, Biodiversity Institute of Ontario - Entry on Pteronotus parnellii at BOLD Systems - Image. The image is taken from Wikipedia and is licensed under the Creative Commons CC BY-SA 3.0

Substantial scientific knowledge of auditory processing within mammalian nervous systems emerged from classic neurophysiological studies of the mustached bat (Pteronotus parnellii, Fig. 7.7) [Manabe et al., 1978, O'Neill and Suga, 1979, O'Neill, 1995]. A comprehensive neurological atlas would increase the likelihood of success for neuroimaging studies in this species. The applicability of SR-DTI on

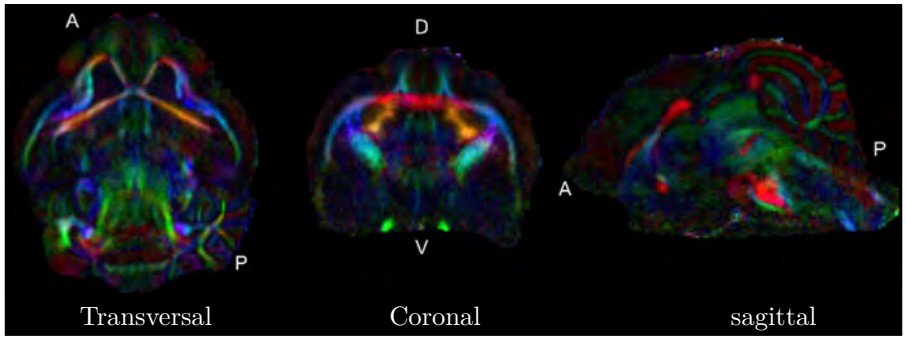

Fig. 7.8: Axial, coronal, and sagittal views of DEC FA maps derived from SR-DTI diffusion tensor parameters.

mustached bat data to generate high resolution diffusion parameters for this atlas was assessed.

7.3.1 Methods

DW data sets were acquired from a formaldehyde-preserved head of a mustached bat using a spin echo sequence on a 9.4 Tesla Biospec MRI system (Bruker, Biospin, Germany) with a quadrature volume coil and a 4-channel surface cryoprobe. Fifteen sets of low resolution multi-slice DW images were acquired, each with a different slice orienation rotated over 12° about the phase encoding axis. Each of these sets consisted of one non DW image ($b = 0\,\mathrm{s/mm^2}$) and six DW images ($b = 2500\,\mathrm{s/mm^2}$) with following acquisition parameters: TE 27 ms, TR 9000 ms, acquisition matrix (256×256), in-plane resolution of $0.08\,\mathrm{mm} \times 0.08\,\mathrm{mm}$, 38 slices, slice thickness 0.4 mm, δ 6 ms, Δ 14 ms, 1 repetition. The total acquisition time was 48h. As the diffusion gradient directions were different for each slice orientations, a total of 90 unique diffusion gradient directions was acquired.

Using SR-DTI, diffusion tensor parameters were estimated on a $0.08\,\mathrm{mm} \times 0.08\,\mathrm{mm} \times 0.08\,\mathrm{mm}$ grid from the low resolution images. The motion parameters used in SR-DTI were estimated using an iterative model-based motion correction scheme [Bai and Alexander, 2008], which included the corresponding correction of the gradient directions [Leemans and Jones, 2009]. Using the resulting DTI parameters, whole brain deterministic tractography was performed.

7.3.2 Results

Figure 7.8 shows a transversal, coronal and sagittal slice of the DEC FA maps derived from the high resolution DTI parameters. Fine structures are clearly visible on the DEC FA maps. In Fig. 7.9 the tractography result is shown in several coronal and sagittal slabs.

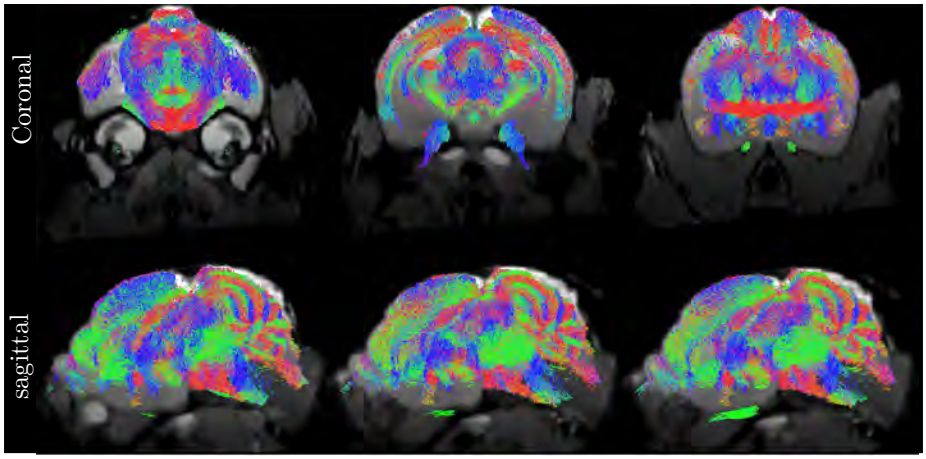

Fig. 7.9: Whole brain tractography reveals the pathways of tracts and nerves in the bat brain.

7.3.3 Conclusion

SR-DTI can be used to map the structural connectivity of the mustached bat bran. This opens up the possibility to build a multi-model brain atlas of the mustached bat brain which will includes the structural connectivity.

Bibliography

J.L.R. Andersson, S. Skare, and J. Ashburner. How to correct susceptibility distortions in spin-echo echo-planar images: Application to diffusion tensor imaging. *NeuroImage*, 20(2):870–888, 2003.

Y. Bai and D.C. Alexander. Model-based registration to correct for motion between acquisitions in diffusion MR imaging. In *Proceedings of the IEEE International symposium on Biomedical Imaging*, volume 5, pages 947–950, Paris, France, 2008.

F. Calamante, J.D. Tournier, G.D. Jackson, and A. Connelly. Track-density imaging (TDI): super-resolution white matter imaging using whole-brain track-density mapping. *NeuroImage*, 53(4):1233–1243, 2010.

G. De Groof, M. Verhoye, V. Van Meir, I. Tindemans, A. Leemans, and A. Van der Linden. In vivo diffusion tensor imaging (DTI) of brain subdivisions and vocal pathways in songbirds. *NeuroImage*, 29(3):754–763, 2006.

J. Hamaide, G. De Groof, J. Van Audekerke, L. Van Ruijssevelt, Z. Mai, F. Kara, M. Verhoye, and A. Van Der Linden. In vivo detection of sexual dimorphisms in the brain of a Passerine songbird, a proof-of-principle study. In *Proceedings of the International Society for Magnetic Resonance in Medicine*, volume 22, page 4553, Milan, Italy, 2014.

B. Jeurissen, J.D. Tournier, T. Dhollander, A. Connely, and J. Sijbers. Multi-tissue constrained spherical deconvolution for improved analysis of multi-shell diffusion MRI data. *NeuroImage*, 103:411–26, 2014.

A. Leemans and D.K. Jones. The B-matrix must be rotated when correcting for subject motion in DTI data. *Magnetic Resonance in Medicine*, 61(6):1336–1349, 2009.

T. Manabe, N. Suga, and J. Ostwald. Aural representation in the Doppler-shifted-CF processing area of the auditory cortex of the mustache bat. *Science*, 200 (4339):339–342, 1978.

G. Van Steenkiste, J. Hamaide, B. Jeurissen, D.H.J. Poot, J. Van Audekerke, J. Sijbers, and M. Verhoye. Super-resolution structural connectivity and anatomy of the zebra finch brain. In *Proceedings of the ISMRM Benelux*, volume 7, page O029, Ghent, Belgium, 2015a.

G. Van Steenkiste, J. Hamaide, B. Jeurissen, D.H.J. Poot, J. Van Audekerke, J. Sijbers, and M. Verhoye. Combination of super-resolution reconstruction diffusion tensor imaging and track density imaging reveals song control system connectivity in zebra finches. In *Proceedings of the International Society for Magnetic Resonance in Medicine*, volume 23, page 2861, Toronto, Ontario, Canada, 2015b.

G. Van Steenkiste, B. Jeurissen, S. Baete, A.J. den Dekker, D.H.J. Poot, F. Boada, and J. Sijbers. High resolution diffusion tensor imaging in a clinically feasible scan time. In *Proceedings of the second Belgian Neuroinformatics Congress*, Leuven, Belgium, 2015c.

G. Van Steenkiste, B. Jeurissen, S. Baete, A.J. den Dekker, D.H.J. Poot, F. Boada, and J. Sijbers. In vivo high resolution diffusion tensor imaging in a clinically acceptable scan time by combining super resolution reconstruction with simultaneous multi-slice acquisition. In *Proceedings of the ISMRM Benelux*, volume 8, pages P–036, Eindhoven, The Netherlands, 2016a.

G. Van Steenkiste, B. Jeurissen, S. Baete, A.J. den Dekker, D.H.J. Poot, F. Boada, and J. Sijbers. High resolution diffusion tensor reconstruction from simultaneous multi-slice acquisitions in a clinically feasible scan time. In *Proceedings of the International Society for Magnetic Resonance in Medicine*, volume 24, page 0002, Singapore, 2016b.

G. Van Steenkiste, B. Jeurissen, J. Veraart, A.J. den Dekker, P.M. Parizel, D.H.J. Poot, and J. Sijbers. Super-resolution reconstruction of diffusion parameters from diffusion-weighted images with different slice orientations. *Magnetic Resonance in Medicine*, 75(1):181–195, 2016c.

F. Nottebohm and A.P. Arnold. Sexual dimorphism in vocal control areas of the songbird brain. *Science*, 194(4261):211–213, 1976.

W.E. O'Neill. The bat auditory cortex. In *Hearing by bats*, pages 416–480. Springer, New York, 1995.

W.E. O'Neill and N. Suga. Target range-sensitive neurons in the auditory cortex of the mustache bat. *Science*, 203(4375):69–73, 1979.

K. Richards, F. Calamante, J.D. Tournier, N.D. Kurniawan, F. Sadeghian, A.R. Retchford, G.D. Jones, C.A. Reid, D.C. Reutens, R. Ordidge, and A. Connelly. Mapping somatosensory connectivity in adult mice using diffusion MRI tractography and super-resolution track density imaging. *NeuroImage*, 102:381–392, 2014.

K. Setsompop, J. Cohen-Adad, B.A. Gagoski, T. Raij, A. Yendiki, B. Keil, V.J.. Wedeen, and L.L. Wald. Improving diffusion MRI using simultaneous multi-slice echo planar imaging. *NeuroImage*, 63(1):569–580, 2012.

S.M. Smith, M. Jenkinson, M.W. Woolrich, C.F. Beckamnn, T.E. Behrens, H. Johansen-Berg, P.R. Bannister, M. De Luca, I. Drobnjak, D.E. Flitney, and R.K. Niazy. Advances in functional and structural MR image analysis and implementation as FSL. *NeuroImage*, 23(1):S208–S219, 2004.

C.M. Tax, B. Jeurissen, S.B. Vos, M.A. Viergever, and A. Leemans. Recursive calibration of the fiber response function fro spherical deconvolution of diffusion MRI data. *NeuroImage*, 86:67–80, 2014.

J-D. Tournier, F. Calamante, and A. Connelly. Improved probabilistic streamlines tractography by 2 nd order integration over fibre orientation distributions. In *Proceedings of the International Society for Magnetic Resonance in Medicine*, volume 18, page 1670, Stockholm, Sweden, 2010.

J.D. Tournier, F. Calamante, and A. Connelly. Robust determination of the fibre orientation distribution in diffusion MRI: non-negativity constrained super-resolved spherical deconvolution. *NeuroImage*, 35(4):1459–72, 2007.

J.D. Tournier, F. Calamante, and A. Connelly. MRtrix: Diffusion tractography in crossing fiber regions. *International Journal of Imaging Systems and Technology*, 22(1):53–66, 2012.

K. Ugurbil, J. Xu, E.J. Auerbach, S. Moeller, A.T. Vu, J.M. Duarte-Carvajalino, C. Lenglet, X. Wu, S. Schmitter, P.F. Van de Moortele, J. Strupp, G. Sapiro, F. De Martino, D. Wang, N. Harel, M. Garwood, L. Chen, D.A.. Feinberg, S.M. Smith, K.L. Miller, S.N. Sotiropoulos, S. Jbabdi, J.L.R. Andersson, T.E.J. Behrens, M.F. Glasser, D.C. Van Essen, and E. Yacoub. Pushing spatial and temporal resolution for functional and diffusion MRI in the Human Connectome Project. *NeuroImage*, 80:80–104, 2013.

J.F.P. Ullman, C. Watson, A.L. Janke, N.D. Kurniawan, G. Paxinos, and D.C. Reutens. An MRI atlas of the mouse basal ganglia. *Brain Structure and Function*, 219(4):1343–1353, 2013.

S.D. Washington, S. Radtke-Schuller, J. Hamaide, **G. Van Steenkiste**, J. Sijbers, S. Deleye, J.S. Kanwal, J.J. Wenstrup, G. de Groof, S. Liang, J. Van Audekerke, M. Verhoye, and A. Van der Linden. Magnetic resonance imaging and histology based brain atlases of the mustached bat, Pteronotus parnellii. In *Proceedings of the ISMRM Benelux*, volume 8, pages P–055, Eindhoven, The Netherlands, 2016.

Conclusion

In this dissertation, two new super-resolution (SR) methods for quantitative MRI (qMRI), SR-T_1 (chapter 5) and SR-DTI (chapter 6), were proposed. These SR methods combine SR reconstruction with the estimation of qMRI parameters, such as the longitudinal relaxation time T_1 or the diffusion tensor $\boldsymbol{D}$. By incorporating the qMRI model (T_1 model, DTI model) into the SR reconstruction, high resolution qMRI parameters (T_1, $\boldsymbol{D}$) can be directly estimated from a set of low resolution images. As discussed in chapter 4 only the spatial resolution in the slice direction can be improved using SR. Therefore, the low resolution images were acquired with a high in-plane resolution and thicker slices. To ensure that each low resolution image contains different resolution information on the imaged object, the slice orientation of the low resolution images is rotated about the phase encoding axis. The number of slice orientation and step size of the rotation will depend on the ratio of the slice thickness to the in-plane resolution.

Through experiments with simulated and in vivo data we showed that both proposed SR methods enhance the spatial resolution of the estimated parameter maps. Moreover, SR outperforms upsampling of low resolution data and direct high resolution acquisitions, without increasing the acquisition time.

In quantitative T_1 mapping, SR-T_1 enables high resolution T_1 mapping from low resolution T_1-weighted images acquired with inversion recovery turbo spin echo, without exceeding specific absorption rate limits. The acquisition time of the set of the low resolution T_1-weighted images was 28 min, which is still too long for clinical routine. However, developing a specific SR-T_1 sequence to acquire the low resolution T_1-weighted images and/or the use of scan time reducing techniques such as simultaneous multi-slice techniques would probably drastically reduce the scan time, enabling the use of SR-T_1 in daily clinical practice.

For diffusion MRI, we demonstrated that our proposed SR-DTI method outperforms two step SR methods such as SR-DWI, which first reconstructs a high resolution DW image for each diffusion gradient direction and then estimates diffusion parameters from the resulting high resolution images. Our proposed SR-DTI method has major advantages. Compared to SR-DWI, it is not necessary to acquire the same set of diffusion gradient directions for each slice orientation. As such, motion correction with the corresponding b-vector rotation can be included in the SR method. Furthermore, more diffusion gradient directions can be acquired in total by optimizing the diffusion gradient directions over the complete set of DW images and over each slice orientation. This also means that less than six diffusion gradient directions can be acquired per slice orientation, reducing the overall acquisition time. The advantage of the proposed q-space sampling was demonstrated both on simulated and in vivo data.

Acquiring the low resolution DW data with simultaneous multi-slice (SMS) reduces the scan time by a factor equal to the number of slices that are acquired simultaneously (which is most often 2 or 3). The high resolution DTI parameters resulting from using SR-DTI on low resolution SMS DW data was compared with high resolution DTI parameters estimated from DW data acquired at the human connectome project (HCP) scanner, which has a stronger gradient set. In equal acquisition times, using the SR-DTI SMS combination results in DTI parameters which visually have a similar quality as the HCP DTI parameters, demonstrating the potential of SR-DTI on revealing small anatomical details. This potential was exploited in two small animal pre-clinical studies. In these studies SR-DTI showed to pick up small structures, previously indistinguishable due to partial volume effects and/or low SNR.

The two proposed SR methods, SR-T_1 and SR-DTI improve the inherent trade-off between acquisition time, spatial resolution and SNR of qMRI experiments. Decreasing the acquisition time without reducing the SNR and spatial resolution, would improve patient comfort and the quality of the parameter maps by decreasing the chance of involuntary motion. Improving the SNR would increase the precision of the qMRI parameter estimates, possibly leading to earlier and better diagnosis. Most importantly, SR-T_1 and SR-DTI enable quantitative high resolution investigation of the brain in clinically compatible scan time on a standard clinical MRI scanner. Quantitative MRI maps at a high spatial resolution would enable a better localization of the changes in the biological parameters, which could improve diagnosis of several diseases as well as the understanding of the brain connectivity. Combining SR-T_1 and SR-DTI with future hardware improvements, may enable qMRI with unprecedented spatial resolution.

List of Abbreviations

1D	One-dimensional
2D	Two-dimensional
3D	Three-dimensional
ADC	Apparent Diffusion Coefficient
AF	Anisotropy Factor
BW	BandWidth
CSF	CerobroSpinal Fluid
DEC	Directionally Encoded Color
dMRI	Diffusion (weighted) Magnetic Resonance Imaging
DSI	Diffusion Spectrum Imaging
DTI	Diffusion Tensor Imaging
DW	Diffusion-Weighted
DWI	Diffusion-Weighted imaging
EPI	Echo Planar Imaging
ETL	Echo Train Length
FA	Fractional anisotropy
FE	First Eigenvector
FID	Free Induction Decay
FOV	Field Of View
FSE	Fast Spin Echo
FWHM	Full Width of Half Maximum
Gd-DTPA	Gadolinium DiethyleneTriaminePentaacetic Acid
GE	Gradient Echo
GM	Grey Matter
GT	Ground truth
GRAPPA	GeneRalized Autocalibrating Partial Parallel Acquisition
HARDI	Higher-Angular-Resolution Diffusion-weighted Imaging
HCP	Human Connectome Project
HR	High Resolution
IES	Inter Echo Spacing
IR	Inversion Recovery
LL	Look-Locker
LLS	Linear Least Squares
LR	Low Resolution
LS	Least Squares
MAE	Median Angular Error
MD	Mean Diffusivity
MOLLI	Modiffied Look-Locker Inversion recovery

MR	Magnetic Resonance
MRI	Magnetic Resonance Imaging
NLS	Non-linear Least Squares
NMR	Nuclear Magnetic Resonance
pcr	posterior region of the corona radiate
PDF	Probability Distribution Function
PGSE	Pulsed Gradient Spin Echo
PSF	Point Spread Function
QBI	Q-Ball Imaging
qMRI	quantitative Magnetic Resonance Imaging
RF	Radio Frequency
RMSE	Root-Mean-Square Error
SAR	Specific Absorption Rate
SE	Spin echo
SENSE	SENSitivity Encoding
ShMOLLI	Shortend Modified Look Locker Inversion recovery
slf	superior longitudinal fasciculus
SMS	Simultaneous Multi-Slice
SNR	Signal-to-Noise Ratio
SPGR	Spoiled Gradient echo
SR	Super-Resolution
SR-DTI	Super-Resolution Diffusion Tensor Imaging
SR-DWI	Super-Resolution Diffusion-Weighted Imaging
SR-T_1	Super-Resolution T_1 mapping
SRR	Super-Resolution Reconstruction
ss-EPI	single-shot Echo Planar Imaging
ss-FSE	single-shot Fast Spin Echo
std	standard deviation
TDI	Track Density Imaging
TE	Echo Time
TF	Turbo Factor
TI	Inversion Time
TOMROP	T One by Multiple Read Out Pulses
TR	Repetition Time
TSE	Turbo Spin Echo
VFA	Variable Flip Angle
WM	White Matter

Academic overview

Journal papers

1. **G. Van Steenkiste**, B. Jeurissen, J. Veraart, A.J. den Dekker, P.M. Parizel, D.H.J. Poot, and J. Sijbers. Super-resolution reconstruction of diffusion parameters from diffusion-weighted images with different slice orientations. *Magnetic Resonance in Medicine*, 75(1):181–195, 2016c

2. **G. Van Steenkiste**, D.H.J. Poot, B. Jeurissen, A.J. den Dekker, F. Vanhevel, P.M. Parizel, and J. Sijbers. Super-resolution T1 estimation: quantitative high resolution T1 mapping from a set of low resolution T1 weighted images with different slice orientations. *Magnetic Resonance in Medicine*, in press, 2016d

3. G. Ramos-Llordén, A.J. den Dekker, **G. Van Steenkiste**, B. Jeurissen, J. Van Audekerke, M. Verhoye, and J. Sijbers. A unified maximum likelihood framework for simultaneous motion and T1 estimation in quantitative MR T1 mapping. *IEEE Transactions on Medical Imaging*, submitted, 2016

4. J. Hamaide, G. De Groof, **G. Van Steenkiste**, B. Jeurissen, J. Van Audekerke, M. Naeyaert, L. Van Ruijssevelt, C. Cornil, J. Sijbers, M. Verhoye, and A. Van der Linden. Exploring sexual dimorphisms in the adult zebra finch brain: in vivo diffusion tensor imaging and ex vivo super-resolution track density imaging. *NeuroImage*, submitted, 2016

Conference papers

1. **G. Van Steenkiste**, D.H.J. Poot, B. Jeurissen, A.J. den Dekker, and J. Sijbers. High resolution T1 estimation from multiple low resolution magnetic resonance images. In *Proceedings of the IEEE International Symposium on Biomedical Imaging*, volume 12, pages 1036–1039, New York, NY, USA, 2015e

2. G. Ramos-Llorden, A.J. den Dekker, **G. Van Steenkiste**, J. van Audekerke, M. Verhoye, and J. Sijbers. Simultaneous motion correction and T1 estimation in quantitative T1 mapping: an ML restoration approach. In *Proceedings of the IEEE International Conference on Image Processing*, pages 3160–3164, Quebec, Canada, 2015c

3. P. Bladt, **G. Van Steenkiste**, G. Ramos-Llordén, A.J. den Dekker, and J. Sijbers. Multi-voxel algorithm for quantitative bi-exponential MRI T1 estimation. In *Proceedings of SPIE Medical Imaging*, pages 978402–978402, San Diego, CA, USA, 2016

Conference abstracts

1. **G. Van Steenkiste**, B. Jeurissen, J. Sijbers, and D.H.J. Poot. Super resolution reconstruction from differently oriented diffusion tensor data sets. In *Proceedings of the ISMRM Benelux*, volume 5, Rotterdam, The Netherlands, 2013a

2. **G. Van Steenkiste**, B. Jeurissen, J. Sijbers, and D.H.J. Poot. Super resolution reconstruction from differently oriented diffusion tensor data sets. In *Proceedings of the International Society for Magnetic Resonance in Medicine*, volume 21, page 3186, Salt Lake City, Utah, USA, 2013b

3. **G. Van Steenkiste**, B. Jeurrisen, D.H.J. Poot, and J. Sijbers. Super-resolution reconstruction of diffusion tensor parameters from multi-oriented diffusion weighted images. In *Proceedings of the workshop "Imaging the brain at different scales: How to integrate multi-scale structural information?"*, Antwerp, Belgium, 2013c

4. **G. Van Steenkiste**, B. Jeurissen, D.H.J. Poot, P.M. Parizel, and J. Sijbers. Super-resolution reconstruction of diffusion parameters from multi-oriented diffusion weighted images. In *Proceedings of the ISMRM Benelux*, volume 6, page 39, Maastricht, The Netherlands, 2014a

5. **G. Van Steenkiste**, B. Jeurissen, D.H.J. Poot, and J. Sijbers. Super-resolution reconstruction of diffusion parameters from multi-oriented diffusion weighted images. In *Proceedings of the International Society for Magnetic Resonance in Medicine*, volume 22, page 2572, Milan, Italy, 2014b

6. **G. Van Steenkiste**, J. Hamaide, B. Jeurissen, D.H.J. Poot, J. Van Audekerke, J. Sijbers, and M. Verhoye. Super-resolution structural connectivity and anatomy of the zebra finch brain. In *Proceedings of the ISMRM Benelux*, volume 7, page O029, Ghent, Belgium, 2015a

7. G. Ramos-Llorden, A.J. den Dekker, **G. Van Steenkiste**, J. Van Audekerke, M. Verhoye, and J. Sijbers. Simultaneous group-wise rigid registration and T1 ML estimation for T1 mapping. In *Proceedings of the ISMRM Benelux*, volume 7, page P051, Ghent, Belgium, 2015b

8. **G. Van Steenkiste**, J. Hamaide, B. Jeurissen, D.H.J. Poot, J. Van Audekerke, J. Sijbers, and M. Verhoye. Combination of super-resolution reconstruction diffusion tensor imaging and track density imaging reveals song control system connectivity in zebra finches. In *Proceedings of the International Society for Magnetic Resonance in Medicine*, volume 23, page 2861, Toronto, Ontario, Canada, 2015b

9. **G. Van Steenkiste**, D.H.J. Poot, B. Jeurissen, A.J. den Dekker, and J. Sijbers. Super-resolution T1 mapping: a simulation study. In *Proceedings of the International Society for Magnetic Resonance in Medicine*, volume 23, page 1679, Toronto, Ontario, Canada, 2015d

10. G. Ramos-Llorden, A.J. den Dekker, **G. Van Steenkiste**, J. Van Audekerke, M. Verhoye, and J. Sijbers. Simultaneous group-wise rigid registration and T1 ML estimation for T1 mapping. In *Proceedings of the International Society for Magnetic Resonance in Medicine*, volume 23, page 447, Toronto, Ontario, Canada, 2015a

11. **G. Van Steenkiste**, B. Jeurissen, S. Baete, A.J. den Dekker, D.H.J. Poot, F. Boada, and J. Sijbers. High resolution diffusion tensor imaging in a clinically feasible scan time. In *Proceedings of the second Belgian Neuroinformatics Congress*, Leuven, Belgium, 2015c

12. P. Bladt, G. Ramos-Llordén, **G. Van Steenkiste**, J. Sijbers, and A.J. den Dekker. Quantitative T1 estimation from T1-weighted images affected by partial volume effects. In *Proceedings of the second Belgian Neuroinformatics Congress*, Leuven, Belgium, 2015

13. **G. Van Steenkiste**, B. Jeurissen, S. Baete, A.J. den Dekker, D.H.J. Poot, F. Boada, and J. Sijbers. In vivo high resolution diffusion tensor imaging in a clinically acceptable scan time by combining super resolution reconstruction with simultaneous multi-slice acquisition. In *Proceedings of the ISMRM Benelux*, volume 8, pages P–036, Eindhoven, The Netherlands, 2016a

14. S.D. Washington, S. Radtke-Schuller, J. Hamaide, **G. Van Steenkiste**, J. Sijbers, S. Deleye, J.S. Kanwal, J.J. Wenstrup, G. de Groof, S. Liang, J. Van Audekerke, M. Verhoye, and A. Van der Linden. Magnetic resonance imaging and histology based brain atlases of the mustached bat, Pteronotus parnellii. In *Proceedings of the ISMRM Benelux*, volume 8, pages P–055, Eindhoven, The Netherlands, 2016

15. **G. Van Steenkiste**, B. Jeurissen, S. Baete, A.J. den Dekker, D.H.J. Poot, F. Boada, and J. Sijbers. High resolution diffusion tensor reconstruction from simultaneous multi-slice acquisitions in a clinically feasible scan time. In *Proceedings of the International Society for Magnetic Resonance in Medicine*, volume 24, page 0002, Singapore, 2016b

Awards

1. *Educational Stipend Award* for the work: **G. Van Steenkiste**, B. Jeurissen, J. Sijbers, and D.H.J. Poot. Super resolution reconstruction from differently oriented diffusion tensor data sets. In *Proceedings of the International Society for Magnetic Resonance in Medicine*, volume 21, page 3186, Salt Lake City, Utah, USA, 2013b

2. *Summa Cum Laude Merit Award* for the work: **G. Van Steenkiste**, B. Jeurissen, J. Sijbers, and D.H.J. Poot. Super resolution reconstruction from differently oriented diffusion tensor data sets. In *Proceedings of the International Society for Magnetic Resonance in Medicine*, volume 21, page 3186, Salt Lake City, Utah, USA, 2013b

3. *Poster award in the Electronic Diffusion Poster Category* for the work: **G. Van Steenkiste**, B. Jeurissen, J. Sijbers, and D.H.J. Poot. Super resolution reconstruction from differently oriented diffusion tensor data sets. In *Proceedings of the International Society for Magnetic Resonance in Medicine*, volume 21, page 3186, Salt Lake City, Utah, USA, 2013b

4. *Educational Stipend Award* for the work: **G. Van Steenkiste**, B. Jeurissen, D.H.J. Poot, and J. Sijbers. Super-resolution reconstruction of diffusion parameters from multi-oriented diffusion weighted images. In *Proceedings of the International Society for Magnetic Resonance in Medicine*, volume 22, page 2572, Milan, Italy, 2014b

5. *Educational Stipend Award* for the work: **G. Van Steenkiste**, D.H.J. Poot, B. Jeurissen, A.J. den Dekker, and J. Sijbers. Super-resolution T1 mapping: a simulation study. In *Proceedings of the International Society for Magnetic Resonance in Medicine*, volume 23, page 1679, Toronto, Ontario, Canada, 2015d

6. *Magna Cum Laude Merit Award* for the work: G. Ramos-Llorden, A.J. den Dekker, **G. Van Steenkiste**, J. Van Audekerke, M. Verhoye, and J. Sijbers. Simultaneous group-wise rigid registration and T1 ML estimation for T1 mapping. In *Proceedings of the International Society for Magnetic Resonance in Medicine*, volume 23, page 447, Toronto, Ontario, Canada, 2015a

7. *Editor's Pick of the month (January 2016) in Magnetic Resonance in Medicine* for the work: **G. Van Steenkiste**, D.H.J. Poot, B. Jeurissen, A.J. den Dekker, and J. Sijbers. High resolution T1 estimation from multiple low resolution magnetic resonance images. In *Proceedings of the IEEE International Symposium on Biomedical Imaging*, volume 12, pages 1036–1039, New York, NY, USA, 2015e

8. *FWO travel grant* for the work: **G. Van Steenkiste**, B. Jeurissen, S. Baete, A.J. den Dekker, D.H.J. Poot, F. Boada, and J. Sijbers. High resolution diffusion tensor reconstruction from simultaneous multi-slice acquisitions in a clinically feasible scan time. In *Proceedings of the International Society for Magnetic Resonance in Medicine*, volume 24, page 0002, Singapore, 2016b

9. *Henri Benedictus - B.A.E.F. fellowship of the Henri Benedictus Fund of the King Baudouin Foundation and the Belgium American Educational Foundation for the academic year 2016-2017.*

Invited talks at research groups

1. *Super-resolution reconstruction of diffusion parameters from diffusion-weighted images with different slice orientations*, Dept of Radiology NYU Langone Medical Center, New York, USA, april 23, 2015

Teaching and supervision

1. **2012-2015**: Tutor exercises 'Fysica m.i.v. wiskunde' (1st year B. Sc. Pharmacy and 1st year B. Sc. Biomedical Sciences), supervising lecturer: Prof. Dr. Jan Sijbers
2. **2013-2016**: Tutor exercises 'Fysica voor biomedisch onderzoek' (1st year B. Sc. Biomedical Sciences), supervising lecturer: Prof. Dr. Jan Sijbers
3. **2014-2015**: Co-supervisor of Piet Bladt (thesis M. Sc. in Physics, University of Antwerp): 'Quantitative Multi-Component T1 mapping ' (Supervisor: Prof. Dr. Jan Sijbers)

Research stay

1. Center for Biomedical Imaging (Dept. Radiology), NYU Langone medical center New York, NY, United States, 24 august 2015 - 18 september 2015, supervised by Prof. Dr. Fernando Boada and Dr. Ir. Steven Baete

Relevant courses and workshops

1. Weekend Educational Program organized by the International Society for Magnetic Resonance in Medicine, several locations, 2013-2016
2. 'Workshop on processing multi-shell diffusion MRI data using MRtrix3', Antwerp, Belgium, September 23, 2015
3. 'Machine learning for NeuroImage', B. Thirion, ISBI 2015 tutorials, New York, USA, April 16, 2015
4. 'Structural an dynamical networks in the brain', Ghent, Belgium, december, 12, 2013
5. 'Symposium on Human Brain Imaging', Donders instituut, Nijmegen, The Netherlands, March, 6, 2013

Part of organizing committee of following conferences

1. 8th Annual meeting of the ISMRM Benelux, Eindhoven, The Netherlands, January, 22, 2016